Short-lived halocarbon species in the Oceans and Atmosphere

Stephen J. Andrews

Doctor of Philosophy

University of York

Department of Chemistry

September 2013

Abstract

This study aimed to improve current understanding of the emissions and distributions of very short-lived halocarbons (VSLH), thus their impact on atmospheric halogen chemistry. VSLH measurements were made during the TROMPEX campaign over the tropical Atlantic Ocean and Mauritanian upwelling region. This produced the first reported measurements of CH_2ICl by a research aircraft and identified an open-ocean source, likely linked to phytoplankton. VSLH emissions over the upwelling, implicated as a major localised source, were similar to previously measured coastal emissions which globally cover a much larger area. Thus it is likely that coastal upwelling systems in themselves are not strong global sources of VSLH.

Ship-borne VSLH measurements were taken in the East Tropical Pacific (ETP) during the TORERO campaign. High sensitivity and frequency sampling gave new information regarding the distribution of VSLH, including a photolytically driven diurnal cycle of CH_2I_2. Fluxes were calculated using simultaneous seawater and air measurements spanning a large area of the ETP where very few other measurements exist. Although individual VSLH depth profiles showed covariance with Chlorophyll-a (Chl-a), cross sections revealed differences in their latitudinal distributions. In fact there was little bulk correlation with surface water concentrations of Chl-a. CH_2I_2 and CH_2ICl displayed a negative relationship with Chl-a, attributed to physical and mixing processes. $CHBr_3$, CH_2Br_2 and $CHBr_2Cl$ showed a relationship between surface and deep maxima concentrations suggesting that if a proxy for their production was found that this would negate the use of water column models to parameterise the surface concentrations of these species.

Wind speed controls VSLH distribution in the ocean mixed layer and may even influence oceanic lifetimes of the shortest-lived species via increased turbidity and solar attenuation. It also exerts a strong control on CH_3I, CH_2ICl, CH_2I_2 and $CHCl_3$ emissions and could form a link between emissions and future changes in climate.

Contents

List of Figures

List of Tables

Acknowledgements

Firstly, immeasurable thanks must be given to my supervisor, Lucy Carpenter. The time and effort that she has put into this project has provided me with an incredible educational and personal experience for which I will always be in her debt.

Starting at the beginning... Big thanks to the entire atmospheric group especially those present at York when I started. Charlotte Jones, who guided me through my first year, introduced me to the instruments and helped with all those TROMPEX calculations, she is now in Japan. Sam Edwards, for helping with the physical chemistry and for clapping when walking into labs where I was delicately working, cheers! He is now in New Zealand. Marv Shaw, mainly for the drinking/smoking but also the goalkeeping acrobatics. He is now in Lancaster, is it me? Rich Lidster, for his friendship, the banter, road trips, snowboarding holidays, squash games and the crazy experiments, he's still here of course. Let's not forget the TORERO campaign; 6 weeks sharing a bunk bed was made bearable by the hilarious giant squid fishing, rocket-flare launching and potato cannon escapades.

All of the PhysChem office, especially Rob and James for the Pub Quiz victories, eating challenges and other, usually drinking related activities. All the newer post-Docs and PhD students: Sina for continuing to push the development of the instruments further and for her terminator-esque fieldwork commitment. Dene for continuing to push the definition of the word "game" of football. Jamie for continuing to push the boundaries of workplace etiquette. Em for being the fastest person ever to learn to snowboard. Shalini for the amazing food when "just popping over for a cup of tea" and Rosie for the marine chemistry knowledge and midnight sun gin and tonic drinking in the Arctic during ACCACIA.

A big thanks to all the "senior" citizens of the atmospheric group! Jimmy, James, Andrew, Ruth, Mustafa, Katie, Martyn (sorry!), Mat, Jacqui and Ally for all the help, campaigns and various opportunities given to me over the years. To all the other BSc, MChem, PhD and post-Docs that I have worked with, you have not been forgotten... I've just forgotten your names.

Lastly, but most importantly, my girlfriend Helen who has had to live with me for 3 years now. I don't know what to say other than thank you for all of your support and love. Now let's go on that holiday!

Declaration

The research described in this thesis is original work, which I undertook at the University of York during 2009–2013. Except where stated, all of the work contained within this thesis represents the original contribution of the author. Some parts of this thesis have been published in journals; where items were published jointly with collaborators, the author of this thesis is responsible for the material presented here. For each published item the primary author is the first listed author. Publications are listed at the beginning of the chapter to which they relate.

Chapter 1

Introduction

1.1 Preface

Asking a member of the general public what they know about atmospheric chemistry will most likely result in a response quoting "the ozone hole" with some reference to chlorofluorocarbons (CFCs). Like it or not, the role of CFCs in ozone depletion and the subsequent discovery of a hole in the ozone layer has become, and still remains, the public face of atmospheric chemistry.

An understanding into the destructive effects of CFCs came in 1974 from chemists Frank Sherwood Rowland and Mario Molina at the University of California (Molina and Rowland, 1974). In 1985 the Antarctic ozone hole was discovered by Farman, Gardiner and Shanklin, its presence attributed to the transportation of very long-lived CFCs into the stratosphere where they are photolysed to produce molecular chlorine and fluorine resulting in catalytic ozone destruction (Farman et al., 1985).

This was the key event that turned the worlds attention toward atmospheric science and controls were put in place restricting the release of ozone depleting substances following the Montreal Protocol in 1987. This has resulted in the current strict controls, restricting the production and release of these long lived species with high ozone depletion potentials (ODPs). Hydrochlorofluorocarbons (HCFCs) have been developed to phase out the use of CFCs but despite their significantly lower ODPs, they still photolyse in the stratosphere and participate in catalytic ozone destruction cycles. Meanwhile, less emphasis was placed on the very short-lived species which were regarded as having too short an atmospheric lifetime to reach the stratosphere and deplete the ozone layer.

Very short-lived halocarbons (VSLH) mainly photolyse within the troposphere where their chemical role is somewhat different to the processes occurring in the stratosphere. However, due to rapid vertical transport at the equatorial inter-tropical convergence zone (ITCZ) where tropospheric-stratospheric mixing times are shorter, some species of VSLH can be convected fast enough to contribute to the halogen radical abundance into the lower stratosphere and hence participate in O_3 destruction. VSLH play an important role in tropospheric chemistry too. They originate from biogenic as well as anthropogenic sources and both sources and sinks of these reactive compounds must be identified and quantified if tropospheric chemistry is to be fully understood.

1.2 Atmospheric dynamics

The atmosphere can be divided into five principle layers: The troposphere, stratosphere, mesosphere, thermosphere and exosphere. Pressure decays exponentially up to the top of the mesosphere whilst temperature has a distinct vertical profile.

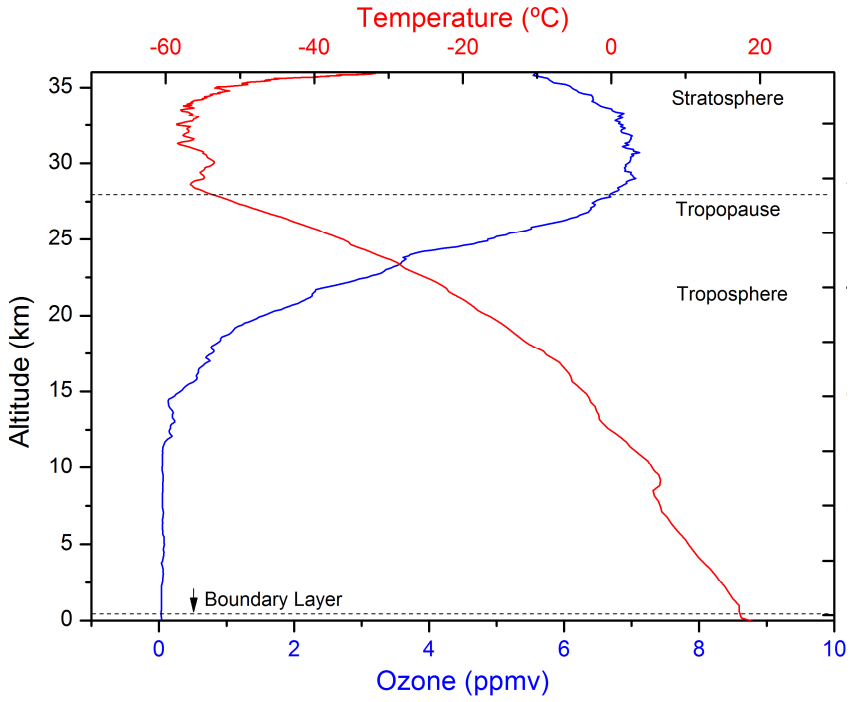

Figure 1.1 – Ozone sonde vertical profile data, 27 August 1997, Trinidad Head, CA. NOAA.

The temperature at the surface of the Earth is high due to absorption of solar radiation, subsequent rising of warm buoyant air and the release of latent heat of condensation during cloud formation. The mixed layer closest to the Earth's surface is called the boundary layer and its height varies between around 500-1000 m diurnally and depending on location and season. The boundary layer is the part of the troposphere directly influenced by the presence of the Earth's surface. Emissions from the surface can be convected to the top of the troposphere, the tropopause. The majority of atmospheric dynamics occurs in the troposphere with water vapour condensing as it rises to form clouds and precipitation. Between the surface and the tropopause the temperature decreases due to proximity to

the warm surface of the Earth.

In the stratosphere the temperature begins to increase. This is due to the absorption and release of energy by O_3 which is present in high concentrations in the stratosphere and, at its peak concentration, referred to as the ozone layer (figure 1.1). This layer of O_3 along with molecular oxygen absorbs radiation in the range 200–310 nm, resulting in only wavelengths longer than this reaching the troposphere and the Earth's surface. This positive temperature gradient results in little mixing by convection and creates a stable, stratified layer, hence the name stratosphere. In the mesosphere the temperature decreases again due to decreasing O_3 concentration until the thermosphere, where increased N_2 and O_2 absorption at wavelengths < 200 nm causes temperatures to rise (Finlayson-Pitts and Pitts Jr, 1986).

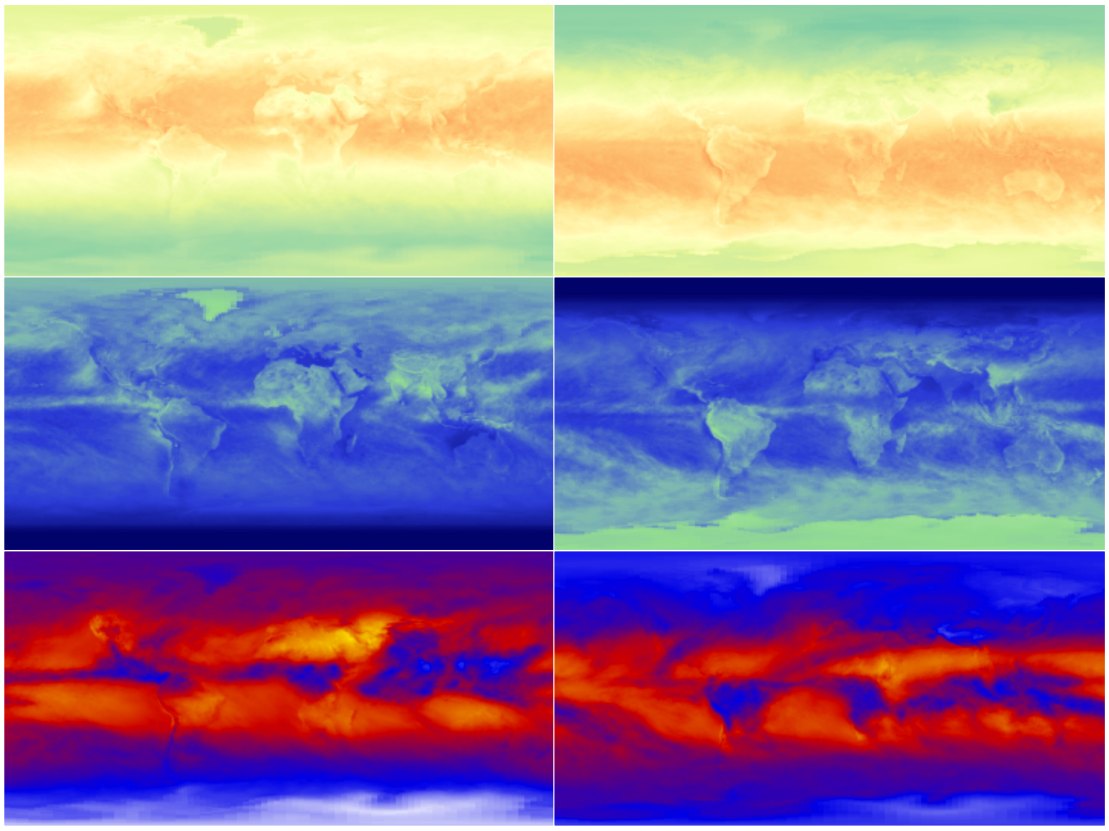

Figure 1.2 – Satellite observations of the Earth's energy system from NASA NEO. August 2012 left, February 2012 right. From top to bottom: Net radiation (Blue-Red, Low-High), reflected short wave radiation (Blue-Green-White, Low-High) and outgoing long wave radiation (Blue-Red-Yellow, Low-High).

1.2.1 Global Energy Budget

In order for the Earth's temperature to remain constant its net energy flux must be zero. That is the outgoing, reflected radiation is equal to the incoming radiation. This is called the global energy budget. At the equator, the net radiation flux (incoming minus outgoing) is positive and at the poles it is negative (figure 1.2). This energy and thus temperature gradient between the equator and the poles drives atmospheric circulation. This is also true of the ocean, driving oceanic circulation (section 1.3). If the Earth was a non-rotating sphere, two large convection cells would form with the air at the equatorial surface ascending and moving toward the poles where it cools and descends.

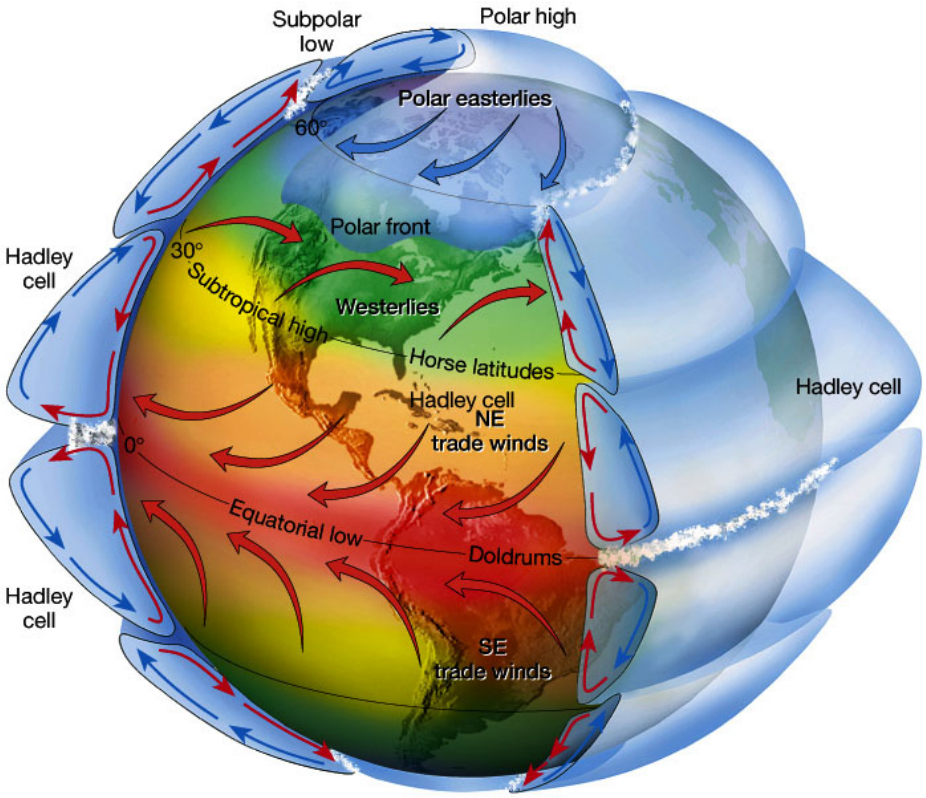

Figure 1.3 – Representation of atmospheric circulation. From The Atmosphere, Lutgens and Tarbuck, 8^{th} edition, 2001. Colour scheme depicts temperature.

In reality, air circulates in cells where warm air descends at mid-latitudes and, due to the rotation of the Earth, is deflected to the right in the northern hemisphere and to the left in the southern hemisphere. This is known as the Coriolis effect (figure 1.3). The

warm air that converges at the equator is transported rapidly upward and can reach the tropopause in a matter of days. The convergence of these air masses is called the inter-tropical convergence zone (ITCZ). Evaporation from the ocean results in high humidity which combined with strong convection produces an almost permanent cloud band at the ITCZ which shifts a few degrees north or south of the equator depending upon the time of year.

1.2.2 Albedo

Low level clouds play an important role in the Earth's radiation budget because they reflect incoming solar radiation back into space. The reflectivity of a surface to short-wave radiation is called its albedo. The influence of surface albedo is significant and is the reason why the polar regions do not heat to the same temperature as the equator during their summer season despite being angled toward the Sun as the white, reflective snow and ice have a high albedo. Albedo is also influenced by human activities such as construction of buildings and laying of concrete/tarmac. The Earth's radiation budget is paramount to atmospheric and ocean dynamics, but also chemistry as most atmospheric reactions require external energy in some form to proceed.

1.3 Ocean dynamics

As with atmospheric dynamics, the dynamics of the ocean are ultimately driven by solar radiation. The Sun can drive ocean currents directly through heating the ocean surface or indirectly from surface wind shear and density gradients from evaporation. Atmospheric pressure differentials create surface winds which drive surface ocean currents. Surface winds and solar irradiance heating the oceans causes evaporation of seawater which increases ocean density. Density is the major driving force for ocean circulation.

1.3.1 Thermohaline circulation

Unlike surface currents which are predominately wind driven, the deep ocean currents are unaffected by wind and are controlled by thermohaline circulation.

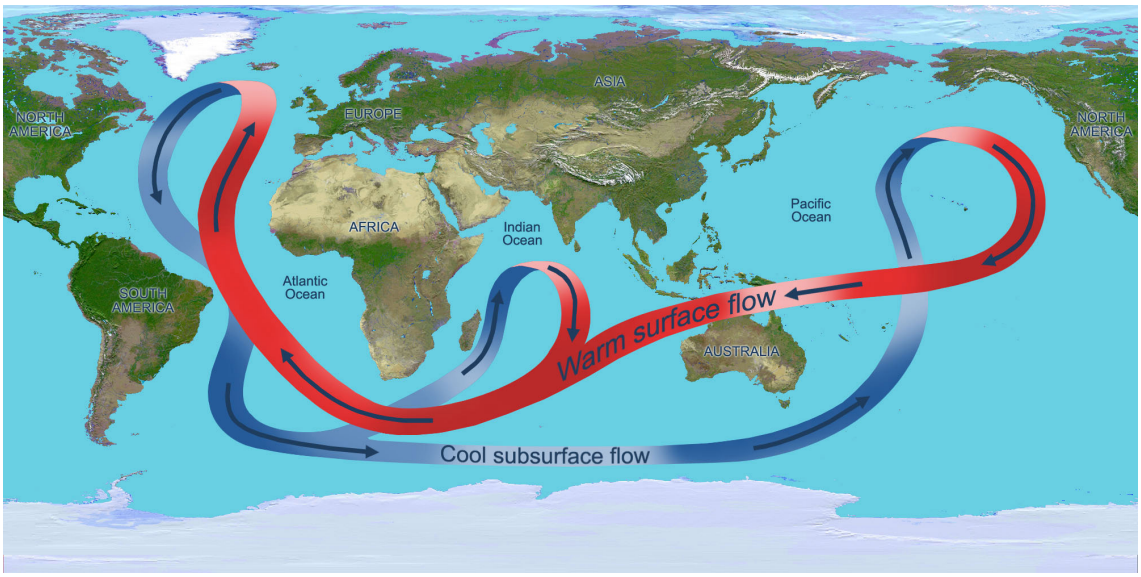

Figure 1.4 – Large scale thermohaline ocean circulation. NASA, http://www.ces.fau.edu/nasa/resources/global-ocean-conveyor.php.

Large scale ocean currents are dominated by density gradients caused by differences in temperature (thermo) and salinity (haline). Water sinks in the polar North Atlantic and Southern Ocean. Surface water is cooled by the wind and surface evaporation increases density, causing the water to sink. Sinking water at high latitudes and equatorial warming creates a circulation somewhat analogous to atmospheric circulation. Also, in the same way as the Earth's surface roughness affects surface wind, the ocean floor affects the flow of deep water during circulation. As the deep water travels it becomes increasingly rich in nutrients which sink from the surface. New, sinking dense water displaces older, nutrient rich water, which is upwelled to the surface, often at equatorial latitudes (section 1.3.3).

Thermohaline circulation plays an important role in regulating the global climate. Cold, nutrient rich upwelled water can produce algal blooms and increased biological activity (Bruland et al., 2001). This can subsequently release atmospherically active gases such as halogens and sulphurs and can exert a control on the concentration of greenhouse gases. Warm surface water moving towards the poles regulates the spatial extent of the polar ice caps, affecting albedo, releasing or trapping gases in the ice and uncovering or covering areas of biologically productive ocean.

1.3.2 Surface Currents

The movement of the ocean at the surface (approximately the top 100–200 m) is driven primarily by momentum gain from surface wind stress. Due to the Coriolis Effect, the direction of movement of the surface water is deflected by a 45° angle to the wind direction. The deflection stops at 45° due to a balance between the wind and the Coriolis force. Water beneath the surface is not in contact with the wind and is only subjected to friction from the water above. Therefore as depth increases, so does the angle of deflection. This is called an Ekman spiral (Figure 1.5).

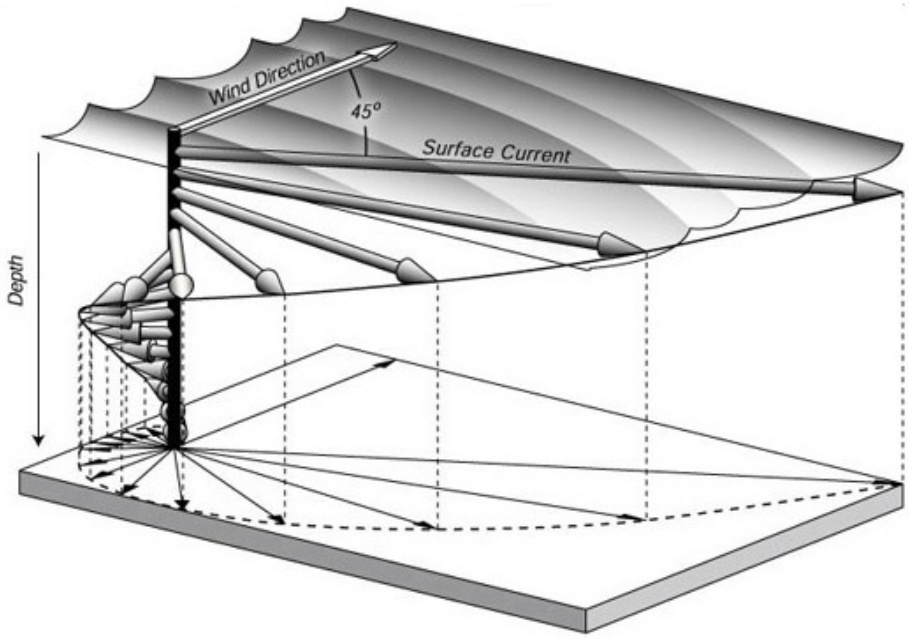

Figure 1.5 – Ekman spiral in the northern hemisphere. ©2004. Oceanworld, Texas A&M University.

1.3.3 Upwelling

This same effect is responsible for localised upwelling in coastal or equatorial regions. At the equator, opposing trade winds collide at the ITCZ which causes longitudinal movement of warm surface water. This brings cold water up from the deep ocean to replace the displaced warm surface water (figure 1.6). A similar situation occurs at coastlines with persistent winds parallel to the shore. The wind driven surface water movement is deflected away from the coast bringing cold water up to the surface. Coastal upwelling can be seen

along (but not limited to) the Gulf of California, the coast of Mauritania and the coast of Peru. As the cold water is rich in nutrients, upwelling regions display enhanced ocean productivity. Nitrates and phosphates are among the nutrients which limit microalgae and phytoplankton growth. Strong upwelling can cause rapid 'algal blooms' with subsequent atmospheric impact (section 1.4.3).

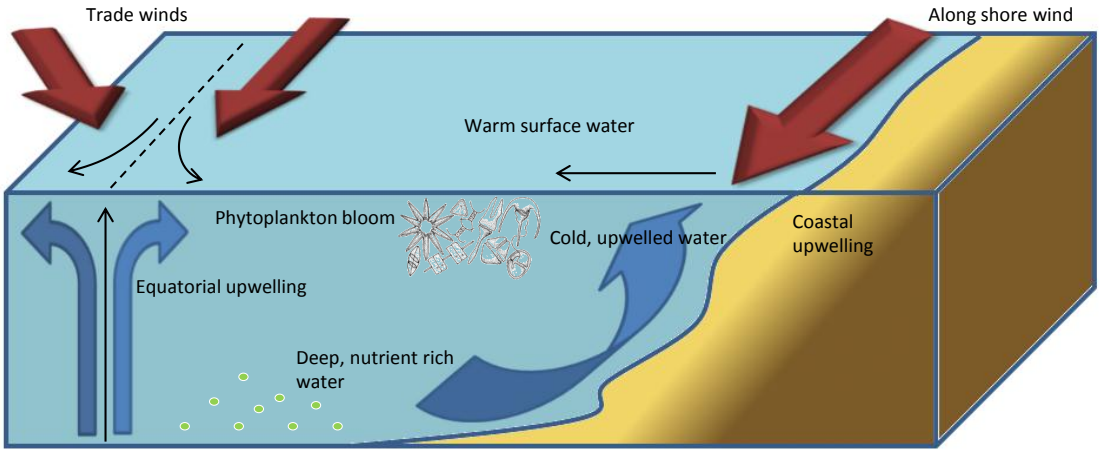

Figure 1.6 – Graphical representation of wind driven coastal and equatorial upwelling. Red arrows represent wind shear, blue arrows show movement of ocean currents. Black arrows represent surface ocean current.

1.4 Atmospheric Compostion

As discussed in section 1.2, the solar radiation spectrum that reaches Earth's surface ranges from around 300 to > 3000 nm. Within this range solar radiation is attenuated due to absorption and scattering by aerosol particles and gases.

Stratospheric O_3 plays an important role in filtering out UV radiation from entering the troposphere. Within the troposphere, O_3 is a pollutant and can cause irritation and even damage to the human respiratory system, crops and vegetation (Mills et al., 2011). The formation of O_3 in the stratosphere takes place due to the presence of UV radiation with high enough energy to dissociate oxygen from its dimer and follows the Chapman cycle:

$$O_2 + h\nu \longrightarrow O + O \qquad \lambda < 240\ nm \tag{1.1}$$

$$O + O_2 + M \longrightarrow O_3 + M \tag{1.2}$$

$$O_3 + h\nu \longrightarrow O(^1D) + O_2 \qquad \lambda < 320\ nm \tag{1.3}$$

$$O + O_3 \longrightarrow O_2 + O_2 \tag{1.4}$$

The only source of O_3 in the troposphere is via the photodissociation of NO_2 shown in equations 1.5 and 1.6. NO_2 is formed from NO during the photooxidation of volatile organic compounds (VOCs) (figure 1.7).

$$NO_2 + h\nu \longrightarrow O(^3P) + NO \tag{1.5}$$

$$O(^3P) + O_2 + M \longrightarrow O_3 + M \tag{1.6}$$

$$NO + O_3 \longrightarrow NO_2 + O_2 \tag{1.7}$$

NO can also react rapidly with O_3 to form NO_2 as shown in equation 1.7. In a high NO_x environment with limited VOC, increasing NO_x would result in a net O_3 loss.

The VOC photooxidation cycle is initiated by the OH radical, which abstracts a proton to form water and an alkyl radical. The oxidative capacity of the atmosphere is highly dependent upon O_3 and OH concentration. During daylight, OH is the main tropospheric oxidant and can be described as the 'Pac-Man' of the atmosphere due to its high reactivity with CO, H_2S, SO_2, CH_4 and other hydrocarbons. OH is produced by the photolysis of O_3 and subsequent reaction of the electronically excited $O(^1D)$ atom with H_2O or CH_4 (equations 1.8–1.10). Alternatively, $O(^1D)$ can undergo collisional quenching with N_2, O_2 or H_2O to form $O(^3P)$ which can react with O_2 to reform O_3.

$$O_3 + h\nu \longrightarrow O(^1D) + O_2 \qquad (\lambda \leq 310\ nm) \tag{1.8}$$

$$O(^1D) + H_2O \longrightarrow OH + OH \tag{1.9}$$

$$O(^1D) + CH_4 \longrightarrow OH + CH_3 \tag{1.10}$$

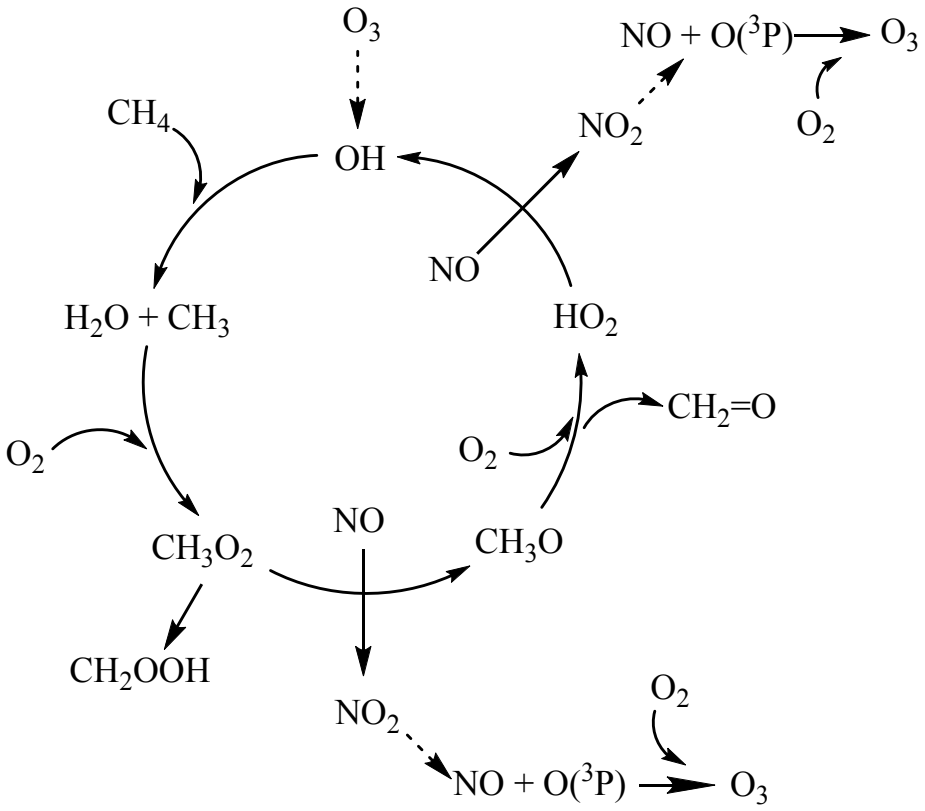

Figure 1.7 – Daytime VOC photooxidation cycle. Dotted arrows represent photolysis.

The VOC oxidation cycle is completed by the regeneration of OH (figure 1.7). In polluted atmospheres with high NO_x, there is net production of O_3 and OH during the day due to the formation of NO_2 and its subsequent photolysis.

During the night, OH production from the photolysis of O_3 stops and oxidation occurs via the nitrate radical (NO_3). NO_3 is photolysed extremely rapidly but at night its concentration increases to up to three orders of magnitude larger than day-time OH concentrations (Wayne, 1993) via its production from NO_2 and O_3 (equation 1.11). NO_x can also be produced from the high energy of a lightning strike dissociating nitrogen and oxygen molecules into their atomic form (Chameides et al., 1977).

$$NO_2 + O_3 \longrightarrow NO_3 + O_2 \tag{1.11}$$

OH can also be formed in poluted atmospheres by photolysis of HONO and H_2O_2. In clean atmospheres, such as remote open ocean sites, the production of OH is limited to

the photolysis of O_3 which in turn is limited by H_2O and CH_4. Without NO_x the only source of O_3 in these remote regions is from long range transport and entrainment from the stratosphere.

Clearly it is imperative that O_3 sources and sinks be well constrained if atmospheric chemistry is to be fully understood and modelled. Processes that impact O_3 concentration in either the troposphere or the stratosphere will have a large influence on the Earth, its climate and ecosystem.

1.4.1 Halogen chemistry

Halogen chemistry is atmospherically important for a multitude of reasons. In the stratosphere, O_3 can be catalytically destroyed by bromine or chlorine (Molina and Rowland, 1974) where the halogen atom is reformed via reaction with atomic oxygen (equations 1.12, 1.13).

$$Cl + O_3 \longrightarrow ClO + O_2 \tag{1.12}$$

$$ClO + O \longrightarrow Cl + O_2 \tag{1.13}$$

This reaction proceeds with any halogen and can occur throughout the atmosphere. Stratospheric ozone depletion is currently dominated by CFCs which were designed to be very inert to be used as refrigerants and fire suppressants. Because they are so unreactive they are eventually convected to the stratosphere where wavelengths of light $<$ 220 nm (Minschwaner et al., 2012), present in the stratosphere but attenuated through the troposphere, provide enough energy to break the covalent bond between chlorine and carbon.

Heterogeneous reactions also play an important role in stratospheric ozone depletion with reactions on sulphate aerosol, uptake of HNO_3 by the sulphate, subsequent growth and the formation of polar stratospheric clouds (PSC) (Molina et al., 1993). These clouds consist as liquid or solid HNO_3 and H_2O and can convert reservoir chlorine compounds such as $ClONO_2$ and HCl into reactive species (Hanson and Ravishankara, 1991) via equations

1.14 and 1.15.

$$\mathrm{HCl_{(ads)} + ClONO_{2(g)} \xrightarrow{PSC} HNO_{3(abs)} + Cl_{2(g)}} \tag{1.14}$$

$$\mathrm{ClONO_{2(g)} + H_2O_{(abs)} \longrightarrow HNO_{3(abs)} + HOCl_{(g)}} \tag{1.15}$$

PSC also remove NO_2 which serves to decrease the formation of $ClONO_2$.

Stratospheric ozone depletion is not just limited to chlorine. Bromine is about 60 times more effective than chlorine in depleting O_3 (Law and Sturges, 2007). Iodine has an even higher ozone depletion potential (ODP) of 150–300 times that of chlorine (Ko et al., 2003) but stratospheric injection is much less likely due to its reactivity.

1.4.1.1 Tropospheric halogen chemistry

In the troposphere, halogen reactions influence the capacity of the atmosphere to oxidise numerous organic and inorganic species. This is due to the products of the photodissociation of O_3 forming OH which then oxidises VOCs (section 1.4). Halogen atoms catalytically deplete O_3 via their reaction to form halogen oxide radicals which can then be reduced back to their atomic form photolytically or by reaction with NO, HO_2 or XO (where X is a halogen). Tropospheric halogen chemistry is estimated to deplete around 10% of the tropical tropospheric ozone column and contributes approximately -0.1 W m^{-2} to the radiative flux at the tropical tropopause due to O_3 acting as a greenhouse gas (Saiz-Lopez et al., 2012).

$$\mathrm{X_2 + h\nu \longrightarrow 2\,X} \tag{1.16}$$

$$\mathrm{X + O_3 \longrightarrow XO + O_2} \tag{1.17}$$

$$\mathrm{XO + h\nu \longrightarrow X + O} \tag{1.18}$$

$$\mathrm{XO + XO \longrightarrow X_2 + O_2} \tag{1.19}$$

(where XO can also be a different halogen, YO)

$$\mathrm{XO + NO \longrightarrow X + NO_2} \tag{1.20}$$

Halogen oxides are rapidly photolysed back to a halogen and an oxygen atom (equation 1.18 which can reform O_3 so it is the subsequent reactions of XO (equations 1.19–1.24) which lead to a net O_3 loss. In addition to the catalytic destruction of O_3, halogen oxides can react with HO_2 and NO_2 which play an important role in the formation of O_3, NO_3 and OH (equations 1.21 and 1.22). Open-ocean marine boundary layer (MBL) iodine oxide (IO) has been observed at mixing ratios up to 1.5 pptv (Read et al., 2008). Another effect on tropospheric O_3 concentration is from the enhancement of dry deposition of O_3 into surface seawater by the presence of I^- in the seawater (Jones and Carpenter, 2005; Carpenter et al., 2013).

$$XO + HO_2 \longrightarrow O_2 + HOX \tag{1.21}$$

$$XO + NO_2 \longrightarrow XONO_2 \tag{1.22}$$

$$XO + XO \longrightarrow X_2O_2 \xrightarrow{h\nu} OXO \tag{1.23}$$

$$XO + XO \longrightarrow OXO \xrightarrow{OH} HXO_3 \tag{1.24}$$

Iodine oxide and iodine dioxide radicals can also combine to form IOPs (iodine oxidation particles) which can then condense (Burkholder et al., 2004; Saunders and Plane, 2006; Saunders et al., 2010). If these IOPs act as cloud condensation nuclei (CCN) (section 1.4.5) they can affect albedo and the Earth's radiative budget (section 1.2.2).

Recently, attention has been drawn to iodine mediated oxidation of gaseous elemental Hg^0 to reactive gaseous Hg^{II} in the polar atmosphere (figure 1.11). Hg^{II} is toxic and can be bioaccumulated in large predatory fish such as Tuna (Selin, 2009).

1.4.2 Halogen oxides and the ozone budget

As discussed, bromine and iodine oxide play an important role in ozone depletion in the troposphere and stratosphere. As there are many processes involved subsequent to the release of Reactive Halogen Species (RHS) into the atmosphere (figure 1.11), models are used to understand and attempt to quantify the effect they have on ozone concentrations. Figure 1.8, calculated from measurements at the Cape Verde observatory, highlights the

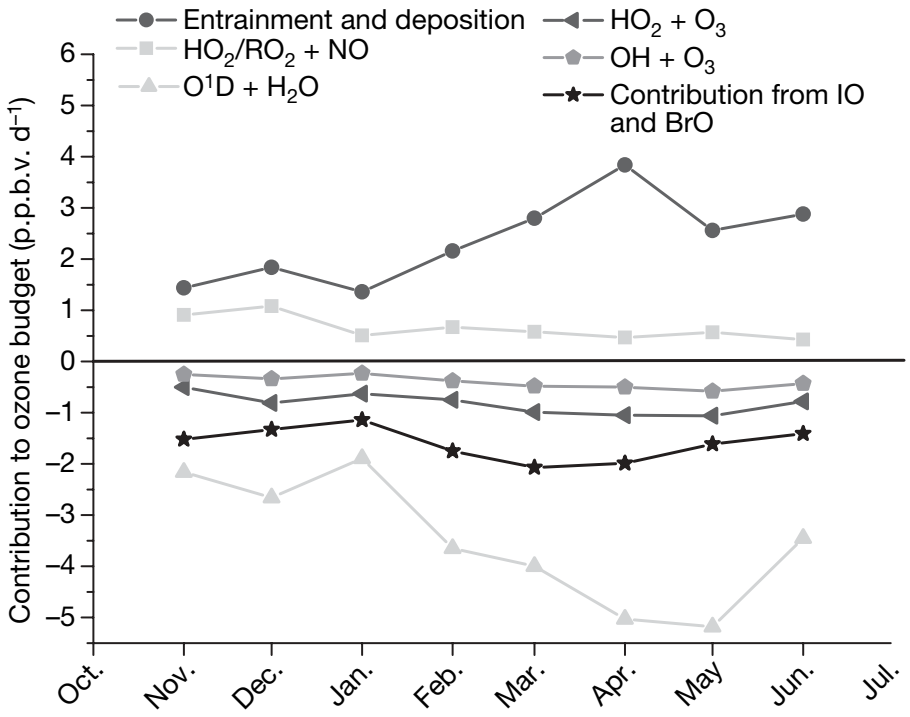

Figure 1.8 – Monthly averaged contributions to the daily ozone budget between 9:00 and 17:00 UTC, reproduced from Read et al. (2008).

importance of RHS when trying to constrain the MBL ozone budget with IO and BrO removing between 1-2 ppbv O_3 d^{-1}. The contribution of RHS to the stratosphere is extremely difficult to quantify but it is possible that even iodine chemistry to some degree, plays an active role in stratospheric ozone destruction (Solomon et al., 1994).

The sources and sinks of IO are not well defined. IO can be measured in the atmosphere but we do not yet have a comprehensive account of where it is coming from to balance the IO budget. It is clear that halogens play an important role in tropospheric ozone depletion but the known sources of reactive iodine, such as organic iodine species, cannot explain the IO concentrations observed (Mahajan et al. (2010), figure 1.9). In order for models to match observations of diurnal ozone destruction, both iodine and bromine chemistry must be factored in (Read et al., 2008). Thus, to accurately model ozone, the global atmospheric halogen budget must be closed.

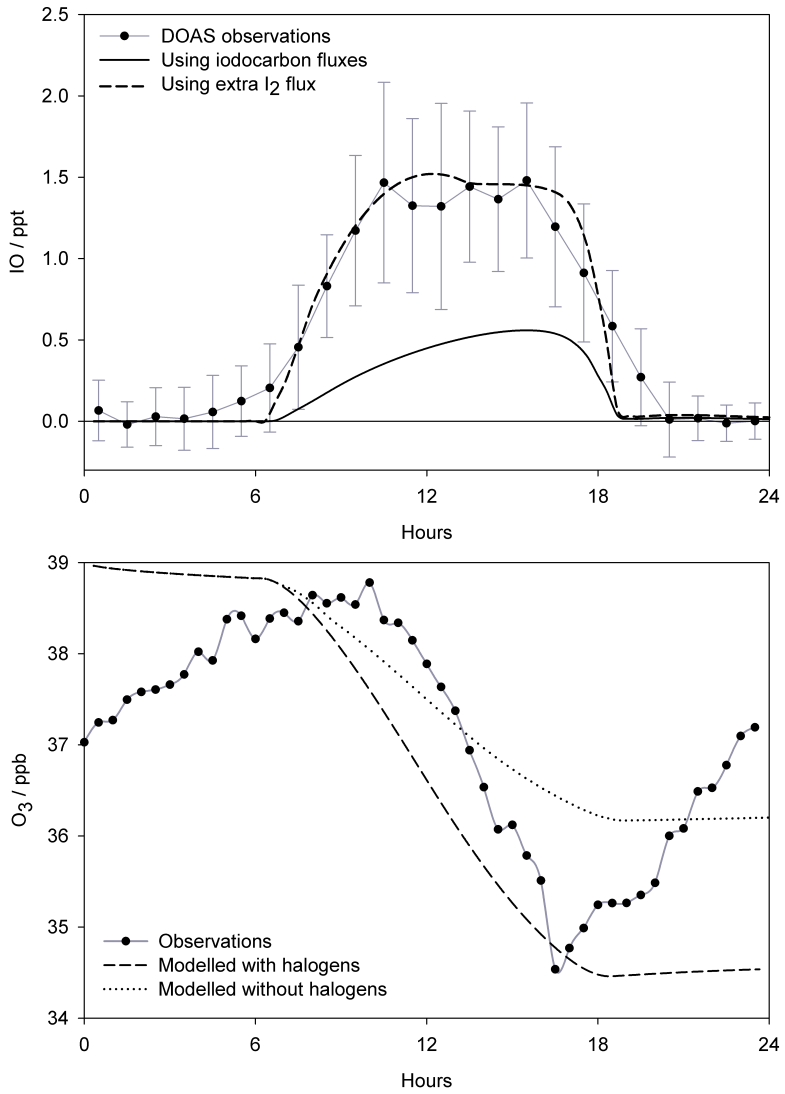

Figure 1.9 – Reproduced from Mahajan et al. (2010). Top: Measured IO concentrations from Differential Optical Absorption Spectroscopy (DOAS), observations shown as circles, solid line represents modeled IO using iodocarbon flux and dashed lines highlights the extra I_2 flux required for models to match observations. Below: The effect of including this extra I_2 flux on modeled O_3 compared to observations.

1.4.3 Sources of Reactive Halogen Species

The most well-known and significant, for stratospheric ozone, source of halogens into the atmosphere is from long-lived halogenated compounds including CFCs, CCl_4, HCFCs, and anthropogenic halons as well as long-lived compounds which are produced both naturally and anthropogenically such as methyl bromide and chloride. The Montreal Protocol has resulted in the phasing out of CFC emissions, although small emissions from 'banks' in existing applications such as refrigerators, air conditioning units, and foams still occur (Montzka et al., 2011). Atmospheric abundance and emissions of HCFCs, which along with HFCs are CFC replacements, are increasing (Montzka et al., 2009), although these deplete much less ozone per kilogram than CFCs. The global budget of these long-lived halogenated species is reasonably well constrained.

The oceans are a major natural source of very short-lived halogenated species into the boundary layer (Ordóñez et al., 2012). The budget of VSLH is much harder to constrain than long-lived compounds and a deeper understanding of their photochemical cycles, from production to destruction, is required. In the lower atmosphere, the Br and Cl burden is also strongly enhanced by heterogeneous reactions occurring on halide-rich marine sea salt and sulphate aerosol (von Glasow and Crutzen, 2007) with lesser contributions to inorganic bromine from terrestrial dust aerosol, biomass burning and fossil fuel production (Sander et al., 2003).

1.4.4 Marine Aerosol

Marine aerosol can be broadly defined as particles encountered above a marine environment. These may also include terrestrial aerosol such as dust and particles of anthropogenic origin transported into the marine environment within their atmospheric lifetime. An important example of terrestrial aerosol impacting the marine environment is the deposition of iron from dust aerosol into high nutrient low chlorophyll (HNLC) waters where the lack of iron limits phytoplankton growth (Jickells et al., 2005). Marine aerosols can be primary aerosols formed mechanically, such as from sea spray, or secondary aerosols formed via the reaction of ocean derived trace gases.

Heterogeneous reactions on aerosol, or salty ice surfaces in polar regions, liberate X_2

and the interhalogens XY (where Y is a different halogen atom to X) and this has been hypothesised as the main source of bromine in the MBL through an auto-catalytic cycle known as the bromine explosion (Fan and Jacob, 1992; McConnell et al., 1992; Platt and Lehrer, 1997; Tang and McConnell, 1996; Wennberg, 1999).

As marine aerosol originates mainly from sea-spray their elemental compositions should be comparable, with similar amounts of inorganic salts such as sulphate and chloride. In fact, aqueous marine aerosol often contains a depleted chloride and bromide ratio to sodium (Duce et al., 1991; Sturges and Barrie, 1988; Baker et al., 2000). This discovery led to the theory that chlorine and bromine partition from marine aerosol into the gas phase due to acid-catalysed reactions (Keene et al., 1998, and references therein). Within the aerosol, iodine is present as iodide and iodate with a significant fraction of soluble, organically bound iodine (Baker, 2005). Sander et al. (2003) observed that large aerosols do not show bromine enhancement, medium sized aerosols (a few micron) show depletion and that sub-micron aerosol are enriched in bromine (Santos and Rast, 2013).

Aerosols provide an effective route for the recycling of $BrONO_2$ due to its fast hydrolysis to form HOBr (figure 1.11, Aguzzi and Rossi (1999)). This hydrolysis produces nitric acid and contributes to aerosol acidity (equation 1.25). Hydrolysis of $BrONO_2$ and direct uptake of HOBr in aerosol leads to the formation of Br_2 and the interhalogens, this requires the presence of halide ions and protons (equation 1.26, Santos and Rast (2013)) and thus is pH dependant (Abbatt and Waschewsky, 1998; Huff and Abbatt, 2002; Deiber et al., 2004; Pratte and Rossi, 2006; Sander et al., 2003). The main control on sea salt aerosol pH is from sulphate acidification and the main source of sulphate in marine environments is DMS (Davis et al., 1998). Santos and Rast (2013) show that without gas-phase sulphur chemistry, bromine mediated ozone destruction would increase by 80% due to the sulphur mediated acidification of aerosol. This also highlights the control of compounds such as DMS on halogen chemistry and that changes in their atmospheric concentrations could strongly influence ozone levels.

$$BrONO_2 + H_2O \longrightarrow HOBr_{(aq)} + HNO_{3(aq)} \tag{1.25}$$

$$HOBr_{(aq)} + Br^-_{(aq)} + H^+_{(aq)} \longleftrightarrow Br_{2(aq)} + H_2O_{(aq)} \tag{1.26}$$

1.4.5 New Particle Formation

New particle formation has been observed in chamber studies from the photoxidation of CH_2I_2 (Jimenez et al., 2003). Iodine has also been linked to new particle formation in coastal regions via correlation with periods of low tide and solar radiation (Hoffman et al. 2001). Coastal brown algae such as *Laminaria digitata* can release I_2 during low tide (Saiz-Lopez and Plane, 2004). They bio-accumulate iodide and release iodine as an antioxidant during stress from reactive oxygen species (Küpper et al., 2008, 2013). The subsequent reactive iodine released into the atmosphere forms oxidation products such as OIO which can nucleate, coagulate and eventually form cloud condensation nuclei (CCN) (O'Dowd et al., 2002; Pechtl et al., 2006). The resultant cloud formation positively impacts albedo and the MBL radiative budget.

MBL IO and OIO concentrations are not sufficient to account for any substantial new particle formation and it was predicted that localised, high concentration "hot spots" were required (Burkholder et al., 2004). New particle formation has been observed at Mace Head, Ireland (Heard et al., 2006) and in Roscoff, Brittany (McFiggans et al., 2010).

1.4.6 Direct Oceanic Flux of RHS

I_2, Br_2, HOI and HOBr can be released as a direct product of haloperoxidase in micro and macro algae (Hill and Manley, 2009). In coastal regions, direct emission of I_2 from kelp is the dominant source of reactive iodine (McFiggans et al., 2004; Leigh et al., 2010). I_2 as well as HOI has also been suggested to be emitted from the ocean via reaction of ozone with iodide on the sea surface. Emission of iodocarbons and I_2 from the ocean alone cannot explain observed IO concentrations.

Carpenter et al. (2013) suggest that, in real world conditions with low sea surface I^- concentrations, the equilibrium between HOI and I_2 lies toward HOI, thus despite having a Henrys Law constant $\sim$160$\times$ lower than I_2, HOI concentrations in surface water result in a significant flux into the atmosphere. Combined emission of HOI, I_2 and iodocarbons, including equilibrium with the atmosphere, can explain the observed concentrations of IO (Carpenter et al., 2013). Despite an ever growing understanding of iodine sources, the general consensus is that the global source of iodine to the atmosphere is curently underestimated (Saiz-Lopez and von Glasow, 2012).

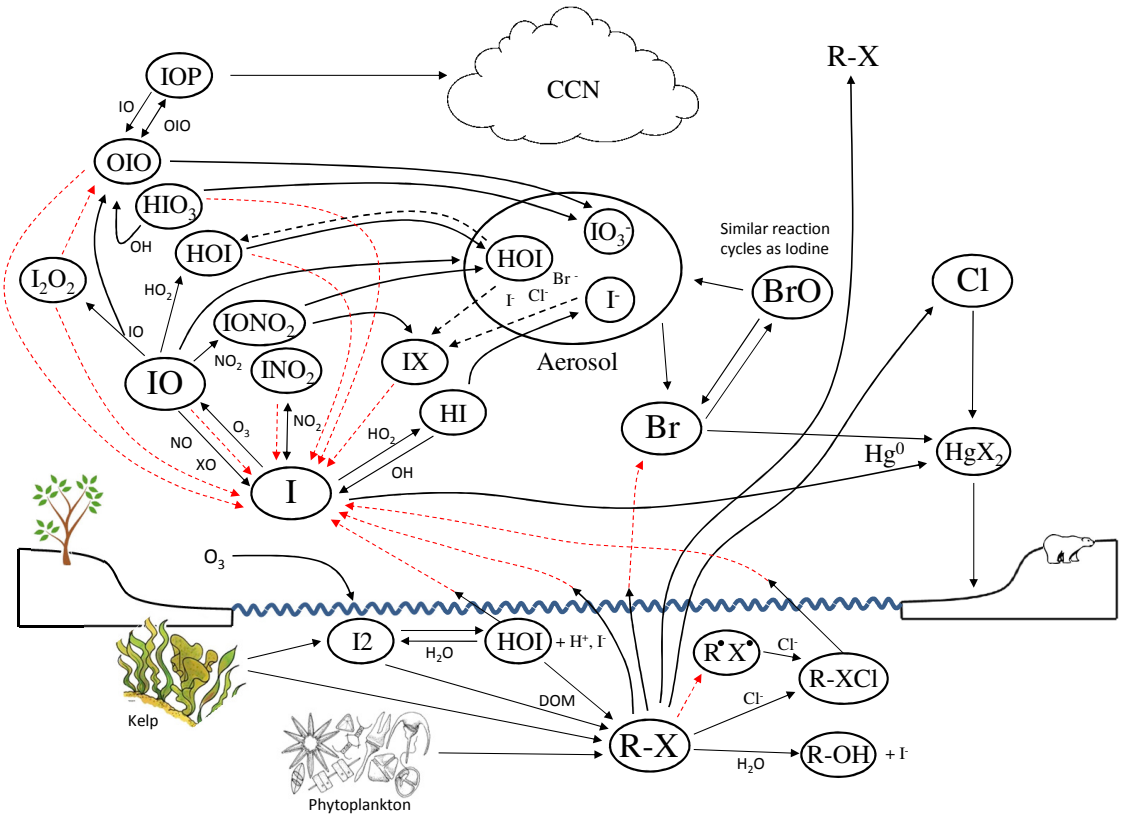

Figure 1.10 – Simplified oceanic and atmospheric halogen chemistry schematic. Red dotted lines represent photolysis. TTL = Tropical Tropopause Layer, CCN = Cloud Condensation Nuclei.

1.4.7 Very Short-Lived Halocarbons (VSLH)

A significant amount of reactive halogen entering into the atmosphere derives from short-lived organic halogens which are released from a multitude of sources including rice paddies and wet-lands (Redeker et al., 2000) but a dominant contribution originates from the oceans (Quack and Wallace, 2003). Very short-lived halocarbons (VSLH) are defined as having atmospheric lifetimes of < 6 months (Law and Sturges, 2007) which is of the same order of magnitude as tropospheric transport times. That is, the concentration in the troposphere depends upon the strength and proximity to the source. VSLH can be biogenic or anthropogenic. Anthropogenic sources can be measured and even controlled, whereas biogenic sources are currently neither comprehensively understood nor consistently quantified. VSLH are significant sources of reactive halogens to the troposphere and lower stratosphere and make an important contribution to photochemical ozone depletion (von

Glasow et al., 2004; Yang et al., 2005; Montzka et al., 2011; Saiz-Lopez et al., 2012). They are readily photolysed to form halogen atoms by wavelengths of radiation present within the troposphere. VSLH are present at pptv level concentrations in the MBL and pmol dm^{-3} levels in the surface ocean (section 1.7).

In the free troposphere, biogenic bromocarbon decomposition is predicted to reduce ozone levels by 5-30% via catalytic ozone destruction via bromine oxide radicals (BrO) and reduced ozone production due to BrO reactions with nitrogen oxides (von Glasow et al., 2004; Yang et al., 2005). BrO can also oxidise dimethyl sulphide (DMS) to form DMSO which can subsequently form CCN (Boucher et al., 2003).

1.4.8 VSLH sources and sinks

Organic halogens are released from marine macro algae (Chance et al., 2009; Goodwin et al., 1997; Carpenter et al., 2000; Carpenter and Liss, 2000; Sturges et al., 1993; Schall et al., 1994; Leedham et al., 2013), from phytoplankton (Tokarczyk and Moore, 1994), from marine bacteria and detritus (Hughes et al., 2008; Asare et al., 2012) and via photochemical breakdown of dissolved organic matter (DOM) in the surface ocean (Happell and Wallace, 1996; Richter and Wallace, 2004). Within marine diatom cultures, VSLH are formed via bromoperoxidase and iodoperoxidase enzymes (Moore et al., 1996). However there are major uncertainties regarding the contribution from these different sources (Carpenter and Liss, 2000). The global distributions and controls of VSLH emissions are also not well known, exacerbated by large spatial variability in sea-air fluxes. VSLH loss processes are controlled by photolysis, oxidation by hydroxyl radicals or oceanic and terrestrial dry deposition.

1.4.9 Transport of VSLH

An important difference between VSLH and longer-lived species is that the ability of VSLH to deplete stratospheric O_3 is dependent upon transport time whereas the longer-lived species are stable in the troposphere and are only photolysed in the stratosphere where solar energy is greater ($\lambda <= 310\ nm$). A model calculation suggests that 70% of oceanic CH_2Br_2 and 28% of $CHBr_3$ emissions reach the tropical tropopause layer (TTL)

(Gettelman et al., 2009). Under normal atmospheric conditions most shorter-lived VSLH will be photolysed within the troposphere however certain circumstances result in rapid vertical transport to the TTL.

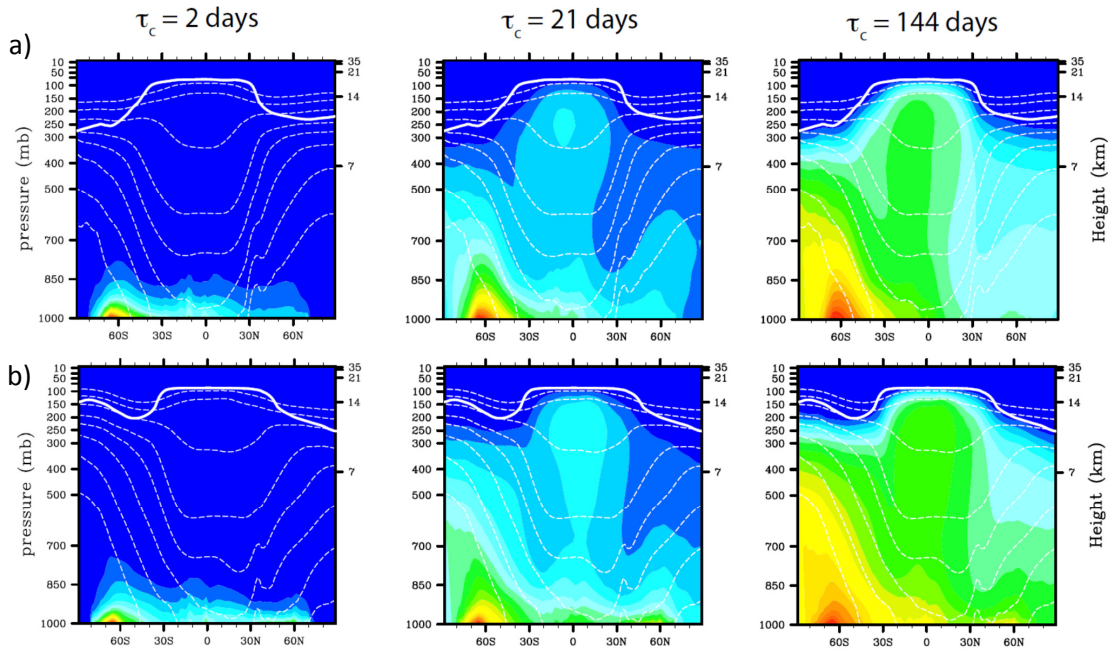

Figure 1.11 – Adapted from Holzer and Polvani (2013). Modeled vertical transport of a constant oceanic emission of short-lived species. Row *a* shows mixing of three species with different chemical lifetimes (τ_c) averaged through December, January and February. Row *b* shows the same for June, July and August. Colour scale is arbitrary, White line indicates the mean tropopause level.

Rapid vertical transport occurs primarily at the equator along the ITCZ (see section 1.2.1). The convergence of northern and southern hemispheric convection cells causes rapid uplifting of air along the equator. This can also occur extra-tropically via weather system frontal uplift. With boundary layer (BL) to tropical tropopause layer (TTL) transport times at the equator as short as 10–30 days, VSLH emitted at equatorial regions can potentially reach the stratosphere. Kritz et al. (1993) measured ^{222}Radon, produced at the Earth's surface with a half-life of 3.8 days, in the lower tropical stratosphere where extremely rapid vertical transport out of the boundary layer was provided by tropical cyclones and overshooting convective clouds.

Bromine and iodine transport to the stratosphere is of increased importance as per-atom,

they are about 60 and 150–300 times more effective than chlorine at depleting O_3, repectively (Law and Sturges, 2007; Ko et al., 2003). The lifetimes of iodine containing VSLH are less than 10 days and thus they are likely to be photolysed within the troposphere. Secondary organic reaction products from VSLH are likely to have such short lifetimes that direct conversion to reactive halogen species from the degradation of VSLH may be assumed (Montzka et al., 2011).

The input of reactive bromine to the lower stratosphere is estimated between 1.1–7.6 ppt (Montzka et al., 2011) whereas no significant quantity of iodine is expected. Holzer and Polvani (2013) find that the globally averaged flux into the stratosphere normalized by surface emissions is ∼1% for a species such as CH_3I (τ_c=8 days) and 30% for τ_c ∼140 days (CH_2Br_2, CH_2BrCl, $CHCl_3$) (figure 1.11). 1% is approximately equal to 0.01 ppt globally and in agreement with Tegtmeier et al. (2013a)

Butz et al. (2009) and Dorf et al. (2008) measured stratospheric upper limit IO and BrO concentrations of <0.1 ppt and 10–20 ppt, respectively from a balloon.

1.4.10 Halogen monoxide in the atmosphere

Due to its extremely short atmospheric lifetime(E. and Barna, 1997) and low mixing ratio, there are very few measurements of IO (table **??**). Recently, satellite retrievals have been used to measure IO although these measurements lie close to the detection limit of the instrument (Schönhardt et al. (2008), see chapter 5 section 5.1.1). Aircraft measurements locate two-thirds of total column IO above the MBL and suggest that most of the signal observed from satellites originates from IO in the free-troposphere (Dix et al., 2013). Detection of IO has predominantly been using the Differential Optical Absorption (DOAS) technique which measures absorption bands in the UV-Vis spectral region (Hönninger et al., 2004). Long path (LP) DOAS uses a fixed light source focused and projected over a very large distance (km), essentially the spectroscopic path length. IO at altitude or vertical profiles profiles can be measured using the Multi-Axis (MAX) DOAS technique which uses solar radiation as the spectroscopic light source.

Table 1.1 – Literature measurements of IO from various platforms

Region	Location	Instrument	Conc. (ppt)	Reference
Land-based	Tenerife, Spain (2010) Free troposphere	MAX-DOAS	0.4	Puentedura et al. (2012)
	Mace Head, Ireland	LP-DOAS	3.5–6.5	Alicke et al. (1999)
	Mace Head, Ireland	LP-DOAS	1.17	Allan et al. (2000)
	Cape Verde (2006-2007)	LP-DOAS	3.1	Mahajan et al. (2010)
	Cape Verde (2010)	MAX-DOAS	1.5	Carpenter et al. (2010)
	Maldives (1999)	MAX-DOAS	2.8	Großmann et al. (2013)
	Tenerife, Spain (1997)	LP-DOAS	1.23	Allan et al. (2000)
	Tasmania (1999)	LP-DOAS	0.88	Allan et al. (2000)
	Neumayer, Antarctica	MAX-DOAS	6.5[1]	Frieß et al. (2001)
	Halley, Antarctica	LP-DOAS	0–20	Saiz-Lopez et al. (2007b)
Ship Bourne	Eastern Pacific (2010)	MAX-DOAS	0.9[2]	Mahajan et al. (2012)
	Western Pacific (2009)	MAX-DOAS	2.2	Großmann et al. (2013)
Airbourne	Balloon, Northern Brazil, Stratosphere	LPMA-DOAS	<0.1[3]	Butz et al. (2009)
Satellite	Antarctic	SIAS SCIAMACHY	0–12	Saiz-Lopez et al. (2007a)
	Antarctic	SIAS SCIAMACHY	0–20	Schönhardt et al. (2008)
	Equatorial	SIAS SCIAMACHY	0–5	Schönhardt et al. (2008)

[1] Maximum concentration

[2] Maximum daily mean

[3] Upper limit

1.5 Bromocarbons, Chlorocarbons and Iodocarbons

VSLH can be broadly divided into three groups, iodocarbons, bromocarbons and chlorocarbons. Here an iodocarbon is defined as an organic halogen that can supply iodine to the atmosphere, sources of iodine are far fewer than those of bromine and the C−I bond is the most likely to be cleaved first in a reaction thus CH_2IBr is classified as an iodocarbon as it does not provide a significant source of bromine to the atmosphere when compared to other bromocarbons. The same applies to differentiating bromocarbons from chlorocarbons where $CHBrCl_2$ is a bromocarbon and $CHCl_3$ is a chlorocarbon. Field studies have as of yet not shown any clear correlation between iodocarbons and bromocarbons (table 1.2 and references therein) despite the similarity of known sources (section 1.4.8).

1.5.1 Bromocarbons

In the lower stratosphere, 5-40% of the bromine present is thought to derive from VSLH entering via rapid vertical transport from the marine boundary layer (MBL) (Kritz et al., 1993; Montzka et al., 2011). Stratospheric bromine contribution from VSLH will herein be referred to as Br_y^{VSLH}. A multitude of models have attempted to assess Br_y^{VSLH} contribution to the stratosphere and estimates continue to improve with better constraint of sources and sinks of bromocarbons from measurements (Dvortsov et al., 1999; Salawitch et al., 2005; Kerkweg et al., 2008; Brioude et al., 2010; Hossaini et al., 2012b; Liang et al., 2010; Schofield et al., 2011).

1.5.2 Bromoform ($CHBr_3$) and dibromomethane (CH_2Br_2)

$CHBr_3$ and CH_2Br_2 are the most prominent bromocarbons present in the MBL and as such have been the subject of the greatest number of measurements (section 1.7). They can be formed from many sources including from bromoperoxidase in oceanic micro/macro algae (Itoh et al., 1997; Wever et al., 1991). Hossaini et al. (2012b) estimate a contribution of 4.9–5.2 ppt Br_y from $CHBr_3$, CH_2Br_2, $CHBr_2Cl$, $CHBrCl_2$, CH_2BrCl and C_2H_5Br of which CH_2Br_2 and $CHBr_3$ contribute 76% of Br_y. These two VSLH are of notable importance due to their relatively large emissions and the long lifetime of CH_2Br_2 compared to other VSLH.

CH_2Br_2 and $CHBr_3$ have local atmospheric lifetimes of approximately 123 and 24 days, respectively (Law and Sturges, 2007). The former has a predominately OH sink with a lifetime of τ_{OH} = 5000 days (using average tropospheric OH of 1×10^6 molecules cm^{-3}). The latter is mainly photolysed ($\tau_{h\nu}$ = 36 days) but does also react with OH (τ_{OH} = 76 days). Model studies quantifying the supply of bromine from CH_2Br_2 and $CHBr_3$ to the stratosphere estimate around 2.4–2.5 ppt (2.4 ppt Hossaini et al. (2010), 2.5 ppt Liang et al. (2010)). Warwick et al. (2006) and Schofield et al. (2011) include $CHBr_2Cl$, $CHBrCl_2$ and CH_2BrCl in their models and calculate 6–7 pptv Br_y^{VSLH} (Hossaini et al., 2012b). CH_2Br_2 and $CHBr_3$ emissions are expected to be predominately biogenic in origin and due to the well-studied correlation between them (Carpenter et al., 2003; Yokouchi et al., 2005; Carpenter et al., 2009) it is assumed that they have similar sources or at least source regions.

1.5.3 Iodocarbons

In the tropical MBL, reactive iodine has been shown to be an important control in the photochemical destruction of ozone (Read et al., 2008; Mahajan et al., 2009; Jones et al., 2010). Methyl iodide, propyl iodide, diiodomethane and chloroiodomethane (CH_3I, C_2H_5I, CH_2I_2 and CH_2ICl) are the primary organic sources of iodine atoms. The monohalogenated iodocarbons such as CH_3I have the longest lifetimes compared to the polyhalogenated species for which the C−I bond is easily cleaved. Organic sources are believed to contribute 20–25% of reactive iodine to the tropical MBL (Carpenter et al., 2003; Mahajan et al., 2010; Jones et al., 2010).

Observations from the Cape Verde Atmospheric Observatory (16°51'N, 24°52'W) in the tropical east Atlantic Ocean indicate that reactive halogen chemistry increases surface photochemical ozone destruction by ca. 50% and is widespread in this region (Read et al., 2008). CH_3I is thought to be the most significant organic source of iodine to the MBL due to its greater concentration compared to the other iodocarbons (Tegtmeier et al., 2013b). However, polyhalogenated iodocarbons are so rapidly photolysed that measurements need to be taken very close to source to detect them before they release their reactive halogen into the atmosphere. CH_2I_2 is also capable of releasing both of its halogen atoms either by photolysis or by oxidation via CH_2IO_2 to form CH_2IO, which can readily photolyse to release the second iodine (Kroger et al., 1976). As the sources of polyhalogenated

iodocarbons are still uncertain it is difficult to estimate their global emission and thus they may be a significantly greater source of reactive iodine than previously thought.

1.5.3.1 Methyl iodide

Methyl iodide undergoes photolysis at wavelengths between 300–340 nm and has an atmospheric lifetime of approximately 7 days in tropical regions (Montzka et al., 2011). OH is not a major sink with τ_{OH} = 158 days (Montzka et al., 2011). The lifetime of CH_3I is similar to the timescale for ventilation of the marine boundary layer (Bell et al., 2002a) and as such has been used as a tracer of marine convection. CH_3I has been detected up to 12 km altitude (Blake et al., 1999) which can be attributed to extremely rapid vertical transport when considering its atmospheric lifetime. Using the Lagrangian transport model FLEXPART initiated with surface ocean measurements, Tegtmeier et al. (2013a) predict around 0.01–0.02 ppt entrainment of CH_3I to the stratosphere.

The main anthropogenic source of CH_3I is from its use as a pesticide replacing CH_3Br in the United States (Pelley, 2009) as 29% of CH_3I applied to soil can directly volatilise back into the atmosphere (Luo et al., 2011). However, Japanese manufacturers are currently no longer supplying CH_3I to the US (Arysta LifeScience Corp.Tokyo).

CH_3I differs from other VSLH because its production is thought to be mainly photochemical (Moore and Zafiriou, 1994). CH_3I is also released from macroalgae (Laturnus et al., 1998; Giese et al., 1999; Moore and Tokarczyk, 1993; Peters et al., 2005; Nightingale et al., 1995), microalgae (Itoh et al., 1997; Moore et al., 1996) and phytoplankton (Moore and Tokarczyk, 1993; Manley and de la Cuesta, 1997) although these sources are small; 0.5 Gg yr^{-1} of CH_3I is emitted from kelp (Manley and Dastoor, 1987) with distribution limited to coastal regions (Wang et al., 2009). CH_3I can be formed in the surface ocean from photo-chemically produced radical recombination (Moore and Zafiriou, 1994; Happell and Wallace, 1996; Chuck et al., 2005; Yokouchi et al., 2008) (equation 1.27). Bell et al. (2002a) suggest that CH_3I produced photochemically in the ocean is removed via emission to the atmosphere and by reaction with Cl^- with a net CH_3I flux to the MBL of 214 Gg yr^{-1}.

$$CH_3 + I \xrightarrow{h\nu} CH_3I \tag{1.27}$$

CH_3I also has a terrestrial source (estimated at 32–83 Gg yr^{-1}, Bell et al. (2002a)) from rice paddies (20–71 Gg yr^{-1}), wetlands (7.3 Gg yr^{-1}), biomass burning (3.4 Gg yr^{-1}) and peatlands (1.4 Gg yr^{-1}). Sive et al. (2007) estimate a 2600 ng m^{-2} d^{-1} (315 Gg yr^{-1}) flux from the oceans and a similar, 2270 ng m^{-2} d^{-1} terrestrial source strength. However, the area of terrestrial emission is much smaller, resulting in a 33 Gg yr^{-1} flux, less than 10 times that of the ocean. Williams et al. (2007) suggest the production of CH_3I from the addition of Saharan dust to seawater and Amachi et al. (2001) show that marine and terrestrial bacteria are capable of methylating iodide to form CH_3I.

1.5.3.2 Polyhalogenated iodocarbons

CH_2I_2, CH_2ICl and CH_2IBr are produced from similar marine biogenic sources as CH_3I such as macro/micro algae and phytoplankton (Carpenter et al., 2001) however the size and global distribution of the sources of these species are still unknown. CH_2I_2, CH_2ICl and CH_3I can be produced via interaction of dissolved iodide, dissolved organic mater (DOM) and ozone in the sea surface (Martino et al., 2009).

CH_2I_2 is present at extremely low concentrations in surface water and has only recently been measured in open-ocean air (Jones et al., 2010) due to its photolytic lifetime of 0.003 days. CH_2ICl can be formed via the S_N2 chlorination of CH_2I_2 (Class and Ballschmiter, 1988), direct photolysis (Tokarczyk and Moore, 1994) and also directly from macroalgal (Moore and Tokarczyk, 1993; Klick, 1993; Laturnus, 1996; Carpenter et al., 2000; Baker et al., 2001), plankton (Klick and Abrahamsson, 1992; Tokarczyk and Moore, 1994; Moore et al., 1996; Yamamoto et al., 2001) and bacterial sources (Amachi et al., 2005a,b).

As a product of the formation of CH_2I_2 and due to its longer lifetime ($\tau_{h\nu}$ = 0.1 days), CH_2ICl is more easily measured and can be linked to CH_2I_2 sources. In the Northwest Atlantic, CH_2ICl has been shown to increase toward open ocean regions and display higher concentrations away from coastal regions, which is the opposite of most other VSLH (Andrews et al., 2013). In fact the highest measured CH_2ICl concentration (0.71 ppt) to date is over the open Atlantic Ocean on-board the RV Polarstern (Chuck et al., 2005). This highlights the potential role of phytoplankton production of CH_2ICl (Moore and

Tokarczyk, 1993). CH_2IBr has been measured in coastal and Arctic regions (Carpenter et al., 2003, 2005) but is usually the least abundant of the poly-halogenated iodocarbons and is rarely seen in the open ocean.

The polyhalogenated iodocarbons can provide a global iodine source similar in magnitude to CH_3I (Jones et al. 2010). Because these species have such short local lifetimes they release their iodine atoms within the boundary layer providing a surface ocean source 3–4 fold higher than from CH_3I. In the case of CH_2I_2, photolysis likely occurs in the water column, surface or within the first few meters of the atmosphere.

1.5.4 Halocarbon exchange

Due to the ready availability of halogen ions present in seawater, VSLH can undergo halocarbon exchange processes. CH_2I_2 forms CH_2ICl in artificial seawater in the presence of light >290 nm but does not form in darkness (Class and Ballschmiter, 1987) which suggests the substitution of iodine is photochemically driven. Theoretically, a multitude of halocarbon exchange reactions can take place in the ocean in the presence of sunlight (figure 1.12). This scheme would suggest that unless a species transitions into the gas phase it will eventually form chloroform or dichloromethane.

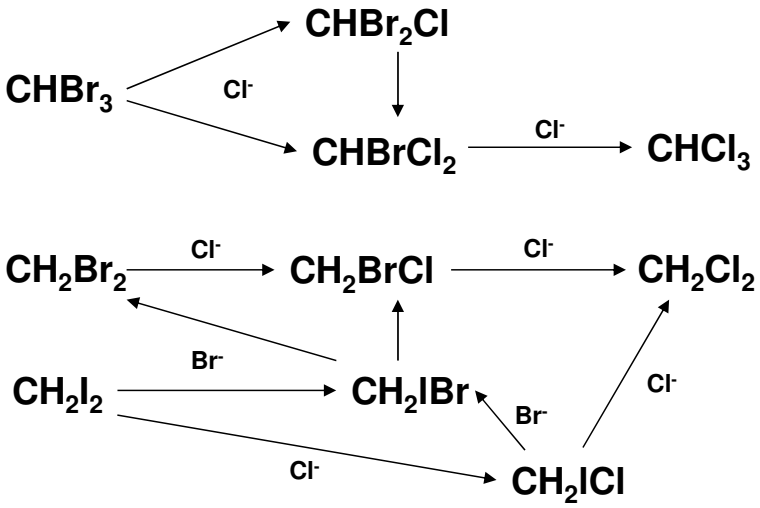

Figure 1.12 – Potential halocarbon exchange reactions in the ocean in the presence of sunlight.

1.6 VSLH models

Models assume a variety of scenarios (Bell et al., 2002b; von Glasow et al., 2004; Yang et al., 2005; Warwick et al., 2006; Kerkweg et al., 2008; Liang et al., 2010) for oceanic VSLH emissions, characterised according to geographical region. These require better validation by global oceanic and atmospheric measurements. Organic sources from VSLH and inorganic sources from sea-salt aerosols or oceanic surfaces (Carpenter et al., 2013) need to be better constrained due to their high spatial and temporal variability. Due to limited datasets, models use basic assumptions for VLSH fluxes which may not be entirely valid, such as the assumption of a constant 2.5 fold larger flux over coastal regions compared to open-ocean in the CAM-Chem based model by Ordóñez et al. (2012). Although this is the first model that attempts to incorporate iodocarbon species, other than CH_3I, into a global model.

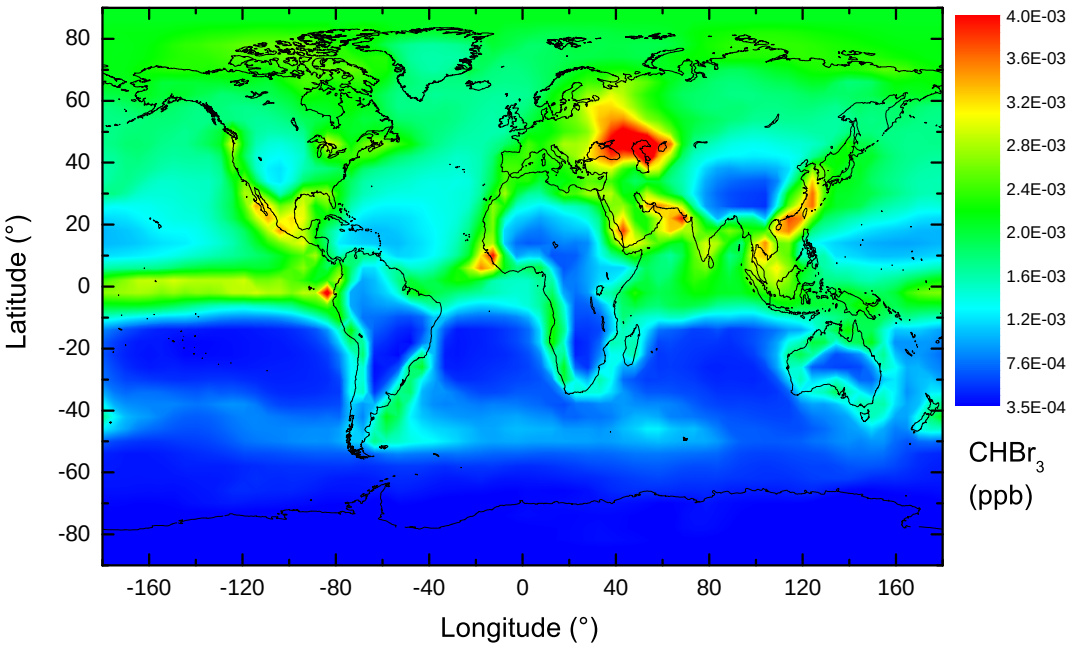

Figure 1.13 – Global bromoform atmospheric mixing ratio map for February 2012 predicted by the GeosChem model.

Tropospheric chemistry models incorporating bromocarbons, such as GeosChem, make similar assumptions (Liang et al., 2010). GeosChem assumes a fixed, non-meteorology driven flux per unit of time with enhanced emissions between 20° north and south of the

equator, in line with measurements over this region (Quack and Wallace, 2003; Quack et al., 2004, 2007a; Class and Ballschmiter, 1988; Atlas et al., 1993). Limited seawater measurements prohibit the use of modelled fluxes as used for species such as DMS which have much larger measurement datasets. The GeosChem model also assumes a greater coastal vs. open ocean source based upon a distance from shore, a relationship highlighted in Carpenter et al. (2009).

Better understanding of the underlying processes involved in halogen chemistry is required in order to predict the impact of environmental change on emissions. Hossaini et al. (2012a) predict that the stratospheric source gas injection of VSLH will likely increase in response to climate change.

1.7 VSLH in literature

CH_3I, CH_2Br_2 and $CHBr_3$ are fairly well studied and a large amount of data has been compiled in the HalOcAt database project (GEOMAR, Kiel). From all the collated data, a grid-based approach estimates a mean atmospheric mixing ratio of 0.7 ppt (0.05–7.3) for CH_3I, 1.0 ppt (0.07–7.8) for CH_2Br_2 and 0.9 ppt (0.01–53.1) for $CHBr_3$ (Ziska et al., 2013). This value of 0.7 ppt for CH_3I compares well to the combined means from individual open ocean studies shown in table 1.2 (0.74 ppt). This would suggest that open ocean concentrations contribute the majority of the emission source and that despite coastal areas being strong local sources, their global contribution is less significant. This is investigated in chapter 4 at the Mauritanian upwelling region.

Much effort has been given to the compilation of the HalOcAt database but there are still large geographic areas where no data exists. There is a notable lack of data in the Indian Ocean, Arctic Ocean and the south east Pacific. Data from TORERO (chapter 5) fills a gap in the longitudinal coverage in the East Tropical Pacific where only the latitudinal transect of BLAST I (1994) exists. Air and seawater concentrations measured during the 2013 ACCACIA campaign will provide novel measurements in the Greenland Sea. Including these measurements however, there is still a lack of data from the Southern Hemisphere, especially in the Indian and Pacific Oceans.

The shorter lived iodocarbons CH_2ICl and CH_2I_2 have very limited global data coverage

due to the difficulties measuring their extremely low concentrations and producing accurate calibrations. Measurements of these species and CH_3I have been compiled in table 1.2. Open ocean measurements of the shortest lived species are extremely sparse and without more measurements and greater understanding as to the sources, sinks and related processes we cannot hope to model or predict their global atmospheric distribution.

Table 1.2 – Summary of iodocarbon data in literature

Species	Region	Mean (ppt)	Range (ppt)	Reference
CH_3I	Coastal	1.47		
	Spitzbergen, Norway	1.04	<0.004–2.12	Schall and Heumann (1993)
	Mace Head, Ireland (spring)	0.43	0.12–1.47	Carpenter et al. (1999)
	Mace Head, Ireland (summer)	3.4	1.9–8.7	Bassford et al. (1999)
	Mace Head, Ireland (summer)	3.78	1.3–12.0	Carpenter et al. (2003)
	Cape Grim, Australia	2.6	1.0–7.3	Carpenter et al. (2003)
	Cape Grim, Australia	0.53	0.14–0.9	Yokouchi et al. (2008)
	Okinawa, Japan	1.2	0.5–2	Li et al. (1999)
	Pacific and Atlantic Coast	0.8	0.4–1.6	Butler et al. (2007)
	Appledore Island, United States	1.39	1.3–1.5	Sive et al. (2007)
	NW Pacific Islands	0.86	0.1–4.5	Yokouchi et al. (2008)
	San Cristobal Island, Ecuador	1.13	0.53–2.55	Yokouchi et al. (2008)
	Antarctic Peninsular	2.4	0.6–7.9	Heumann et al. (1992)
	Barrow, Alaska	1.3		Rasmussen et al. (1982)
	Cape Meares	1.5		Rasmussen et al. (1982)
	Cape Kumakahi	2.5		Rasmussen et al. (1982)
	Marshall Island	3.4		Rasmussen et al. (1982)
	Samoa	2.6		Rasmussen et al. (1982)
	Tasmania	2.4		Rasmussen et al. (1982)
	South pole	1.8		Rasmussen et al. (1982)
	Hateruma Island	0.82	0.3–1.69	Yokouchi et al. (2001)
	Cape Grim, Australia (summer)	1.2		Krummel et al. (2007)
	Cape Grim, Australia (autumn)	1.43		Krummel et al. (2007)
	Cape Grim, Australia (winter)	1.21		Krummel et al. (2007)
	Cape Grim, Australia (spring)	0.84		Krummel et al. (2007)
	Coastal waters	0.8	0.4–1.6	Butler et al. (2007)
	Cape Ochiishi	0.98	0.2–4.47	Yokouchi et al. (2008)
	Tsukuba	1.16	0.35–4.32	Yokouchi et al. (2008)
	Happo Ridge	0.51	0.09–1.36	Yokouchi et al. (2008)
	Hateruma Island	0.77	0.28–1.88	Yokouchi et al. (2008)
	Syowa	0.24	0.01-0.53	Yokouchi et al. (2008)
	Lilia		7.6–1830	Peters et al. (2005)
	Dagebull		4.7–23.5	Peters et al. (2005)
	Gran Canaria		24–84	Ekdahl et al. (1998)
	Great Bay, New Hampshire, US	1.43	0.44–3.1	Zhou et al. (2005)
	Cape Ochiishi	0.81	0.12–5.2	Yokouchi et al. (2011)
	Hateruma Island	1.2	0.43–5.2	Yokouchi et al. (2011)
	North Atlantic Ocean	1.55	0.90–3.29	Fuhlbrügge et al. (2013)
	Open ocean	0.74		
	East and Southeast Asian seas	0.63	0.24–2.0	Yokouchi et al. (1997)
	Western Pacific	0.87	0.05–5.0	Yokouchi et al. (1997)

	Northwestern Pacific	0.74	0.08–1.94	Yokouchi et al. (2001)
	Alert (82.5N)	0.31	0.05–0.64	Yokouchi et al. (2001)
	Pacific 50degS	0.44	0.3–0.57	Blake et al. (1999)
	Pacific, tropics	0.62	0.56–0.68	Blake et al. (1999)
	Tropics	0.6	0.2–1.1	Butler et al. (2007)
	Southern Ocean	0.3	0.1–0.7	Butler et al. (2007)
	North Pacific	0.7	0.19–2.09	Yokouchi et al. (2008)
	Western Pacific	1.07	0.6–1.8	Atlas et al. (1993)
	Western Pacific	0.6	0.12–1.15	Blake et al. (1997)
	Western Pacific	1.2	0.5–1.9	Yokouchi et al. (1997)
	Asian seas	0.63	0.24–2.0	Yokouchi et al. (1997)
	Western Pacific	0.7	0.6–0.8	Li et al. (2001)
	Pacific	0.7	0.4–1.6	Butler et al. (2007)
	Western Pacific	0.7	0.25–1.7	Yokouchi et al. (2008)
	Atlantic	0.8	0.4–1.2	Butler et al. (2007)
	Eastern Atlantic	1.63	0.4–2.24	Chuck et al. (2005)
	North Atlantic Ocean	0.93	0.51–2.11	Fuhlbrügge et al. (2013)

Species	Region	Mean (ppt)	Range (ppt)	Reference
CH_2ICl	Coastal	0.40		
	Mace Head, Ireland (spring)	0.06	<0.02–0.21	Carpenter et al. (1999)
	Mace Head, Ireland (summer)	0.16	<0.02–0.50	Carpenter et al. (1999)
	Spitzbergen, Norway	0.07	0.02–0.12	Schall and Heumann (1993)
	Norfolk, UK	0.46	0.21–0.8	Baker et al. (2001)
	Cape Grim, Austrailia	1.42	0.94-2.61	Carpenter et al. (2003)
	Lilia		0.35–12.4	Peters et al. (2005)
	Gran Canaria		nd–19	Ekdahl et al. (1998)
	Dagebull		0.1–3	Peters et al. (2005)
	Appeldore Island, US	0.15	0.01–1.6	Varner et al. (2008)
	Thompson Farm, US	0.68	0.03–3.4	Varner et al. (2008)
	Christmas Island	0.1	0.03–0.24	Varner et al. (2008)
	Oahu, Hawaii	0.04	0.01–0.07	Varner et al. (2008)
	Roscoff, France	0.1	0.03–0.17	Jones et al. (2009)
	Outer Hebrides, UK	1.42	0.94–2.61	Jones et al. (2010)
	Hateruma island, Japan	0.12	nd–0.99	Yokouchi et al. (2011)
	Cape Ochiishi, Japan	0.18	nd–2.1	Yokouchi et al. (2011)
	Mauritania upwelling	0.6	0.4–0.7	Andrews et al. (2013)
	Open ocean	0.16		
	North East Atlantic 26–36degN	0.04	<0.01–0.07	Jones et al. (2010)
	North East Atlantic 15–25degN	0.03	<0.02–0.04	Jones et al. (2010)
	Atlantic and Southern Oceans	0.32	0.18–0.71	Chuck et al. (2005)
	NE Atlantic (shelf)	0.23	<0.08–0.88	Jones et al. (2010)
	West of Cape Verde	0.2	nd–0.4	Andrews et al. (2013)

CH_2I_2	Coastal	0.14		
	North East Atlantic	0.1	0.02–0.18	Jones et al. (2010)
	Mace Head, Ireland (spring)	0.05	<0.02–0.36	Carpenter et al. (1999)
	Mace Head, Ireland (summer)	0.1	<0.02–0.46	Carpenter et al. (1999)
	Spitzbergen, Norway	0.46	<0.08–1.02	Schall and Heumann (1993)
	Roscoff, France	0.03	0.01–0.07	Jones et al. (2009)
	Outer Hebrides, UK	0.1	0.02–0.18	Jones et al. (2010)
	Cape Ochiishi, Japan	0.03	nd–0.4	Yokouchi et al. (2011)
	Hateruma island, Japan	0.008	nd–0.07	Yokouchi et al. (2011)
	Open ocean			
	North East Atlantic	0.01	<0.009–0.01	Jones et al. (2010)

1.8 Ocean-Atmosphere Exchange

The flux of a gas across the ocean–atmosphere interface is calculated from its concentration gradient across the two layers and its transfer velocity. This can be conceptualised as a two layer film system proposed by Liss and Slater (1974). In this system the concentrations of the gas of interest in air (C_A) and water (C_W) are assumed to be homogeneous. The concentrations on either side of the sea-air interface (C_{SA} and C_{SW}) are in equilibrium and controlled by molecular diffusion through the liquid and gas interfacial layers.

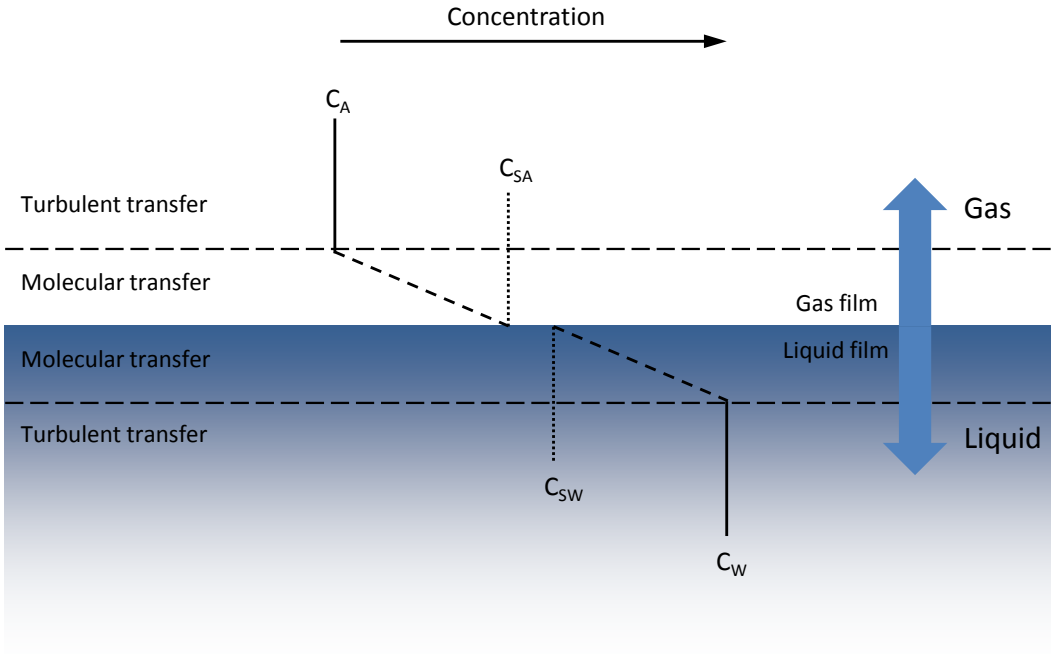

Figure 1.14 – Two layer model of a gas–liquid interface (Liss and Slater, 1974).

The concentration gradient can be measured directly by the simultaneous analysis of water and air. The transfer velocity (K, cm h^{-1}) is a function of wind speed (u, m s^{-1}):

$$K = f(u){S_c}^{-n} \tag{1.28}$$

Where S_c is the Schmidt number, a ratio of the kinematic viscosity and gas diffusivity (Jähne et al., 1984) scaled to n which represents the degree of renewal of the surface layers due to turbulent mixing (Johnson, 2010).

The reciprocal of the transfer velocity of a gas between the two phases, known as the total transfer velocity (K_t), represents the resistance encountered as it passes through each phase and results in separate transfer velocities for the liquid and gas phases, K_W and K_A respectively:

$$\frac{1}{K_t} = \frac{1}{K_W} + \frac{1}{H_{\frac{A}{W}}\ K_A} \tag{1.29}$$

Where $H_{\frac{A}{W}}$ is the dimensionless gas-over-liquid form of the Henry's law constant (See chapter 1.8.3). Hence flux (F) can be calculated using equation 1.30, where C_W and C_A are the concentrations of the gas in the liquid and gas phases respectively (mol cm^{-3}).

$$F = K_t(C_W - \left(\frac{C_A}{H_{\frac{A}{W}}}\right)) \tag{1.30}$$

1.8.1 Gas phase transfer velocity, K_A

The parameterization for K_A (m s^{-1}) used here is taken from Johnson (2010) and is derived in part, from Duce et al. (1991), Jeffery et al. (2007) and uses the Smith (1980) term for the drag coefficient, C_d. This parameterization accounts for a non-linear wind speed relationship and assumes that at zero wind speed, transfer is exclusively diffusive (Eq. 1.31):

$$K_A = 1 \times 10^{-3} + \frac{u_*}{13.3{S_{cA}}^{\frac{1}{2}} + {C_D}^{-\frac{1}{2}} - 5 + \frac{ln(S_{cA})}{2\kappa}} \tag{1.31}$$

Where κ is the von Karman constant (0.4 for seawater), S_{cA} is the Schmidt number in air and u_* is the friction velocity which is related to wind speed (u) and the drag coefficient (C_D) by equation 1.32 (Smith, 1980).

$$C_D = \left(\frac{u_*}{u_{10}}\right)^2 \tag{1.32}$$

$$u_* = u_{10}\sqrt{6.1 \times 10^{-4} + 6.3 \times 10^{-5} u_{10}} \tag{1.33}$$

u_* is calculated from equation 1.32 and a wind tunnel derived parameterization by Mackay and Yeun (1983) to yield equation 1.33. u_10 is the wind speed at 10 m ASL. The Schmidt number in air can be calculated using:

$$S_{cA} = \frac{\eta_A}{(\rho_A \times D_A)} \tag{1.34}$$

Where η_A is the dynamic viscosity of air ($\approx 1.82 \times 10^{-5}$ kg m^{-1} s^{-1}), ρ_A is the density of air (≈ 1.2 kg m^{-3}) and D_A is the diffusivity of the gas of interest in air (cm^2 s^{-1}) which can be calculated from Equation 1.35 (Fuller et al., 1966).

$$D_A = 0.001 \times T^{1.75} \frac{{M_r}^{0.5}}{[(P{V_A}^{\frac{1}{3}}) + {V_b}^{\frac{1}{3}}]^2} \tag{1.35}$$

Where V_A and V_b are the molar volumes of air and the gas of interest respectively (cm^3 mol^{-1}), P is the pressure in atmospheres and M_r is a function of the molecular masses of air (M_A) and the gas of interest (M_b), as described in equation 1.36.

$$M_r = \frac{M_A + M_b}{M_A M_b} \tag{1.36}$$

The density of air (ρ_A) is temperature and humidity dependent. Water vapor is lighter than air, thus as the percentage water vapor in air increases, the density decreases as the the amount of air decreases per unit volume. ρ_A can be calculated using equation 1.37 if measured values for relative humidity (%RH, Φ) are known.

$$\rho_A = \frac{P_{(dry)}}{R_{(dry)}T} + \frac{P_{(H_2O)}}{R_{(H_2O)}T} \tag{1.37}$$

Where $P_{(dry)}$ and $P_{(H_2O)}$ are the partial pressures (Pascal, Pa = 100 mbar) and $R_{(dry)}$ and $R_{(H_2O)}$ are the specific gas constants (287.058 and 461.495 J kg^{-1} K^{-1}) of dry air and water vapor respectively. T is the air temperature in Kelvin. Values of $P_{(dry)}$ and $P_{(H_2O)}$ can be calculated using:

$$P_{(dry)} = P_{abs} - P_{(H_2O)} \qquad \text{and} \qquad P_{(H_2O)} = \Phi P_{sat} \tag{1.38}$$

Where P_{abs} is the absolute (measured) atmospheric pressure.

The dynamic viscosity of air (η_A), as with ρ_A, is also temperature and humidity dependent. It can be calculated from an adaption of a formula according to Studnikov (1970) (equation 1.39) which itself is based upon an empirical formula for the calculation of the thermal conductivity of mixtures containing a polar solvent, in this case H_2O.

$$\eta_A = (x_A \times \eta_{dry}) \left(1 + \frac{x_{H_2O} - {x_{H_2O}}^2}{\vartheta}\right) \tag{1.39}$$

Where x_A and x_{H_2O} are the mole fractions of air and water respectively in the humid air mixture. $x_{H_2O} = P_{(H_2O)}/P_{(abs)}$ as calculated in equation 1.38 and $x_A = 1 - x_{H_2O}$.

η_{dry} is the dynamic viscosity of dry air, equation 1.40 and ϑ is an experimentally derived constant (2.75).

$$\eta_{dry} = \eta_0 \frac{T_0 + C}{T + C} \left(\frac{T}{T_0} \right)^{\frac{3}{2}} \tag{1.40}$$

Where C, T_0 and η_0 are reference values for air. C is Sutherland's constant for air (120 K), T_0 is the reference temperature (291.15 K), η_0 is the reference viscosity (18.27 $\mu Pa.s$) and T is the actual (measured) temperature (in K).

1.8.2 Liquid phase transfer velocity, K_W

For the majority of relatively insoluble gases studied in flux estimates the resistance of gas transfer exerted by the water is far greater than that of the air, therefore $\frac{1}{HK_A}$ is negligible, thus $K_T \approx K_W$. Hence the far greater number of parameterizations for K_W available compared to that of K_A. This rate controlling phase boundary can be attributed to the solubility and chemical reactivity of the gas of interest, with air-side resistance exerting a greater control on highly soluble and/or reactive gases in the aqueous phase (Liss and Slater, 1974).

K_W has been parameterized using direct micro-meteorological methods, global ^{14}C as a tracer and by deliberately adding one or more tracers into the atmosphere and ocean such as ^3He and SF_6. The latter approach was used by Nightingale et al. (2000) who provide the most widely used parameterization of K_W to date:

$$K_W = (0.222{u_{10}}^2 + 0.333u_{10}) \left(\frac{S_{cW}}{S_{c\ 660}} \right)^{-\frac{1}{2}} \tag{1.41}$$

which scales the Schmidt number of the gas of interest in water (S_{cW}) to 660 — the Schmidt number of CO_2 in saltwater at 20°C ($S_{c\ 660}$). S_{cW} can be estimated in equation 1.42, as

applied by Khalil et al. (1999) and Yokouchi et al. (2001). Where M is the molecular weight of the gas of interest and T is the sea surface temperature (SST, °C).

$$S_{cW} = 335.6M^{\frac{1}{2}}(1 - 0.065T + 0.002043T^2 - 2.6 \times 10^{-5}T^3) \tag{1.42}$$

A more complex approach for calculating S_{cW} which takes salinity into account is presented in Johnson (2010) and uses the same relationship as used when calculating S_{cA} (equation 1.43). Dissolved salts in seawater reduce gas solubility leading to an increased partitioning into the gas phase, known as the "salting out" effect (Xie et al., 1997). The opposite can occur ("salting in") as salts increase the polarity of water where the more non-polar the solute, the greater it is influenced by solvent polarity (Ni and Yalkowsky, 2003).

$$S_{cW} = \frac{\eta_{SW}}{\rho_W D_W} \tag{1.43}$$

ρ_W is the density of water (kg m^{-3}) which, in this case, is seawater. ρ_W can be calculated with equation 1.44 from Millero and Poisson (1981) using the temperature and salinity measured at the same time as the gas of interest.

$$\rho_W = \rho_0 + A.S + B.S^{\frac{3}{2}} + C.S \tag{1.44}$$

Where S is the salinity and and ρ_0 is the density of pure water which is calculated using Equation 1.45. A, B and C are calculated using Equations 1.46–1.48.

$$\rho_0 = 999.842594 + 0.06793952T - 9.09529 \times 10^{-3}T^2 + 1.001685 \times 10^{-4}T^3 - 1.120083 \times 10^{-6}T^4 + 6.536332 \times 10^{-9}T^5 \quad (1.45)$$

$$A = 0.824493 - 0.040899T + 7.6438 \times 10^{-5}T^2 - 8.2467 \times 10^{-7}T^3 + 5.3875 \times 10^{-9}T^4 \quad (1.46)$$

$$B = -0.00572466 + 1.0277 \times 10^{-4}T - 1.6546 \times 10^{-6}T^2 \quad (1.47)$$

$$C = 4.8314 \times 10^{-4} \quad (1.48)$$

η_{SW} (cP) represents the dynamic viscosity of seawater (in cP = centipose = 10^{-3} kg m^{-1} s^{-1}) . This variable includes the dynamic viscosity of each salt (η_i) as a mass fraction of total salinity combined with the dynamic viscosity of pure water (η_0) to yield equation 1.49 (Laliberté, 2007).

$$ln(\eta_{SW}) = w_0 ln(\eta_0) + \sum w_i ln(\eta_i) \quad (1.49)$$

Where w_0 and w_i represent the mass fraction of water and each solute in solution respectively. The dynamic viscosities of pure water and of each salt individually are calculated according to equations 1.50 and 1.51 respectively.

$$\eta_0 = \frac{T + 246}{0.05594T^2 + 5.2842T + 137.37} \quad (1.50)$$

$$\eta_i = \frac{e^{\frac{\nu_1(1-w_0)^{\nu_2}+\nu_3}{\nu_4 T+1}}}{\nu_5(1-w_0)^{\nu 6}+1} \tag{1.51}$$

ν_1 – ν_6 are empirical constants for each solute in seawater from Laliberté (2007) as presented in table 1.3 and T is the temperature in $^\circ C$.

Table 1.3 – Seawater solute composition and experimentally derived constants (ν_x).

Solute	mass fraction(w)	ν_1	ν_2	ν_3	ν_4	ν_5	ν_6
NaCl	0.798	16.22	1.3229	1.4849	0.0074691	30.78	2.0583
KCl	0.022	6.4883	1.3175	-0.7785	0.09272	-1.3	2.0811
$CaCl_2$	0.033	32.028	0.78792	-1.1495	0.0026995	780860	5.8442
$MgCl_2$	0.047	24.032	2.2694	3.7108	0.021853	-1.1236	0.14474
$MgSO_4$	0.100	72.269	2.2238	6.6037	0.0079004	3340.1	6.1304

Finally, we must calculate D_W ($cm^2\ s^{-1}$). Following the scheme suggested in Johnson (2010), D_W is averaged from the mean of two methods presented by Wilke and Chang (1955) (equation 1.52) and Hayduk and Minhas (1982) (equation 1.53 and 1.54).

$$D_W = \frac{7.4 \times 10^{-8} T \sqrt{\phi M_W}}{\eta_{SW} V_b^{0.6}} \tag{1.52}$$

$$D_W = 1.25 \times 10^{-8} T^{1.52} {\eta_{SW}}^{\epsilon *} ({V_b}^{-0.19} - 0.292) \tag{1.53}$$

$$\epsilon * = \frac{9.58}{V_b} - 1.12 \tag{1.54}$$

Where M_W is the relative molecular mass of the seawater, $\eta_S W$ is its dynamic viscosity in units of cP, ϕ is the association factor of water (2.6), T is the temperature in Kelvin and V_b is the liquid molar volume at boiling point of the gas of interest (cm^3 mol^{-1}). V_b can be calculated using the Schroeder additive method where $V_b = \sum increment$ where the increments are listed in Table 1.4.

Table 1.4 – Increments for use in the Schroeder additive method for calculating V_b. *Any cyclic feature to only be applied to each summation only once.

Atom/feature	Increment (cm^3 mol^{-1})
Carbon	7.0
Hydrogen	7.0
Oxygen	7.0
Nitrogen	7.0
Bromine	31.5
Chlorine	24.5
Fluorine	10.5
Iodine	38.5
Sulphur	21.0
Ring*	-7.0
Double bond	7.0
Triple Bond	14.0

1.8.3 Henry's law

Formulated in 1803 by William Henry, Henry's law describes the solubility of a gas as being directly proportional to its partial pressure. Henry's law constants in pure water for most atmospheric gases are available in the publication "Compilation of Henry's Law Constants for Inorganic and Organic Species of Potential Importance in Environmental Chemistry" (Sander, 1999). These constants can be described as a function of temperature (equations 1.55) and are then converted into the dimensionless gas-over-liquid form K_H^{cc} by equations 1.55–1.57.

$$K_H = K_H^{\ominus} \times exp\left(\frac{-\delta_{soln}H}{R}\left(\frac{1}{T} - \frac{1}{T^{\ominus}}\right)\right) \tag{1.55}$$

Where:

$$\frac{\delta_{soln}H}{R} = \frac{-dlnK_H}{d(\frac{1}{T})} \tag{1.56}$$

$$H_{\frac{A}{W}} = \frac{1}{C_W/C_A} = \frac{1}{K_H \times RT} \tag{1.57}$$

Where $K_H^{\ominus}$ refers to standard conditions ($T^{\ominus}$, 298.15 K) and R is the gas constant (12.2 M atm^{-1} K^{-1}).

1.8.3.1 Salinity dependent Henry's Law

In seawater the Henry's Law constants in pure water are affected by salinity via equation 1.58:

$$K_H = K_{H,0} + 10^{(K_S S)} \tag{1.58}$$

Where $K_{H,0}$ is the dimensionless gas over liquid form of the Henry's law constant for pure water and K_S is the Setschenow constant (Setschenow, 1889) defined in equation 1.59:

$$K_S = \theta ln(Vb) \tag{1.59}$$

A numerical scheme by Johnson (2010) provided a close fit to measurements of K_S by estimating Vb (molar volume, cm^3 mol^{-1}) using the "Schroeder" additive method and solving equation 1.59 for θ. Here $K_H^{\ominus}$ is the dimensionless gas over liquid form of the Henry's law constant at 298.15 K. They then provide a cubic relationship between θ and $ln(K_H^{\ominus})$ (equation 1.60).

$$\begin{aligned}\theta = {} & 7.33532 \times 10^{-4} + 3.39615 \times 10^{-5} lnK_H^{\ominus} \\ & - 2.40888 \times 10^{-6} (lnK_H^{\ominus})^2 + 1.57114 \times 10^{-7} (lnK_H^{\ominus})^3\end{aligned} \tag{1.60}$$

Table 1.5 – Summary of constants used for VSLH flux calculation.

Compound	M_R	Reference	$K_H^{\ominus}$	$\frac{-dlnK_H}{d(1/T)}$	ν_b (cm^3 mol^{-1})	ρ (g cm^{-}3)
CH_3I	141.94	Moore et al, 1995	0.14	4300	66.5	2.279
CH_2ICl	176.38	Moore et al, 1995	0.89	4300	84.0	2.416
CH_2I_2	267.84	Moore et al, 1995	2.30	5000	98.0	3.325
$CHCl_3$	119.38	Moore et al, 1995	0.23	3800	87.5	1.483
CCl_4	153.82	Hansen et al., 1995	0.034	3600	105.0	1.587
$CHBrCl_2$	163.83	Moore et al, 1995	0.40	4700	94.5	1.980
$CHBr_2Cl$	208.28	Moore et al, 1995	0.73	4900	101.5	2.451
CH_2Br_2	173.84	Moore et al, 1995	0.93	4400	84	2.477
$CHBr_3$	252.73	Staudinger & Roberts, 1996	1.7	5200	108.5	2.89

1.9 Summary

Very short-lived halocarbons are significant sources of reactive halogen to the troposphere and lower stratosphere and make an important contribution to photochemical ozone depletion. They are released from marine sources including macro algae, phytoplankton, bacteria and surface photochemical processes. However there are major uncertainties regarding the contribution from these different sources. The global distributions and controls of VSLH emissions are also not well known, exacerbated by large spatial variability in sea-air fluxes.

In the lower stratosphere, 5-40% of the bromine present is thought to derive from VSLH entering via rapid vertical transport from the marine boundary layer (Kritz et al., 1993; Montzka et al., 2011). Due to greater convection, emissions at tropical latitudes are more likely to reach the stratosphere, hence identification of major bromocarbon sources in this region is of significant global atmospheric importance. Inorganic bromine from biogenic organohalogen decomposition is predicted to reduce tropospheric ozone levels by 5-30% via catalytic ozone destruction by bromine oxide radicals (BrO) and reduced ozone production due to BrO reactions with NO_x species (Yang et al., 2005).

In the tropical MBL, reactive iodine has shown to be an important control in the photochemical destruction of ozone (Read et al., 2008). CH_3I, C_2H_5I, CH_2I_2 and CH_2ICl are the primary organic sources of iodine atoms in the MBL, although these precursors do not explain the total reactive iodine abundance at the surface (Jones et al., 2009; Mahajan et al., 2009).

Chapter 2

Instrumental Analysis of VSLH in Air and Water

2.1 Overview

Gas Chromatography coupled to a Mass Spectrometer (GC-MS) was the main analytical technique used throughout this body of work. This chapter will describe the basic operation of GC-MS systems, how this theory translates to actual instrumentation and how the instruments were developed to meet the analytical needs of this project.

2.2 Chromatography

The basic principle of chromatography has remained fundamentally unchanged since its invention by Mikhail Tsvet at the beginning of the 19th century. The most basic example being the separation of a mixture of pigments by their differing rates of diffusion through blotting paper, an experimental demonstration often seen in primary education. These principles are analogous to those employed in even the most modern of chromatographic technology today.

The ocean and atmosphere are extremely complex sample matrices where by utilising chromatography, individual analytes such as VSLH can be isolated, characterised and quantified. A mixture of analytes is carried via the mobile phase (a transport medium) through a system containing a stationary phase. The speed at which each analyte travels through the system is dependent upon its partitioning between the mobile and stationary phases. An analyte which interacts with the the stationary phase is said to be 'retained' and one which travels through the system without partitioning into the stationary phase is unretained. Once the analyte has passed through the system it has 'eluted' and is either collected or measured using a detector. The less retention, the sooner an analyte will elute.

With regard to gas chromatography (GC), the mobile phase is a gas, usually helium, and the stationary phase is a silicone based substrate contained within a polyimide coated, fused silica column. The type of interaction between the analytes and the stationary phase is controlled by the stationary phase material and determines the order of analyte elution. Non-polar columns will separate according to increasing boiling point. Adding polar functional groups such as phenyls to a column's stationary phase will increase the retention of polar analytes. The speed at which an analyte elutes through a column is also dependent upon the temperature and the flow rate of the mobile phase. The GC column is commonly placed inside a fan oven which allows accurate temperature control and hence control over the speed of elution during a GC run.

2.2.1 Chromatographic theory

An analyte (A) moving through a GC column is in constant equilibrium between the mobile phase (A_{mobile}) and the stationary phase ($A_{stationary}$). Its speed is dependent on the equilibrium constant between the two phases known as the partition coefficient (K).

$$A_{mobile} \overset{K}{\rightleftharpoons} A_{stationary} \tag{2.1}$$

The equilibrium constant is directly proportional to the capacity factor (k'), a measure of the columns ability to retain a specific analyte.

$$k' = \frac{t_R - t_M}{t_M} \tag{2.2}$$

The longer an analyte is retained (t_R– retention time) compared to an unretained analyte (t_M– dead time), the greater the capacity factor of the column. If an analyte is retained on a column, logic dictates that increasing the length of the column (L) will increase the retention time and the dead time. To describe the efficiency of a column with respect to analyte separation a theoretical "plate" model is used. This model visualises a column as being divided into a number of equal parts or 'plates' (N). The number of plates, the plate height (H) and the column length (L) are used to define the efficiency.

$$N = \frac{L}{H} \tag{2.3}$$

The smaller and more numerous the plates and the longer the column; the greater the efficiency. The efficiency can be calculated in practice using equation 2.4 where W is the peak width measured at the baseline.

$$N = 16 \left(\frac{t_R}{W} \right)^2 \tag{2.4}$$

The parameters which affect plate height (N), and thus efficiency, are described by the van Deemter equation (equation 2.5, van Deemter et al. (1956)). As the analytes move

through the column they are subject to band broadening. A narrow band of analyte will spread out as it travels due to eddy diffusion (A), longitudinal diffusion (B) and the mass transfer term (C).

$$H = A + \frac{B}{u} + Cu \tag{2.5}$$

The Eddy diffusion term (A) describes the multiple pathways through a column. Some may be shorter than others and consequently molecules taking differing routes will elute at slightly different times. This is only applicable to a packed GC column. The diffusion coefficient (B) is the diffusion of an analyte longitudinally along the column within the carrier gas. The mass transfer term (C) is the sum of the resistance encountered as the analyte transitions into and out of the stationary phase and is analogous to the transfer velocity term used in flux calculations (section 1.8). u is the linear velocity of the carrier.

$$Resolution = \frac{2(t_{R1} - t_{R2})}{W_1 + W_2} \tag{2.6}$$

Resolution in chromatography describes the separation time achieved between two analytes (1 and 2) as they elute from the column. Resolution is determined by the difference in retention times of the two analytes (ΔT_R) and the peak widths according to equation 2.6. Narrower peaks and greater separation results in higher resolution. A resolution value of at least 1.5 is desirable for baseline separation and accurate quantification.

2.3 Mass spectrometry

A mass spectrometer (MS) is an instrument used to determine the mass to charge ratio (m/z) of an analyte. For mass spectral analysis a sample is first ionised. Depending on the type of ionisation used, the sample can gain single or multiple charges and even fragment into multiple ions. The mass of the intact analyte (parent ion), and/or its fragments, provides an insight into the analytes composition. All MS (with the exception of ion mobility mass spectrometry) require a vacuum so that the ion can travel through the system with minimum collisions. The greater the vacuum, the better the transmission and more ions will reach the detector, resulting in greater sensitivity.

The mass is usually measured by one of two techniques: filtering the ions so that only one specific mass passes through the system (quadrupole, magnetic sector and ion trap) or by measuring the time in which it takes an ion to travel through a vacuum chamber of set length (Time Of Flight, TOF). Both techniques employ a simple detector such as an electron multiplier to count the number of ions passing through the system. Filtering the ions simplifies their detection but only allows for one mass to be observed at any one time whereas TOF can measure multiple masses simultaneously.

In order to accurately identify an analyte in a mixture, its mass must be measured with extremely high resolution. This is due to numerous compounds having the same nominal mass whereas none (excluding isomers) have identical accurate masses. For example: methyl iodide and decane both have the same nominal mass of 142 but can be identified by their more accurate masses of 141.94 and 142.28, respectively. However, an MS with high resolution is required for accurate mass determination such as a magnetic sector or a TOF with an adequately long flight tube, both of which are expensive relative to lower resolution MS such as quadrupole. In addition, the introduction of a complex mixture would produce an extremely complicated mass spectrum, especially if fragmentation of the parent ion was to occur.

An alternative way to achieve greater resolution is to couple the MS to a chromatography system (GC/LC-MS). Here the extra resolution is achieved by the separation of analytes (including isomers) chromatographically before their introduction into the MS. This virtually eliminates the problem of a complex mixture and the successful identification of an analyte can be aided by considering its retention time in the chromatographic system (see section 2.2.1).

A capillary GC is very easy to couple to an MS as it outputs a gas at low flow rates, which can be introduced directly to the high vacuum environment of an MS. A liquid chromatography–MS interface was a greater challenge as the liquid solvent must be removed before entering the MS, as it would create huge quantities of gas, and decrease the vacuum.

A high resolution MS can be coupled to a chromatographic system and is a powerful analytical tool for the identification and quantitation of unknown compounds. A low resolution quadrupole MS (QMS) was used throughout this research for multiple reasons. Firstly, if

the structure of an analyte is known, high resolution MS is not required for identification and does not necessarily increase sensitivity. Higher resolution would increase selectivity but complete chromatographic separation negates this requirement. QMS systems are cheaper to buy, run and have smaller physical footprints than high resolution MS, which make them more suitable for use in fieldwork. A QMS was deployed on the Mars Rover Curiosity for the same reasons (Leshin et al., 2013).

2.3.1 Quadrupole Mass Spectrometry (QMS)

A quadrupole can be referred to as a mass spectrometer or often as a mass filter. The latter definition accurately describing its mode of operation as it works by filtering out masses whilst allowing a mass of interest to pass through the system to the detector. The QMS can be operated in three modes: Single Ion Monitoring (SIM), SCAN or SIM/SCAN. SIM is the most sensitive mode as it only allows ions of a specific mass to reach the detector (usually 1 atomic mass unit (amu) ±0.5 amu). The QMS can only transmit one mass (±0.5) at any one time so in order to capture a full mass spectrum (SCAN) the QMS must scan through a range of masses sequentially, with the result that sensitivity is reduced, as the time at which one mass is being observed (dwell time) others are being lost. A typical scan range is 35-500 m/z at 4 Hz. SIM/SCAN is a technique employed in modern QMS utilising fast electronics where a SCAN is performed between periods of SIM and is designed to offer some of the sensitivity enhancement of SIM whilst still providing a full mass spectrum.

Ignoring performance differences from different ionisation schemes, a QMS in SIM should theoretically achieve greater sensitivity than TOF instruments as they both employ similar detectors, with QMS delivering a constant stream of ions to the detector whilst a TOF has to release ions in bursts in order to record the time of flight. In a very complex sample which is not perfectly separated chromatographically, the extra mass resolution of some TOFs can give a better signal to noise ratio (S/N). The obvious benefit of a TOF is that a full mass spectrum is always being recorded.

2.3.2 Electron Ionisation (EI)

Fragmentation of ions can be both desirable and undesirable. Keeping the ions in one piece allows easy identification using accurate mass whereas fragmentation is more useful in low resolution techniques as it can yield more unique ions. Electron Ionisation (EI) is most commonly used with QMS and utilises high energy electrons that usually cause multiple fragmentations of the parent ion into smaller ions. Different compounds will fragment differently and by keeping the electron energy constant (70 eV), analytes will fragment in the same way every time. This has allowed the compilation of fragmentation databases such as the National Institute of Standards and Technology (NIST) MS spectral database. Pure analytes' fragmentation patterns are recorded and can be compared to unknown spectra in sample chromatograms to aid identification.

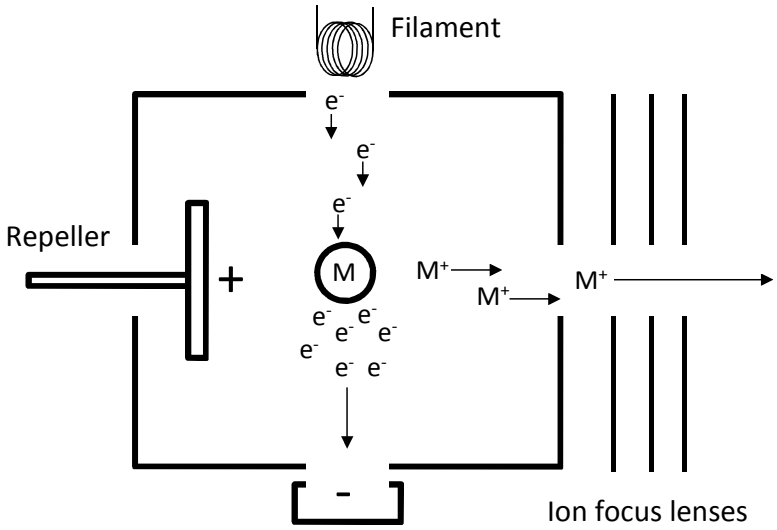

Figure 2.1 – Schematic of an EI source showing the production of ions from the introduction of analytes orthogonally to the plane of the drawing represented by the central circle.

An EI source is very simple in its operation (figure 2.1). The analytes first enter an evacuated ionisation chamber where they are positively ionised by electrons ejected via thermal emission from a resistively heated rhenium filament following equation:

$$\mathrm{M} + \mathrm{e}^{-} \longrightarrow \mathrm{M}^{+\cdot} + 2\,\mathrm{e}^{-} \tag{2.7}$$

Perceiving electrons as a wave, energy transfer occurs when the wavelength is similar to the

bond length of the analyte. The ionisation energy of the molecule is often substantially less than the energy transferred with the resultant energy causing molecular fragmentation. The number of ions produced in a volume is linked to pressure (concentration of the analyte) and the electron current. The ions are then pushed orthogonally to the electron beam using a positively charged repeller plate. They are focussed by charged lenses and exit the source toward the quadrupole.

2.3.3 Chemical Ionisation Mass Spectrometry (CI-MS)

Chemical ionisation (CI) is referred to as a soft ionisation technique comparative to EI due to the reduced fragmentation of the parent ion. This is achieved using an ionisation reagent gas, such as methane, to transfer charge to the analyte without transferring the high energy of the electrons which cause fragmentation. A QMS can easily be adapted to utilise chemical ionisation by changing the inner ion source or in some instruments, a single ion source can be used for both techniques. Generally, CI ion sources have more enclosed inner source regions to contain the CI gas within the ionisation region. The high energy electrons produced from the filament collide with the CI gas which becomes ionised. It is these CI gas ions which then pass on their charge via proton transfer (not exclusive mechanism) resulting in protonated analyte molecules. CI is useful when it is desirable to maintain the parent ion intact but can have a reduced sensitivity up to one order of magnitude less than using EI due to the increased pressure in the source(Gross, 2011).

$$\mathrm{CH_4} + \mathrm{e^-} \longrightarrow \mathrm{CH_4^+} + 2\,\mathrm{e^-} \tag{2.8}$$

A by-product of the collisions between high energy electrons and the CI gas is the production of numerous thermal (low kinetic energy) electrons. Thermal electrons are produced both from electrons which have lost their energy through collisions or from electrons ejected from an ionised CI reagent gas (equation 2.8). These electrons can be incorporated into the orbital of an electrophillic analyte to produce a negative ion. This is known as electron capture (EC) or negative chemical ionisation (NCI). Electron capture occurs for compounds with high electron affinity such as those with extensive electron de-localisation or containing electronegative elements or groups such as halogens, sulphurs or oxygen containing species such as nitrates.

A mass spectrometer is not required to exploit this mechanism and a dedicated Electron

Capture Detector (ECD), invented in 1960 by Lovelock (Lovelock and Lipsky, 1960), can be used, coupled to a GC. This detector allowed for the pioneering analysis of CFC's in the atmosphere and essentially led to the discovery of their role in ozone depletion (Molina and Rowland, 1974). The advantage of NCI-MS over an ECD is that the former is mass selective and can resolve co-eluting GC peaks by filtering which mass reaches the detector using the quadrupole. NCI differs from standard chemical ionisation in numerous ways. Firstly, because an electron is being transferred and not a proton the mass of the analyte does not increase as per CI. All that is required to measure these negatively charged ions is to change the acceleration voltage polarity of the source repeller so that the ions transit the quadrupole toward the detector. Due to the high selectivity and resultant signal to noise ratio, electron capture is an extremely sensitive technique. Unlike CI, NCI often results in fragmentation of the parent ion. In fact, three mechanisms of ion formation exist (equations 2.9–2.11):

$$\textit{electron capture} \quad \mathrm{M} + \mathrm{e}^- \longrightarrow \mathrm{M}^- \tag{2.9}$$

$$\textit{dissociative electron capture} \quad \mathrm{M} + \mathrm{e}^- \longrightarrow [\mathrm{M{-}A}]^- + \mathrm{A}^- \tag{2.10}$$

$$\textit{ion pair formation} \quad \mathrm{M} + \mathrm{e}^- \longrightarrow [\mathrm{M{-}B}]^- + \mathrm{B}^+ + \mathrm{e}^- \tag{2.11}$$

NCI sensitivity is notoriously dependent upon ion source conditions and rapid sensitivity changes may occur over time due to low source operating temperatures, requiring a strict calibration and maintenance schedule (Oehme, 1994).

2.3.4 The Quadrupole Mass Filter

A quadrupole mass spectrometer consists of four parallel rods in electrical isolation. The rods are typically around 10 cm long in modern systems with the distance between two diagonally opposite poles 1/1.148 times the rod diameter, a ratio chosen to achieve a hyperbolic field between them. The quadrupole system is evacuated to allow ion transmission without collision. The entire system is heated to around 150–200°C to prevent molecules sticking to its surface. Opposite pairs of rods are connected to DC power supplies with opposite polarity. Each power supply is connected to an RF transformer which induces an alternating current in each pair of rods 180° out of phase between pairs. A specific combination of RF and DC voltages allows a stable ion trajectory of a specific mass through the quadrupole to the detector. Ions with too high an m/z collide with the poles and lose

their charge. Ions which are too low an m/z are thrown out of the quadrupole and do not reach the detector.

The regions of RF/DC combinations (stability regions) which allow successful passage of an ion through the system increase in size with increasing ion m/z (figure 2.2). This results in decreasing resolution at higher masses, a reason QMS is suitable for GC where small, volatile analytes are encountered, especially after fragmentation in an EI source. A non-linear relationship between RF and DC voltage is used to 'tune' the QMS in-order to achieve the greatest mass resolution.

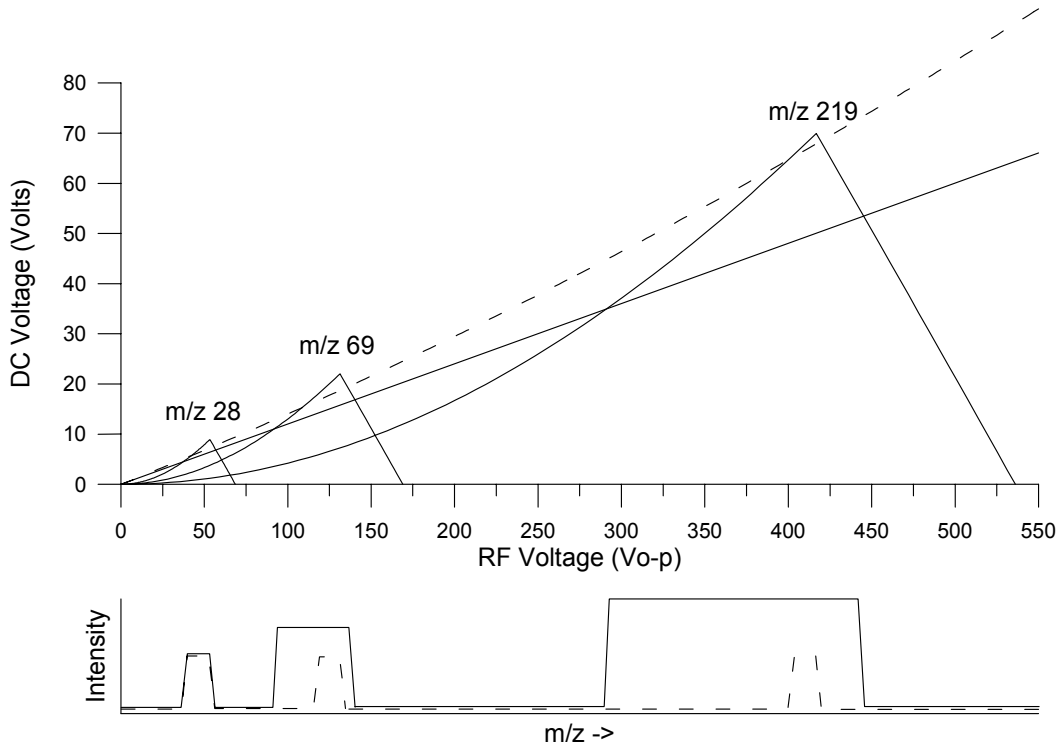

Figure 2.2 – Depiction of the relationship between RF and DC voltages producing stable ion trajectory zones (area beneath curves). Solid and dotted lines represent linear and non-linear relationships, respectively. Reproduced from Pedder (2001).

The Agilent 5975 mass selective detectors used for the majority of this work employ true hyperbolic quadrupoles made from gold plated quartz (figure 2.3). The true hyperbolic shape allows for maximum mass resolution and transmission of stable ion trajectories whilst the quartz is inert and is not prone to thermal expansion when heated. The gold

Figure 2.3 – Gold coated, quartz, true hyperbolic quad employed in the Agilent 5973, 5975 and 5977 MSDs.

coating provides electrical conductivity for application of the RF and DC voltages. The design is monolithic which prevents shifting of the pole alignment if the instrument is transported and experiences large shocks or vibration.

2.4 Thermal Desorption

Gas phase analysis should be simple using a GC, as the analyte needs to be in the gas phase for separation. In reality, concentrations of analytes in the gas phase are low and large volumes must be sampled. As described in section 2.2.1, sample introduction must occur in a narrow band in order to achieve efficient separation. If a capillary GC-MS system has a column flow rate of 1.5 mL min^{-1}, a 1.5 mL injection volume would have a minimum peak width of 1 min, which is very wide. In order to analyse large volumes of gas, pre-concentration is required. This is achieved using thermal desorption.

2.4.1 Thermal desorption overview

Thermal desorption is the process of pre-concentrating analytes from a volume of gas onto an adsorbent and subsequently desorbing them using a much smaller volume of carrier

gas. The process is analogous to liquid or solid phase extraction of liquid samples, except in the gas phase. Analytes can be trapped from large quantities (litres) of gas, up to the breakthrough volume (the volume at which analytes begin to be displaced or removed by the sample media) of the trapping system being used.

Thermal desorption has evolved since its first use and in some cases has come full circle as GC technology has changed. The earliest form of thermal desorption is likely pyrolysis-GC which involves the heating of a sample to release gas-phase analytes. This could be classified as a slightly different technique as the analytes were not in the gas phase originally and the adsorbent material is destroyed during analysis. Some of the earliest forms of thermal desorption trapped gas phase analytes using liquid nitrogen (LN_2) to cryogenically pre-concentrate (McClenny et al., 1984). Due to the extremely low temperatures, the gases could be trapped on virtually any material such as glass or stainless steel but usually in the form of a narrow bore tube. This method of trapping is extremely effective, however numerous problems are associated with the use of LN_2 including blockage of the trap with ice, low breakthrough volumes, the inconvenience of large quantities of hazardous LN_2 and lack of portability.

In order to overcome problems associated with blockage of the cryo-trap and the lack of portability of these systems, adsorbent tube sampling is used (figure 2.4). This involves pre-concentration onto a physically large amount of sorbent packed into a metal or glass tube. The tubes are about 4 inches long and 1/4 inch diameter containing as much as 1 g of material. These tubes can then be taken outside of the laboratory and environmental samples taken in-situ. This is done either by diffusion (qualitative) or by pumping a known volume of gas through the tube (quantitative). The tubes can be thermally desorbed onto a GC directly but the volume of the tube results in poor chromatographic performance. A cyro-trap can be used to re-focus the analytes into a narrow band before GC separation. The tubes can be sampled quickly with high breakthrough volumes and stored for analysis at a later date. The tubes are used at ambient temperatures and can be flushed with carrier gas before desorption to minimise the quantity of water entering the cryo-trap.

Although refocusing using LN_2 is very effective it still carries the complication and expense of sourcing liquid cryogen. Cooled absorbent traps (cold-traps) were developed to remove the requirement for cryogen yet maintain the chromatographic performance of such a system. This is achieved by using a much smaller I.D. tube (generally quartz) packed with

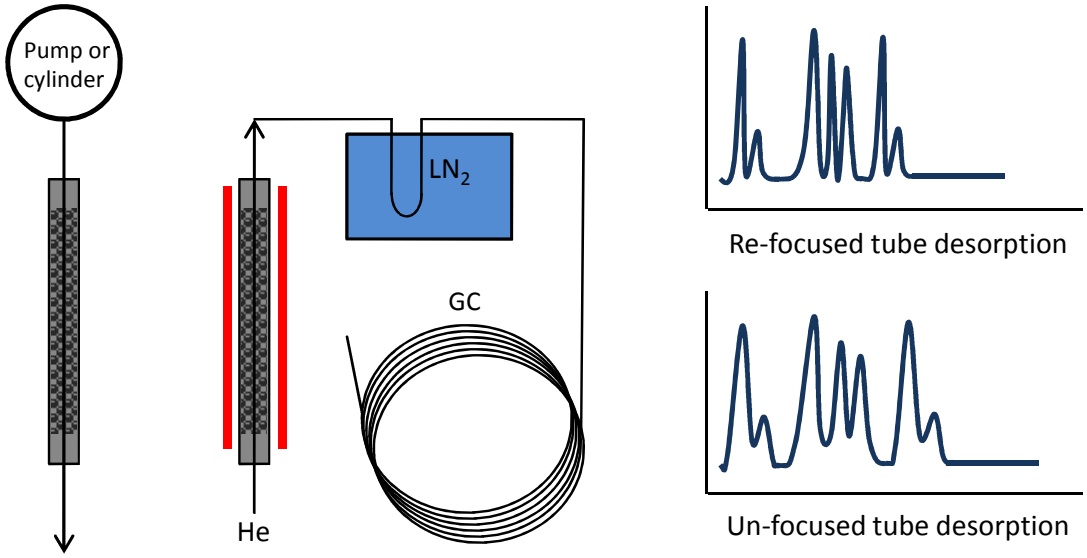

Figure 2.4 – Adsorbtion of analytes onto tubes followed by desorption and cryogenic refocusing. Sample is drawn through an absorbent tube where analytes are trapped. The tube is heated (red bars) to desorb the analytes onto the GC column. Liquid nitrogen can be used to refocus the analytes before separation.

a small quantity of sorbent. The lower breakthrough volume of using less adsorbent is countered by cooling the cold-trap to sub-ambient temperatures depending on the nature of the analytes. The small quantity of sorbent in the cold trap is flash heated to allow rapid desorption onto the GC column and maintain chromatographic performance (figure 2.5). In addition to adsorbent tube samples being re-focussed by the cold-trap, the large breakthrough volume allows for pre-concentration directly onto the cold-trap, known as 'on-line sampling'. This enables the analysis of reactive species which can be lost over time on sorbent materials, low molecular weight species which are not fully retained on the un-cooled tubes and generally increases reproducibility of the analysis, a problem which hinders tube samples that have been stored for long periods or in-correctly sealed. A common use of on-line sampling is for the off-line analysis of gas cylinders filled with air known as 'whole air samples' (WAS, see chapter 4 section 4.1.1.2).

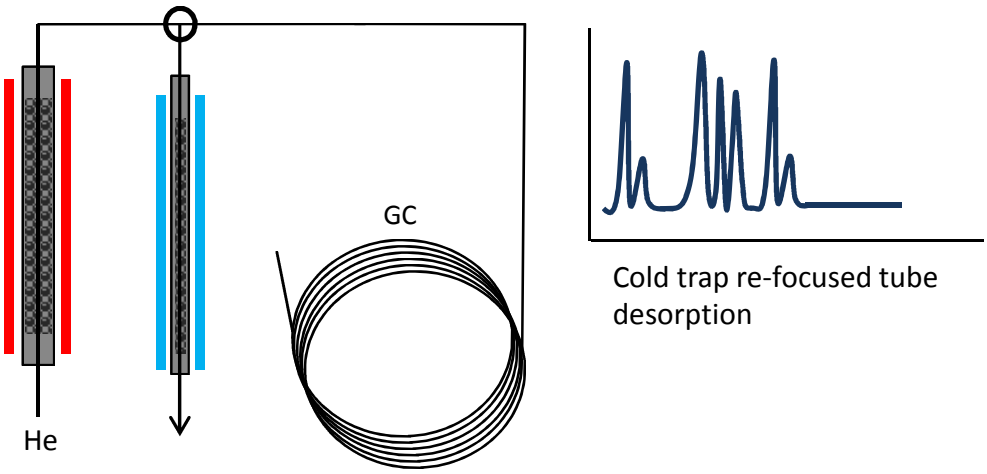

Figure 2.5 – Focussing of tube desorbed or on-line samples via a low volume, cooled adsorbent trap. Adsorbent tube is heated (red bars) to desorb analytes which are re-focused onto a smaller, cooled (blue bars) adsorbent trap prior to desorption onto the GC column.

2.4.2 Cooled absorbents for online sampling

Due to the desire for removing the requirement of cryogens from the thermal desorption system, other methods of cooling the cold-trap are required. The most common being thermoelectric cooling, utilising the Peltier effect.

2.4.2.1 The Peltier effect

The Peltier cooler is a thermoelectric device named after the Peltier effect discovered by French physicist Jean Charles Athanase Peltier. The Peltier effect is the opposite of the Seebeck effect, where a potential difference is generated across the junction between two materials as they respond differently to temperature. The same principle is used in thermocouples to detect temperature. In the Peltier effect, an electric current is used to induce a temperature differential across the junction.

In practice, a Peltier cooler is made up of many junctions in series, mechanically bonded to two ceramic insulator plates (figure 2.6). This is known as a Peltier plate. When a current is applied to the plate, one side will cool and the opposite side will heat as energy is pumped across the junctions. The Peltier plate is not a cooler but rather a heat pump.

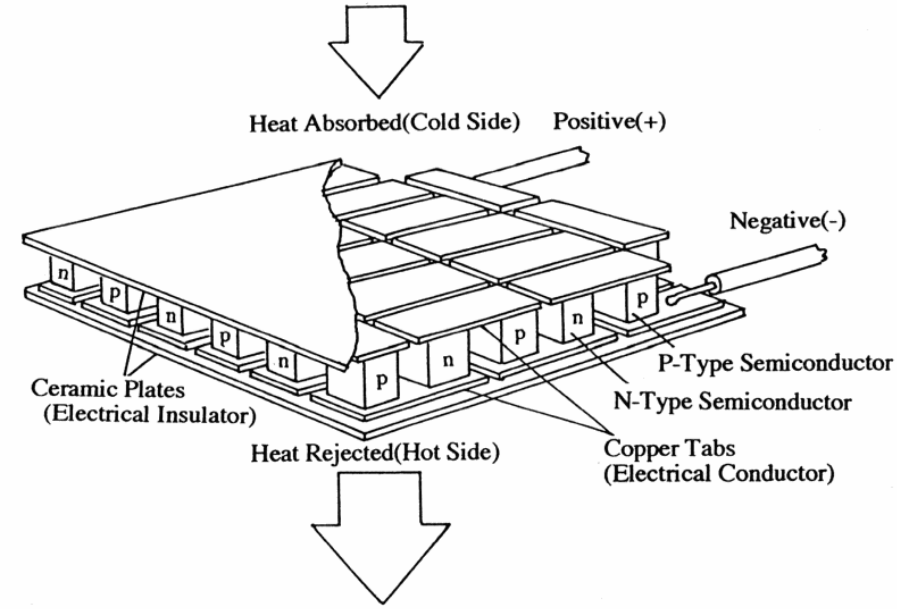

Figure 2.6 – Schematic of a Peltier plate. n-type and p-type semiconductors have different electron densities and are connected in series.

To use a Peltier as an effective cooler, heat must be constantly removed from the hot side in-order that energy be absorbed by the cold side. This is usually done with an air or liquid cooled heat sink. The cooling power is provided by, and limited to, the heat exchange capacity of the heat sink with the Peltier plate usually providing focussed cooling to a small area. A common setup is to stack Peltiers in a pyramid with a larger plate removing the heat generated at the cold side of a smaller plate. This allows for a greater temperature differential across the stack (ΔT_{max}) compared to a single plate. Stacks are easily powered in series with the larger plate dropping the voltage across the smaller plate. There is potentially no limit to the number of plates that can be used in a stack.

Typical Peltier plates are cheap ($\approx$ £20) and are quoted as having a ΔT_{max} of 70°C. This specified maximum is only valid with zero thermal load (nothing to cool) and drops to around 50°C in practise, resulting in minimum cooling temperatures of around -30°C with a 20°C heat sink. A Peltier is not very efficient as it produces a lot of heat simply via joule heating of the materials which increases with Peltier power. This extra heat must also be removed by the heat sink and eventually, increasing power to the Peltier will produce too much heat and the cold side will become warm. This limits their usefulness and often requires expensive power supplies to produce the low voltage and high current a Peltier requires. Both the Perkin Elmer and Markes thermal desorption units utilised in

this work used a Peltier stack and forced air heat sink to cool their adsorbent filled cold traps.

2.4.3 Adsorbent traps

A wide range of adsorbent materials are available for use with thermal desorption from graphitized carbon to porous polymers, each one has individual characteristics not always advantageous to an analysis. Some materials are better able to retain low molecular weight species, i.e. Carboxen 1000, but irreversibly bind larger compounds. Carbon based adsorbents can provide reaction surfaces where analytes are lost due to chemical degradation or modification. This is especially true for sulphur based compounds. Polymers such as Tenax TA offer stability for sulphur compounds but are not particularly strong adsorbents and are not hydrophobic. As air samples are complex mixtures of compounds with a wide range of boiling points, adsorbent material selection is vital.

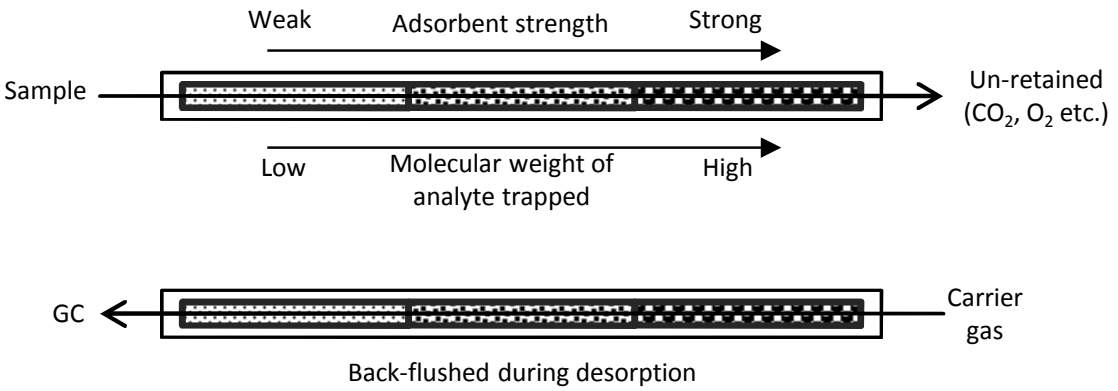

Figure 2.7 – Graphical representation of a multi-bed adsorbent trap and its operation.

A technique to allow the sampling of a wider range of analytes is the use of a multi-bed adsorbent trap (figure 2.7). By positioning weaker adsorbent materials toward the front of the trap and stronger ones further along the flow path, high molecular weight/ boiling point analytes will be trapped on the weak adsorbent without being irreversibly trapped on the stronger material. Smaller, more volatile species that break-through the weaker adsorbent will be trapped by the subsequent one. When desorbed the flow is reversed. All of the thermal desorption units used during this research utilised multi-bed adsorbent traps with quartz wool, Carbotrap B and Carboxen 1000 as the weak, medium and strong

adsorbents, respectively.

Due to the development of increasingly narrow-bore GC capillary columns <180 μm I.D., cooled adsorbent traps now display the same issues as direct desorption of adsorbent tubes onto columns >180 μm I.D. this is because the dead-volume inside the trap is too large for rapid transfer into the narrow column, which acts like a bottleneck. The characteristic sign for insufficient flow during desorption is the widening of peaks at the beginning of the chromatogram. As the GC program progresses, the peaks will become narrow again due to refocusing of the larger analytes on the column at the initial GC temperature. Splitting some of the flow from the trap to waste during desorption provides faster carrier gas flow rates through the trap and improves chromatographic resolution but impacts on sensitivity as a portion of sample is lost. The solution is either to reduce the trap volume, reducing capacity and thus breakthrough volume, or to re-focus the analytes at the head of the column which brings us full circle back to cryogens (figure 2.8).

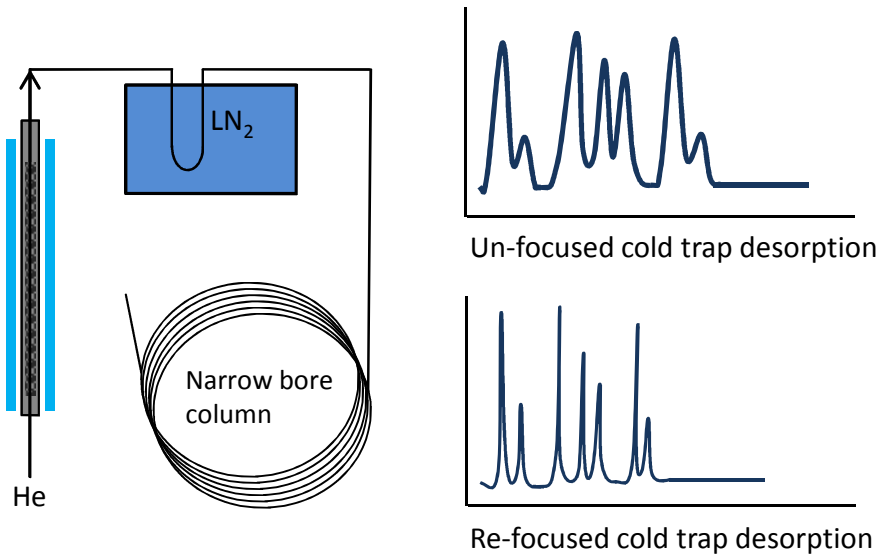

Figure 2.8 – Cryogenically re-focussing analytes from a cooled absorbent trap (blue bars) onto a narrow bore column for fast GC analysis.

There are now alternatives to achieve cryogenic or near-cryogenic temperatures without LN_2, such as the use of compressors. Compressors operate using the same principle as a household refrigerator and large compressors are how the LN_2 is originally manufactured. LN_2 compressors are physically large, expensive and require large amounts of power but smaller, thermo-acoustic and Stirling Cycle units are available (see section 2.4.3.1). These

lack the cooling capacity required to liquefy nitrogen but can cool the head of a GC column to cryogenic temperatures and re-focus analytes.

2.4.3.1 Free-Piston Stirling Cooler (FPSC)

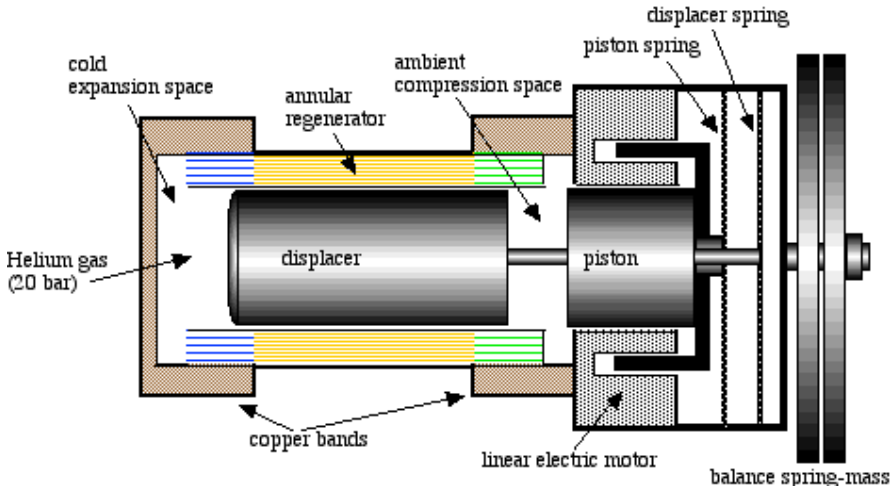

Figure 2.9 – Schematic showing a Free-Piston Stirling Cooler (FPSC). Objects to be cooled are placed in contact with a 'cold head' thermally bonded to the cold expansion space. Reproduced from Ohio University.

A free piston stirling cooler (FPSC) moves heat from one surface (cold tip) to another (heat sink) via expansion and compression. Expanding helium at the cold side absorbs thermal energy from the environment. The helium is then displaced and compressed at the heat sink, where its temperature increases and is subsequently lost to the environment via the heat sink. It then returns to the cold side and expands, replacing the energy lost at the heat sink by absorbing heat from the cold tip. This process occurs rapidly, pumping thermal energy away from the cold tip and from whatever material with which the cold tip is in contact. The stroke of the piston is very short with the movement generated using a varying magnetic field, resulting in a very efficient system with very few mechanical heat losses. In fact, a FPSC can achieve greater than 90% efficiency. A FPSC can also be used as part of an effective water removal system called a 'cold-finger' drier (section 2.4.4).

2.4.4 Water removal

Water removal from a gas stream prior to analysis is very important for both thermal desorption and GC-MS. Water entering a GC column can cause damage to non-bonded stationary phase and will de-stabilise retention times if different amounts of water are injected for different runs. Mass Spectrometers are sensitive to water as it can surpress ion formation, damage the filament and its rapid expansion in the ion source leads to reduced vacuum and more ion collisions, reducing the free path for analyte ions.

Thermal desorption systems usually concentrate sample on cooled traps and water will physically block the cooled capillary traps found in cryogenic TD systems. Absorbent traps ran at ambient temperatures can be purged with dry helium to selectively remove water whilst maintaining sample integrity but very volatile analytes will be lost. For a dry helium purge to work efficiently the absorbent material to sample volume ratio must be high, resulting in very large traps with poor desorption characteristics (see section 2.4.1) or very small traps with very low sample breakthrough volumes (e.g. μDirac, Robinson et al. (2000)).

Water trapped on cooled absorbent traps will expand to 1400 times its liquid volume upon heating causing a huge pressure increase and very poor desorption as the volume of gas trying to enter the narrow GC column will be very large. Often in these situations the pressure causes back-flushing of the system which can lead to contamination of the instrument upstream of the trap.

There are many techniques for water removal from a gas stream but none offer a complete solution for all analytical scenarios. Magnesium perchlorate is often used as a direct water absorbent with the air sample passing through a container filled with the powder. As a strong oxidising agent, $Mg(ClO_4)_2$ has health implications and has also been shown to remove some analytes from the sample stream (Doskey, 1991).

A highly effective water removal technique is the use of a Nafion membrane (figure 2.10). Nafion is a DuPont trade name for a sulfonated tetrafluoroethylene ($C_7HF_{13}O_5S \cdot C_2F_4$) similar to PTFE. Nafion allows water to selectively pass through the membrane, removing it from the sample stream. The water partitions into the polymer very quickly and is removed from the other side of the membrane by an absorbent or a dry counter flow

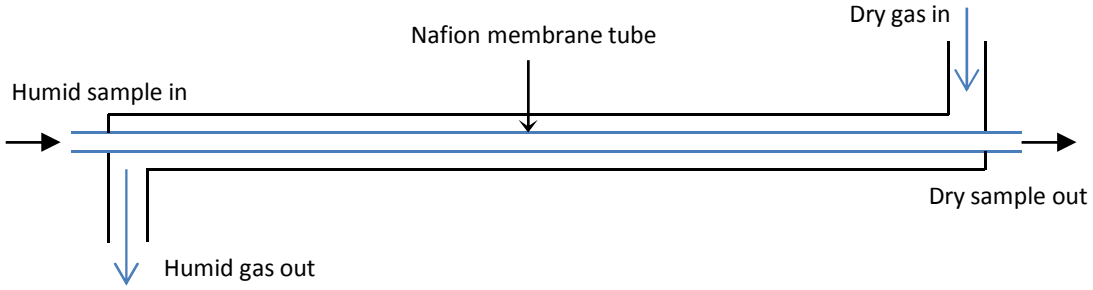

Figure 2.10 – Schematic drawing representing a counter-current nafion type drier.

of gas. Nafion is not perfect as oxygenated and sulphur species can pass through the membrane and are lost from the sample. Halocarbon species are completely retained and do not transition into the membrane. Nafion can also be used to separate gases to remove interferences or as a membrane separating two phases, such as removing analytes from a water supply into a gas sample stream.

Oxygenated and sulphur containing analytes can be measured in humid gas samples using a 'coldfinger' drier (unpublished work at the University of York). This involves trapping the water in the sample stream as ice in a cooled glass tube. This technique maintains most analytes without losses if carried out properly. Coldfinger water removal was not tested for halocarbons prior to this work as Nafion was satisfactory and it was assumed that they would dissolve in water and be trapped in the ice. In fact, halocarbon containing samples can be dried using a coldfinger and thus methods incorporating the analysis of a wider suite of analytes can be used (figure 2.11).

In order to maintain sample integrity using a cold finger, the water in the sample must transition between the gas and solid phases very quickly. If liquid water is present in the system, losses may occur. The system appears to work at an optimum when some ice crystals are already present in the glass tube. This allows water to be removed by the growth of these crystals rather than condensation. The gas entering the coldfinger is kept hot and is cooled to <-20°C as rapidly as possible.

A coldfinger can dry an air sample to a lower dew point than a Nafion, which is limited by flow rates and the dew point of the counter current drying gas. The downside to using a coldfinger is its size and the requirement for trapped ice to be removed regularly which

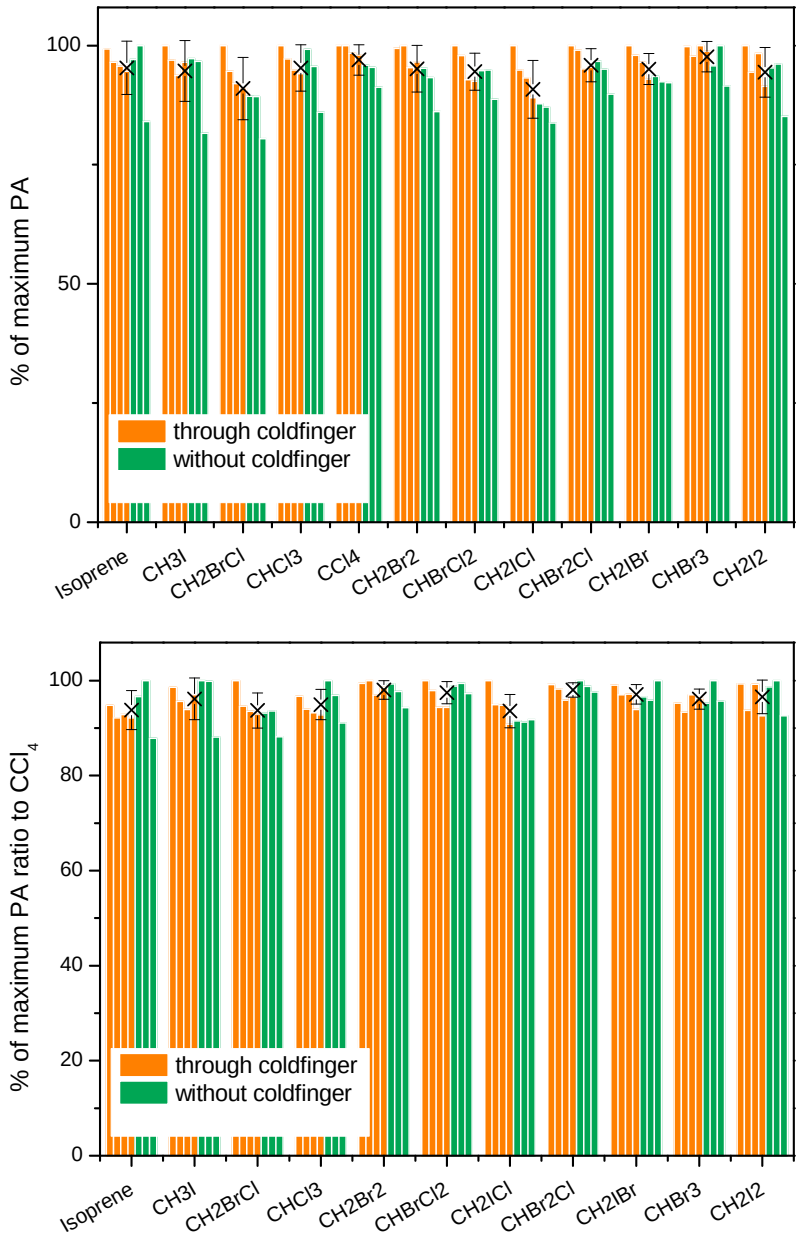

Figure 2.11 – Top: Recovery tests of replicate VSLS analyses through a coldfinger drier at -30°C. The maximum peak area is scaled to 100%. Bottom: ratio to CCl_4 to take into account instrument response changes.

is currently a manual process.

2.4.4.1 FPSC coldfinger

The cold finger water removal technique usually employs an ethylene glycol chiller bath to cool the glass tube to around -30°C. These chillers are large, heavy, expensive and the ethylene glycol can spill. All of these problems lead to a reduction in their usefulness on-board moving research platforms such as ships or aircraft.

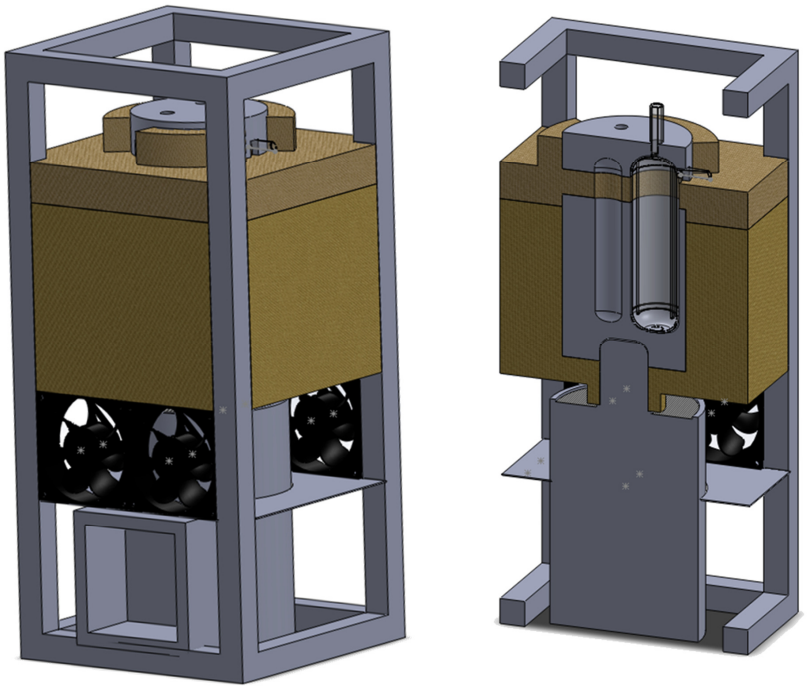

Figure 2.12 – CAD drawing of FPSC coldfinger design shown without covers and as a cross-section with one glass tube insert. Brown coloured block is expanded polyurethane insulation. Glass 'coldfinger' traps are housed within an aluminium block which is cooled by contact with the FPSC cold-head. The sample stream passes through the glass tube where the water is removed to a dew point determined by a set point temperature (-20 to -80°C).

A new design of coldfinger was created to address these problems using a FPSC unit (section 2.4.3.1). The FPSC was used to cool an aluminium block insulated with closed-cell expanded polyurethane foam into which the glass tube was inserted. The unit uses

significantly less power (100 W vs. 1500 W), can cool to lower temperatures (-80°C vs. -30°C), weighs around 1/4 of the weight and costs $1/3^{rd}$ of the price of an ethylene glycol chiller and has no liquid to spill.

2.5 Analysis of VSLH using TD-GC-MS

VSLH species studied during this project were all measured using GC-MS with sample pre-concentration via thermal desorption. GC columns with 3 different phases and many different dimensions were used throughout this project due to the requirements of different analysis and the purchase of newer instrumentation.

2.5.1 Perkin Elmer system

During early work a Perkin Elmer AutosystemXL GC-MS was used in conjunction with a Perkin Elmer TurboMatrix300 thermal desorption unit. The Perkin Elmer TD was equipped with the on-line air sampling accessory. This allowed for gas phase samples to be introduced directly onto the Peltier cooled absorbent trap. When the TD was not collecting sample, during desorption for example, the flow continues through the system. This is useful with regard to pre-purging the lines prior to sampling but care must be taken when using expensive gas standards as a lot of sample can be wasted if the cylinder is not turned off.

This system was robust but had limitations with regard to sample throughput due to long sampling and analysis times (figure 2.13). The TD unit used a peltier cooled, multibed adsorbent cold trap with an I.D. of 3 mm. This resulted in slow desorption onto the GC column and a large baseline fluctuation due to thermal expansion in the large volume of the trap. The slow desorption resulted in poor chromatography at the beginning of the chromatogram (see section 2.4.3). The manufacturer employed a permanent 'split' during the desorption of the trap where a portion of the desorbed sample is diverted and does not enter the GC column. This helps to achieve faster flow rates through the trap during desorption but ultimately reduces sensitivity due to reduction in sample quantity. Even with this split in place the chromatography was limited and a wide-bore, thick film PLOT (Porous Layer Open Tubular) column was used to retain analytes long enough for

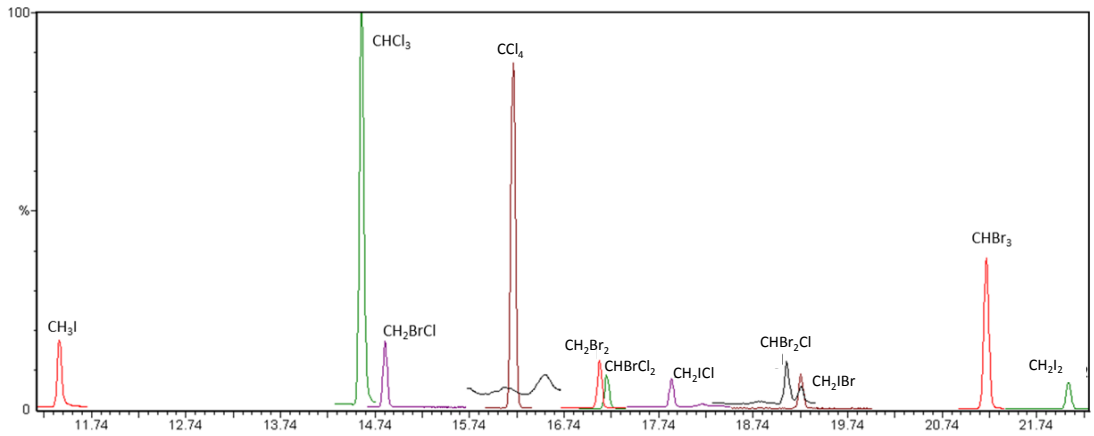

Figure 2.13 – Perkin Elmer TurboMatrix300 TD-AutosystemXL GC-MS chromatogram of VSLH in 1 permeation loop (chapter 3, section 3.3.1) using a Varian PoraBondQ 0.32 mm ID, 3 micron film column, 30 m length.

the baseline to settle and even re-focus the analytes on the column at a low initial oven temperature. 3 L of sample was required to achieve usable sensitivity and as sample flow rate was restricted to 100 mL min^{-1} this resulted in a long sampling time of 30 min.

2.5.2 Markes Unity2– Agilent GC-MS

The instruments were upgraded to Markes thermal desorption systems (Unity2 and CIA8) coupled to Agilent GC-MS (6850/7890-5975C) in July 2010. The Markes TD unit offered significant improvements over the Perkin Elmer system. Most importantly was its smaller cold trap volume which was 2 mm in the packed section. The reduction in absorbent resulted in much better chromatography even when operating completely split-less. Breakthrough volumes (the volume a trap can quantitatively retain) were not reached until over 3 L but as the entire sample entered the GC and the new MS was more sensitive, 1 L of sample was sufficient, reducing sampling time to 10 min. The faster desorption negated the use of a PLOT column to refocus the analytes and allowed faster analysis times (figure 2.14).

It was later discovered that due to the Unity2 utilising the GC's electronic pressure control unit (EPC) from a split/split-less inlet, the septum purge acts as a small split at the head of the column resulting in faster flow during desorption. The septum purge is fixed at 3 mL min^{-1} on Agilent 6890 and 6850 GCs but can be switched off on 7890 or later models.

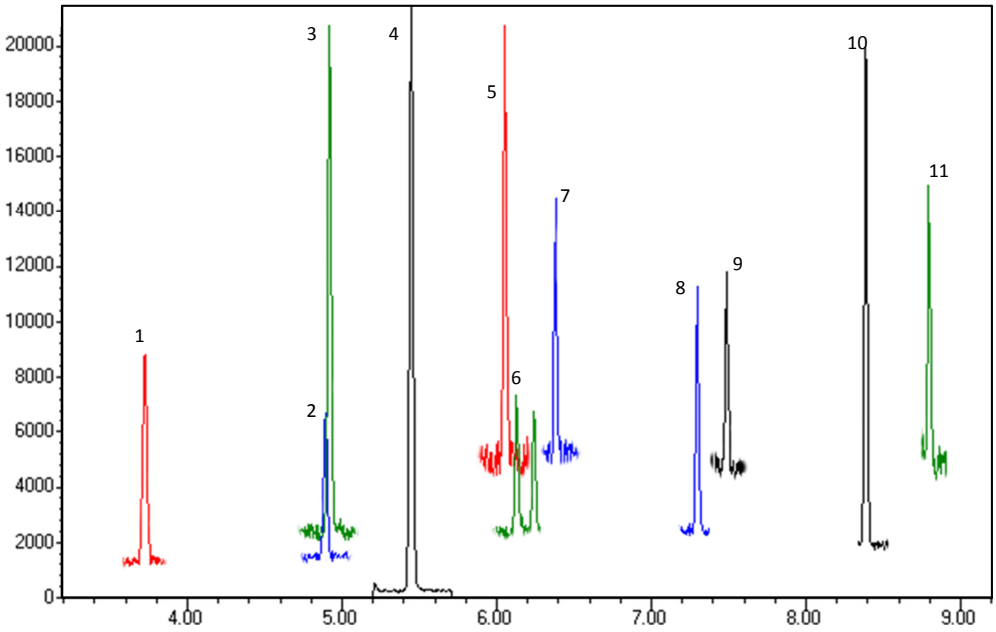

Figure 2.14 – Typical open-ocean marine air sample chromatogram from the Unity2–Agilent GC-MS system using a Restek RTX502.2, 0.25 mm I.D., 1.2 micron film column, 30 m in length. Peak I.D. numbers correspond to species in table 2.1.

Switching off the septum purge did not improve sensitivity as peaks became broader.

Another major advantage with this system was the automation of sample collection from multiple flow paths. This allowed for modification of the system to incorporate more autonomous ancillary systems such as the automated purge and trap (section 2.6).

2.5.2.1 VSLH using Negative Chemical Ionisation (NCI)

Atmospheric concentrations of VSLH can be extremely low (sub-ppt), especially in unproductive regions such as the open ocean gyres (Jones et al., 2010; Chuck et al., 2005). Species with very short lifetimes of minutes to hours such as CH_2ICl or CH_2I_2 have a rapidly decreasing vertical profile with increasing altitude in the atmosphere. Their concentration at the surface is often usually <1 ppt and at altitude they are below the LOD of TD-GC-MS systems running in EI mode (Andrews et al., 2013). NCI was tested using methane as a chemical ionisation gas (CI gas). For the VSLH, negative ions 35, 37; 79, 81 and 127 were monitored corresponding to the stable isotopes of chlorine, bromine

and iodine, respectively. Negative ions are formed via electron capture and upon receipt of an electron, the easiest route to a lower energy is to fragment into a negatively charged halogen and a neutral molecule. In the case of polyhalogenated species the molecule will exist in its lowest energy state with the greatest interatomic distance between the carbon and the largest halogen with the most electrons, leading to cleavage of the weakest (longest) C−X bond in the order iodine–bromine–chlorine. For example NCI of $CHBrCl_2$ will result in fragmentation via electron capture with preferential cleavage of the C−Br bond to form Br^- and $[CHCl_2]^{\cdot}$. Preferential cleavage is stated as loss of a chlorine ion is also possible but not favoured. Chromatographic resolution is important in NCI (and thus also for ECD) as often there are issues resolving CH_2Br_2 from $CHBrCl_2$ as they elute at a similar time on many columns and the low abundance of the negative ion 35 for chlorine hinders using individual masses for separation, as possible in EI. Larger molecules such as halogenated aromatics are more likely to form molecular negative ions as they can de-localise the electron around the ring structure (Buser, 1986).

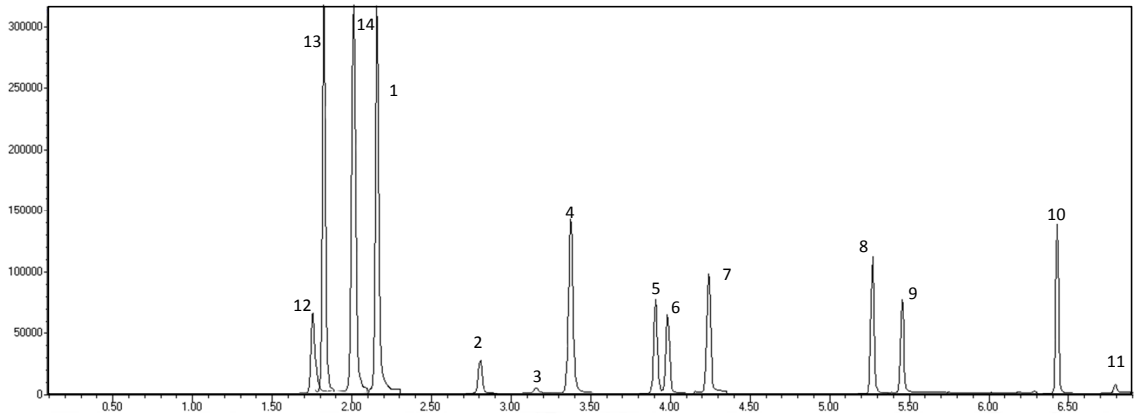

Figure 2.15 – Analysis of a gas standard containing mixed VSLH ranging between 0.4–2.7 ppt using NCI, methane as the CI gas and a Restek RTX502.2, 0.18 mm I.D., 1 micron film column, 20 m in length. Peak I.D. numbers correspond to species in table 2.1.

For aircraft measurements the use of NCI is desirable due to the lower LODs attainable. NCI is much more sensitive than using EI but is less robust and requires the use of a CI gas, typically methane. Methane is a product of the natural gas industry and very high purity methane is difficult to produce making it expensive and likely to contain contaminants. The latter, combined with lower source temperatures and the lower vacuum due to the introduction of such high flows into the MS chamber results in rapid oxidation of the ion

Table 2.1 – Limits of detection for the Unity2–Agilent GC-MS system using EI and NCI sources. LOD defined as 3 x S/N, LOQ is 5 x S/N and Qion is the mass of the ion used for quantification. PA is integrated GC peak area.

Species	Label	Conc. in standard (ppt)	NCI PA in 1 L	NCI Qion	NCI S/N	NCI LOD (pptv)	NCI LOQ (pptv)	EI PA in 1 L	EI Qion	EI S/N	EI LOD (pptv)	EI LOQ (pptv)
CH_3Cl	12	575.4	8585089	35	624	2.766	4.611	-	-	-	-	-
CH_3Br	13	14.8	2688585	79	669	0.066	0.111	-	-	-	-	-
CH_2Cl_2	14	34.5	40735083	35	3477	0.030	0.050	-	-	-	-	-
CH_3I	1	3.8	4785880	127	1829	0.006	0.010	80460	142	393.6	0.029	0.048
CH_2BrCl	2	5.8	277248	79	1085	0.016	0.027	44662	130	198	0.088	0.146
$CHCl_3$	3	8.4	540318	35	499	0.051	0.084	123006	83	362	0.070	0.116
CCl_4	4	86.8	20340929	35	21913	0.012	0.020	1375825	117	2148	0.121	0.202
CH_2Br_2	5	2.6	751732	79	7162	0.001	0.002	28649	174	231	0.034	0.056
$CHBrCl_2$	6	2.2	651481	79	5808	0.001	0.002	33088	83	122	0.054	0.090
CH_2ICl	7	1.3	1587356	127	1479	0.003	0.004	18517	176	189	0.021	0.034
$CHBr_2Cl$	8	3.7	936946	79	14573	0.001	0.001	51480	129	340	0.033	0.054
CH_2IBr	9	1.4	1087920	127	734	0.006	0.010	13836	220	118	0.036	0.059
$CHBr_3$	10	5.4	1041424	79	16950	0.001	0.002	94848	173	751	0.022	0.036
CH_2I_2	11	0.8	89694	127	227	0.011	0.018	21828	268	170	0.014	0.024

source known as ion burn. The rapid downward drift of NCI-QMS was also documented by Worton et al. (2008) who observed a loss in sensitivity >60% over 6 days of continuous ambient air sampling. Because QMS sources use relatively low voltages to accelerate ions out of the source, ion burn negatively affects sensitivity. The other major disadvantage of methane is that it is a flammable gas and its use on-board aircraft is very difficult as it will always be in close proximity to an oxygen cylinder (used for NO_x instrumentation).

For these reasons an alternative reagent gas was investigated. An NCI gas produces thermal electrons by absorbing the kinetic energy from the electrons ejected from the filament and releasing secondary electrons post collision with the high energy electrons. Even if the NCI gas does not release secondary electrons it will still convert enough high energy electrons to thermal electrons for electron capture to take place in the ion source. Thus, a NCI gas just needs to be inert.

Argon can be used as an ionisation gas for PCI and NCI and is useful for the production of ions without forming adducts due to its inertness. It is also widely used as a collision gas for collision induced dissociation (CID) and as a shielding/ionisation gas for inductively coupled plasma-MS (ICP-MS). Argon has an ionisation efficiency energy of 15.76 eV which is greater than methane (12.61 eV). However, argon can be produced very cleanly and is very inert which may help to lengthen the inner source cleaning schedule and reduce background contamination. Most importantly, Argon can easily be certified for aircraft use due to its inertness.

A difficulty encountered testing argon as an NCI gas was that in NCI the reagent ions cannot be seen, therefore it is difficult to determine the amount of Ar entering the MSD. The mass flow controller (MFC) used in the Agilent 5975C is calibrated for 0-10 mL min^{-1} of methane and whilst it can control the Ar flow, it requires re-calibration for the actual flow rate to be known. This can be done using a Gillibrator (Sensidyne) but would require removing the gasket sealed VCR fittings on the ionisation gas inlet and rebuilding with new gaskets after testing. The high vacuum gauge can be used to estimate the amount of Ar in the MSD by monitoring the pressure and comparing with the use of methane. Ar does produce ions in PCI and the mass spec itself can be used to measure the amount entering the system.

2.5.2.2 MSD source modification

In an effort to prolong instrument sensitivity the MSD source and operating conditions were modified. Firstly the source and quadrupole were ran at higher than standard operating temperatures of 200°C for the quadrupole (150°C standard) and 250°C for the source body (230°C standard). Secondly, the ion drawout plate inside the inner source was modified to increase the hole from 3 mm to 6 mm diameter. The drawout plate encloses the ionisation chamber where ions are formed using high energy electrons. The charged ions are accelerated out of the chamber through the drawput plate by the repeller. A larger drawout plate hole allows for the removal of column eluent from the inner source by the vacuum which includes the removal of water entering the MSD. A larger drawout plate may reduce ionisation efficiency as some of analytes are removed before being ionised but should reduce ion suppression by water and help to prolong the cleanliness of the inner source.

Chemical ionisation sources differ to an EI source as the ionisation chamber is more enclosed. This allows the CI gas to remain in the inner source for longer as interaction with analytes is required for proton transfer. Enclosing the ionisation chamber is achieved by fitting an interface tip to seal the MS transfer line into the inner source, removal of one of the filaments and by using a drawout plate with a very small opening. Because the ionisation chamber is so enclosed, any water entering the MS resides inside the source for much longer. Higher performance turbo pumps are used for CI in order to deal with the removal of excess CI reagent gas but the expansion of water inside the inner source leads to fluctuations in pressure which, due to the enclosed design, cannot be rapidly dealt with by the vacuum system.

This source design, the use of a hydrocarbon ionisation gas and the increased pressure inside the vacuum chamber results in CI sensitivity being highly variable and source cleaning is required on a shorter time frequency.

2.5.2.3 GC-MS for fieldwork application

GC-MS systems are not designed to be moved around. Portable instruments are available but often lack the performance of lab based equipment (Eckenrode, 2001). Problems trans-

porting systems include, but not limited to: Damage during transportation, contamination and increased wear on gas fittings not designed for multiple connections/disconnections.

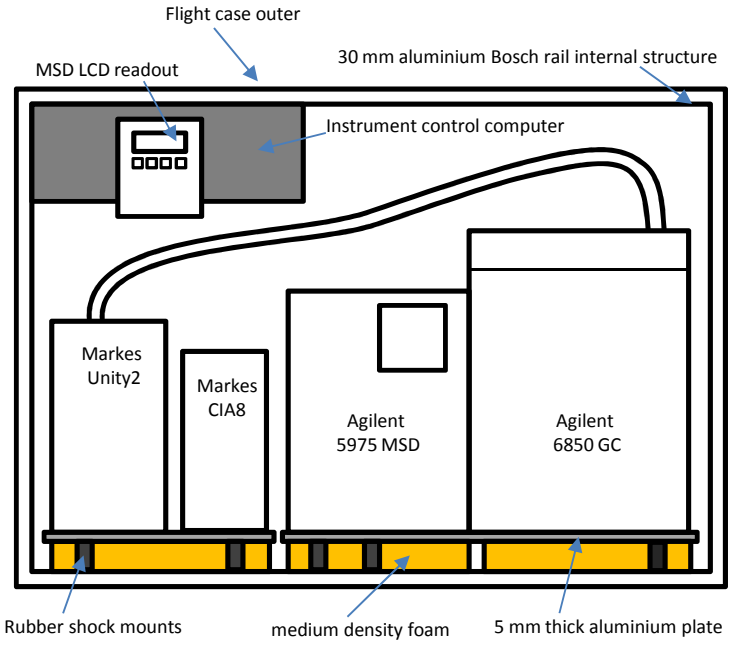

Figure 2.16 – TD-GC-MS system in a custom built, ruggedised flight case.

In an effort to make the transportation of a TD-GC-MS system more simple, the system was built into a flight case (Jetlife) so that it could be transported as one unit. The case was built on four heavy duty castors and incorporated an internal rail system (Rexforth Bosch) which added support to the flight case. The TD and GC-MS were mounted to separate 5 mm thick aluminium plates and mounted to the rail with rubber shock mounts. The TD weighs 22 kg and the GC-MS 67 kg. To support this weight many shock mounts would be required but this would make the mounting very rigid. In order to maintain lateral flex in the shock mounts, medium density foam was placed between the instruments and the flight case base. This spreads and supports the weight of the system allowing for the use of softer shock mounts to deal with lateral movement and absorb impacts during transport and deployment. The system could then be left partially connected, decreasing mobilisation time.

The major disadvantage to mounting and transporting the system in this manner is the size and weight of the combined system. The system has been used on multiple research vessels and is often slightly too large for some of the ship doors. In total the system weighs

Figure 2.17 – Field portable TD-GC-MS system mounted in flight case. AutoP&T system (section 2.6.2) mounted on top.

around 150 kg and requires 4 people to safely lift. Reducing the size and weight by 50% is easily achievable by stripping away unnecessary parts and minimising the weight of others. This would progress a useful but cumbersome system into a truly portable solution.

2.5.3 Data processing

Processing of chromatographic data is often overlooked as a research subject compared to physical instrument design but is of utmost importance. Without reproducible integration of GC peaks the instrument reproducibility is lost. Often, instrument manufacturers produce software designed to meet the requirements of a wide demographic with a focus on pharmaceutical and as such are unsuitable for the requirements of atmospheric monitoring. Previous instrumentation relied on manual integration, which can be biased and required many hours of labour that could result in errors being made.

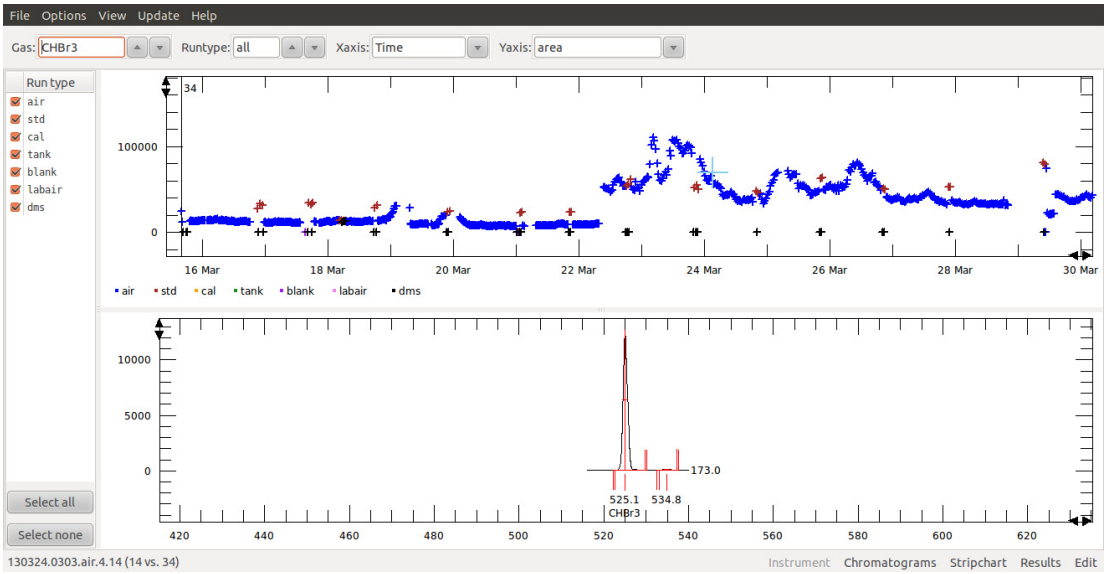

Figure 2.18 – GCWerks program modified to accept Agilent Chemstation data files. Blue, red and black crosses represent the peak area of $CHBr_3$ for air samples, calibrations and blanks respectively plotted along a time series. Light blue cross shows currently selected peak which is displayed in the window below.

GCWerks is a program designed especially for the AGAGE network of MEDUSA instruments (Miller et al. (2008)). It runs on Linux and controls the running and data analysis of

GC-FID/ECD and GC-MS instruments. Through collaboration with the developer (Peter Salameh, GCsoft) GCWerks was modified to work as a stand-alone data analysis program into which data from the York TD-GC-MS system could be input. GCWerks is unique in that it displays all data in a time resolved manner. This is a logical format for atmospheric measurement data as all data collected is taken at a specific time and location.

Once set up for a particular GC method, the software allows for completely automated integration with the potential for automated quantification. By labeling the sample names correctly in the GC method during analysis, the software can split and sort run types such as air, water, calibrations and blanks. As an example, over 2000 samples were collected during the TORERO campaign (see chapter 5). This software saved weeks of post-processing time and even allows for near real-time processing of the data. This is extremely useful for troubleshooting as instrument performance can be monitored and issues identified quickly.

2.6 Analysis of VSLH in water

An automated purge and trap unit was developed for the analysis of VSLH in seawater. This allows for the measurement of trace gases, not limited to VLSH, in any liquid sample but was designed predominantly for operation on-board research ships sampling seawater from pumped underway supplies and discrete samples taken directly from the ocean.

2.6.1 Water analysis

The accurate determination of volatile organic compounds (VOCs) in water is of significant importance both environmentally and with regard to human health. Drinking water contaminants such as trihalomethanes (THMs), aromatic hydrocarbons, pesticides and waste pharmaceuticals must be closely monitored and have legally enforceable limits. Biogenic VOCs created in-situ or absorbed into water from the atmosphere also play an important role in the environment.

VOC mixtures in water are often separated using gas chromatography (GC) and identified and quantified using mass spectroscopy (MS), however the sources of error for the direct

GC-MS analysis of seawater are inherently high. Water is an extremely difficult solvent for GC-MS analysis causing problems such as injection issues, damage to GC capillary columns and decreasing detector sensitivity. Accurate determination of VOCs in water at trace levels usually requires pre-concentration of the sample in order to achieve the desired analytical sensitivity.

Purge and trap in conjunction with thermal desorption is used as an alternative to direct liquid injection as much less water enters the GC system and large volumes of water can be purged to pre-concentrate the sample prior to analysis. Purge and trap techniques often require extensive sample preparation which can make continuous sampling difficult, especially when taking measurements in the field. Automating the sample collection and analysis procedure significantly reduces sources of error and allows continuous sampling 24 hours per day.

2.6.2 Purge and Trap

To analyse volatile organic compounds (VOCs) in water samples, the VOCs are removed from the solvent by heating and degassing with nitrogen. The VOCs are stripped from the water into the gas phase and are subsequently trapped on a cooled absorbent bed prior to thermal desorption onto a gas chromatograph. As per the method used by Jones et al. (2009), water is collected as a discrete sample, filtered and transferred into a glass purge tube (figure 2.19).

A 0.45 micron PTFE filter is used to remove phytoplankton and other biological species from the water. This type of filter has a maximum pore diameter of 0.45 micron, capturing any phytoplankton (larger than 0.45 micron (Le Bouteiller et al., 1992)) and also retaining smaller species such as picoplankton in its smaller pores. The purge tube is heated to 50°C and purged with n6 grade nitrogen or catalytically scrubbed air at 50 mL min^{-1} for 20 min, which enters through a quartz frit (porosity 3).

The VOC enriched nitrogen exiting the purge tube has a high water content which is reduced using water removal techniques which vary depending on the properties of the species being analysed. For organic halogen compounds, saturated aromatic/aliphatic hydrocarbons and sulphur compounds a ME^{TM}-series Nafion® moisture exchanger and a counterflow MD^{TM}-series Nafion® gas drier (Permapure^{TM}) can be used in series. Water

is able to permeate the Nafion® membrane whilst the analytes are retained. For Oxygenated VOCs and unsaturated hydrocarbons such as monoterpenes the water is crystallised out in a cold finger- a glass tube cooled to -30°C. The VOC enriched nitrogen then passes through an absorbent trap held at -30°C (Markes Unity2) where the VOCs pre-concentrate before being thermally desorbed (300°C) onto the GC column.

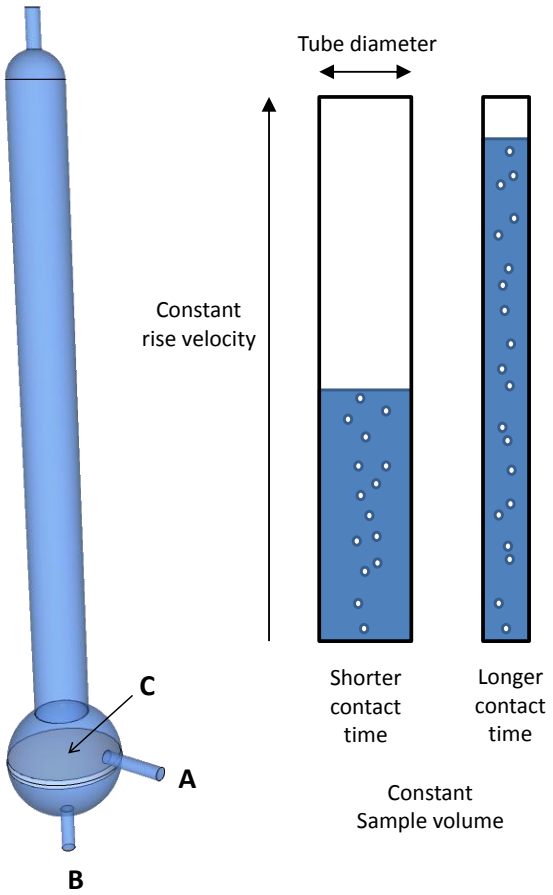

Figure 2.19 – Design of glass purge tube to optimise gas-liquid contact time. Labels A, B and C mark the water inlet, N_2 inlet and quartz frit, respectively.

autopandt The glass purge tube was designed to maximize the purge efficiency. A highly sensitive instrument, in theory, would allow the use of less sample volume. This introduces less moisture into the instrument. Further, a smaller water volume means less gas to purge from the sample and hence faster purge times, although this relationship is not linear.

The out-gassing of analytes from the sample is dependent upon partitioning between the

liquid and gas phase. The dissolved gases in the sample partition between phases across the interface surrounding each bubble of nitrogen that passes through the liquid. Assuming that the purge gas is never saturated, the rate of gas removal from the sample is dependent upon four factors: the total surface area of all the nitrogen bubbles that pass through the sample, the temperature of the sample, the time in which the gas contacts the sample and the Henry's law constant of the analyte. Therefore, in order to achieve the most efficient de-gassing of a sample the bubbles must spend as long as possible in contact with the sample. By reducing the volume of the sample the residence time of each bubble is decreased also.

Bubble hydrodynamics also highlights a number of other parameters which are relevant to this system: Bubbles must be small and numerous to ensure maximum surface area. Bubbles reach terminal velocity shortly after formation (< 0.1 seconds) (Leifer et al., 2000) This terminal velocity is determined by a combination of the bubbles drag and its buoyancy.

Whereas buoyancy is relative to the gas which forms the bubble, drag is dependent upon bubble size and viscosity of the water. For bubbles with radius (r) < 700 micron, rise time is dependent on viscosity of the liquid due to drag. Increasing bubble size increases velocity as the bubble is more buoyant. Increasing temperature increases velocity as the liquid is less viscous. Bubbles with $r > 700$ micron will begin to oscillate in trajectory. This increases the bubbles rise time and eventually ($r \approx 2000$ micron, $T = 20°C$) the rise time becomes independent of bubble size.

Increasing temperature causes greater oscillation so, for large bubbles, rise time will be increased as a function of temperature. For bubbles larger than 2 mm, rise time is independent of temperature (Leifer et al., 2000). Bubble size generated in this system is dependent upon the porosity of the quartz frit and can be kept constant. However, due to its effect upon the VOC vapour pressure, the bubble trajectory and the viscosity of the water, it is clear that accurate temperature control is vital if de-gassing is to be reproducible.

2.6.3 Manual Purge and Trap

Manual water sampling is still commonly used for purge and trap systems. If performed correctly, the technique is able to quantify volatile species in water with sufficient accuracy

and precision to visualize trends and provide useful data for oceanic and atmospheric models. However, as with all manual sampling methods, human error can influence the data significantly.

Automation of a method removes sources of human error, discussed in depth in the next section. Just as important and often overlooked is the reduction in workload that automation can bring. This is particularly crucial on-board research vessels, where sea-sickness and the fact that often only one scientist operates an instrument places a significant pressure on the analysts time. It also allows more time for the analyst to concentrate on the upkeep of the instrument and the interpretation of the data.

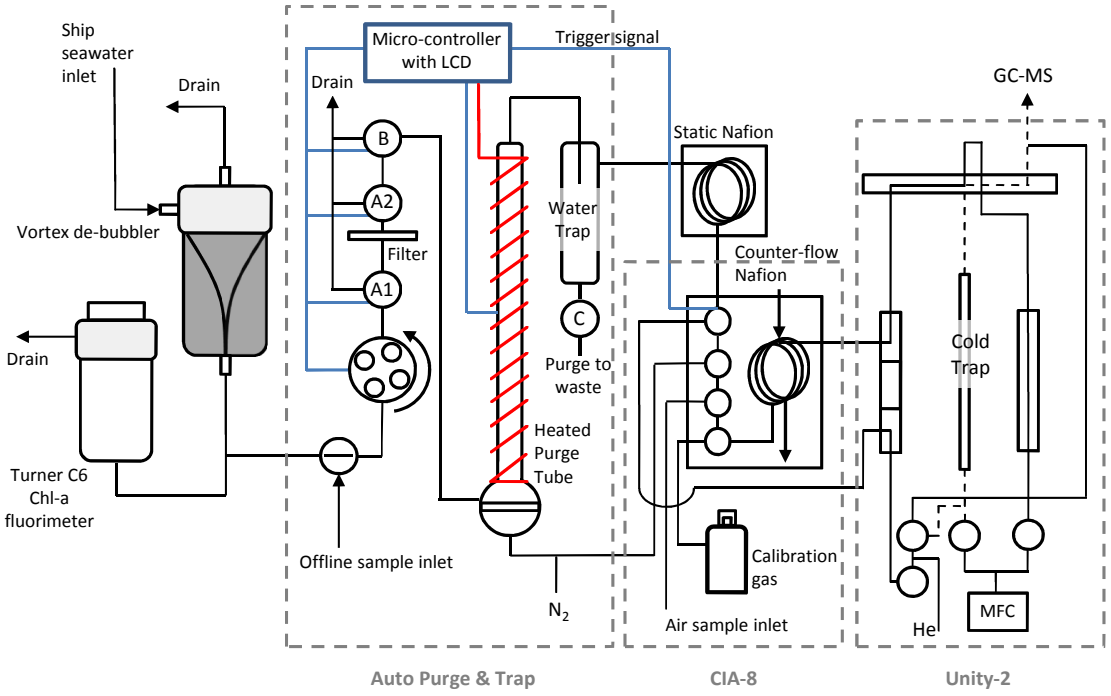

Figure 2.20 – Schematic of the AutoP&T system coupled to a Markes Unity2 CIA8 thermal desorption system and Turner Chlorophyll-a fluorimeter.

2.6.4 Automation of the system

The automated purge and trap is built around the glass purge tube design (figure 2.19) without modification of the interactive system between the purge gas and the seawater. The purge and trap automation is achieved very simply by the addition of a peristaltic pump (Watson Marlow, 1208/DV), four three-way PTFE diaphragm solenoid valves (A1,

A2, B and C) (BioChemValve) and a programmable micro-controller (Arduino Uno). The software for Arduino is open source and the code used for the automated purge and trap is available in the appendix (section A.2).

The four solenoid valves allow for a multitude of flow paths through the system (figure 2.22), letting the user fill/empty the purge tube, de-gas the water to waste, de-gas the water and trap the gases for analysis or to purge the tube with nitrogen to clean it.

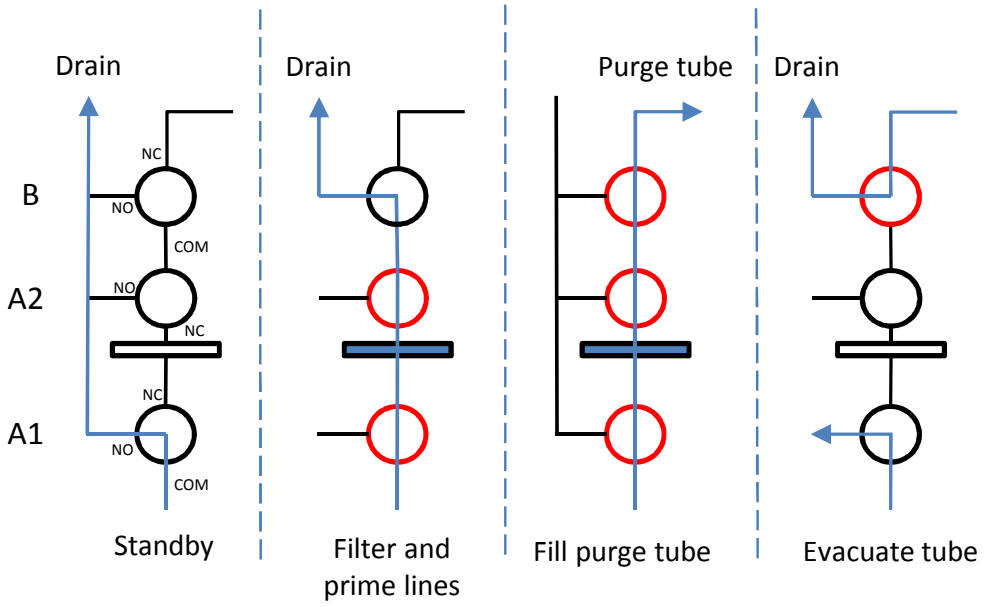

Figure 2.21 – Valve flow diagram showing the four water flow paths through the three main valves and filter during one operation of the system.

The system can work in one of two modes, inline and offline, as outlined below.

2.6.4.1 Inline analysis

Designed to sample from the clean water supply of a research vessel, a water stream is pumped into the system continuously. At all times during the instruments operation, except whilst filling the tube, the water passes through the system and out to waste which maintains a supply of fresh water to the instrument. The flow is set at 30 mL min^{-1} through 1/8" PFA tubing (Swagelok) which maintains a low dead volume. This ensures that when the instrument takes a sample, that sample is representative of the seawater at the vessels present geographical location at that specific date and time. This allows easy

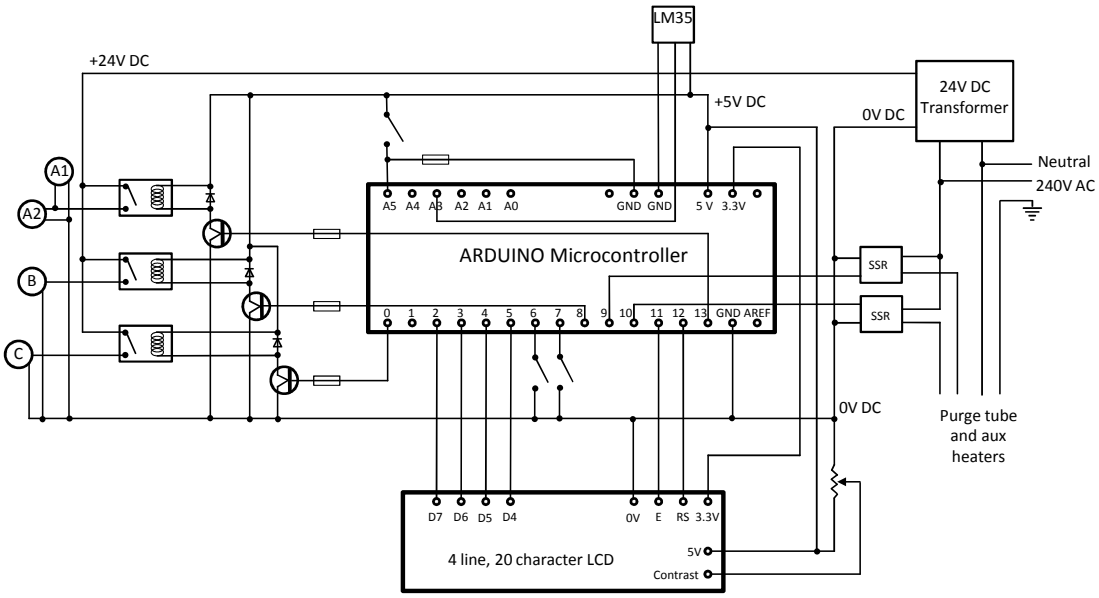

Figure 2.22 – Circuit diagram for automated control of the purge and trap system.

comparison with other measurements taken simultaneously and with remote sensing data.

The system was designed to work alongside a commercial thermal desorption unit; Markes Unity2 and CIA8 air server accessory. The CIA8 is simply 8 heated valves used to select a sample gas stream. The system could easily be modified to work with any commercial or custom thermal desorption technique.

The timings of the system during each sample are outlined in figure 2.23. To take a sample the instrument is triggered by the opening of the valve on the CIA8 air server to which the instruments sample outlet is connected. A pre-set pre-purge time on both the AutoP&T and the CIA8 allows gas flow through the glass purge tube and through the lines of the CIA8 and Unity2 and out of the mass flow controller to waste. During the last twenty seconds of this purge time, the seawater entering the system is diverted through a 0.45 micron PTFE filter to remove bubbles and pre-purge the filter before the tube is filled (figure 2.22). This is only done twenty seconds prior to analysis to help preserve the life of the filter. Once the purge time is over, the nitrogen flow is diverted into the cold trap and seawater is pumped into the purge tube at a constant rate for a pre-set time. The tube is thermostatic at the set point temperature and extra power is given to the heating coil during filling to counteract the cooling effect of the seawater. Once the tube is filled the

water is thermostatic again within 10 seconds. The water is purged with nitrogen for the duration of the trapping time. Once the sampling is finished and all the volatile gases have been stripped from the water, the valve on the CIA8 closes and nitrogen flow through the system ceases. The water is then emptied from the tube by utilising the nitrogen pressure within the tube to expel the water to waste.

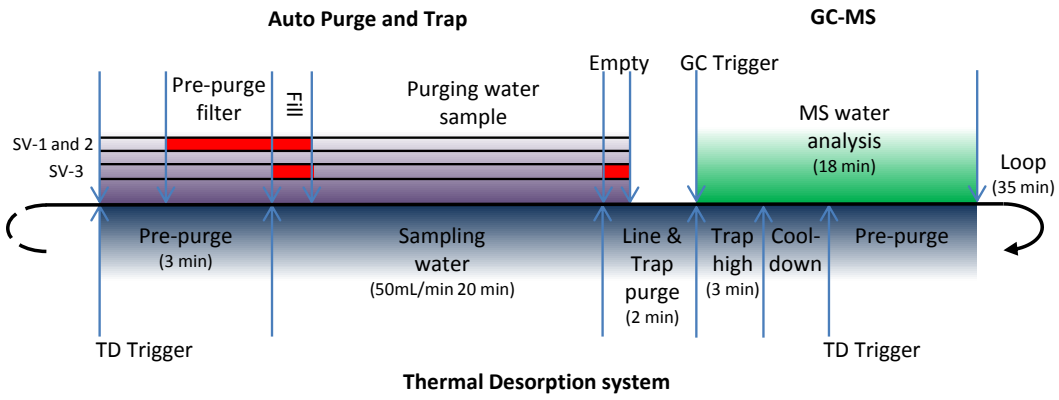

Figure 2.23 – Timing diagram for Auto-P&T operation. Red bars represent actuation of valves. The blue, purple and green shaded areas relate to Thermal Desorption, AutoP&T and GC-MS operations, respectively.

2.6.4.2 Offline analysis

In addition to constant, automated sampling from a sample stream, the system can be used for analysing discrete samples taken manually; such as depth profiles from Niskin bottles on a CTD. This can be achieved by simply switching the flow so that the peristaltic pump draws the sample from the container in which the water was collected just before the flow is diverted to fill the purge tube. This maximises the sample frequency as the instrument will start to sample as soon as the Unity2 is ready. In manual sampling, if the timing is incorrectly judged a sample can be missed.

The other option is to manually trigger each sample. The manual sample inlet line is placed in a sample bottle and a button is pressed on the front of the instrument. It then transfers a set amount of sample into the purge tube and stops once the analysis is finished. In both options air is never allowed to enter the system as air bubbles can be trapped in the valves and effect the sample volume and the analysis results.

The purge tube can be cleaned with gas and/or liquid. In constant use it is not necessary to clean the purge tube as the previous sample was stripped of >90% of the volatile gases (figure 2.25) and <1% of the previous sample will remain in the tube; therefore carryover of volatile compounds will be negligible. If cleaning is required the tube can be purged with pure nitrogen by opening SV-C. For liquid cleaning; the tube can be filled using the manual sample line to introduce the liquid which can be heated, purged/not purged with nitrogen and subsequently emptied to waste automatically.

The automated purge and trap aims to reduce the error associated with manual purge and trap techniques. This error can be significantly large and although the de-gassing of liquid samples is unlikely to ever be described as a highly accurate technique, there are numerous improvements that can be made to improve the precision, which is important if environmental trends are to be observed.

Without changing the construction of the glass purge tube there are three main improvements that can be made over manual purge and trap at previous/subsequent stages during the analysis. Firstly, the quantity of water introduced into the system can be measured more accurately and delivered more precisely. Percentage error in sample volume is directly proportional to measurement percentage error. Inconsistencies in sample volume can be large due to human error associated with manual operation of a glass syringe. Increasing the sample volume will decrease the percentage error and also increase sensitivity. However, a greater volume will require longer purge times, longer temperature equilibration and introduce more water vapour into a water sensitive instrument. The use of a peristaltic pump which delivers a constant flow rate allows the introduction of a consistent volume of sample.

The second stage of the improvement process involves the heating and degassing of the sample. Previously the glass purge tube has been wrapped in a resistively heated rubber cable to which power is applied until the temperature equilibrates at 50°C. Due to the low power required to maintain a well-insulated tube at any given temperature the initial heating time is substantial. For this same reason, when the cold-water sample is introduced into the tube, it takes a long time for the water to equilibrate to the desired temperature, as the power delivered to the system remains constant.

The automated system works using a high-powered resistive heater in a thermally sta-

ble fabric weave with feedback of the temperature to the micro-controller. The micro-controller decides the amount of power to give the tube via a PID algorithm which looks at the difference between the actual temperature and the set-point. Temperature is controlled using pulse width modulation of the power input. Equilibrium is achieved to within $\pm$ 0.1 degrees using short pulses of high power. The reserve of power is then utilised when the cold water enters the tube, the temperature difference increases and the high power is delivered for a longer percentage of the time allowing the sample to be heated rapidly to the desired set-point. The water acts as a thermal buffer so that the set-point is reached without overshoot. The temperature feedback loop keeps the sample thermostatic regardless of ambient temperature changes. Alarm temperatures are pre-allocated to prevent thermal runaway if, for example, the temperature sensor fails, becomes separated from the heating coil or is not plugged in. The added control over the temperature of the sample should improve precision due to a more consistent removal of volatile organics from the water.

The third stage of the process is the timing of each stage of the analysis. As all timings are controlled by the micro-controller, samples are purged for equal time and always undergo the same residence time within the instrument.

2.6.5 Experimental results

The automated purge and trap can be used for sampling water from any source but was designed for continuous underway sampling of seawater aboard research ships and thus the performance tests carried out reflect this requirement. Due to the high sensitivity of the instrument and the high concentration of trihalomethanes and other halocarbons in domestic water supplies, bottled mineral water was used to test the system in the lab. Mineral water contains greater concentrations than seawater for all of the measured halocarbons and was used for reproducibility and purge efficiency tests. These tests were then repeated using seawater samples during the TORERO field campaign (see chapter 5). Chromatograms with very clean baselines and quantification of 24 analytes in real seawater samples was achieved (figure 2.24). Hydrocarbons and monoterpenes analysis shown here was developed for the AMT22 cruise which is not covered in this PhD.

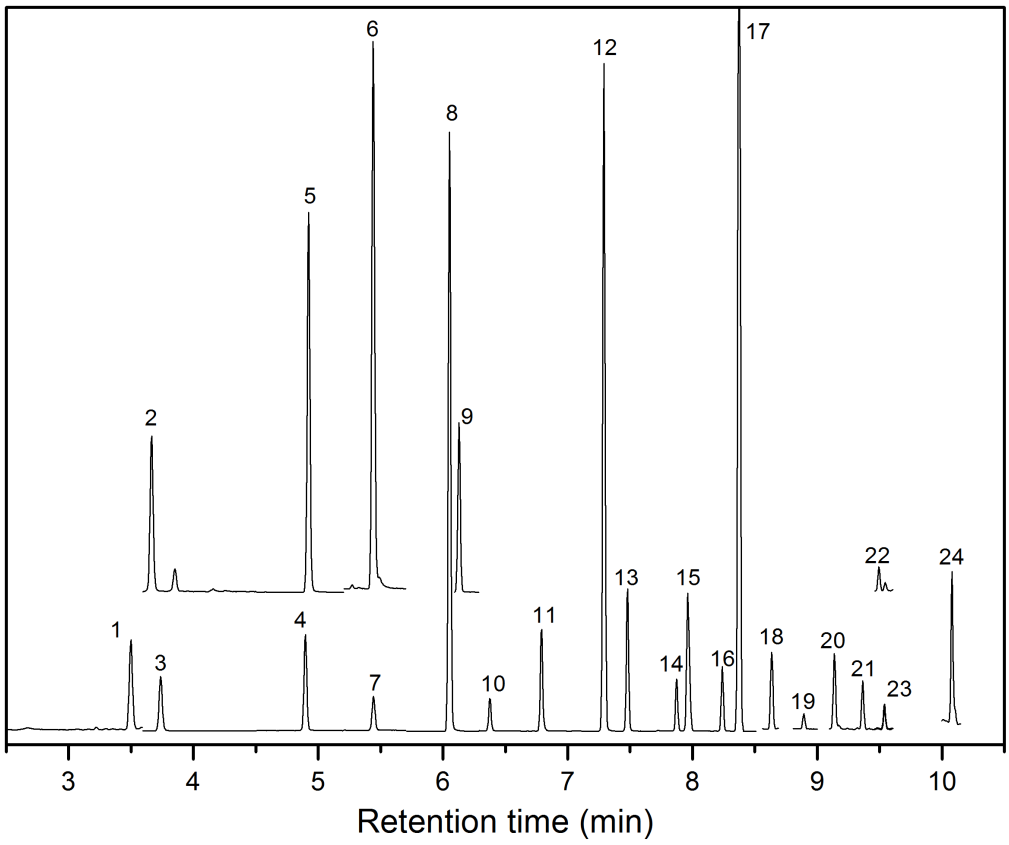

Figure 2.24 – Extracted ion chromatogram for seawater analysed using the automated purge and trap system. Peak numbers correspond to table 2.2.

Table 2.2 – Automated purge and trap compound list with typical purge efficiencies and reproducibility

Label	Compound	Molecular formula	Purge efficiency	Reproducibility
			%	%RSD
1	Isoprene	C_5H_8	-	-
2	DMS	C_2H_6S	-	-
3	Methyl iodide	CH_3I	> 90	2.1
4	Bromochloromethane	CH_2BrCl	> 95	-
5	Chloroform	$CHCl_3$	> 95	-
6	Benzene	C_6H_6	-	-
7	Carbon Tetrachloride	CCl_4	> 99	-
8	Dibromomethane	CH_2Br_2	> 99	6.9
9	Bromodichloromethane	$CHBrCl_2$	> 99	12.2
10	Chloroiodomethane	CH_2ClI	> 99	6.7
11	Toluene	C_7H_8	-	-
12	Dibromochloromethane	$CHBr_2Cl$	> 98	9.4
13	Bromoiodomethane	CH_2BrI	> 99	0.7
14	Ethyl Benzene	C_8H_{10}	-	-
15	m/p-xylene	C_8H_{10}	-	-
16	o-xylene	C_8H_{10}	-	-
17	Bromoform	$CHBr_3$	> 95	5.5
18	α-pinene	$C_{10}H_{16}$	-	-
19	Diiodomethane	CH_2I_2	> 80	3.6
20	β-pinene	$C_{10}H_{16}$	-	-

2.6.5.1 Purge efficiency

The volume of water sample used for analysis was 20 mL, chosen to allow adequate GC peak areas below the concentrations normally observed in seawater. A larger sample would give greater sensitivity but would require longer purge times and introduce more water vapour into the system. The purge time for 20 mL of water was then evaluated by purging one sample of Evian mineral water for 10 minute intervals (figure 2.26). It can be seen that the majority of the analytes are removed from the water within the first 10 minutes but it is necessary to purge for 20 minutes in order to remove some of the 'stickier' species such as CH_2I_2.

Reproducibility and carry-over were evaluated by analysing multiple samples from a single bottle of Evian with nitrogen blanks between each sample (figure 2.25). The water was taken from the bottle without letting in any air, eliminating head space to reduce out-gassing between samples. Some carry-over existed after a water sample but concentrations measured in mineral water are much greater than found in seawater samples. Blank runs eliminate this problem but a second revision of the system introduced a cleaning step to flush the tube with nitrogen after each sample (using valve C, figure 2.20) without the reduction in sample throughput that blank runs would necessitate.

2.6.5.2 Results and sample storage tests

The instrument ran halocarbon measurements continuously throughout a research cruise as part of the 2012 TORERO campaign (chapter 5). During this voyage the instrument collected >800 surface water samples from a continuously pumped seawater inlet and via Niskin bottle samples from numerous CTD profiles. At the start of the campaign the purge efficiency was tested again, which showed that all species had a purge efficiency greater than 90% from seawater. The samples taken from the Niskin bottles from the CTD profiles were filtered and stored in amberised glass bottles, in the dark at around 18°C. The error introduced by this sample handling was measured by re-analysing the same sample from 40 m depth 6 times to simulate any changes from the storage of water from 6 different depths taking into account the length of time required to complete the analysis of each CTD profile (table 2.3).

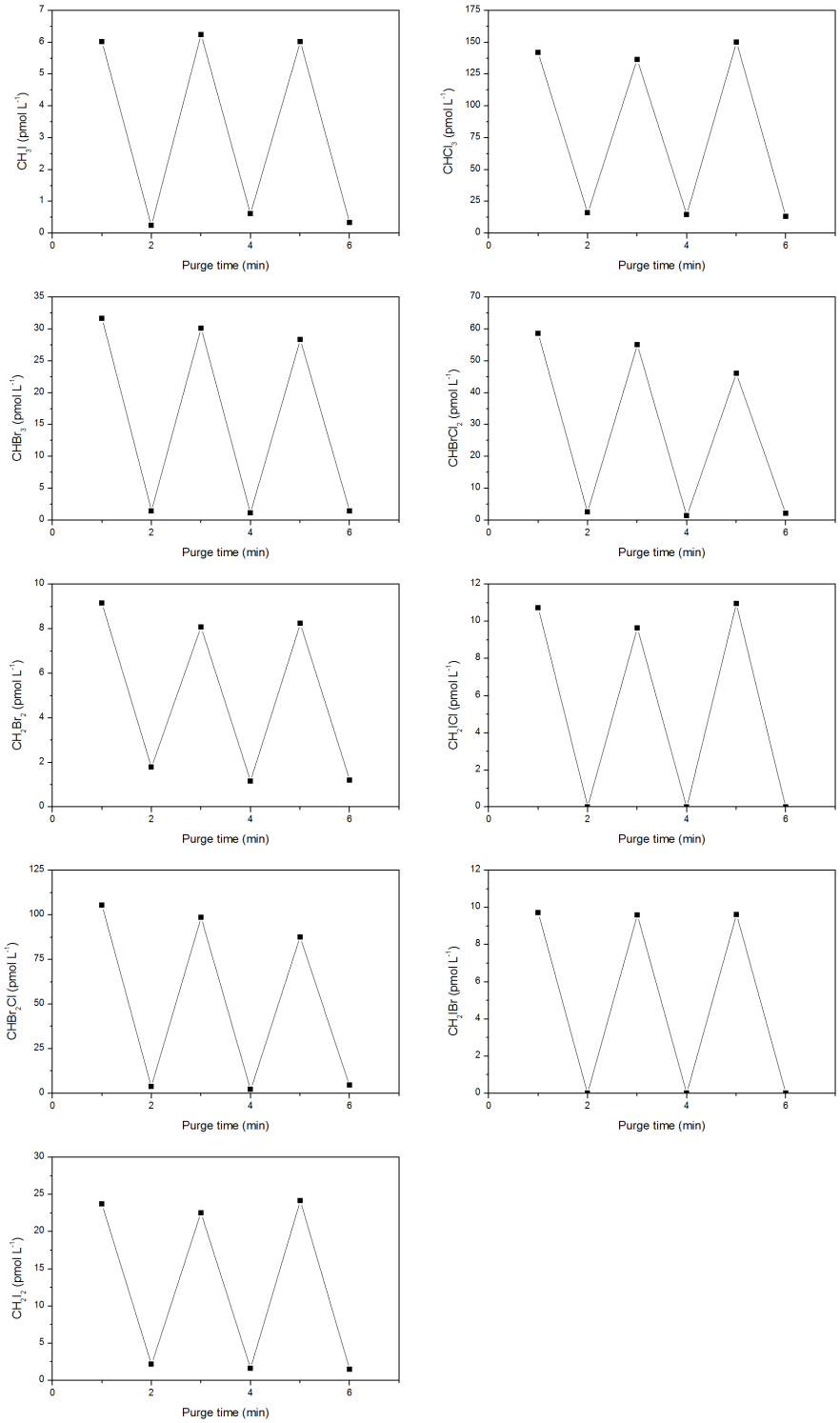

Figure 2.25 – Purge efficiencies for Evian water at 50°C with 1 L (50 mL min^{-1} for 20 mins) of N_2

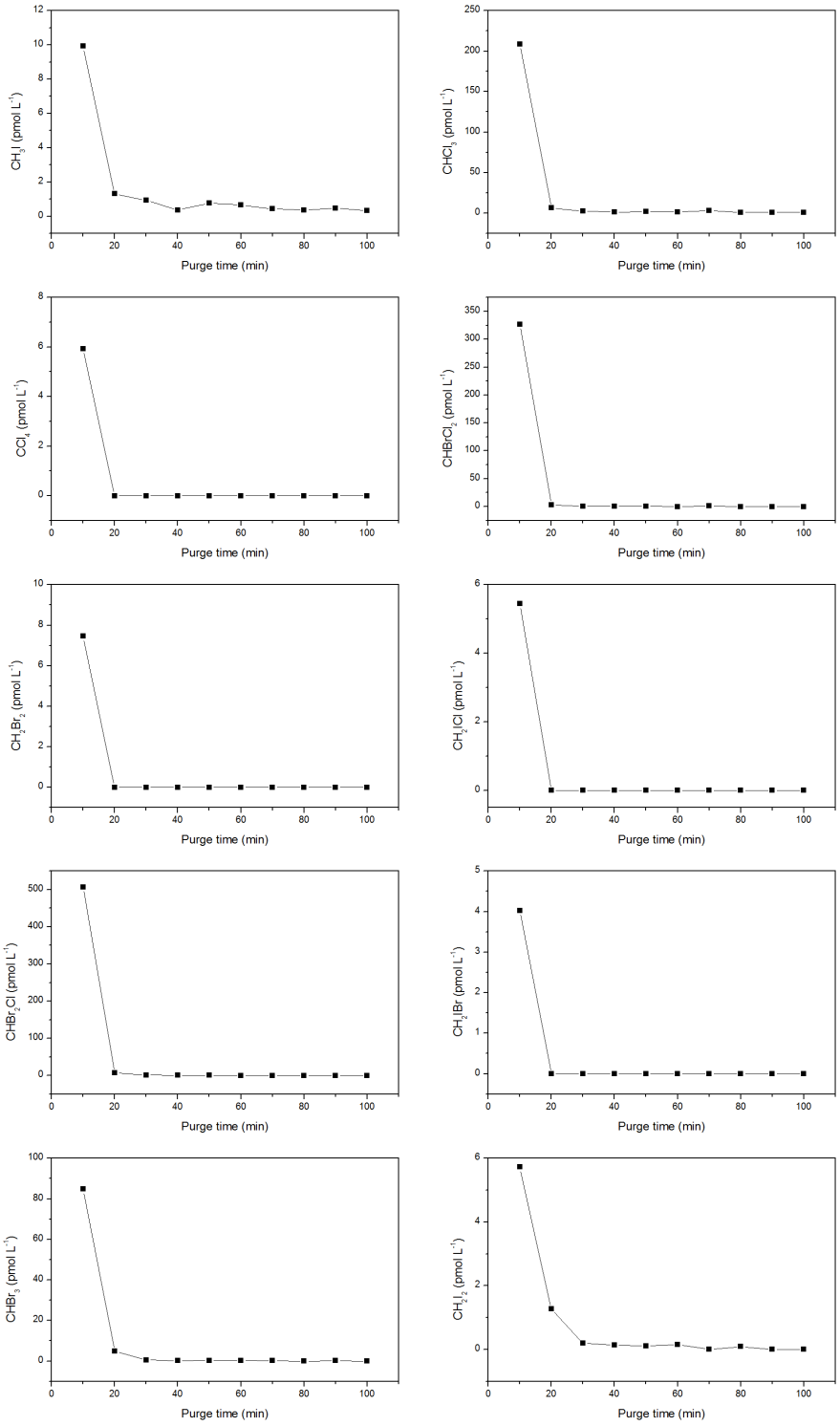

Figure 2.26 – Reproducibility and carry-over tests for Evian water at 50°C with 1 L (50 mL min^{-1} for 20 mins) of N_2

Table 2.3 – Reproducibility of CTD batch sampled water from 40 m depth, filtered and stored in amberised glass bottles at ambient temperature

	% of maximum peak area										
Sampling time	CH_3I	$CHCl_3$	C_2H_5I	CH_2BrCl	CCl_4	$CHBrCl_2$	CH_2Br_2	CH_2ClI	$CHBr_2Cl$	$CHBr_3$	CH_2I_2
13/02/12 18:38	58	100	100	97	95	100	100	95	87	96	100
13/02/12 19:33	82	87	61	72	83	77	99	96	84	93	94
13/02/12 20:29	100	97	96	80	100	99	96	95	100	100	98
13/02/12 21:24	80	99	67	70	96	85	100	96	84	93	86
13/02/12 22:19	65	81	0	100	86	65	95	100	82	94	91
13/02/12 23:14	65	90	79	92	80	69	94	92	84	88	90
% Standard deviation	20.6	8.2	54.2	15.3	9.0	18.1	2.6	2.8	7.5	4.0	5.6

2.6.5.3 Underway supply vs. CTD bottles

Table 2.4 – Difference between batch samples taken from 3 m CTDs and 2–5 m underway water supply samples represented by the standard error of the difference between 10 consecutive comparisons.

Compound	Mean standard error (%)	Range (standard error %)
CH_3I	10.8	1.8–44.7
$CHCl_3$	4.0	2.0–7.1
C_2H_5I	24.0	1.4–44.7
CH_2BrCl	16.6	0.9–44.7
CCl_4	2.2	0.1–6.8
$CHBrCl_2$	7.9	0.5–14.2
CH_2Br_2	3.5	1.6–13.5
CH_2ClI	5.8	0.4–20.5
$CHBr_2Cl$	1.8	0.6–3.0
$CHBr_3$	1.7	0.0–6.1
CH_2I_2	5.5	0.6–15.2

A potential source of error from sampling underway seawater from a ship is from contamination or loss in the ships pumped seawater supply. Water is drawn into the ship at around 3 m depth and pumped to the supply taps in the ship wet labs. These taps are turned on throughout the voyage so the water moves through the system at a high flow rate > 10 L min^{-1}. However, these sample inlets are not installed with trace gas analysis in mind and the pumps and tubing materials used can introduce contamination or induce losses as the water transits the system. It is difficult to obtain information regarding the materials used and the cleaning/maintenance of these inlet systems and as such data obtained via their use should be treated with caution.

In order to ascertain sample integrity, pumped inlet supply samples can be compared to surface CTD samples from Niskin bottles. As the samples are not taken concurrently they cannot be expected to compare directly but should provide an indication of sample

integrity between the two techniques. This approach was used during the TORERO campaign and the results can be seen in table 2.4. This shows that there is good agreement between the two sampling techniques and that it is unlikely either technique introduces major contamination or resulting losses. This analysis is only valid for NOAA vessel Ka'imimoana and use of other sampling systems must be tested accordingly.

2.6.6 Further work

Recent changes and improvements included moving valve c from the top to the bottom of the water trap and is now used to remove water in addition to purging the system post sampling. For the analysis of DMS, filters must be changes after each sample due to cell bursting during filtration.

Although housed in protective casing, the system is quite fragile with glass to Teflon to stainless steel fittings and tube work. A system where these fragile parts are hard mounted with quick-connect purge tubes and water traps would be beneficial for fieldwork on-board ships.

If using one filter per analysis it requires changing each run and is prone to air bubbles and human error. An automated filter change could easily be incorporated using the current electronics but would still introduce air into the system. The greatest issue with air bubbles is for sample volume reproducibility as the system relies upon time and flow rate to introduce the correct volume into the purge tube. A physical detection of water volume such as an infrared sensor would improve this.

Despite careful design of this system and reduction in the error associated with manual purge and trap, major issues remain such as the requirement for filtration and heating of the sample (causing biological cell bursting), the introduction of water vapour into the instrument and electro-mechanical parts which can fail. A membrane-based system where gases could equilibrate into a carrier gas across a hydrophobic membrane without the need for filtration could offer many benefits especially for longer-term sampling.

2.7 Summary

In this chapter the theory of GC, MS and TD was discussed. A complete understanding of each technique is necessary in order to maximise measurement potential and accurately quantify VSLH. New analytical methods were created that take advantage of the latest instrumentation and improve on previous methods with respect to sensitivity, stability and sample throughput.

The use of a cooled glass trap was found to be the most appropriate method for the removal of water from a sample stream and a highly efficient design was produced incorporating Stirling cooler technology. GC methods were tested for various scenarios including a fast method utilising NCI. This method is appropriate for use on an aircraft due to its fast run-time and the increased sensitivity provided by NCI allowing for detection of trace VSLH at altitude.

Instruments were also optimised for use aboard research ships. For analysis of seawater a fully automated purge and trap system was designed and built which runs continuously from a vessels pumped seawater supply whilst still allowing the introduction of batch samples from CTDs.

The automated system offers significant improvements over the previous manual method and has successfully been deployed on 5 research cruises to date, totaling >190 days of continuous sampling.

Chapter 3

Accurate Quantification of VSLH

Several factors currently limit the understanding of spatial and seasonal variability of VSLH. These include measurement, calibration, data processing and modelling issues. These factors are discussed here along with solutions, potential or current, for better constraint of sources and sinks of these important trace gases.

Data from section 3.4 in this chapter has been published in the article:
Jones, C., Andrews, S., Carpenter, L., Hogan, C., Hopkins, F., Laube, J., Robinson, A., Spain, T., Archer, S., Harris, N., et al.: Results from the first national UK interlaboratory calibration for very short-lived halocarbons, Atmospheric Measurement Techniques 4, 865–874, 2011.

3.1 Overview

The development of new measurement techniques was discussed in chapter 2 and the next step is to characterise these techniques in terms of their ability to produce precise and accurate quantification of VSLH. Quantification ultimately relies on an accurate calibration standard but first a method must display a predictable and reproducible response to the analytes of interest.

The analyses carried out in this chapter were performed on a TD-GC-MS consisting of a Markes Unity2 and CIA8 coupled to an Agilent 6850/7890 GC and 5975C MSD, the latest instrument development from the previous chapter.

3.2 Calibration

To accurately determine the concentration of a sample the instrument should be calibrated with concentrations spanning the concentration range of the samples. That is the sample concentration must lie within the linear dynamic range (LDR) of the instrument (non-linear calibrations are also possible but must not be extrapolated). When it is impossible to generate a standard with concentrations low enough, it is common practise to extrapolate the instrument response and assume linearity. This method is valid if indeed the response remains linear but that is difficult to prove experimentally.

3.2.1 Linearity and breakthrough tests

Whilst running with an EI source, calibrations were linear down to the lowest point of the calibration range (figure 3.1). Some of the linear fits such as CH_2I_2 and CH_2BrI displayed a positive offset, which suggests that at zero concentration the instrument was still detecting those specific ions. This could be due to blank contamination or from poor integration caused by a noisy baseline. For these two gases it is possible that the positive offset is due to them "sticking" on sampling lines, a known problem especially for CH_2I_2. If positive offsets were encountered during the calibration of samples then a background subtraction would be applied but this issue was later solved by pre-purging sampling lines prior to analysis. As these calibrations remained linear up to 3 L sample volume it can be

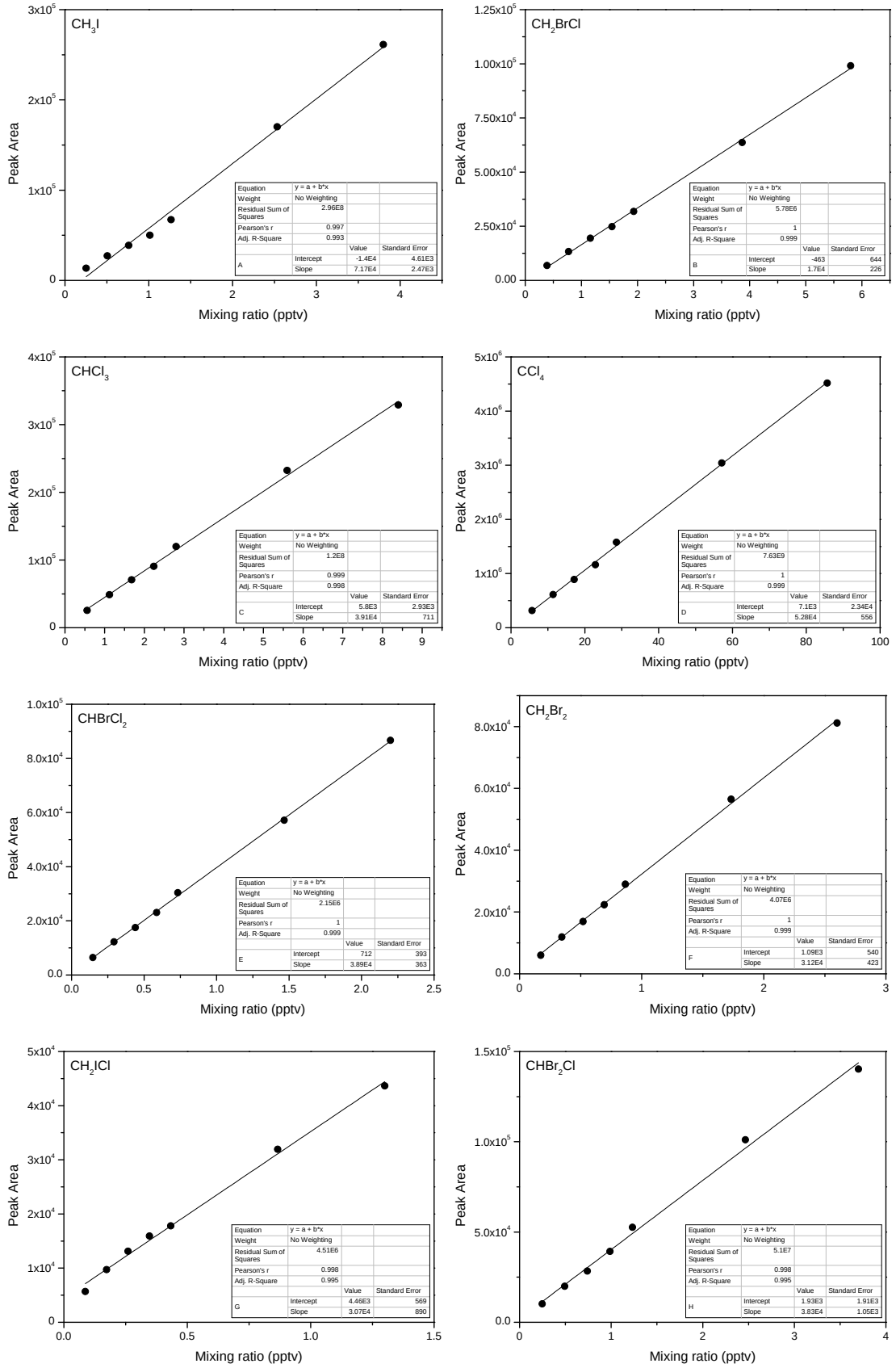

Figure 3.1 – Continued over...

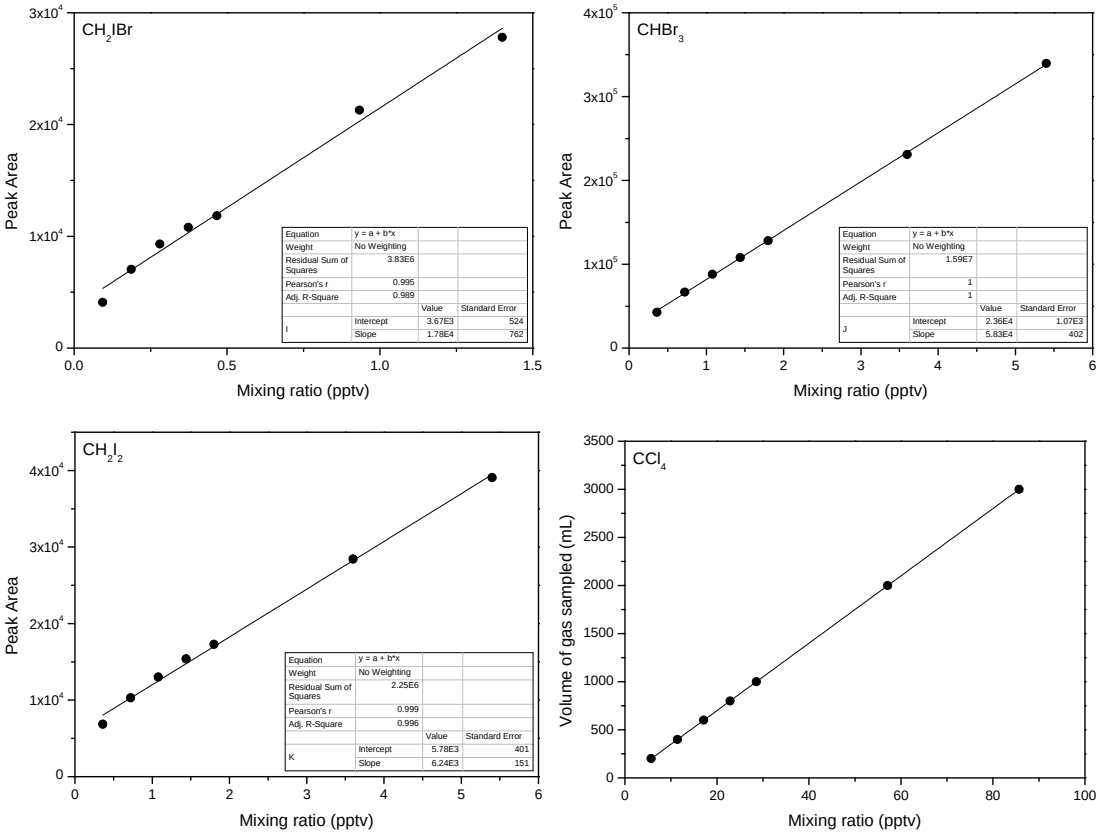

Figure 3.1 – TD-GC-MS linearity tests using EI source. Mixing ratios in 3 L of air corresponding to CCl_4 concentration of 86.8 ppt (bottom right graph). Instrument reproducibility shown in table 3.1.

assumed that the breakthrough volume of the trap has not been exceeded and that up to 3 L of sample can be analysed quantitatively.

3.2.2 Linearity tests NCI

Linearity tests using NCI (Figure 3.2) showed that the instrument gave a high response to very low concentrations of analyte but was not linear over large concentration ranges. Interestingly, CH_2Cl_2 became non-linear at concentrations greater than around 20 ppt whereas $CHCl_3$ looked to be linear beyond this. CCl_4 was also non-linear. Clearly care must be taken if working at higher concentrations with NCI and single point calibrations should be avoided. It is unlikely that the non-linearity is caused by adsorbent trap breakthrough of analytes as this was tested using the same sample volumes in EI. Only the negatively charged halogen ions were analysed and it may be possible that for chlorine containing species, where the carbon-chlorine bond is stronger than for bromine or iodine, there is production of a negatively charged molecular ion, which could contribute to the non-linearity.

Table 3.1 – Mean peak area (PA), standard deviation (SD) and percentage standard deviation (%SD) of 10 repliate synthetic air samples.

Species	Mean PA	SD	%SD
CH_3I	88012	2673	3.0
$CHCl_3$	144314	4217	2.9
CCl_4	1587144	34952	2.2
CH_2Br_2	32762	991	3.0
CH_2ICl	20940	632	3.0
$CHBr_2Cl$	57763	1515	2.6
CH_2IBr	15558	455	2.9
$CHBr_3$	107880	2842	2.6
CH_2I_2	24205	610	2.5

In order to apply these calibration curves to quantify samples it is assumed that the

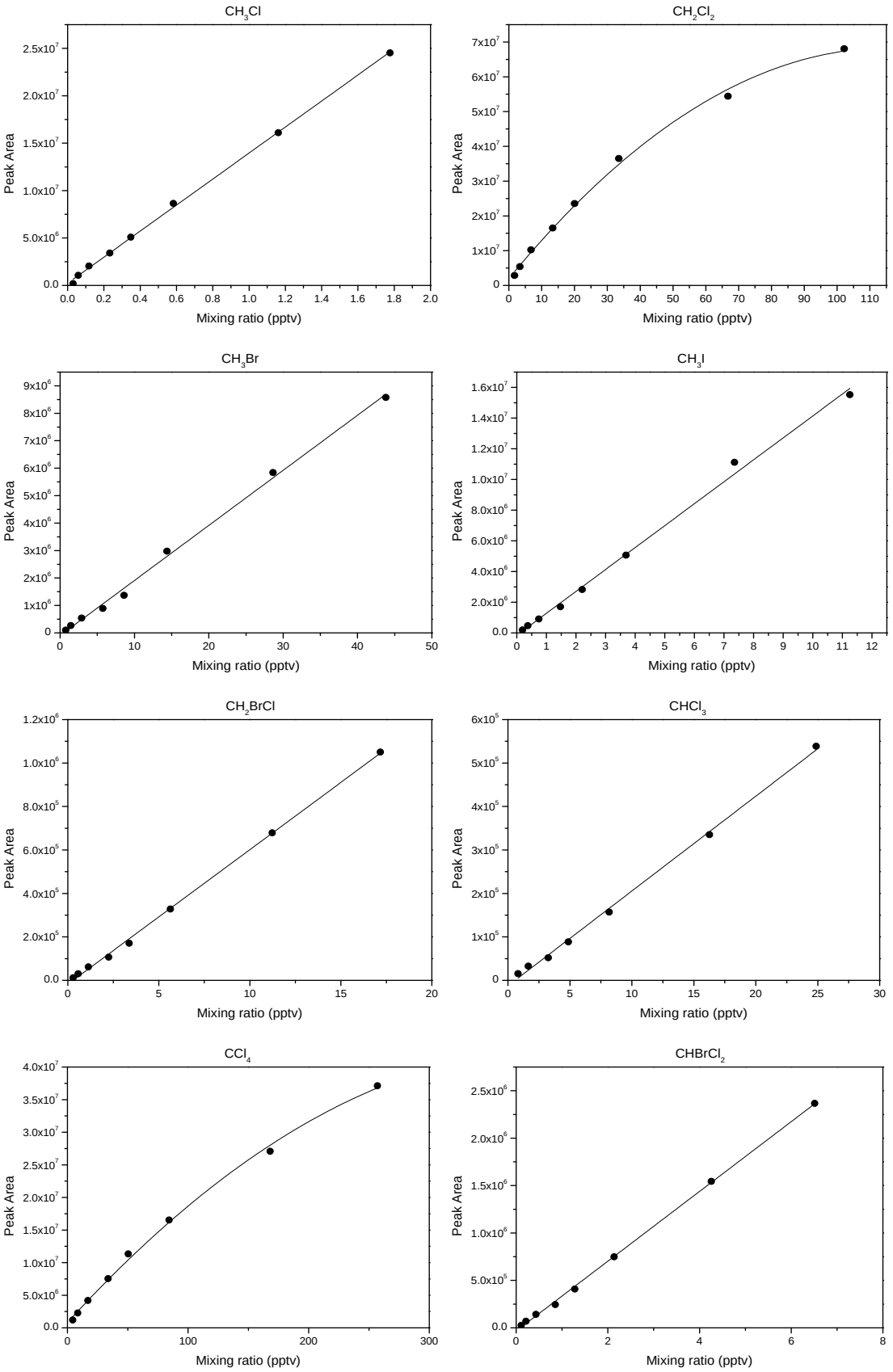

Figure 3.2 – Continued over...

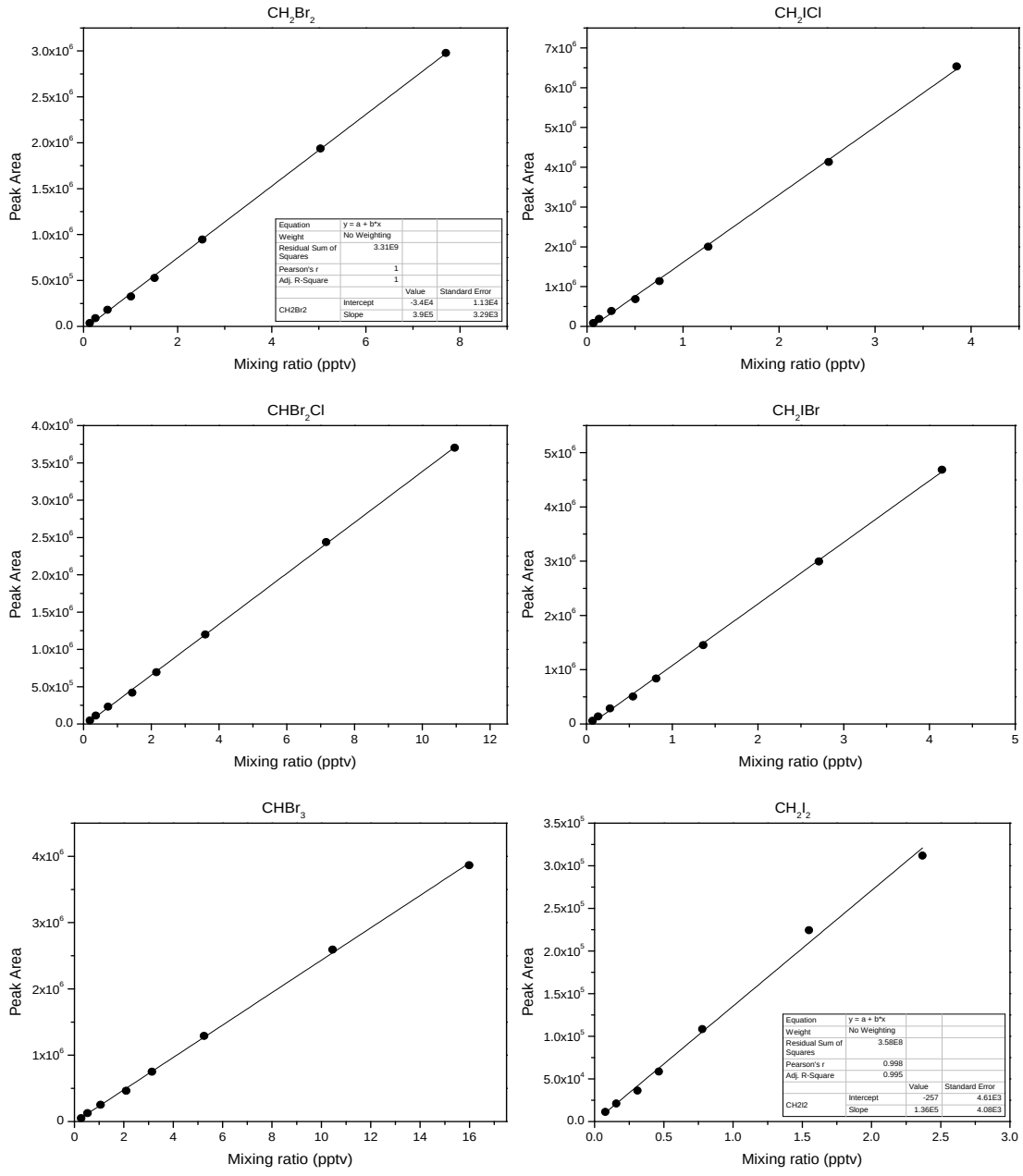

Figure 3.2 – TD-GC-MS linearity tests using NCI source with methane as the CI gas. Mixing ratios in 1 L of air corresponding to CCl_4 concentration of 86.8 ppt. Instrument reproducibility shown in table 3.1.

instrument response during the calibration remains the same as during the analysis of a sample. In reality the instrument response changes even between subsequent samples (table 3.1). Although the actual %SD during a calibration is <3 %, the longer term stability can vary more (figure 3.5). The resulting error can be minimised by the use of an internal standard.

3.2.3 Internal standards

Mass spectrometers are useful detectors for gas chromatographs but their sensitivity can vary significantly between runs. This is especially true of samples containing water which can increase vacuum pressure and quench ion formation. In order to accurately quantify analytes a calibration must be run frequently or an internal standard used to account for sensitivity changes.

An internal standard (IS) is a compound that is spiked into each sample at a known concentration. The response of the instrument to each analyte is normalised to the response to the IS. As the IS remains constant, any fluctuations in sensitivity will be cancelled out.

Addition of an IS to a liquid sample is easy but for gas phase samples the process is more involved. Typical systems involve the addition of a fixed volume loop to the sample flow path to introduce a constant quantity of IS. Knowing the concentration of the IS is not a requirement, so long as it remains constant. An IS must not be present in the sample itself and the difficulty encountered with air samples is that they could potentially contain any compound. For example, toluene cannot be used as an internal standard for air samples as it is already present in air at varying concentration. Instead, un-natural forms of gases are used such as deuterated compounds. These are unlikely ever to be present in air so the instrument response will only reflect the amount added as the IS.

Additionally, the mass spectrometer should have a similar response to the IS as it does to the analytes of interest. Mass spectrometer sensitivity can vary by different amounts for different masses, although this only occurs significantly during re-tuning of the instrument and it is usually assumed that the change in response to the internal standard is similar to the change in response to an analyte.

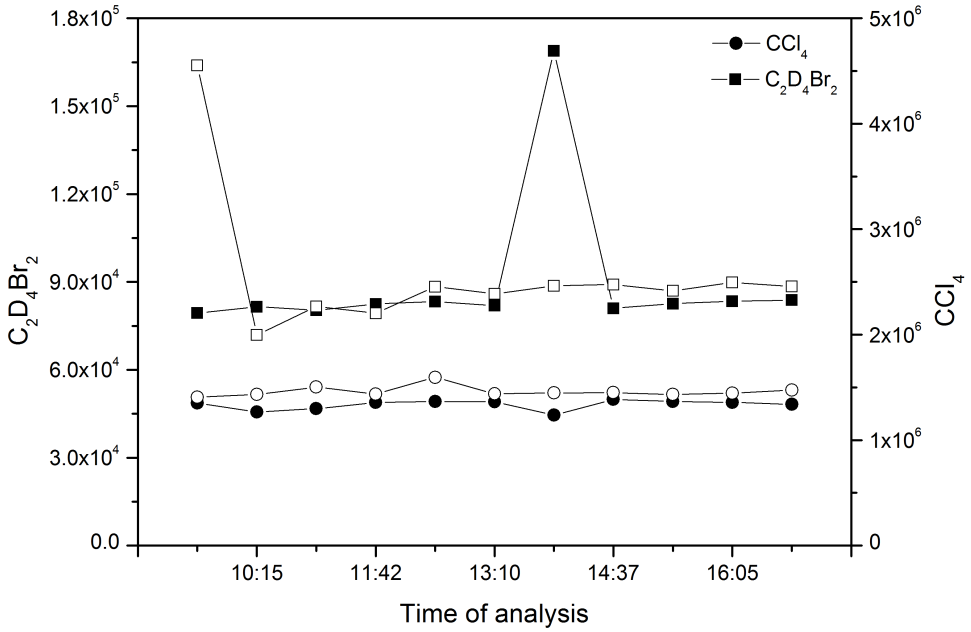

Figure 3.3 – Reproducibility of an IS addition via the Unity2 loop (squares) compared to carbon tetrachloride (circles) in an air sample. Black markers ran 04/07/2011; white markers ran 05/07/2011.

3.2.3.1 Internal standard loop injections

A commercially available IS addition loop (Markes CIA8) was tested for the addition of 1,2-dibromoethane-d4 during the analysis of VSLH. The loop was 1 mL in volume and made from SilcoSteel (Restek) heated to 50°C. As deuterated compounds are not completely pure (∼99%) and can decompose to form their non-deuterated counterpart, it was decided not to use a deuterated form of a compound which was actually being quantified. The IS gas was created by evacuating an aluminium cylinder (aculife coated), injecting 1 μL of 1,2-dibromoethane-d4 and pressurising to 100 bar with zero grade nitrogen. A 1 mL injection resulted in a peak area response similar in magnitude to the instrument response to atmospheric concentrations in 1 L of air sample.

Unfortunately, reproducibility of the IS loop injections was poor (Figure 3.3). Although the %RSD between injections was often <2%, periodic spikes were observed. In figure 3.3, these spikes are around twice the magnitude and could be the result of a double injection. In other analysis the RSD was substantially worse and despite the loop being heated it is

possible that the IS was sticking to the loop. For an IS addition to be useable it must be consistent and reliable. For these reasons it was decided that loop injections of IS were not suitable for this particular analysis.

3.2.3.2 Carbon tetrachloride as an internal standard

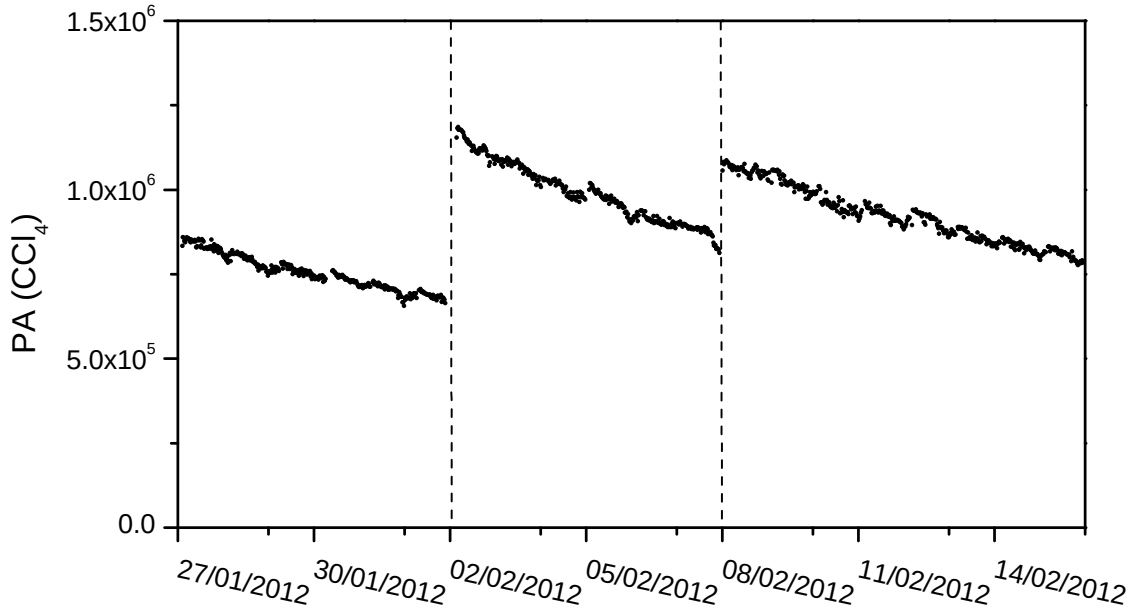

Figure 3.4 – Carbon tetrachloride measurements in air taken during the TORERO campaign. Dashed lines indicate periods of ion source tuning.

A different approach to IS addition is the use of carbon tetrachloride. CCl_4 is present in the atmosphere at a known concentration (88.7 pptv in 2008, AGAGE scale, Montzka et al. (2011)) and is well mixed globally. CCl_4 was used mainly in the manufacture of CFCs as refrigerants. It is still used to manufacture HCFCs, though its production has been reduced since the Montreal Protocol phase out of CFCs. Its concentration decreases by around 1.1 ppt per annum (AGAGE scale). Therefore, any atmospheric samples taken within a few months should contain approximately the same concentrations of CCl_4 within them. Despite the ban, some local sources do exist near urban centres (de Blas et al., 2013).

Figure 3.4 shows carbon tetrachloride measurements in air taken during the TORERO campaign (chapter 5). The peak area response tracks the instrument sensitivity with large jumps coinciding with tuning of the mass spectrometer. The two spikes above 7×10^5 are likely contaminated, are the result of larger anomalous sample volumes or have heightened

baselines or other integration errors and can be removed from the dataset. The CCl_4 data is then used to ratio the other analytes and compensate for instrument sensitivity drift. This is done using equations 3.1 and 3.2 where PA is the integrated area beneath a chromatogram peak and MRR is the molar response ratio– the response of the mass spectrometer per mole of analyte relative to CCl_4.

$$MMR = \frac{Analyte\ PA_{std}}{CCl_4\ PA_{std}} \times \frac{[CCl_4]_{std}}{[Analyte]_{std}} \tag{3.1}$$

$$[Analyte]_{sample} = \frac{\frac{Analyte\ PA_{sample}}{CCl_4\ PA_{sample}} \times [CCl_4]_{sample}}{MRR} \tag{3.2}$$

3.2.3.3 Medium term instrument stability

The ratio to CCl_4 takes into account rapid changes in instrument response during instances of, for example; increased sample humidity, trapping of an incomplete sample volume or incomplete sample desorption. However, instrument sensitivity and its response to individual species will change over time resulting in the response ratio to CCl_4 changing for each species differently. This can be seen in figure 3.5 where the response ratio to CCl_4 for nine VSLH species present in NOAA SX-3570 calibration standard was monitored over a two month period. Although instrument stability is remarkably good over this time period the analysis highlights the requirement for regular external calibration to complement the use of CCl_4 as an internal standard.

It is also worth noting that although these tests were carried out over an extended period of time, the instrument was not used intensively throughout only processing a few hundred samples. During a fieldwork campaign the instrument is used continuously and in the same time period will process an order of magnitude more samples.

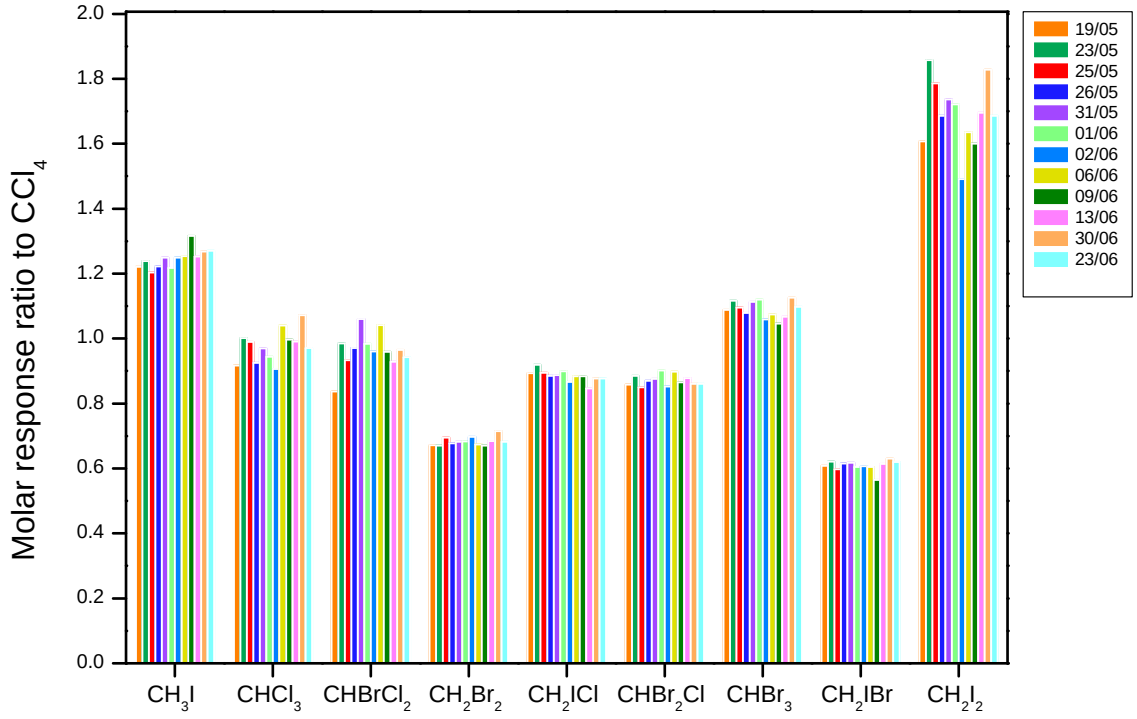

Figure 3.5 – Changes in instrument response to CCl_4 of various VSLH using NOAA SX-3570 calibration standard over a two month period

3.2.4 Maintaining sample integrity- VSLH compatible materials

Determining the suitability of different materials for use with VSLH is non-trivial and maintaining sample integrity throughout analysis is vital for accurate results. These details are often overlooked or fraught with speculation and personal opinion. In this study, materials were tested by the addition or removal of 1 m of each material from a sample flow path. They were tested for the transmission of CH_3I, $CHCl_3$, CH_2BrCl, CCl_4, CH_2Br_2, $CHBrCl_2$, CH_2ICl, CH_2IBr, CH_2Br_2Cl, $CHBr_3$ and CH_2I_2. The results are summerised in table 3.2.

None of the materials tested suffered a noticeable loss of VSLH along a short length (< 1 m). Silco-Steel is often used for VSLH analysis but is very expensive and was not found to perform any better than instrument grade stainless steel and some batches of Silco-Steel produced noisy GC baselines. Heating the lines helps prevent condensation and PTFE lines should be used where the line cannot be heated. PTFE and PEEK valves are appropriate and PTFE is a useful material for o-rings, seals and is used in the reed valve bodies of metal bellows pumps (used for air sampling see chapter 5).

Table 3.2 – Material suitability for the analysis of VSLH

Material	VSLH loss	Comments
Silco-Steel (Restek)	None	Heated > 30°C to avoid condensation, batch contamination
Instrument grade stainless steel (Restek)	None	Heated > 30°C to avoid condensation
PFA	None	Contamination peaks and raised baseline
PTFE	None	Porous to some small polar compounds
Natural PEEK	None	Tested only as a valve base material

3.3 Calibration Sources

3.3.1 Permeation Oven

Accurate calibration is possibly the most demanding aspect of VSLH measurement as atmospheric concentrations of VSLH are low–sub parts per trillion (ppt). Liquid standards can be used but often instruments are designed for air sampling and introduction of liquids is not representative. Due to the reactivity of VSLH, gas standards are often unstable and suffer concentration drift or non-linear losses onto cylinder walls or via reaction with other present species.

A permeation oven is a useful method for the dynamic production of low concentrations of VSLH in the gas phase. Each individual organic halogen, as a pure liquid standard, is filled into a permeation tube (Eco Scientific). Permeation tubes consist of combination of porous, PTFE–based polymer and stainless steel tube (figure 3.7) where the length of the steel and polymer sections can vary depending on the desired permeation rate. The longer the polymer section the greater the permeation rate. Zero grade (BOC Gases) nitrogen is passed over the tube and the pure standard evaporates into the gas phase at a steady rate.

Permeation rates are dependent upon the temperature dependant vapour pressure of the liquid standard, the proportional size ratio of steel to polymer and the flow rate of gas (figure A.1). The permeation oven setup is designed to control the rate of transfer of liquid standard into the gas phase to a constant value. This was achieved by housing

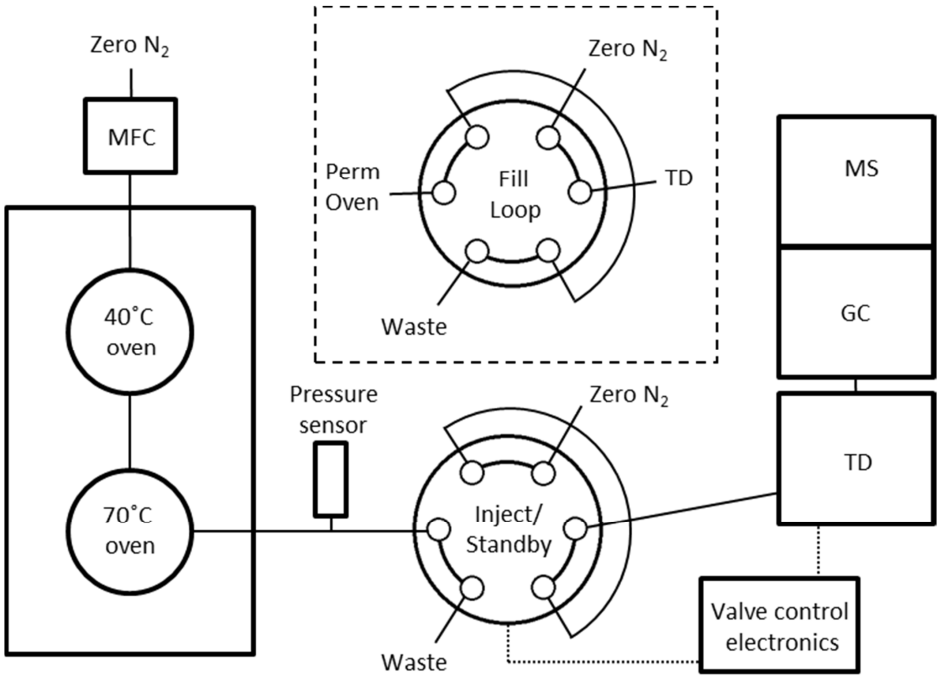

Figure 3.6 – Permeation oven schematic. Valve diagram in dashed box shows the valve actuated position to fill the sample loop. Solid lines represent gas tubing and dotted lines control electronics.

twelve permeation tubes, each containing a separate pure liquid organic halogen, between two air-tight glass containers known as permeation vessels which are housed in temperature controlled ovens (figure 3.6). One vessel, containing the more volatile species, was thermostatic at 40°C and the other, containing the less volatile species, at 70°C. Mass flow controlled N_2 was passed through each vessel in turn at 100 mL min^{-1} and flows out to waste, scrubbed by a hydrocarbon trap. The method is described in more detail in Wevill and Carpenter (2004). The system was then modified from this method as part of this body of work, to include automated introduction of one, two or three sample loops consecutively when required by the thermal desorption unit without the need for analyst supervision.

3.3.1.1 Permeation rates

This setup was maintained continuously with no interruption of N_2 supply or deviation of temperature. The permeation tubes were removed from the system every few months and weighed on a mass balance (Kern 770, accurate to 0.01 mg) to determine mass loss between weighings (for mass loss graphs see appendix figure A.1). As the permeation rate is kept constant, the mass loss over time is linear and as such a permeation rate (mol min^{-1}) can be calculated (table 3.3). Non-linearity is discussed in section 3.3.1.3.

3.3.1.2 Instrument calibration using permeation oven

The output of the permeation oven provides parts per million concentrations in the gas phase. This is much too high to be of use for calibration of atmospheric concentrations (ppt). More suitable levels were attained by loop sampling of the permeation oven output. Zero grade N_2 was passed through at 100 mL min^{-1} through a 6-port, 2-position, pneumatically actuated rotary valve (Vici Valco) and 25 μL loop. When a calibration was required the valve was switched so that the loop was in-line with the output from the permeation oven which flowed through the loop and out to waste (figure 3.6). The number of moles of analyte per loop was calculated using equations 3.3 and 3.4:

$$Moles\ per\ loop = \frac{Mass\ per\ loop\ (g)}{RMM\ (g\ mol^{-1})} \tag{3.3}$$

Table 3.3 – Mass loss rates for VSLH permeation tubes with calculated moles and ppt concentrations per 25 μL loop injection

Species	Mass loss g yr^{-1}	Moles /25 μL loop	ppt /25 μL loop
CH_3I	1.26	4.24×10^{-12}	103.8
C_2H_5I	0.36	3.67×10^{-12}	26.7
$CHCl_3$	0.92	1.09×10^{-12}	89.9
2- C_3H_7I	0.33	6.38×10^{-12}	22.6
CH_2Br_2	1.23	3.38×10^{-12}	82.6
1- C_3H_7I	0.79	6.86×10^{-13}	54.1
CH_2ClI	0.25	9.25×10^{-13}	16.8
CH_2BrI	0.27	2.21×10^{-12}	14.3
$CHBr_2Cl$	0.11	2.57×10^{-13}	6.3
$CHBr_3$	0.31	5.84×10^{-13}	14.4
CH_2I_2	0.09	5.89×10^{-13}	3.8
CCl_4	2.06	1.57×10^{-13}	155.9

$$Mass\ per\ loop = \frac{Permeation\ rate\ (g\ min^{-1})}{diluent\ flow\ rate\ (mL\ min^{-1})} \times volume\ of\ loop\ (mL) \qquad (3.4)$$

A 10 μL loop was originally used but had too small an internal diameter (I.D.) and the restriction produced a pressure drop and subsequent 'over-filling' of the loop. The 25 μL loop was the smallest possible volume loop with a wider I.D. that would fit around the valve. After a few seconds of filling, the valve was switched back and the contents of the loop swept into the nitrogen flow which was subsequently trapped with a thermal desorption unit. In total 1 L of nitrogen was used to sweep the loop resulting in a dilution of the 25 μL in 1 L. For linear calibrations, multiple loops were injected into the 1 L of N_2.

As the Permeation oven supplies a 'slug' of halocarbon rich gas from the sample loop into the nitrogen stream going to the TD cold trap, the volume of sample trapped has no effect on the concentration assuming that all the gas from the loop is swept onto the trap. The

dead volume for the entire transfer line between the permeation oven and TD is < 60 mL (1/8" tubing, 2.5 mm ID, 3 m length). Flow is set at 100 mL min^{-1} thus 1 min would allow the perm loop slug to clear the transfer line. 1 L (10 min at 100 mL min^{-1}) of the diluent nitrogen is taken to give the same conditions as sampling 1 L of air or gas standard. For the calculations 1 L is the set sample volume and it is assumed that the loop of perm gas is mixed into 1 L volume.

The number of molecules in 1 L is calculated using the ideal gas law (Equation 3.5):

$$PV = nRT \tag{3.5}$$

$$Molecules = Avogadro's\ constant\ \times \left(\frac{PV}{RT}\right) \tag{3.6}$$

It is important to note that the flow, and hence the volume, is controlled by the permeation oven mass flow controller. This gives a mass flow (100 mL min^{-1}) and this is calculated at standard temperature and pressure (1 atm, 298 K) . Therefore R = 0.08205746 L atm K^{-1} mol^{-1} (so, V = 1 L, P = 1 atm and T = 298 K) and ppt per loop in 1 L N_2 is calculated using the following equation:

$$ppt = \left(\frac{(moles \times Avagadro's\ constant)}{molecules\ in\ 1\ L}\right) \quad 1 \times 10^{12} \tag{3.7}$$

To ensure that the permeation loop was fully swept with the 1 L of nitrogen diluent, 10 replicate 25 μL loop injections were performed (Table 3.4) and proved reproducible.

3.3.1.3 Permeation oven drawbacks

There are multiple drawbacks to using the permeation oven method. The system must be kept at a constant temperature and use a constant flow of nitrogen over the tubes. If either fluctuates, the mass loss will change and the calibration will be invalid. This makes the system very difficult to transport.

Table 3.4 – Reproducibility of ten replicate 25 μL permeation loop injections

Species	PA %SD	$\frac{PA}{CCl_4}$ %SD	Error (ppt)
CH_3I	3.0	1.8	1.8
$CHCl_3$	2.5	1.6	1.4
C_2H_5I	2.6	1.5	0.4
CCl_4	1.7	n/a	n/a
CH_2Br_2	1.8	0.6	0.5
CH_2ICl	1.9	0.8	0.1
2- C_3H_7I	1.9	1.6	0.4
1- C_3H_7I	1.6	1.7	0.9
$CHBr_2Cl$	2.0	1.4	0.1
CH_2IBr	1.1	0.9	0.1
$CHBr_3$	1.3	0.5	0.1
CH_2I_2	0.9	1.3	0.1

The permeation oven must be operated over a long time period to measure a significant mass loss and calculate an accurate calibration. The concentration output of the permeation oven is quite high despite only sampling a small loop of the output gas. Calibrations with the permeation oven are carried out at higher concentrations than encountered in atmospheric samples and a linear instrument response below the dynamic range of the calibration must be assumed.

As highlighted in table 3.4, errors $< 2\%$ standard deviation can result in uncertainties $>$ 10% of actual atmospheric concentrations (sub-ppt). The concentration of the permeation output can be reduced by reducing the permeation rate but this would result in less mass loss, longer times between weighings and greater weighing error. The sample loop size cannot be reduced without causing a pressure restriction in the system. These drawbacks led to the requirement for stable gas standards to be investigated.

Another drawback with the permeation oven method is the degradation of the pure standard within the permeation tube (figure 3.7). If the composition of the liquid inside the perm tube changes the permeation rate of the specific pure compound will change. Degra-

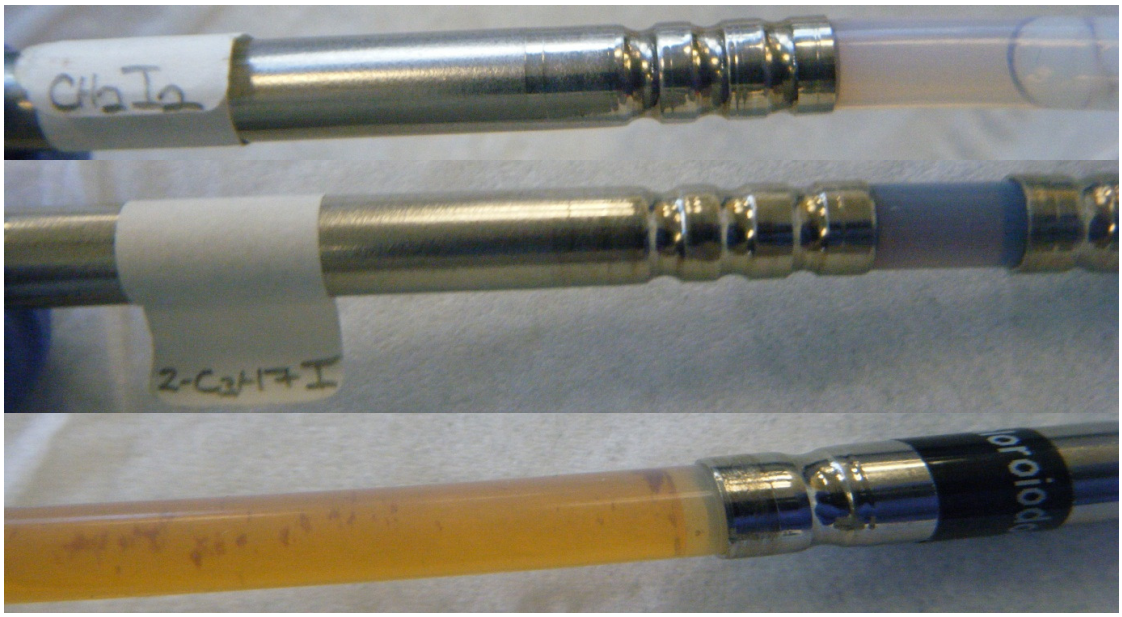

Figure 3.7 – Permeation tubes with varying permeation window lengths. From top: CH_2I_2, 2- C_3H_7I and CH_2ICl. Liquid discolouration is due to compound decomposition

dation is likely photolytic thus the tube holders are kept in the dark. Standards tend to degrade after 8 months depending upon the compound but this is difficult to track without constantly disturbing the system. A GC-MS can be used to characterise the degradation by analysing the output but this would require permeation tubes to be stored in separate ovens, each with their own flow and sample loop otherwise it is impossible to know which standard is degrading.

3.3.2 Gas standards

3.3.2.1 Cylinder material and stability

Low concentration gas standards provide the perfect method for calibrating an instrument. They can be transported easily, require no consumables and provide calibration gas instantly on demand. VSLH present a significant challenge when producing low concentration gas standards as their concentrations are often very unstable once compressed into a cylinder. In-order for a gas standard to be useful for calibration, the concentration of its contents must remain constant or, less desirably, increase or decrease at a constant

rate.

Often, humidification of a sample can help to avoid cylinder and sample line losses. In compressing a gas, its output humidity will be reduced by the reciprocal of the cylinder fill pressure in atmospheres. Stability testing of numerous cylinder materials was carried out by NOAA and electro polished stainless steel cylinders (Essex Cryogenics) were found to be the most stable for long-term storage of VSLH (figure 3.8). Stability studies of NOAA halocarbon gas in these cylinders indicate that CH_3I, CH_2Br_2 and $CHBr_3$ mixing ratios are generally relatively stable over this timescale, with drift rates of $<$ 2-5 % yr^{-1} (Butler et al., 2007, supplement).

The National Oceanic and Atmospheric Administration- Earth System Research Laboratory (NOAA- ESRL) carried out long term stability tests on six Essex canisters containing continental background mixing ratios of $CHBr_3$, CH_2Br_2, and CH_3I ($<$ 1 ppt) over a three year period (2004–2007; during the International HALocarbons in Air Comparison Experiment (IHALACE), Hall et al. (2013)). All three gases showed no significant concentration change over this time.

3.3.2.2 SX-3570 NOAA VSLH standard

In September 2009, a low concentration gas standard (SX-3570) containing both VSLH and longer-lived halocarbons in modified continental background air (from Niwot Ridge, Colorado) was prepared and analysed by the NOAA-ESRL Global Monitoring Division in Boulder, Colorado. An Essex Cryogenics electro polished stainless steel air sampling cylinder was used and spiked with very low concentrations of VSLH to generate concentrations 2–5 ppt above ambient levels. NOAA-ESRL determined VSLH mixing ratios by GC-MS (Montzka et al., 1993, 1996). Samples were analysed relative to gravimetrically-prepared standards (in Essex cylinders, Butler et al. (2007)).

As ambient air was used, some humidity was retained which is thought to reduce VSLH wall losses in the cylinder. Using ambient air mimics a real air sample matrix and consequently the standard gas contains other non-VSLH species such as hydrocarbons at atmospheric concentrations and terpenoids due to the proximity of forested areas close to the filling site. Table 3.5 lists the CFC's and VSLH present in the calibration gas and their concentration as quantified either by NOAA or from subsequent comparison with

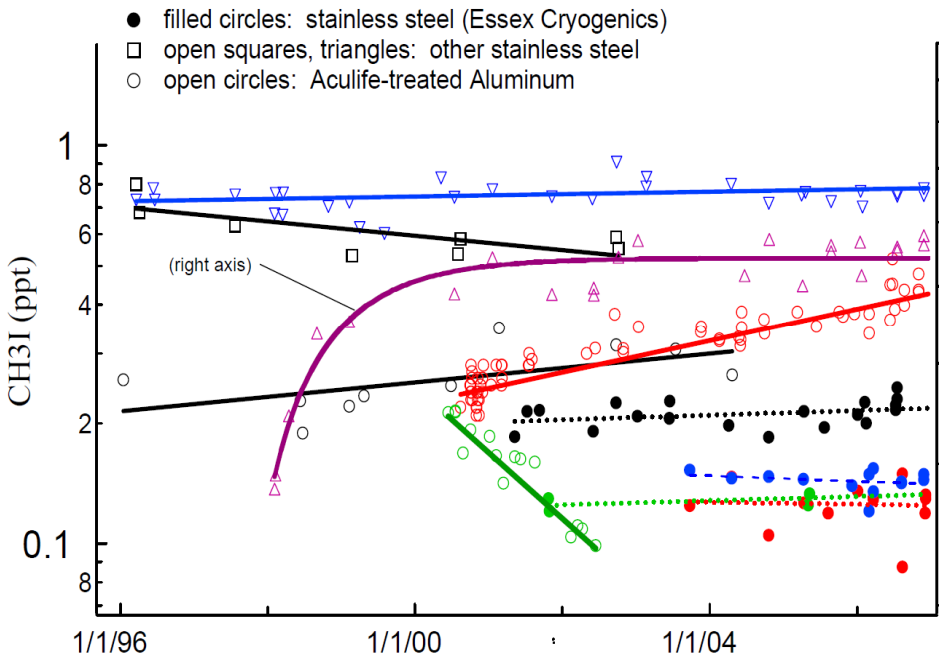

Figure 3.8 – Long-term stability testing of CH_3I in numerous cylinder materials carried out by NOAA-ESRL (Butler et al., 2010). Colours represent different cylinders

other gas standard mixtures at York University.

Table 3.5 – Composition and NOAA quoted values for gas standard SX-3570. Provisional scale is based purely on gravimetric data.

Species	Concentration (ppt)	SD (ppt)	NOAA scale
HCFC-141$_b$	20.9	0.1	1994
HCFC-142$_b$	21.1	0.1	1994
HFC-134$_a$	59.5	0.2	1995
HCFC-22	210.5	0.2	2006
CH_3Cl	575.4	0.6	2003
CH_3Br	14.8	0.1	2003
CH_3I	3.8	0.1	2004
CH_2Cl_2	34.5	0.1	2003
$CHCl_3$	8.4	0.1	2003
CH_2Br_2	2.6	0.1	2004
$CHBr_3$	5.4	0.1	2003
COS	452	2	2004
CH_2BrCl	5.8	0.1	provisional
CH_2BrI	1.4	0.1	provisional
CH_2ClI	1.3	0.1	provisional
CH_2I_2	0.8	0.1	provisional
$CHBrCl_2$	2.2	0.1	provisional
$CHBr_2Cl$	3.7	0.2	provisional

3.3.2.3 VSLH cylinder stability testing

Long-term stability of VSLH in Essex cylinders was studied by intracalibration of two NOAA calibration standards filled two years apart. A NOAA standard gas (SX-3576) was analysed 'blind' (concentrations unknown) using the Markes/Agilent system and quantified using a calibration scale from the analysis of SX-3570. The measured concentrations in SX-3576 were then compared to concentrations quoted by NOAA. The measured con-

centrations matched the quoted concentrations to within the quoted error window for the majority of VSLH species. This result confirms that the standard gas SX-3570 has been stable for two years and even difficult compounds such as CH_2I_2 have not deviated from their original concentrations (Table 3.5). The study also validates the NOAA standard production process from one standard to the next.

Table 3.6 – 'Blind' quantification of NOAA standard SX-3576 using SX-3570. Qion = mass of ion used for quantification.

Species	Qion	Measured conc. (ppt)	%SD	NOAA Quoted conc. (ppt)	%difference
CH_3I	142	2.6	1.8	2.2 (±0.1)	+18.2
$CHCl_3$	83	10.1	10.5	10.3 (±0.2)	-1.9
$CHBrCl_2$	83	3.3	4.8	3.2 (±0.1)	+3.1
CH_2Br_2	174	3.4	1.8	3.3 (±0.1)	+3.0
CH_2ClI	176	2.1	1.6	2.1 (±0.1)	0.0
$CHBr_2Cl$	129	4.6	1.7	4.4 (±0.2)	+4.5
CH_2BrI	220	2.6	3.0	2.3 (±0.1)	+13.0
$CHBr_3$	173	5.0	1.9	5.0 (±0.1)	0.0
CH_2I_2	268	0.7	4.7	0.7 (±0.1)	0.0

3.3.2.4 SilcoCan stability testing

SilcoCans (Thames Restek) are small stainless steel cylinders (2–5 L) with an internal coating designed to create an inert surface and maintain integrity of the contained gases. Exact coating materials are undisclosed but often consist of a silica based coating applied by vapour deposition. The long and short-term stability of these cylinders is important as they are used to collect Whole Air Samples (WAS) from on-board aircraft. Cylinders are filled during aircraft flights and transported back to the lab for later analysis. The stability of gases in these cylinders needs to be sufficient such that the analysis is representative of the air sample at the time of filling the cylinder.

Two SilcoCans (labelled A & B) were evacuated using an Edwards XDS5 scroll vacuum pump then filled directly from the NOAA SX-3570 cylinder to a pressure of 30 psig. Using this standard allowed for testing at concentrations close to ambient levels. They were immediately analysed alongside the SX-3570 standard to ascertain their initial concentrations. SilcoCan A showed elevated $CHCl_3$ concentrations which was likely due to cylinder contamination. The SilcoCans were then analysed periodically over the course of one month. Results showed that the SilcoCans remained remarkably stable over this time period with concentrations decreasing by as little as 0.001 ppt day^{-1} (table 3.7). The concentrations of all species remained linear and would likely continue this trend for an extended time period however a lack of volume (maximum fill pressure 40 psig) required for sampling prohibited the continuation of this study for any longer. These results validate the use SilcoCans for collection of WAS and subsequent quantification of VSLH over time periods of a few weeks.

Table 3.7 – Stability of VSLH from NOAA SX-3570 stored in SilcoCans

		SX-3570		**SilcoCan A**			**SilcoCan B**			**Silco Can**
Compound	Quatification ion	Quoted (ppt)	%SD	Initial (ppt)	Final (ppt)	%SD	Initial (ppt)	Final (ppt)	%SD	Mean Δppt d^{-1}
CH_3I	142	3.8 ($\pm$0.1)	2.4	4.14	3.95	6.2	4.14	3.86	4.2	0.006
$CHCl_3$	83	8.4 ($\pm$0.1)	5.1	10.64	10.45	6.3	8.75	8.46	5.6	0.006
$CHBrCl_2$	83	2.2 ($\pm$0.1)	5.8	2.52	2.10	3.1	2.20	2.17	3.9	0.005
CH_2Br_2	174	2.6 ($\pm$0.1)	2.0	2.73	2.49	1.5	2.61	2.43	2.1	0.005
CH_2ICl	176	1.3 ($\pm$0.1)	2.0	1.37	1.45	2.7	1.29	1.30	1.6	0.001
$CHBr_2Cl$	129	3.7 ($\pm$0.2)	1.9	3.73	3.64	1.4	3.66	3.58	2.0	0.002
CH_2IBr	220	1.4 ($\pm$0.1)	2.7	1.40	1.29	2.6	1.35	1.26	4.1	0.002
$CHBr_3$	173	5.4 ($\pm$0.1)	2.4	5.47	4.93	1.8	5.16	4.88	2.4	0.010
CH_2I_2	268	0.8 ($\pm$0.1)	6.1	0.84	0.63	6.3	0.69	0.55	7.7	0.004

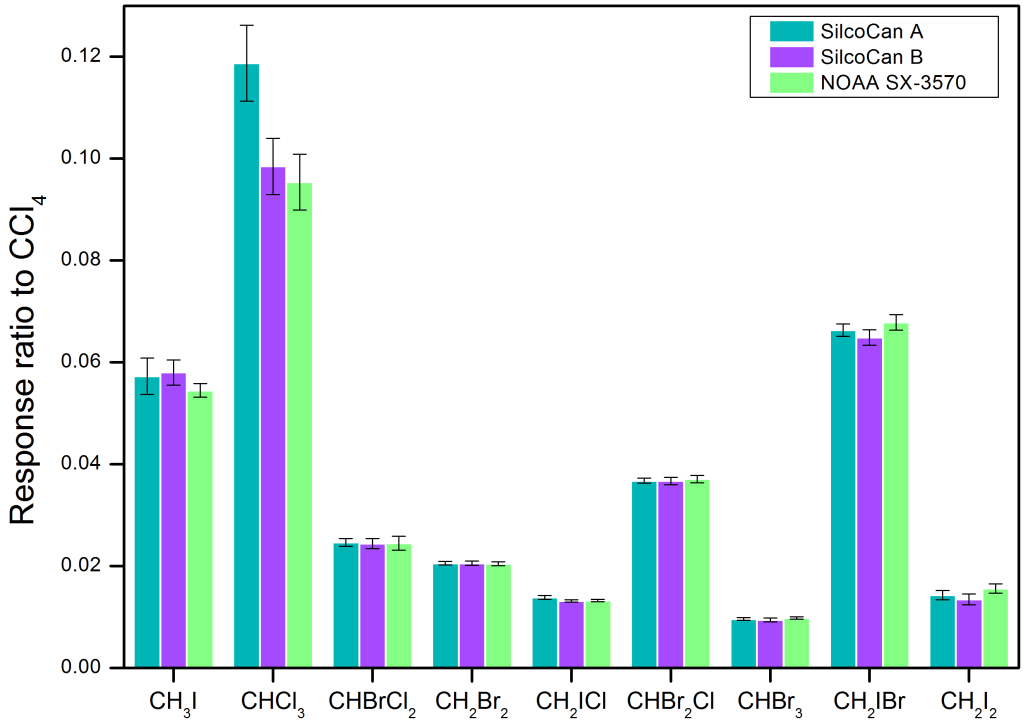

Figure 3.9 – Stability of NOAA standard SX-3570 stored in two SilcoCans over a one month period. Error bars represent the total %RSD of the 10 analyses.

3.3.3 Comparison of permeation oven with SX-3570

The output of the permeation oven was verified against the NOAA SX-3570 standard. It must be highlighted that the NOAA standard is not necessarily accurate, such that the quoted concentrations of the gas species present may not be exactly the amount present in the cylinder due to errors or losses during its manufacture. Conversely, the permeation oven may not output the exact concentrations calculated (see section 3.3.1.2). Comparing these two calibration techniques does not indicate which technique is better for the quantification of an exact amount but rather the differences between two valid calibration techniques and the magnitude of error associated with this particular analysis.

For the comparison, 10 replicates of 25 μL loops of permeation gas were analysed followed by 10 replicates of 1 L of NOAA SX-3570. 8 analytes present in SX-3570 were quantified using the permeation oven and compared to the concentrations quoted by NOAA (figure 3.8). CH_3I, $CHCl_3$, CH_2Br_2, CH_2ClI, CH_2BrI and CH_2I_2 showed good agreement with < 0.5 ppt difference. $CHBr_3$ was not in as close agreement and $CHBr_2Cl$ was four times

Table 3.8 – Comparison of the permeation oven calibration system with NOAA SX-3570

Species	Gravimetric concentration (ppt)	%SD (10 replicates)	Error (ppt)	Quoted (ppt)	%SD (10 replicates)	ppt (using Perm Cal)	Difference (ppt)
CH_3I	103.8	1.8	1.84	3.8	1.9	3.3	-0.5
$CHCl_3$	89.9	1.6	1.40	8.4	1.5	8.1	-0.3
CH_2Br_2	82.6	0.6	0.50	2.6	1.5	2.9	0.3
CH_2ICl	16.8	0.8	0.13	1.3	1.2	1.0	-0.3
$CHBr_2Cl$	6.3	1.4	0.09	3.7	1.5	13.3	9.6
CH_2IBr	14.3	0.9	0.13	1.4	2.3	1.2	-0.2
$CHBr_3$	14.4	0.5	0.08	5.4	1.1	4.3	-1.1
CH_2I_2	3.8	1.3	0.05	0.8	0.8	0.5	-0.3

greater than quoted. The difference in $CHBr_2Cl$ quantification was likely the fault of the permeation oven as the mass loss was non-linear (see appendix for all mass loss graphs) indicating some degradation of this compound in the permeation tube.

This comparison helps to validate previous measurements which utilised the permeation oven as their calibration source (Jones and Carpenter, 2005; Jones et al., 2010, 2009; Carpenter et al., 2007, 2009).

3.4 Intercalibration

3.4.1 UK intercalibration

Due to their large scale variability, VSLH global emission estimates are difficult to predict and can even vary by an order of magnitude (Montzka et al., 2011). With the possible exception of IO and BrO, there are no satellite measurements or indirect tracers for remote sensing of VSLH. Chl-a is often used to define areas of increased biological activity and hence the release of VSLH but correlation between the two is inconsistent. The drawback with collating measurements from multiple institutions is the lack of any established measurement guidelines, collective quality control or intercalibration between the data. This makes it difficult to distinguish between true environmental variation and that arising from differences in measurement and calibration techniques. As such, lack of intercalibration is currently a major limitation for accurate global emission estimates.

Due to cost and time constraints, one single institution cannot possibly obtain enough VSLH measurements to encompass the global distribution and its range of seasonal and temporal variation. Currently the only viable method for globally quantifying VSLH is to combine all of the measurements into one large dataset. This has already been achieved with the release of the HalOcAt (Halocarbons in the Oceans and Atmosphere) database (Ziska et al., 2013).

In 2010, as part of this body of work, the first national UK inter-laboratory comparison for calibrations of VSLH was carried out. The aim of this inter-calibration was to provide transparency between halocarbon calibrations from major UK research institutions, an important step towards enabling all measurements from these institutions to be treated as one coherent integrated dataset for use in global emission estimates and models.

At the time of the intercalibration the stability of some of the shorter lived species stored in Essex cylinders was unknown (now known to be stable, see section Essex cylinder intra-comparison). For this reason it was decided that CH_3I, $CHBr_3$ and CH_2Br_2 would be targeted as their stability was known and these are the most widely reported of VSLH (Butler et al. (2010)). $CHBr_3$ was calibrated based upon the NOAA-2003 scale, whilst CH_3I and CH_2Br_2 were calibrated according to the NOAA-2004 scale. The initial quantification of VSLH in SX-3570 was carried out by NOAA in September 2009. Analyses by UK research groups took place between June and November 2010.

3.4.1.1 Analysis of the intercalibration standard

The University of Bristol, University of Cambridge, Plymouth Marine Laboratory (PML), The University of East Anglia (UEA) and The University of York took part in the intercalibration. Each institution employed different methods of analysis and each used a different method of calibration (table 3.9).

Table 3.9 – Details of the different analysis techniques employed by the collaborating institutions during the intercalibration.

Institution	Calibration gas	Instrument	Pre-concentrating technique	Water removal technique	Column	Sample size	Calibration scale
University of Bristol (Mace Head)	Tertiary standard (J-128)	Medusa-MS, Agilent 6890-5973, EI-SIM-MS	HayeSep-D at -150 to -170 °C	Counter-current Nafion	CP-PoraBOND Q, 0.32 mm ID, 25 m, 5 μm film Varian (now Agilent)	2 L	Scripps secondary standard, Linde Gas Ltd primary, NIES (CH_3I).
University of Cambridge	NOAA SX-3568	μ-Dirac GC-ECD	Carboxen 1016/1001 at 15°C	Dry helium trap purge	MXT 502.2, 0.18 mm ID, 20 m, 1μm film	20 mL	NOAA 2003/2004
Plymouth Marine Laboratory (PML)	Pure liquid standards in MeOH	Agilent GC-MS 6890-5973N EI-SIM-MS, Markes Unity TD	Markes sorbent tubes, adsorbent cold trap at -10°C	Nafion	Agilent DB-VRX, 60 m, 0.32 mm ID	0.5–2.0 L	PML-Liquid standards
UEA	Internal standard-air in Aculife cylinder	Agilent 6890-magnetic sector MS (Waters AutoSpec Premier)	HayeSep-D at -78°C	$Mg(ClO_4)_2$	Agilent GS-GasPro, 30 m, 0.32 mm ID	250 mL	NOAA 2003/2004
York	Permeation oven	Agilent 6850-5975C GC-MS, EI-SIM-MS, Markes Unity 2	Multi-bed adsorbent trap-Tenax, Carbopak, Carboxen at -20°C	Counter-current Nafion	Agilent HP-5MS, 25 m, 0.25 mm ID, 0.25μm film	1–2 L	York- permeation oven

3.4.1.2 Results from the intercalibration

Because each institution used a different method of analysis and calibration, the intercalibration data is representative of a scenario where multiple datasets have been collected and collated. Bristol used their own self-prepared calibration standard (J-128) consisting of real air filled into an Essex cylinder (using a SA-6 RIX Industries compressor) during relatively clean conditions at Trinidad Head (41°N, 124°W) and measured against secondary standards at Scripps Institution of Oceanography (SIO) to check for drift before and after usage. For CH_2Br_2 and $CHBr_3$, calibrations values were assigned by comparison to a commercial gas standard (Linde Gas Ltd.) and for CH_3I, a preliminary calibration was assigned via comparison to a gas standard provided by Dr. Y. Yokouchi (National Institute for Environmental Studies, NIES, Japan). Despite having no link to the NOAA calibration scale, their analysis of $CHBr_3$ and CH_3I matched the NOAA quoted values closely. However, they were much lower in their analysis of CH_2Br_2 when compared to the other institutions and the quoted values. Bristol uses a GC-MS system called MEDUSA that is part of the AGAGE network (Miller et al., 2008). The MEDUSA system is a large, lab based system that employs a cryogenic trap for refocusing. By running calibration standards and air samples alternately, this system is able to achieve very high precision.

Cambridge employs a vastly different approach with their μ-Dirac instrument (Robinson et al., 2000). This system was designed to be launched on-board a balloon to collect atmospheric vertical profiles. As such it is extremely compact with very low power consumption. It was the only non-MS system used in this intercomparison, instead taking advantage of the size and sensitivity of an ECD (see chapter 2, section 2.3.3). Due to an ECDs sensitivity a very small, un-cooled adsorbent trap may be used to pre-concentrate just a few hundred mL of sample. An ECD is selective to electrophilic analytes but unlike an MS it only has one detector channel. Where an MS can utilise SIM to extract specific ions and de-convolute co-eluted peaks, an ECD relies solely upon chromatographic separation.

Due to power and size constraints of the GC system of Cambridge's μ-Dirac, the current GC column configuration results in incomplete separation of the CH_3I peak which displays an interfering shoulder peak. This can be seen in the intercalibration results although the quantification is still within 2σ of the NOAA quoted values. For the same reasons, the

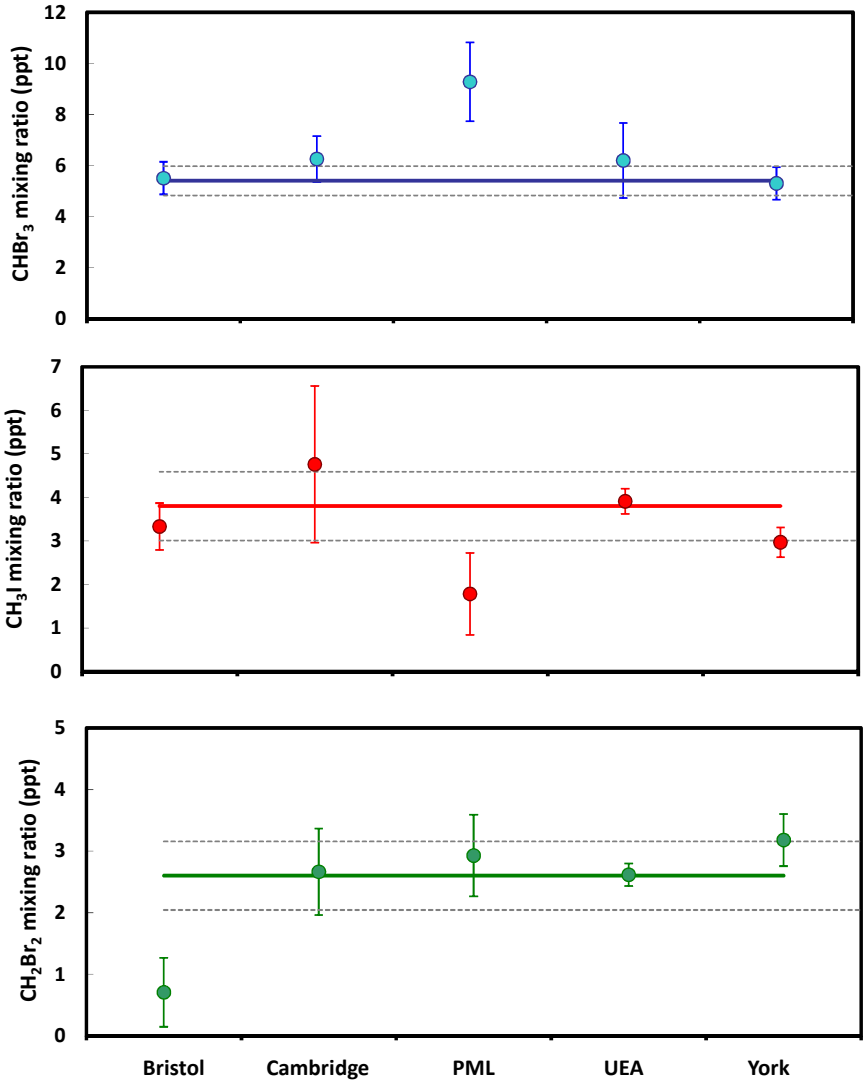

Figure 3.10 – Intercalibration results of $CHBr_3$ (blue), CH_3I (red) and CH_2Br_2 (green). Solid coloured lines correspond to the NOAA quoted concentration and dotted lines show the estimated 2 σ error in the NOAA values.

μ-Dirac system cannot resolve CH_2Br_2 from $CHBrCl_2$ and both are quoted as a combined value. The concentration of CH_2Br_2 quoted by Cambridge for this intercalibration was calculated by subtraction of the NOAA quoted $CHBrCl_2$ concentration from the total CH_2Br_2 + $CHBrCl_2$ concentration analysed. Despite this, CH_2Br_2 compared very well. This is likely due to Cambridge already using the NOAA scale for their calibration and highlights instrumental errors rather than calibration differences.

From the results of the intercalibration it would appear that Plymouth Marine Laboratorys analysis is the least comparable to the other institutions and the NOAA quoted values. However, this test was centred on the analysis of a standard gas cylinder and PML's analysis method was designed for water sampling. They did not use a gas calibration standard but instead introduced liquid standards from diluted pure compounds onto sorbent tubes that were then desorbed onto a cooled adsorbent trap prior to analysis by GC-MS. The intercalibration standard was also sampled onto a sorbent tube before analysis. This method is more suited to water analysis and it is possible that lighter compounds such as CH_3I can be lost from the sorbent tubes before analysis. With this in mind the results were surprisingly comparable with the NOAA quoted values and the use of liquid standards validates the accurate production of the NOAA standard gas. It is useful to see the differences in values obtained with different pre-concentration methods in addition to differences in separation and analysis and the participation of PML in this study increases our understanding of dataset limitations.

The University of East Anglia used a high resolution MS for their analysis. This is a large and very power heavy instrument, the opposite approach to that of Cambridge's μ-Dirac. UEA calibrated against a gas standard prepared in an aluminium aculife^{TM}(Scott Specialty Gas) cylinder filled with remote tropospheric air from Niwot Ridge near Boulder, USA which was quantified with reference to two NOAA VSLSH standards obtained from, and calibrated by, NOAA-ESRL in 2009. This links the UEA standard to the 2003 NOAA scale for $CHBr_3$ and the 2004 scale for CH_2Br_2 and CH_3I. Aculife cylinders are not always very stable over long time periods (figure 3.8) but in this case the UEA values compared well to NOAA quoted values.

Measurements at the University of York were carried out using the Perkin Elmer TD-GC-MS described in chapter 2, section 2.5.1. The permeation oven method described in section 3.3.1 was used to quantify SX-3570 as this was the calibration method used

prior to using the NOAA scale. $CHBr_3$ displayed good agreement but CH_3I and CH_2Br_2 were slightly under and over-reported, respectively. This analysis validates the use of the permeation oven and the full comparison of all species is discussed in section 3.3.3.

Another interesting observation from the intercalibration is the use of different water removal techniques (water removal techniques are covered in chapter 2 section 2.4.4.). Three different techniques are used here: Nafion, $Mg(ClO_4)_2$ and dry Helium purge. Although the NOAA standard SX-3570 is primarily ambient air, it does not contain high humidity. The data does at least show that multiple water removal techniques can be employed whilst maintaining the integrity of the quantification.

3.4.2 US intercalibration

During the TORERO campaign (chapter 5), the NOAA SX-3570 standard was intercompared with two research institutions in the US. A SilcoCan was evacuated and filled to 30 psi from SX-3570. This was then analysed against SX-3570 and compared well. The SilcoCan was used as its stability was known from the previous tests (section3.3.2.4). This was then sent to Eric Apel at NCAR (National Centre for Atmospheric Research) in Boulder Colorado. The cylinder was analysed using the TOGA GC-MS (Trace Organic Gas Analyser) regularly operated on-board the NSF/NCAR GV research aircraft (Apel et al., 2003). SX-3570 was then quantified using a variety of calibration methods (table 3.10).

The results show that the NCAR calibrations are comparable to the NOAA SX-3570 standard, if not during in-flight calibration, during later lab tests but highlight the variability of different calibration techniques. The intercalibration allowed direct comparison of TORERO data from both ship and aircraft showing the importance of intercalibration exercises. The SilcoCan was then sent to the University of Miami, Marine and Atmospheric Chemistry, RSMAS, Miami, Florida but the results of this analysis had not been received at the time of writing.

Table 3.10 – Results of an intercalibration exercise with NCAR using various calibration techniques

Species	NCAR lab (ppt)	NOAA air spike (ppt)	NOAA Gravimetric	NOAA in-flight	SX-3570
CH_3I	3.5	2.75	-	3.71	3.8 (±0.1)
CH_2Br_2	2.25	2.04	2.39	2.13	2.6 (±s0.1)
$CHBr_3$	-	5.14	5.89	4.6	5.4(±0.1)
CH_2BrCl	7.43	5.87	-	6.71	5.8(±0.2)
CH_2BrI	1.79	1.49	2.03	1.72	1.4(±0.1)
CH_2I_2	0.79	1.12	0.5	0.72	0.8 (±0.1)
$CHBr_2Cl$	-	3.53	-	1.64	3.7 (±0.2)

3.4.2.1 Ambient air intercomparison

The TOGA instrument was inter-calibrated with the York air GC-MS directly after the TORERO campaign. During the campaign the GV aircraft over-passed or flew close to the vicinity the boat on five occasions. This allowed for an intercomparison of the two instruments as they sampled roughly the same air masses. On some occasions the sampling occurred at different times and locations and the altitude was always greater for the GV but the data does allow for comparison of instrumentation and calibration during operation in ambient conditions, rather than in laboratory tests, which is invaluable. When interpreting the results from these overpasses it is worth noting that an air parcel in contact with the surface ocean can travel a significant lateral distance before it is transported vertically, even to just 100 ft. As many of the VSLH have extremely short lifetimes, the concentration at 100 ft above the ship or even downwind can be significantly different than that measured from the ship itself.

Of the five overpasses, RF13 and RF17 are the most comparable due to the low altitude at which the plane flew. RF13 intersected the cruise track around 4 hours after the ship whereas RF17 flew directly over the ship. From the data it appears that the time delay of RF13 did not contribute a significant difference in the concentrations measured. Chloroform and dibromomethane appear comparable between platforms which could be due to their relatively long local lifetimes of 149 and 123 days, respectively compared to bromo-

Table 3.11 – Comparison of measured air concentrations between the KA and GV at similar times and locations during aircraft overpasses of the ship

	RF13 - 17/02/2012		**RF15 - 22/02/2012**		**RF16 - 24/02/2012**		**RF16 - 24/02/2012**		**RF17 - 26/02/2012**	
	KA	GV	KA	GV	KA	GV	KA	GV	KA	GV
Time (GMT)	13:50	17:49	16:11	16:11	16:35	16:35	17:36	17:37	15:37	15:33
Latitude (°N)	-7.4	-7.4	2.1	2.2	6.9	6.9	7.0	7.0	5.87	5.881794
Longitude (°E)	-93.5	-93.5	-95.4	-95.3	-94.9	-95.0	-94.9	-95.0	-92.016	-91.9517
Altitude (ft)	SL*	101.0	SL	454	SL	469	SL	13692	SL	106
Compound (pptv)										
CH_3I	0.68	0.59	0.56	0.49	1.20	0.8	1.21	0.25	1.45	0.69
$CHCl_3$	5.13	4.86	8.09	7.01	9.95	8.24	10.50	4.61	9.69	8.74
CH_2BrCl	0.36	nd	0.08	0.55	0.27	0.99	0.20	0.285	0.16	1.24
CH_2Br_2	0.95	0.9	1.05	0.95	1.54	1.2	1.59	0.525	1.40	1.15
CH_2ICl	0.02	nd	<0.00	nd	0.02	nd	0.01	nd	0.02	nd
$CHBr_2Cl$	0.16	0.07	0.16	0.077	0.32	0.15	0.34	0.0515	0.25	0.09
$CHBr_3$	1.39	2.08	1.08	2.086	1.96	2.686	1.94	0.32	1.62	3.05
CH_2I_2	<0.01	nd	<0.01	nd	<0.01	nd	<0.01	nd	< 0.01	nd

*SL is abbreviated from Sea Level

forms short, 24 day photolytic lifetime. This does not explain why bromoform measured at altitude was higher than at the surface which is more likely to be an instrumental issue

3.5 Summary

The importance of accurate calibration of an instrument cannot be over-stated. For a TD-GC-MS this begins with ensuring that the sample introduction is representative by testing pre-concentration trap breakthrough. The system must be able to deal with large changes in sample humidity and analyte concentration and it should be possible to run a blank, post-sample. The reproducibility of the method must then be assessed which includes the sample pre-concentration, chromatographic method and detector response. The detector should remain linear across the dynamic range of the samples if a linear calibration response is assumed.

Once the instrument performance is well constrained, it is necessary to provide an accurate and stable calibration source which is representative of the sample. The use of a permeation oven was tested, automated and compared to compressed gas standards. A permeation oven can provide accurate calibration and remain stable for long periods of time but requires long periods to stablise before calibrations are accurate and it is difficult to produce concentrations at levels representative of VSLH atmospheric mixing ratios.

The NOAA calibration standard SX-3570 in an electropolished stainless steel cylinder (Essex Cryogenics) proved to remain stable for >3 years and provided the best calibration method for VSLH. SilcoSteel (Restek) canisters were also tested for stability and were found to be stable for all VSLH measured over a few months. This validates their use for whole air sampling (WAS) aboard aircraft. The NOAA scale was adopted in 2009 and the SX-3570 standard used for both campaigns discussed in this thesis, TROMPEX and TORERO.

Multiple UK and US institutions were intercalibrated using NOAA SX-3570 for CH_3I, CH_2Br_2 and $CHBr_3$. All institution's results agreed with much less variation than current variability in global flux estimates but would benefit from the use of a common calibration scales with the NOAA scale proposed.

Chapter 4

Halocarbons in the Tropical Atlantic Ocean

The tropical marine atmosphere is a highly important region for atmospheric chemistry as the oceans are a massive source of important trace gases and aerosols. Equatorial and tropical regions have high photochemical activity (Horowitz et al., 2003) which has implications for the production and loss of tropospheric OH radicals and ozone. VSLH are an important control on tropospheric ozone and source gas injection into the upper troposphere/lower stratosphere occurs predominantly in the tropics so the measurement of species that are able to perturb stratospheric ozone is of increased importance in this region (Bridgeman et al., 2000). The trade winds provide relatively predictable air mass trajectories and drive coastal upwelling, enhanced along the coast of Mauritania.

Data from this chapter has been published in the article:
Andrews, S. J., Jones, C. E., and Carpenter, L. J.: Aircraft measurements of very short-lived halocarbons over the tropical Atlantic Ocean, Geophysical Research Letters, 40, 10051010, 2013.

4.1 Aircraft measurements of VSLH over the tropical Atlantic Ocean

In September 2009, atmospheric mixing ratios of CH_3I, C_2H_5I, CH_2ICl, CH_2Br_2 and $CHBr_3$ were quantified from Whole Air Samples (WAS) taken aboard the FAAM BAe 146-301 atmospheric research aircraft at 144 points spanning a longitudinal range of 30°, between 30°N and 10°S at various altitudes during flights over the tropical Atlantic Ocean as part of the TRade wind Ozone Photochemistry EXperiment (TROMPEX).

It has been suggested that biologically active oceanic upwelling regions are a major localised source of VSLH emissions (Quack and Wallace, 2003) and that in tropical regions, where vertical transport times are short, this may contribute a substantial fraction of CH_2Br_2 and $CHBr_3$ to the upper troposphere/ lower stratosphere (Quack et al., 2004).

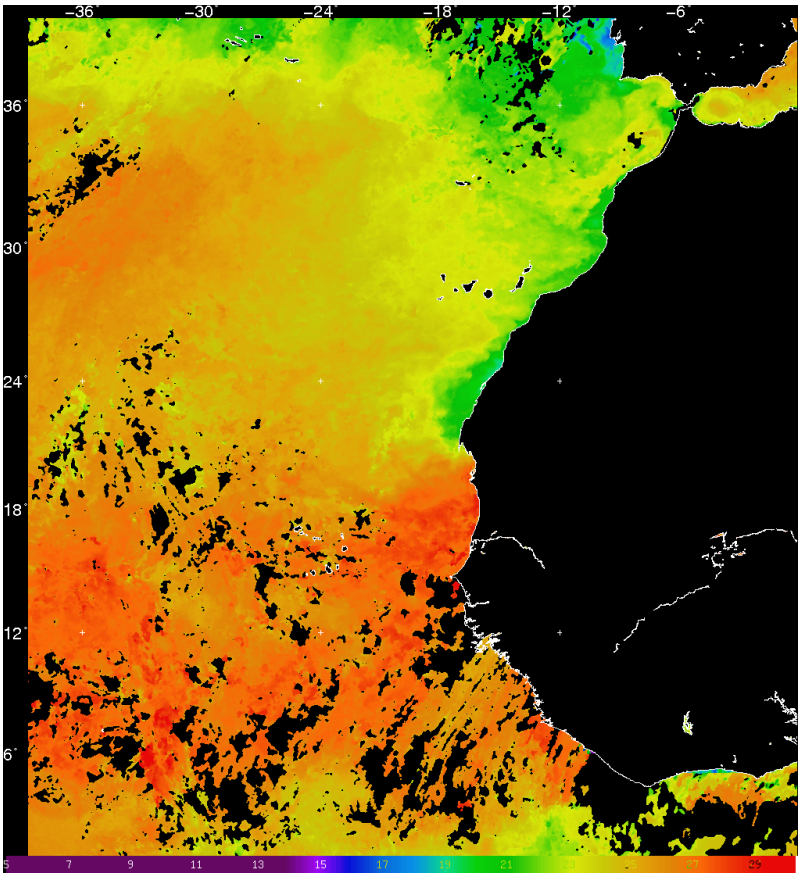

Figure 4.1 – Sea surface temperature (SST) along the African coast and east equatorial Atlantic during the TROMPEX campaign. Measured by the MODIS satellite, image courtesy of NEODAAS. Colour scale in °C.

If upwelling is a significant source of reactive bromine, controls on the production and release of brominated VSLH species in these regions would impart a subsequent control over tropospheric and possibly stratospheric ozone concentrations. Salawitch (2006) suggested that atmospheric VSLH concentrations in upwelling regions are sensitive to temperature, nutrient supply and upwelling and that future changes in climate could result in higher concentrations if the atmosphere was to warm. Increased VSLH concentrations might then lower tropospheric and stratospheric ozone levels. More recent analysis has shown that oceanic emissions of these species from the Mauritanian upwelling region cannot explain the high atmospheric concentrations observed in this region (Quack et al., 2007a; Carpenter et al., 2009; Liu et al., 2013b,a).

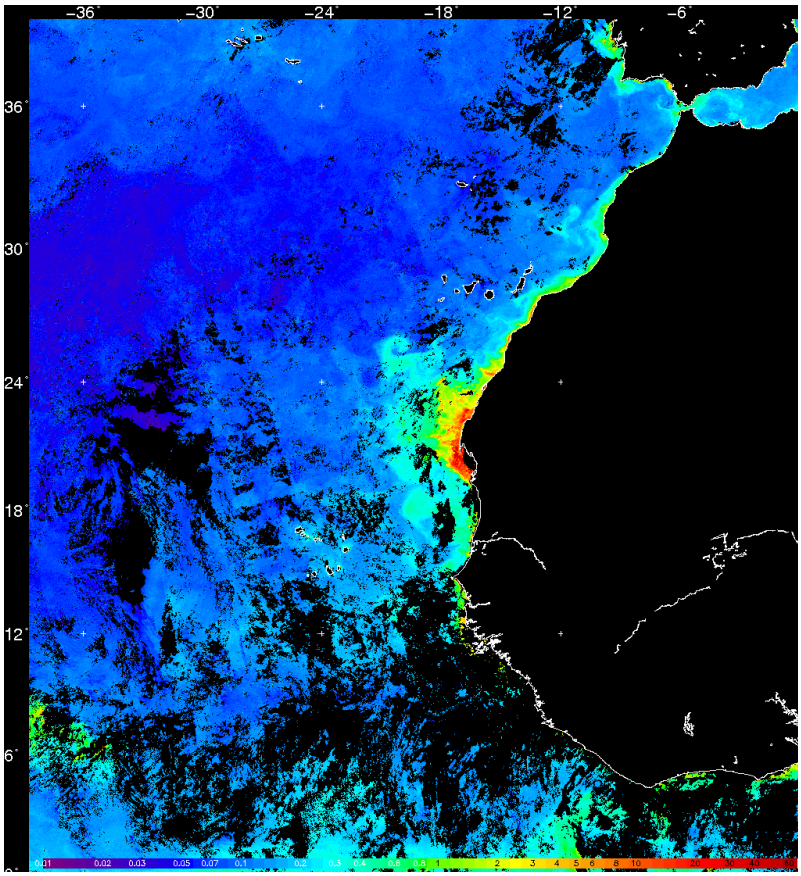

Figure 4.2 – Surface chlorophyll-a concentration along the African coast and east equatorial Atlantic during the TROMPEX campaign. Measured by the MODIS satellite, image courtesy of NEODAAS. Colour scale in mg m^{-3}.

Carpenter et al. (2009) show that east tropical Atlantic upwelling along the African coast is an enhanced VSLH source region but is likely not of major global significance due to the small geographical area of these regions which only account for about 2.5% of the

global ocean. Similarly, coastal regions provide a large VLSH flux per unit area (Carpenter et al., 2001) but only comprise around 0.1% of the ocean surface (Ryther, 1969). Emissions from high productivity regions, such as coastal upwellings, are therefore only estimated to account for around 1% of the global emission estimate (Carpenter et al., 2009).

Very recently, Ashfold et al. (2013) have modelled emissions from high productivity, coastal regions in the west tropical Pacific and extrapolated them for the entire tropics (20°N–20°S band). Their resulting emissions estimates are similar to previous studies (Ordóñez et al., 2012; Pyle et al., 2011; Liang et al., 2010; Warwick et al., 2006) and suggest that coastline emissions are no more significant than that of the rest of the ocean.

Very high air concentrations previously measured in this region could be attributed to an unknown coastal or continental source with air masses originating from the African continent. The use of an aircraft in TROMPEX gave a wide spatial coverage and allowed for a more detailed investigation of air mass origins and their link to VSLH concentrations. At the time of publication of the TROMPEX results there were no aircraft measurements of very short-lived iodocarbons, excluding CH_3I, from an aircraft. These measurements are vital to constrain any contribution of CH_2ICl to O_3 loss occurring above the MBL.

4.1.1 Methodology

TROMPEX was the first analysis VSLH in air samples, taken from an aircraft, performed at the University of York. This involved slight adaptation of the instrumentation (section 4.1.1.2) and verification of sample integrity (section 3.3.2.3).

4.1.1.1 BAE-146

The BAE-146 is a large research aircraft operated by FAAM (Facility for Airborne Atmospheric Measurements). It carries a payload of core scientific instrumentation but can also be fitted with instruments specific to certain roles. For this work the aircraft was fitted out for Whole Air Sample (WAS) collection.

Figure 4.3 – FAAM BAE-146 large research aircraft

Core instruments used to complement the WAS samples included carbon monoxide concentration using an Aerolaser 5002 fast fluorescence CO analyser and O_3 concentration using a Thermo Scientific TE49C UV photometric O_3 analyser.

4.1.1.2 Whole Air Sampling (WAS) samples

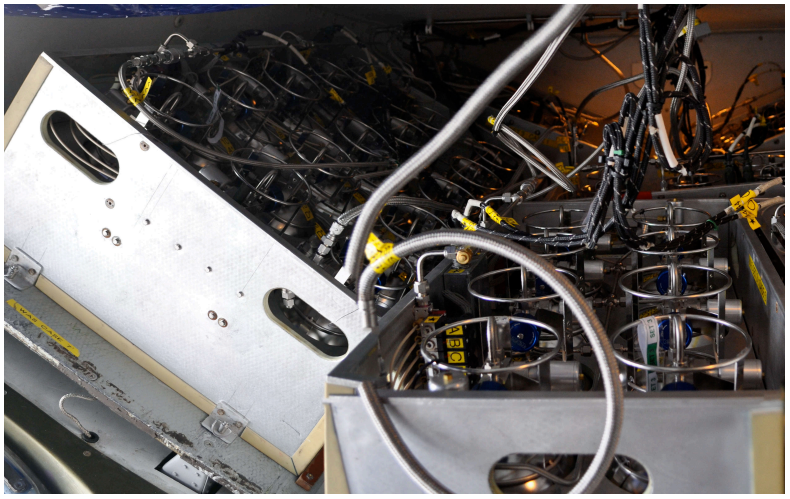

Figure 4.4 – WAS cylinders loaded in the hold of the FAAM BAE-146 ready for automated filling during flight.

WAS samples are discrete samples of air collected in 3 L SilcoCan cylinders (Thames Restek) during a flight. Air was drawn in through a forward facing air sampling pipe on the exterior of the aircraft and pressurised into the canisters using a metal bellows pump (Senior Aerospace) to approximately 3 bar. The aircraft can be fitted with 64 canisters per flight and 3 sets of 64 canisters were available. The WAS cylinders were housed in cases of

8, 9 or 15 with all cylinders in each case connected to a common manifold. Cylinders are opened to the manifold via a pneumatically operated 2-way valve (Swagelok). The valves are all fed from a compressed airline connection on the case and individually actuated using solenoid valves. After being filled aboard the aircraft they are taken back to the lab to be analysed. In order to fully automate the sampling of the WAS cylinders by the TD-GC-MS, a custom built control unit named La Vespa was used. This Labview software based device takes a signal from the thermal desorption unit and starts a timer. The WAS cylinders are opened before the TD unit starts collecting a sample in order to pre-purge the lines and remain open for the sampling duration. The cylinders are automatically closed post-sampling. The La Vespa software opens each cylinder consecutively until all cylinders are sampled. Up to two cases can be run at any one time.

4.2 Experimental

Sampling was carried out onboard the FAAM BAe 146-301 research aircraft in the boundary layer and lower free troposphere between the Canary Islands, the island of Sao Vicente in the Cape Verde archipelago, and the Mauritanian upwelling, from the 7–9^{th} September 2009 (fights B475–B479). The position of the upwelling was identified during the flight as corresponding to a 1–2°C drop in sea surface temperature (SST) measured from a downward facing (Heimann KT 19.82) radiometer mounted to the exterior of the aircraft, later confirmed from MODIS chlorophyll-a averaged data for the week of the flight (7^{th}–14^{th} September 2009) (figure 4.2). The algal bloom size appears slightly smaller relative to previous campaigns in this area (Carpenter et al., 2009; Quack et al., 2007a).

Air samples were collected at an average frequency of 1 min^{-1}, pressurised into evacuated 3 L Silco Steel® (Restek Corporation) cylinders at 2–3.25 bar using a metal bellows pump (Senior Aerospace). Samples were analysed at the University of York within two weeks of being collected. Analysis was carried out using a Perkin Elmer AutosystemXL gas chromatograph coupled to a Perkin Elmer Turbomass mass selective detector with an electron ionization source and operating in single ion mode (SIM). The Perkin Elmer TDU was used and equipped with the on-line air sampling accessory. This allowed for gas phase samples to be introduced directly onto the Peltier- cooled absorbent trap.

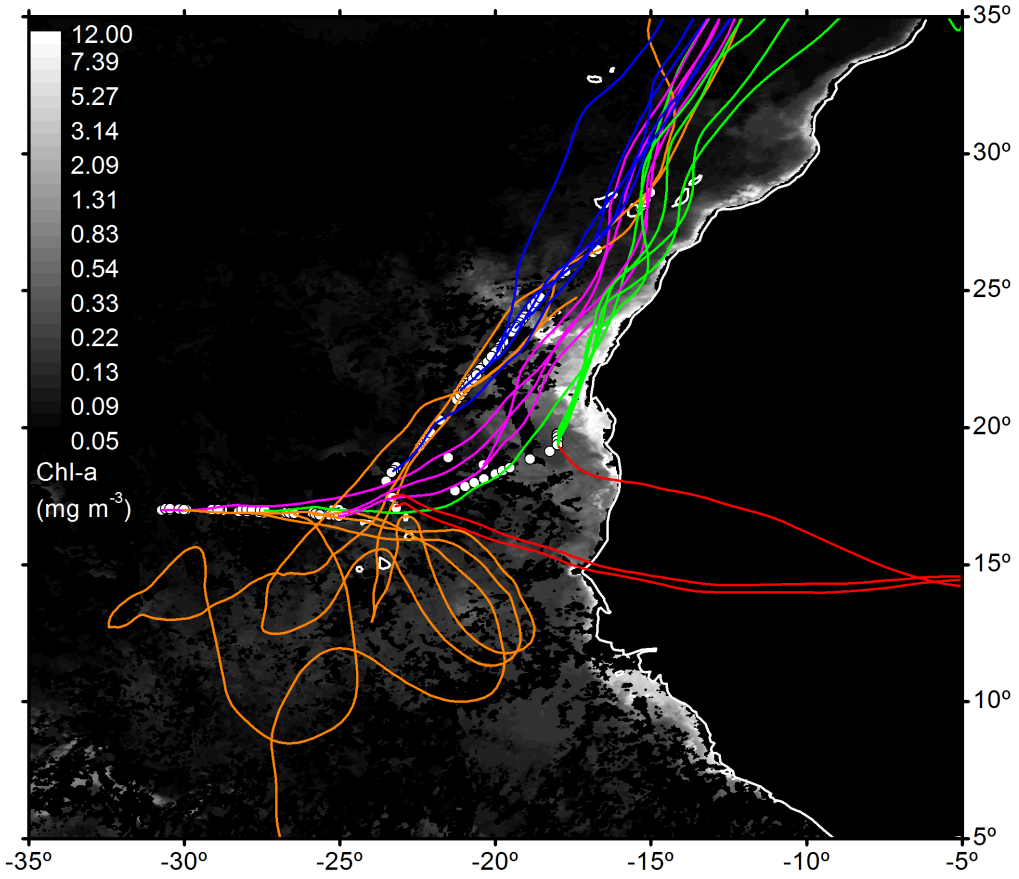

Figure 4.5 – NOAA Hysplit backtrajectories along flight track overlaid onto Chl-a MODIS February 2009 average (NASA, Giovanni). White circles represent air sampling points. Colours represent air mass origin categories, blue: trade wind trajectories, pink: trade wind, moderate upwelling influence, green: trade wind, strong upwelling influence, red: African, terrestrial origin, orange: southerly (hurricane) air.

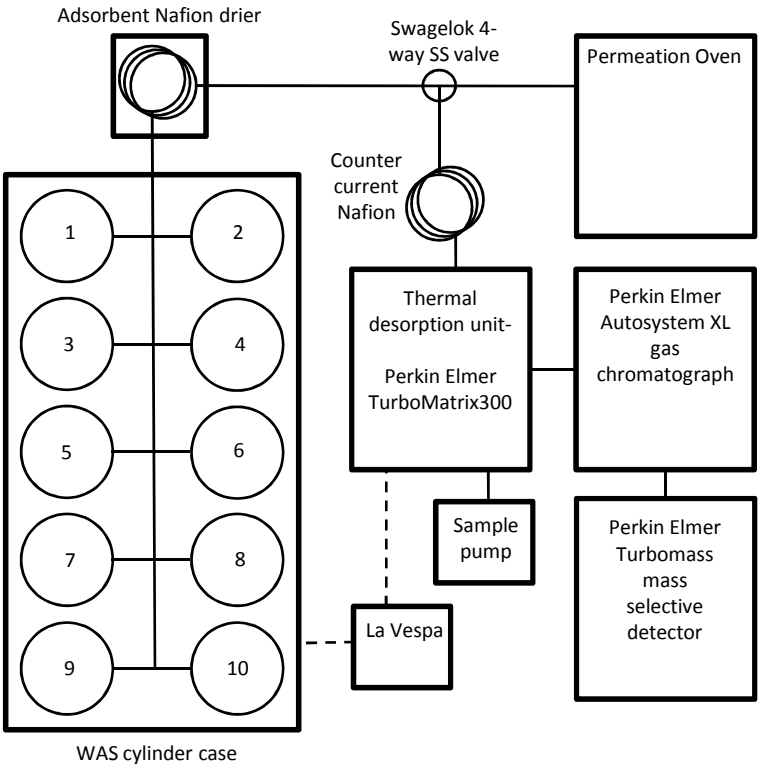

Figure 4.6 – Schematic of the instrument used for the analysis of WAS cylinders during the TROMPEX campaign. Solid lines represent gas lines and dashes represent electrical connections.

3 L of each sample was passed through an ME^{TM}-series Nafion® moisture exchanger and a counterflow MD^{TM}-series Nafion® gas drier (Permapure^{TM}) prior to pre-concentration of volatile components on a Peltier cooled (-30°C) adsorbent trap (Perkin Elmer TurboMatrix300). Analytes were thermally desorbed at 300°C, and separated using a CP-PoraBOND Q column (0.32 mm ID, 25 m, 5 μm, Varian Chrompack). CH_3I was quantified using the CH_3I^+ ion (*m/z* 142) with I^+ (*m/z* 127) as a qualifier ion. C_2H_5I, CH_2ICl, $CHBr_2Cl$, CH_2Br_2 and $CHBr_3$ responses were measured using *m/z* 156/127, 176/178, 129/127, 174/176 and 173/171 as quantification/qualification ions, respectively.

VSLH were calibrated according to the NOAA (National Oceanic and Atmospheric Administration) 2003/2004 scale (excluding C_2H_5I) using gas standard SX-3570 (created 2009). Because this standard was not available during the TROMPEX analysis period, calibration was performed using a permeation oven system (Wevill and Carpenter, 2004) used routinely in the laboratory to provide parts per trillion (ppt) gas phase halocarbon

mixtures from dynamic dilution of each pure compound with a N_2 flow over the permeation tubes (Eco Scientific). Comparison of the permeation oven system to the NOAA standard in November 2009 provided the necessary data to adopt the NOAA scale for this dataset (excluding C_2H_5I). The agreement between these scales ranged from 2–22% (Jones et al. (2011), chapter 3 section 3.3.3).

The SX-3570 standard consists of 18 halogenated species at parts per trillion concentrations in a 35 L electropolished air sampling cylinder (Essex Cryogenics). The concentration of CH_3I, CH_2Br_2, and $CHBr_3$ in the gas standard is known to be stable and scale relationships are available publicly (http://www.esrl.noaa.gov/gmd/hats/standard/scales.html). CH_2ICl and $CHBr_2Cl$ concentrations are based on a preliminary scale with the stability in the Essex cylinder unknown. The stability of the standard SX-3570 was tested by intra-comparison with an equivalent NOAA standard- SX-3576 created in 2011 (chapter 3, section 3.3.2.3). The cylinder SX-3576 was analysed 'blind' and quantified using SX-3570. The concentrations measured in SX-3576 matched the concentrations quoted by NOAA to within 8% for the maximum deviation CH_3I, showing good stability for all compounds.

4.3 Results and Discussion

4.3.1 Air Mass Origins

NOAA HYSPLIT (HYbrid Single Particle Lagrangian Integrated Trajectory model) 3-day back trajectories were calculated for the time and location of each data point in order to establish the origin of the air parcel at each specific latitude, longitude and altitude where samples were collected. The data was then categorised according to five distinct air mass origins (figure 4.5).

The majority of the air masses followed the expected northeasterly trade winds and travelled parallel to the African coastline, without any contribution from continental air. A few of the air masses arriving at high altitude originated from over Africa; moderate levels of CO (77–83 ppb) and O_3 (23–25 ppb) in these air masses indicated they were not strongly influenced by anthropogenic or biomass burning sources. VSLH levels in these air masses were not depleted, and in some cases were enhanced, relative to those in open ocean trajectories suggesting either a terrestrial source or strong coastal input (figure 4.7). High O_3 (Blue +, figure 4.7. E) was observed in open ocean trajectories over the Canaries which will have significant European influence (figure 4.5).

The presence of hurricane Fred, south of flight B477 (09/09/2009) which travelled west from Cape Verde islands at 17°N, produced unusual, southerly trajectories which looped around and were possibly influenced by the southern hemisphere African continent. This is supported by the unusual CO and O_3 concentrations for these trajectories (figure 4.7. E, F) which displayed relatively low O_3 characteristic of southern hemisphere air masses but also enhanced CO which may be attributable to African biomass burning. O_3 concentrations are noticeably higher over the upwelling region, this could be attributed to the emission of NO_x from shipping close to the coast of Mauritania.

4.3.2 Iodocarbons

Average VSLH mixing ratios measured during TROMPEX are shown in table 4.1. CH_2I_2 was not detected in any of the canister samples, likely due to its rapid photolysis (<5 min (Montzka et al., 2011)) resulting in levels below the limit of detection at the altitudes

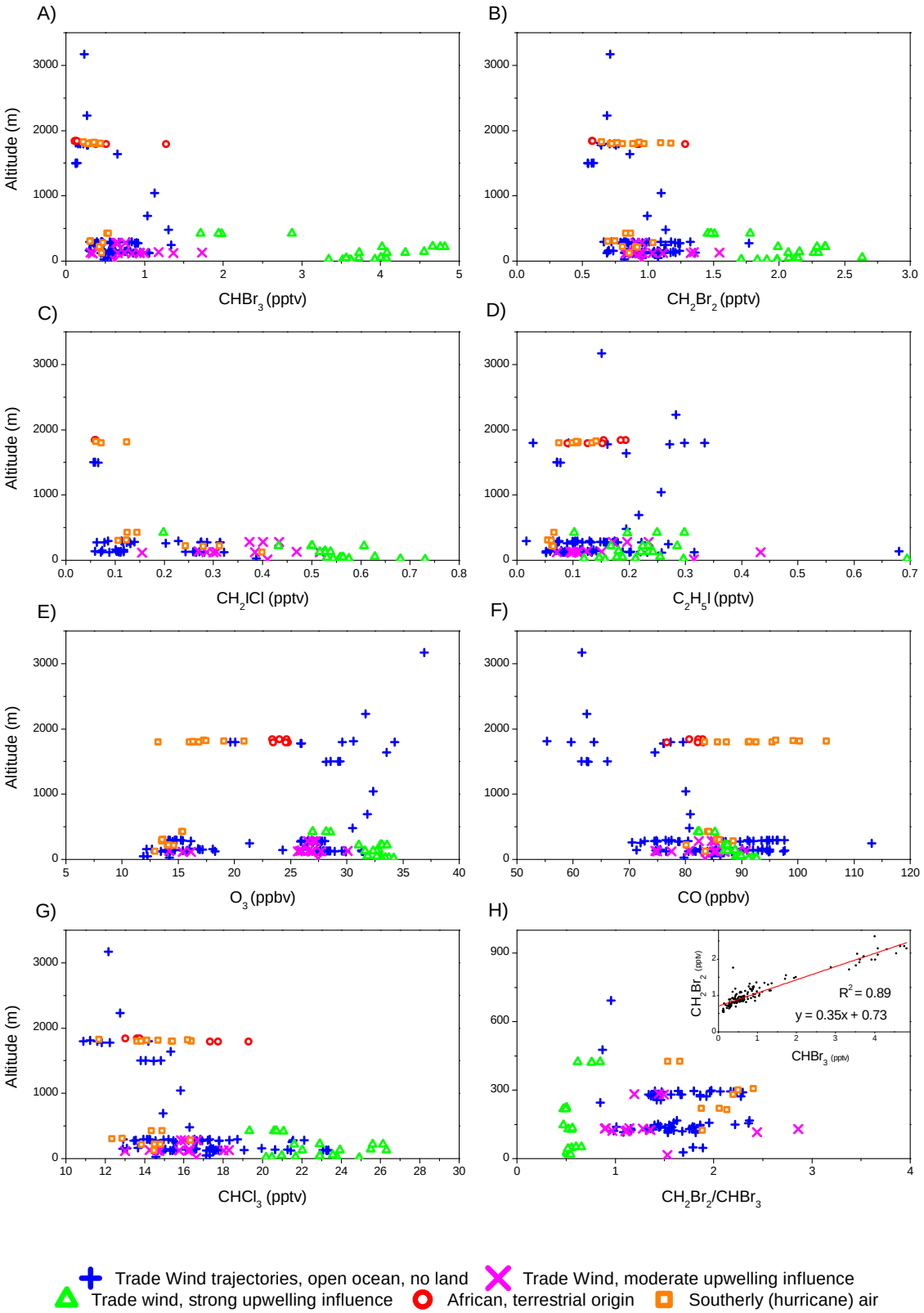

Figure 4.7 – Vertical profiles of measured VSLH, CO and O_3 categorised into separate air mass origins. H. inset shows $CH_2Br_2/CHBr_3$ ratio with open blue circles representing free tropospheric samples.

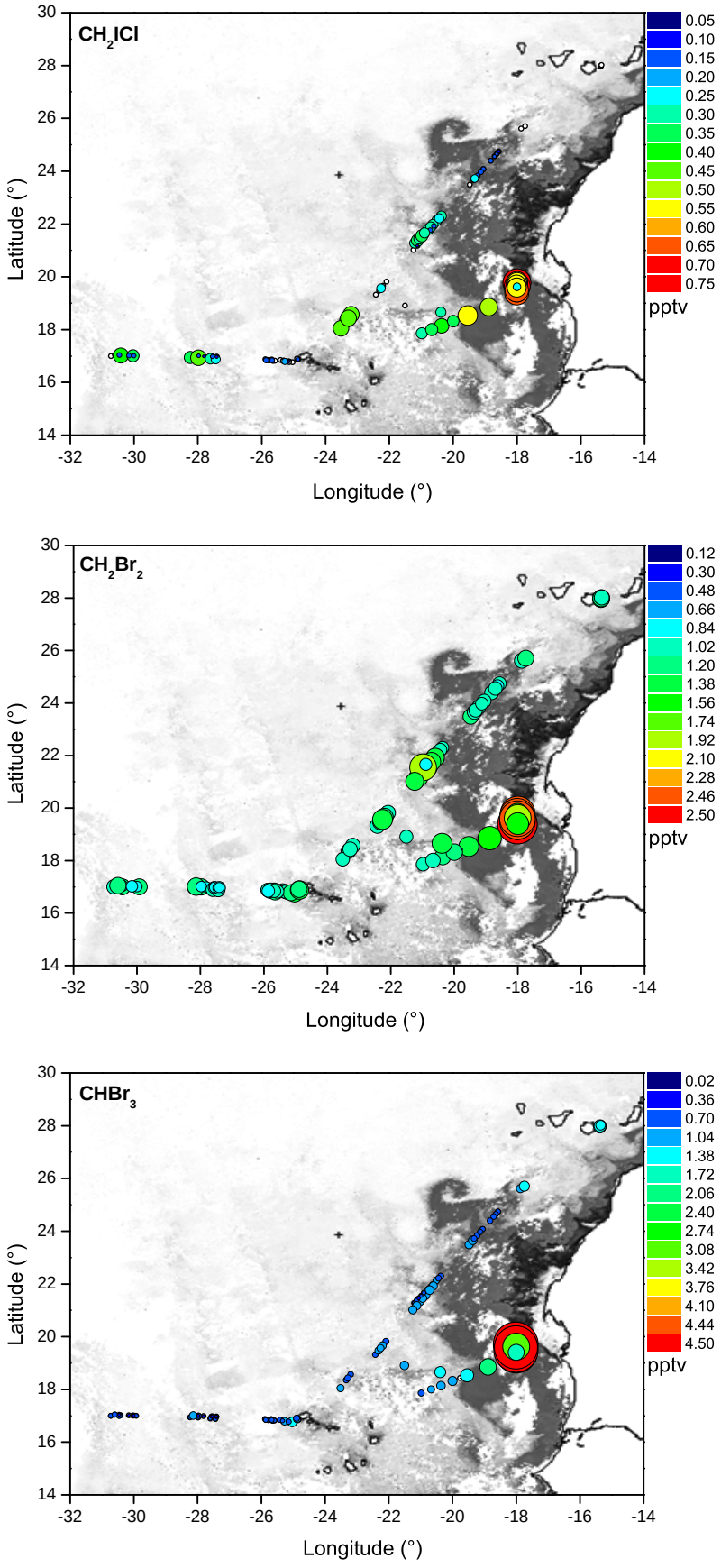

Figure 4.8 – Continued over...

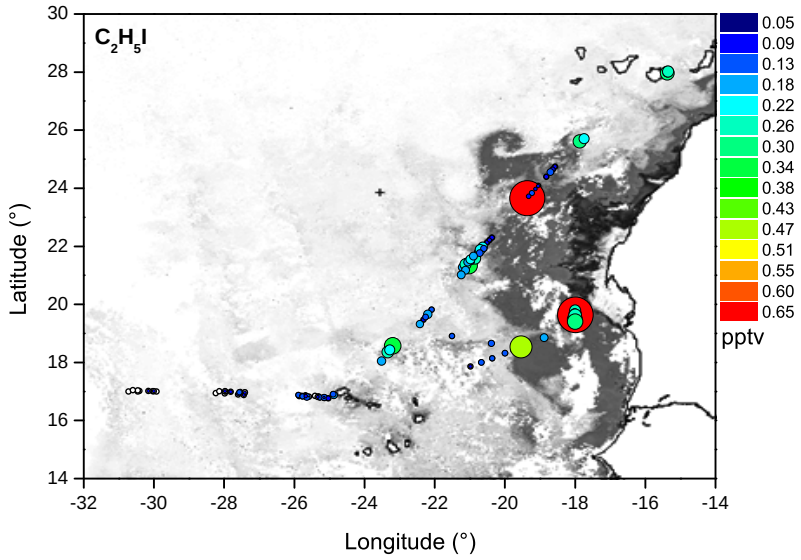

Figure 4.8 – MBL concentrations of CH_2ICl, C_2H_5I, $CHBr_3$ and C_2H_5I scaled by size and colour, overlaid onto a grey-scaled chlorophyll-a image (MODIS) showing the Mauritanian upwelling region.

sampled. The mean MBL mixing ratio of CH_2ICl of 0.27 pptv agrees well with springtime measurements in the western north Pacific of 0.27 pptv (Kurihara et al., 2010) and previous measurements made in the Mauritanian upwelling region of 0.24 pptv in the summer of 2007 (Jones et al., 2010). The mean mixing ratio however, is skewed by the presence of the upwelling and by changes in altitude.

Outside of the upwelling region, the average MBL background level was between 0.1–0.2 pptv (Figure 4.8) which is more consistent with coastal measurements of 0.11 pptv at Mace Head, Ireland (Carpenter et al., 1999, 2000), 0.1 pptv at Christmas Island (Varner et al., 2008) and with long term measurements at Hateruma Island (East of Taiwan, 24° 3'N 123°48'E) and Cape Ochiishi (Oshiishinishi, Nemino, Hokkaido 43° 9'N 145°30'E) of 0.12 pptv and 0.18 pptv, respectively (Yokouchi et al., 2011).

To our knowledge these are the first airborne measurements of CH_2ICl reported to date. Due to its short atmospheric photodissociation lifetime of ≈ 2 hours (Rattigan et al., 1997) mixing ratios of CH_2ICl at altitudes >MBL (≈ 500 m) were very low (< 0.02 pptv). This suggests that the majority of CH_2ICl is photolysed below 500 m, releasing iodine atoms into the boundary layer. Figure 4.8 shows that mixing ratios of CH_2ICl in the MBL (defined as 500 m above mean sea level in this region shown by NOAA Hysplit analysis)

were elevated above background over the open-ocean as well as over the Mauritanian upwelling, a known source region (Jones et al., 2010).

Concentrations were higher in the morning than in the afternoon presumably due to rapid photolysis of CH_2ICl; this was also apparent in the two flights between the Canaries and Cape Verde Islands (Figure 4.9, Top). Back trajectory analyses (Figure 4.5) showed that the open ocean regions with elevated CH_2ICl corresponded to trade wind and hurricane influenced air masses of marine origin. These air masses had not been influenced by any coastal or upwelling regions for at least 24 hours, which is more than ten times the photolytic lifetime of CH_2ICl. CH_2ICl can be produced directly from phytoplankton or indirectly from the photolysis of CH_2I_2 in surface seawater (Martino et al., 2005; Jones and Carpenter, 2005). The observations suggest an open ocean, possibly phytoplankton derived source of either CH_2ICl, its precursor CH_2I_2, or both. Moore and Tokarczyk (1993) observed enhanced seawater concentrations of CH_2ICl at open ocean sites compared to coastal regions and suggest a plankton source due to maxima in near-surface water (top 200 m).

During the open ocean flights between the Canaries (25°N) and Cape Verde Islands (17°N), a latitudinal dependence of CH_2ICl and C_2H_5I was observed with their concentrations doubling and quadrupling, respectively. The mixing ratio increased with decreasing latitude between these latitudes and broadly corresponded to changes in sea surface temperature (figure 4.9). CH_2ICl fluxes measured during the RHaMBLe (Reactive Halogens in the Marine Boundary Layer) campaign conducted in the same geographical region between the Canaries and Cape Verde Islands in summer 2007 (figure 4.9, bottom, Jones et al. (2010)) showed a similar pattern, thus it can be suggested that the latitudinal dependence of MBL iodinated VSLH may be driven by temperature or photochemically driven processes in the surface ocean.

CH_3I was measured in all of the samples but due to problems with the calibration at the time of analysis, the concentrations could not be quantified. The trend in the CH_3I data was very similar to CH_2Br_2 and $CHBr_3$ (Section 4.3.3) with concentrations increasing over the upwelling region. CH_3I concentrations also increased with decreasing latitude, similarly to CH_2ICl, although did not show elevated amounts over the open ocean.

The mean C_2H_5I mixing ratio was 0.13 pptv, in agreement with measurements from

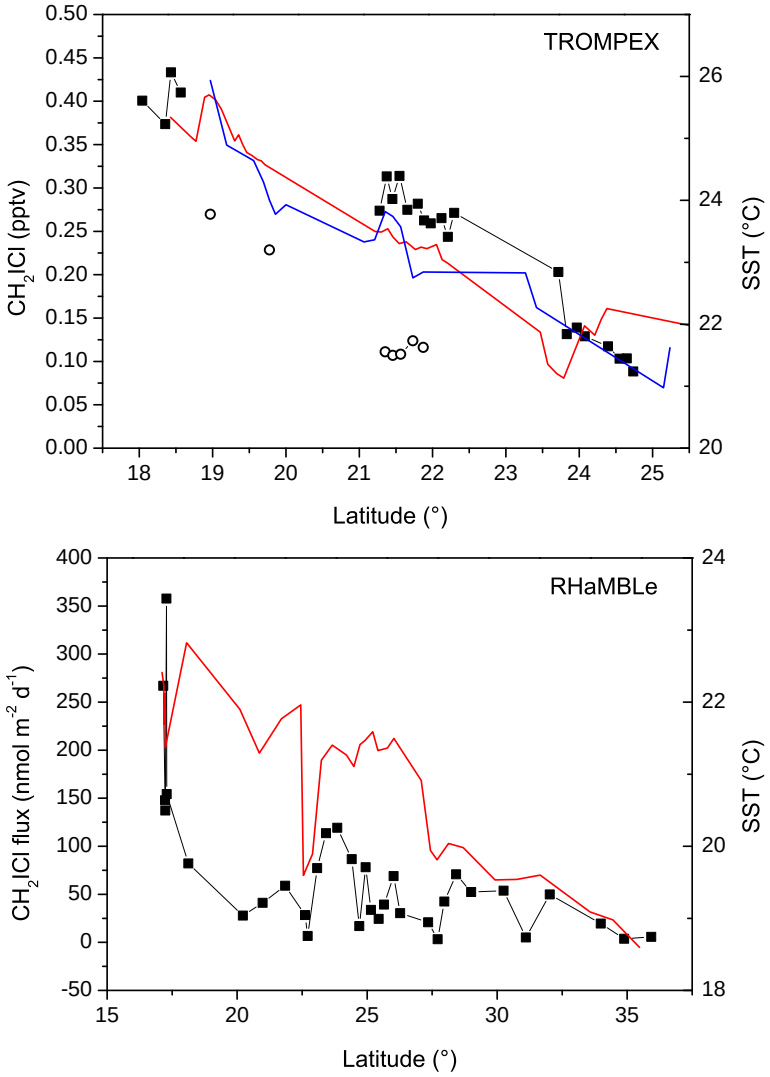

Figure 4.9 – Top: CH_2ICl concentrations measured during TROMPEX. Black squares are flight B476 from Canaries to Cape Verde Islands (07:16–10:00 08/09/09) and open circles are flight B478 returning to the Canary Islands two days later (15:16–17:30 10/09/09). Red and blue lines are the sea surface temperatures (SST) measured during each flight respectively. Bottom: Black squares denote CH_2ICl fluxes measured during the RHaMBLe cruise (Jones et al., 2010). Red line denotes measured SST.

Table 4.1 – Overview of measured VSLH concentrations

	Mixing Ratio (pptv)			
Species	MBL	MBL Open Ocean	Upwelling[a]	Free Troposphere
$CHCl_3$	17.8 (11.8–32.7)	15.1 (11.7–20.0)	23.3 (20.2–26.3)	14.2 (10.9–19.3)
C_2H_5I[b]	0.1 (nd–0.7)	0.05 (nd–0.14)	0.2 (0.1–0.7)	0.1 (nd–0.3)
CH_2ICl	0.3 (nd–0.7)	0.2 (nd–0.4)	0.6 (0.4–0.7)	0.1 (nd–0.1)
CH_2Br_2	1.1 (0.1–2.6)	0.9 (0.6–1.2)	2.1 (1.7–2.6)	0.8 (0.5–1.3)
$CHBr_3$	1.2 (0.1–4.8)	0.5 (0.2–1.1)	4.0 (3.4–4.8)	0.3 (0.1–1.3)

[a] Upwelling defined as average concentration directly above upwelling area. Filtered positionally using Modis Chl-a and GPS.

[b] C_2H_5I not on NOAA scale, permeation oven method used.

Hateruma Island (0.15 pptv) and Cape Ochiishi (0.08 pptv, Yokouchi et al. (2011)), Asian seas (0.09 pptv, Yokouchi et al. (1997)) and at Mace Head (0.06 pptv, Carpenter et al. (1999)).

4.3.3 Bromocarbons

$CHBr_3$ and CH_2Br_2 both showed distinct upwelling influence (figure 4.7.A, B) with $CHBr_3$ concentrations increasing to 3–5 pptv, more than three fold higher than the mean background MBL $CHBr_3$ concentration in that area. Bromocarbon levels in the southerly air masses were similar to, although at the low end, of those in northern hemisphere open ocean air. CH_2Br_2 concentrations were strongly correlated to those of $CHBr_3$ ($R^2 = 0.89$) throughout the flights (figure 4.7.H (inset)).

The injection of fresh emissions from the upwelling into the free troposphere is indicated in figure 4.7.H which shows $CH_2Br_2/CHBr_3$ ratios grouped by air mass origin. CH_2Br_2 has an atmospheric lifetime of 124 days and is primarily removed via reaction with OH (Montzka et al., 2011). $CHBr_3$ is photolysed within 24 days therefore an increasing $CH_2Br_2/CHBr_3$ ratio suggests ageing of the air mass, if the emissions are co-located and the emission ratio

remains constant. The southerly and African air masses, plus some trade wind trajectories from Europe contain relatively aged emissions.

The mean mixing ratios of CH_2Br_2 and $CHBr_3$ of 1.01 pptv and 1.08 pptv are within the range of previous, ship based measurements in the area. Higher mean mixing ratios of 2.4 pptv for CH_2Br_2 and 6.2 pptv for $CHBr_3$ (Quack et al., 2007a) were observed in spring 2005 and lower mean mixing ratios of 0.4 pptv for CH_2Br_2 and 1.1 pptv for $CHBr_3$ (Carpenter et al., 2009) during summer 2007. Over the open ocean $CHBr_3$ surface concentrations are generally higher than CH_2Br_2 (Butler et al., 2007; Kurihara et al., 2010). However, throughout the flights, background levels of CH_2Br_2 were generally higher than $CHBr_3$. This can be explained by considering the altitude at which the TROMPEX samples were taken (500–3000m) and from the shorter lifetime of $CHBr_3$ compared to CH_2Br_2 indicating an aged background air mass. Unlike the iodocarbons, the brominated species did not show a clear latitudinal dependence .

4.4 Summary

The Mauritanian upwelling was confirmed as a significant regional source of $CHBr_3$, CH_2Br_2, $CHCl_3$, C_2H_5I and CH_2ICl to the MBL. However, mixing ratios over the upwelling were similar to if not slightly lower than observed in coastal regions (e.g. Carpenter et al. (1999); Quack and Wallace (2003)) which cover a much larger total surface area, implying that coastal upwelling systems in themselves are not strong global sources of VSLH (Carpenter et al., 2009).

Ratios of $CH_2Br_2/CHBr_3$ revealed distinct clusters of data which correspond to different air mass origins, with the lowest ratios corresponding to fresh emission from the upwelling region. The ubiquitous presence of CH_2ICl over the open ocean shows that it must have an open ocean source. Although concentrations measured were very low, CH_2ICl has an extremely short lifetime and is an important source of reactive iodine to the MBL (Jones et al., 2010).

Concentrations of all measured halocarbons were elevated with increasing proximity to the oceanic upwelling observed along the coast of Mauritania. The collected data provided distinct, vertical profiles highlighting the rapid, photolytic degradation of these compounds

within the tropical troposphere, with the shortest lived halocarbon concentrations reduced by 50% within the boundary layer. Iodocarbons showed a latitudinal dependence with concentrations increasing with decreasing latitude similarly to SST, in line with previous flux measurements of CH_2ICl in the same region. Greater iodocarbon emissions would result in an overall increase in tropospheric ozone destruction towards the equator.

Chapter 5

VSLH in the tropical Pacific Ocean

This chapter discusses results from the TORERO campaign (Tropical Ocean tRoposphere Exchange of Reactive halogen species and Oxygenated VOC) in the East Tropical Pacific (ETP). This was a large, multi-platform campaign involving measurements aboard the NOAA ship *Kaimimoana, R/V Hakuho-Maru* and the NSF/NCAR Gulfstream V aircraft. The *R/V Hakuho-Maru* was part of a study called EqPOS (Equatorial Pacific Ocean and stratospheric/tropospheric atmosphere Study) but the complementary measurements were incorporated into TORERO.

The scientific objective of the TORERO campaign was to study the release, transport and fate of reactive halogen gases and oxidized VOCs, and their effect on the atmospheric oxidation capacity.

Figure 5.1 – NOAA ship Kaimimoana in dock at Pearl harbour for mobilisation before TORERO.

5.1 The East Tropical Pacific

As discussed in section 1.4.9, quantifying short-lived organic halogen sources in the tropics is of particular importance as deep convection in this region can rapidly transport reactive halogen species into the free troposphere and even as high as the stratosphere. Measurements in the tropical Pacific are sparse, especially the eastern tropical Pacific ocean (figure 5.2), defined as a 28 million km^2 box from the coast of America to 140°W between the Tropic of Cancer and the Tropic of Capricorn. This area accounts for approximately 10% of the global oceanic primary production (Pennington et al., 2006). This region is also where the net radiation balance is positive meaning there is more incoming energy than outgoing.

Normal East Pacific Ocean temperatures vary between 20 and 32°C with the coldest waters at the higher latitudes and the Equatorial Cold Tongue. The Californian Current and North Equatorial Current bring cooler water down from the North Pacific, driven by the trade winds along the coast of California. The Cold tongue is driven by the opposing cell with southerly winds pushing the Peru Current. These subtropical gyres rotate clock-wise and counter clock-wise, respectively driving warm water westward. This pooling of warm water in the Western Pacific increases sea level by 30–50 cm and deepens the thermocline compared to the coast of Peru (Pennington et al., 2006). This thermocline imbalance across the Pacific results in enhanced nutrient supply to the eastern Pacific

euphotic zone.

These counter-rotating cells cause large scale vertical movement when coupled with the Coriolis force. This, combined with wind-driven upwelling along the equator, results in a constant supply of nutrients to the surface from the coast of Ecuador extending out along the equator. The trade winds also drive upwelling and thus a temperature minima on the west coast of the Galapagos Islands.

The warmest water of the east tropical Pacific resides in the Central Pacific southern hemisphere and eastern Pacific warm pool. The large net solar irradiance and weak, wind driven ocean mixing at the warm pool results in surface temperatures exceeding 30°C (Wang and Enfield, 2001). The Costa Rica Dome is an area of oceanic upwelling where the thermocline ascends to near the surface bringing cold water and nutrients (figure 5.2, Fiedler and Talley (2006)).

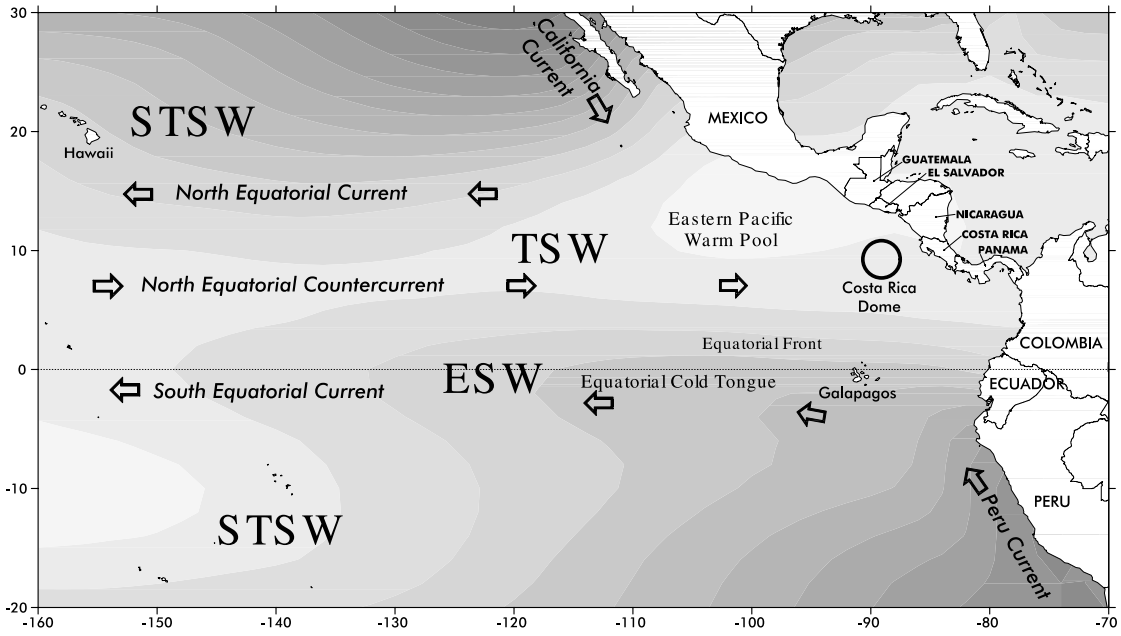

Figure 5.2 – Diagram of the East Tropical Pacific (ETP). STSW, Sub Tropical Surface Water; TSW, Tropical Surface Water; ESW, Equatorial Surface Water. Contours represent sea surface temperature. Reproduced from Fielder et al. 2006.

As the Pacific is such a vast water mass, temperature anomalies can impact weather on a large spatial scale. Yearly sea surface temperature (SST) deviations from a 30 year mean are called La Niña and El Niño events. During periods of La Niña, the cold tongue

extends further to the west and water temperatures drop by around 1°C (NOAA, ENSO monitoring). For periods of El Niño, temperatures increase by around the same amount and the cold tongue recedes and is often not visible.

La Niña and El Niño temperature deviations are measured from an array of sea buoys moored across the equator in grids called the TAO (Tropical Atmosphere Ocean project) array (Carpenter et al., 2011).

5.1.1 Motivation for measurements of halogens in the East Tropical Pacific (ETP)

Recently, IO column density has been retrieved using differential optical absorption spectroscopy (DOAS) from the SCIAMACHY satellite (figure 5.3, Schonhardt et al. 2008).

From these satellite images there appears to be enhanced IO above the Peruvian upwelling region. It has been hypothesised that short-lived iodocarbons could contribute to MBL IO and the TORERO cruise aimed to test this theory. Mahajan et al. (2012) state that the IO above the Peruvian upwelling could be consistent with the biological production of iodine containing species due to high Chl-a content in the upwelling region but this has not been validated with measurements. Mahajan et al. (2012) also measured IO differential slant column densities as high as 4.9 x 10^{13} molecules cm^{-2} in the ETP. This corresponds to >1 ppt of reactive iodine IO_x in the MBL. However, DOAS measurements made by the GV aircraft during TORERO indicated that the majority of IO was present in the free troposphere (Dix et al., 2013).

It should be noted that the satellite retrievals are not a confirmed measurement of IO in this region and this is made clear in the publication by Schönhardt et al. (2008). The technique utilises Differential Optical Absorption Spectroscopy (DOAS) where the sensitivity is dependent upon incident light intensity. The greater the Earths surface spectral reflectance, the greater the sensitivity. This results in less noise and better signal above polar regions which are covered in highly reflective ice and also benefit from a greater number of data points as the satellites orbit. IO and BrO data from above Antarctica compares well to ground based Long Path DOAS (LP-DOAS) measurements from Halley Station (Saiz-Lopez et al., 2007b).

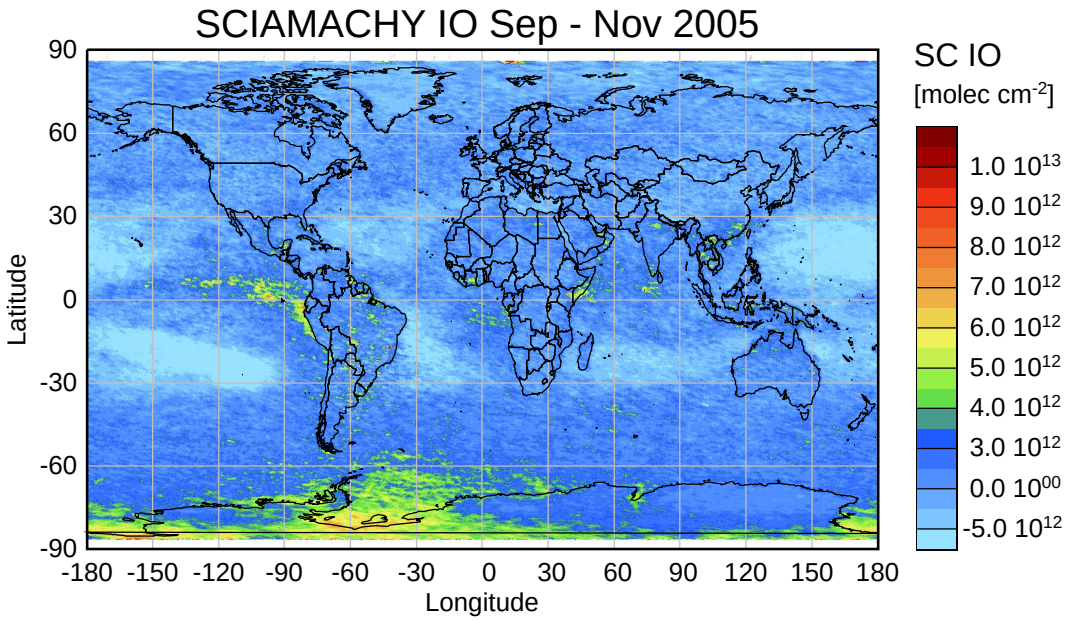

Figure 5.3 – Iodine oxide slant columns retrieved from SCIAMACHY (Sept-Nov 2005), reproduced from Schonhardt et al. 2008.

In contrast to ice and snow, the sea surface is less reflective and scatters reflected light. At the ITCZ, persistent convection results in semi-permanent cloud cover which is highly reflective. In the ETP specifically the ocean is very calm, also known as the doldrums and consequently has greater reflectivity. Because these IO measurements in the ETP are very close to the LOD due to a poor signal-to-noise ratio it is not inconceivable that a baseline zero error exists and that these measurements reflect physical parameters rather than IO concentrations. Longer term averages are currently being processed which may help to strengthen this data with respect to the ETP region.

5.2 Experimental

From 27^{th} Jan until 28^{th} Feb 2012, the NOAA research vessel Kaimimoana sailed from Pearl Harbour, Hawaii to Puntarenas, Costa Rica via the 95°W and 110°W TOA buoy lines.

Very short-lived halocarbons (VSLH) were quantified in air and water samples taken at

regular intervals along the ships track (figure 5.4). Air samples were measured at a frequency of one every 20 minutes, near continuously throughout the voyage resulting in over 1800 data points. Surface seawater samples were taken from the ships seawater inlet at a frequency of one every 55 minutes and at various depths from conductivity, temperature, depth (CTD) casts at specific points during the voyage.

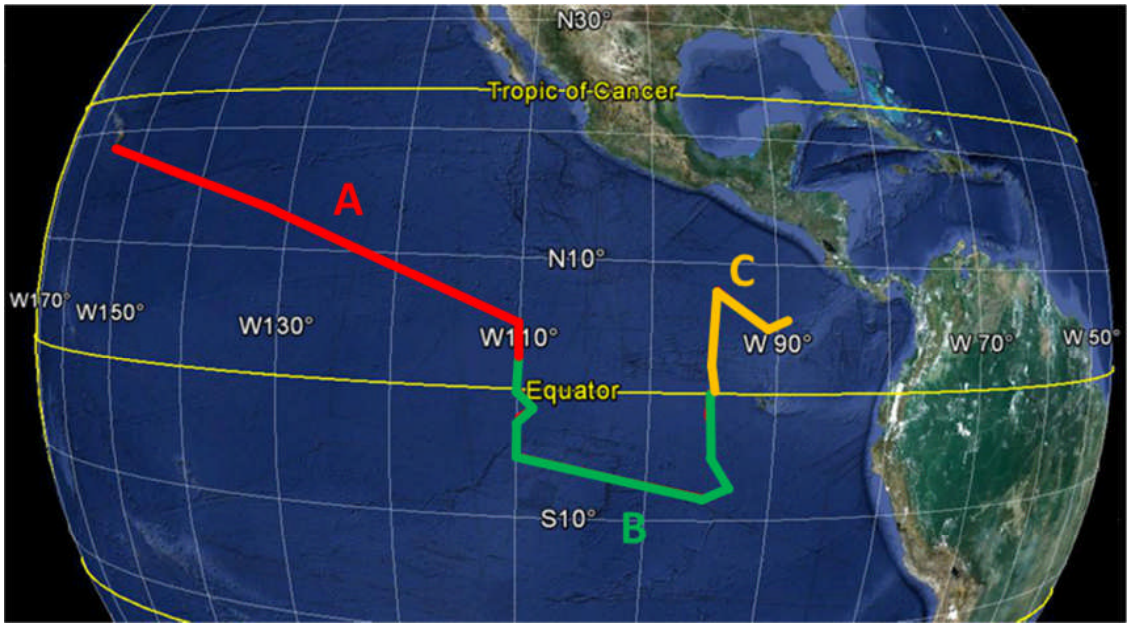

Figure 5.4 – TORERO cruise track split into three sections highlighting specific sampling regions. A, longitudinal transect at constant speed allows characterisation of diurnal cycles; B, CTD latitudinal cross-section; C, Eastern Pacific warm pool region.

Meteorological measurements made from the top of a 10 m bow tower included wind speed, wind direction, pressure and humidity. Sea surface temperature (SST) was measured using a 'sea snake'– a temperature probe which is allowed to drag just below the water surface. Seawater salinity was measured from the conductivity of water sampled from the seawater inlet.

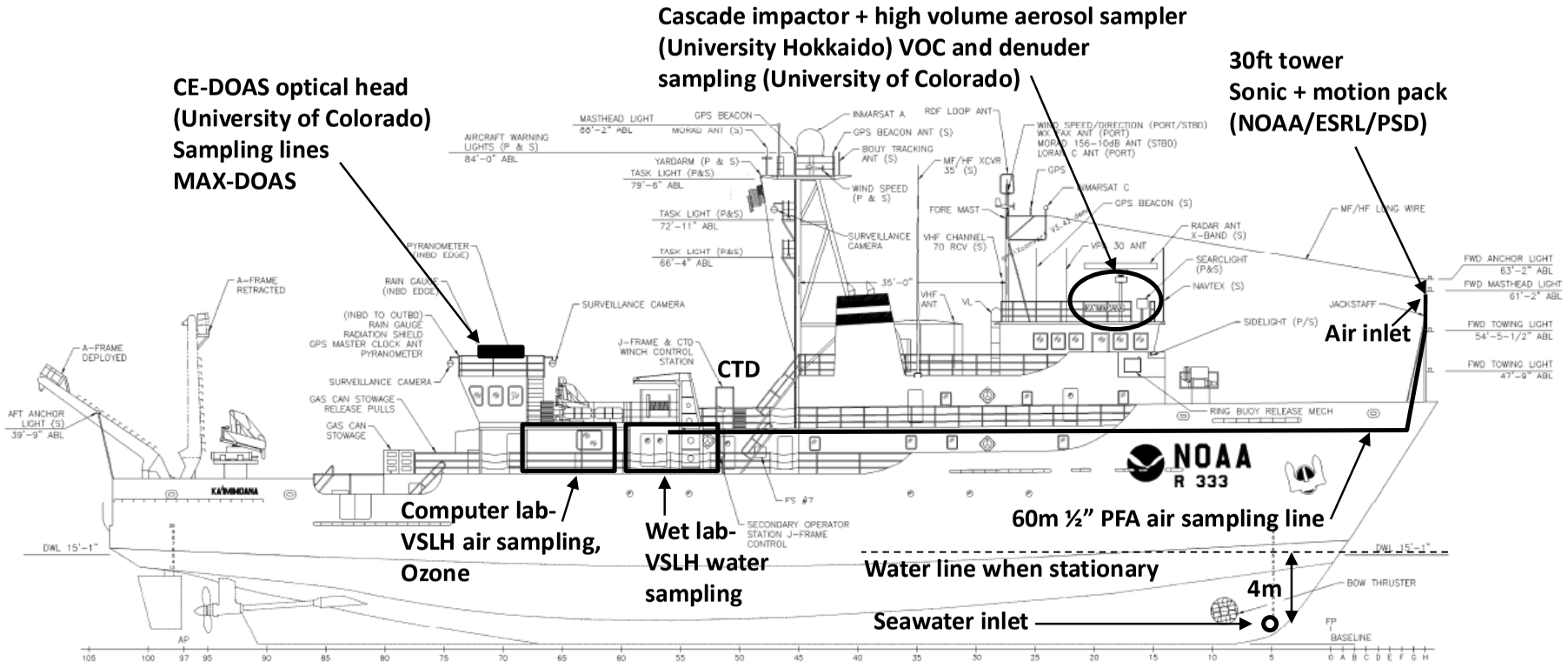

Figure 5.5 – Technical drawing of NOAA vessel Ka'imimoana "Ocean Explorer" showing position of instrumentation and sample lines during the TORERO campaign.

5.2.1 Aircraft overpasses

As part of the TORERO campaign the cruise path of the Kaimimoana was intersected by the flight path of the NSF/NCAR GV research aircraft (figure 5.6) which was fitted with the TOGA GC-MS (Trace Organic Gas Analyser) and operated by NCAR (Apel et al., 2003). The instrument was somewhat similar to the GC-MS used on-board the KA with an Agilent 5975 MSD at its heart. The differences are the resistively heated column and the sample pre-concentration which utilises liquid nitrogen to cryogenically focus analytes rather than an absorbent trap. The cryogenically focussed peaks give increased sensitivity and allow for extremely rapid chromatography. However the sample volume is limited which results in a higher LOD than can be detected on the ship-borne GC-MS which pre-concentrates 1 L of sample.

Figure 5.6 – NSF/NCAR Gulfstream V research aircraft

The GV overpassed the KA as low as 100 ft which allowed for comparison of measured VSLH. The GV intersected the KA on five occasions at the end of the cruise track section B and section C during 4 flights shown in figure 5.7. The TOGA GC-MS aboard the aircraft was inter-calibrated with the GC-MS aboard the KA (section 3.4.2).

5.2.2 *In-vivo* chlorophyll-a

Phytoplankton are a known source of VSLH and are hypothesised to be the dominant source of VSLH in open ocean regions. Phytoplankton abundance can be estimated from chl-a concentration. Chlorophyll-a (Chl-a) fluorescence was measured in-situ using a Turner C6 Multi-Sensor Platform with an installed *in-vivo* chlorophyll Cyclops-7 sensor. This sensor provides an excitation wavelength of 440 nm which is absorbed by

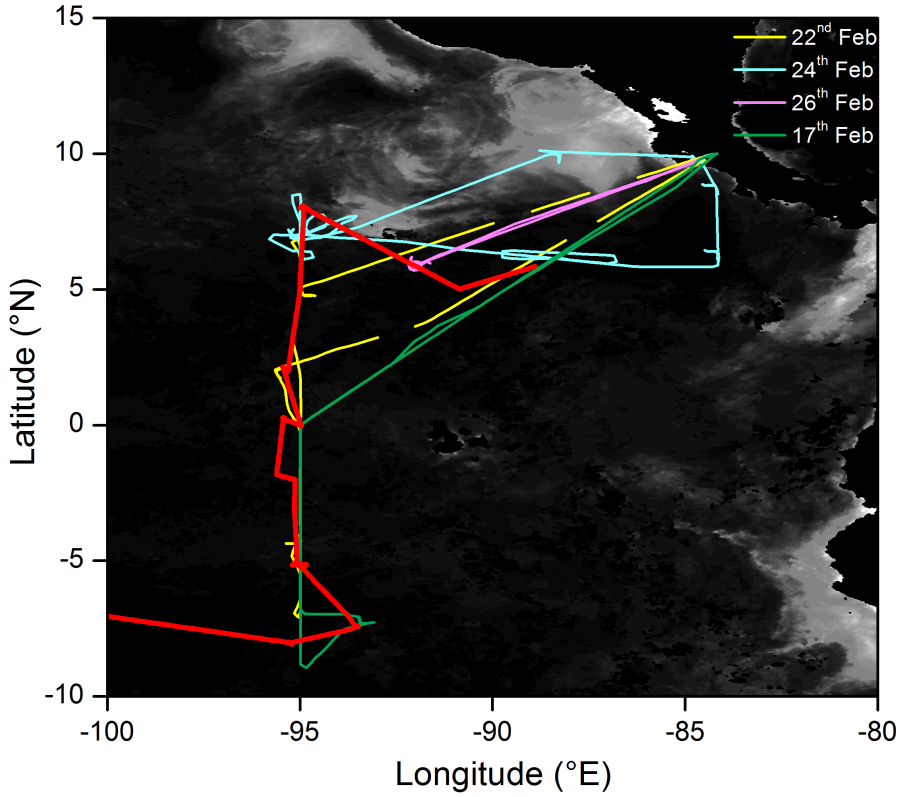

Figure 5.7 – GV flights intersecting the KA cruise track (red line).

the chl-a and subsequently fluoresces at 680 nm. The fluorescence is measured and is proportional to chl-a concentration.

This instrument has a LOD of 0.025 μg L^{-1} and dynamic range of 0–500 μg L^{-1}. It also has an in-built temperature sensor with a range of -2 to 50°C.

Factors affecting phytoplankton estimates using *in-vivo* fluorescence measurements of Chl-a are two-fold.

Firstly, the assumption that Chl-a is directly proportional to phytoplankton must be tested. Phytoplankton is a very broad term for a huge range of biological species. Different phytoplankton functional types will contain different concentrations of Chl-a.

Secondly, the fluorescence measurement of chl-a itself presents a number of significant problems (Falkowski and Kiefer, 1985):

1. Senescent phytoplankton cells will produce a greater per-unit fluorescence than healthy phytoplankton

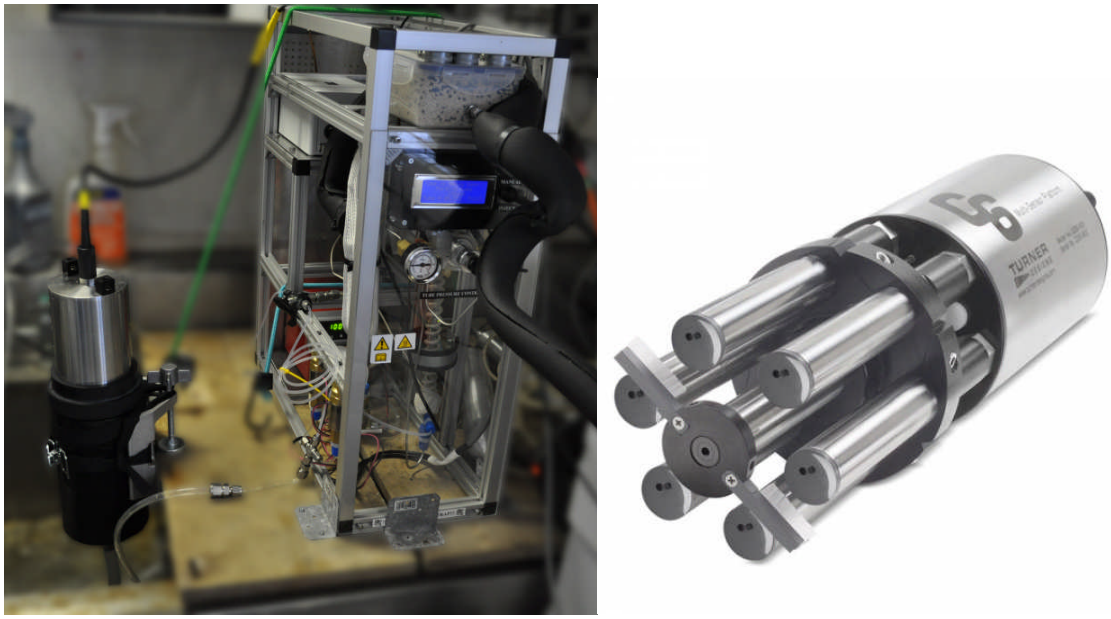

Figure 5.8 – Left: Turner C6 fluorimeter flow-through module coupled to the AutoP&T. Right: C6 unit showing the multi-sensor head and rotating cleaning brushes.

2. Phytoplankton can adapt to light conditions. Therefore a phytoplankton species abundant in equatorial regions will fluoresce less than the same species at mid-latitudes.

3. Cell morphology can interfere with the cells fluorescence

4. Turbidity can cause scattering or absorb the fluoresced light

5. Phytoplankton response to sunlight is to temporarily reduce their *in-vivo* fluorescence per unit of extractable Chl-a as a means of dissipating excess energy

For the reasons stated it is clear that care must be taken when interpreting Chl-a data and making links to phytoplankton and thus VSLH concentrations. Further, different phytoplankton function types may release differing ratios of VSLH. For example; a species which releases a large amount of VSLH may contain less Chl-a than a species which releases none and *vice-versa*. This makes the link between Chl-a and VSLH very indirect. However, Chl-a concentration remains the easiest and in most cases the only technique available to assess biological activity and can still provide useful data on the spatial distribution of ocean biology.

Chl-a can also be mapped globally from satellite retrievals from MODIS (Moderate Resolution Imaging Spectroradiometer) aboard NASA's Terra and AQUA satellites.

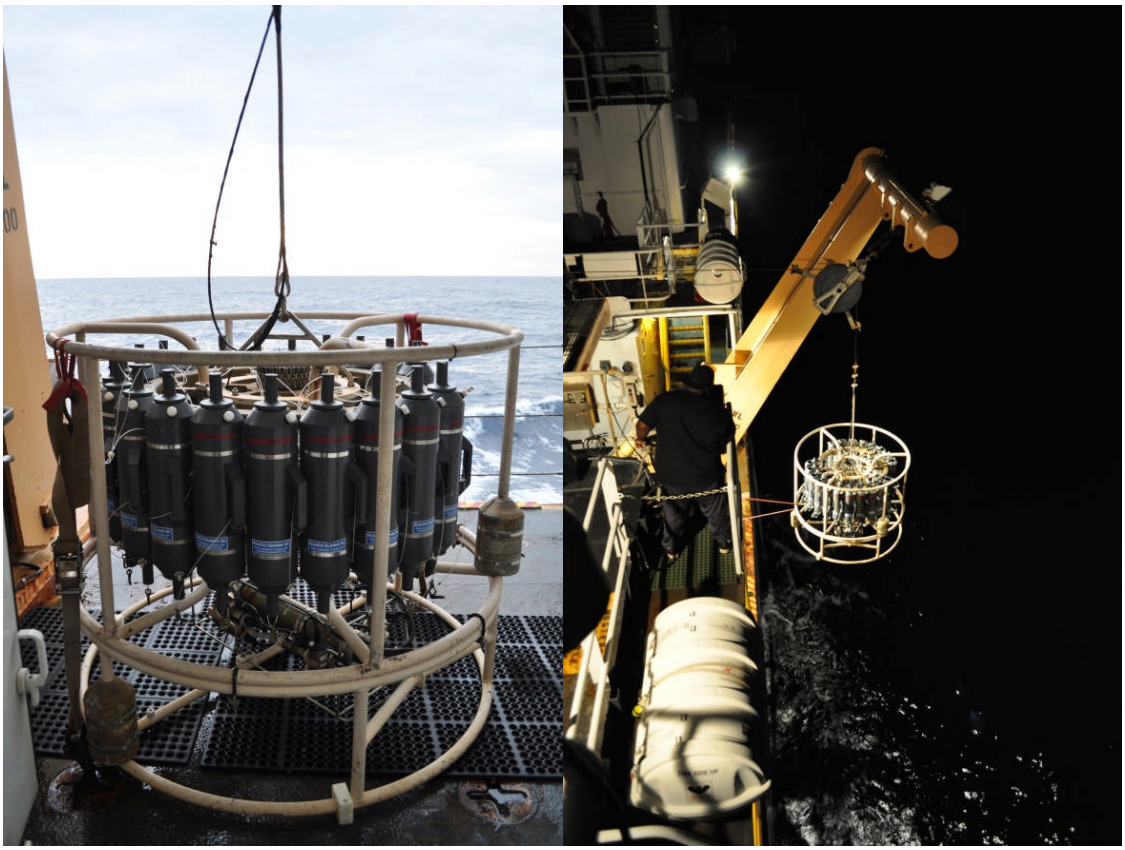

Figure 5.9 – Left: CTD cage fitted with Niskin canisters for the collection of seawater from various depths. Right: Night time CTD cast.

5.2.3 Conductivity, Temperature, Depth (CTD)

A 'CTD' is an instrument for measuring a depth profile of the ocean. It consists of a lead weighted, metal frame which is lowered into the ocean on a long cable up to 3000 m depth. The frame houses at least three instruments for the three basic measurements: Salinity from conductivity, temperature and depth from pressure. The frame can also house other instruments if required. During TORERO a fluorimeter was fitted for the *in-vivo* excitation at 440 nm and subsequent fluorescence at 680 nm of chlorophyll-a. The CTD was also fitted with 'Niskin' bottles; PVC tubes with open ends which allow water to flow through the tube as it descends (figure 5.9). As the CTD ascends the open ends are capped at pre-determined depths allowing for the capture of water samples from a

range of ocean depths.

5.2.4 Instrumental setup

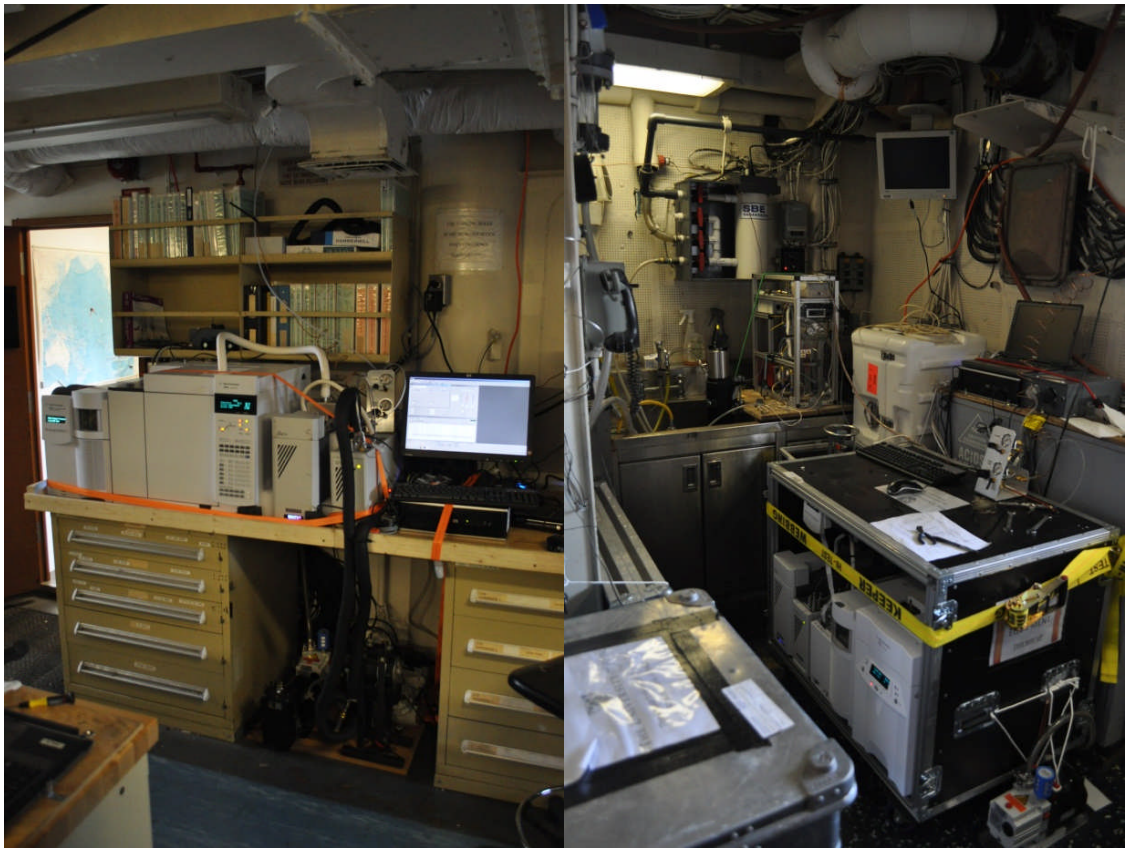

Figure 5.10 – Instruments secured for sea on the ship: Left, the air sampling TD-GC-MS. Right, the water sampling AutoP&T-TD-GC-MS.

5.2.4.1 Air sampling

Air was sampled from the top of the 10 m bow tower through a 60 m sampling line (1/2" PFA, Swagelok). A diaphragm pump (KNF, NO35.1.2AN.18) was used to pull ~30 L/min down the line. At 1 m before the diaphragm pump a T-union connected approximately 50 cm of 1/4" heated instrument grade stainless steel line (Restek) to a metal bellows pump (Senior Aerospace MB-158) which provided 10 psi of positive pressure to the instrument with a pressure relief valve protecting the integrity of the bellows whilst the flow through the instrument was stopped. U-bends and drain plugs were added in-line to allow any water to be removed from the system. Additionally, the metal bellows pump was mounted

upside down in a stand to prevent water from collecting in the bellows. An ozone analyser (Thermo Scientific Model 49i) drawing 3 L min^{-1} was also connected before the diaphragm pump (figure 5.12). The metal bellows pump was connected to the air sampling instrument with approximately 1.5 m of 1/8" heated instrument grade stainless steel. The air sample flow was also diverted to the water measurement instrument in the wet lab using the same steel line but unheated.

Figure 5.11 – Air sampling inlet secured at top of bow tower 10 m above sea level and adjacent to sonic wind measurement for flux calculation.

The air samples, calibration gas and $n5$ nitrogen streams were selected (Markes, CIA8) and pre-concentrated on a cooled absorbent trap at -30°C (Markes, Unity2). Samples of 1 L in total (10 min, 100 mL min^{-1}) were pre-concentrated then desorbed at 300°C onto a gas chromatograph (Agilent 7890) and separated on a capillary column (Restek, RTX502.2, 30 m, 0.25 mm ID, 1.25 micron) using an oven temperature ramp (40-250°C, 3 min hold,

20°C min^{-1} ramp). Eluents were ionized using electron ionization and analysed by m/z (Agilent, 5975C). CH_3I was quantified using the CH_3I^+ ion (m/z 142) with I^+ (m/z 127) as a qualifier ion. CH_2ICl, CH_2I_2, $CHCl_3$, CCl_4, CHBrCl, $CHBrCl_2$, $CHBr_2Cl$, CH_2Br_2 and $CHBr_3$ responses were measured using m/z 176/178, 268/254, 83/85, 117/119, 128/130, 83/85, 129/127, 174/176 and 173/171 as quantification/qualification ions respectively.

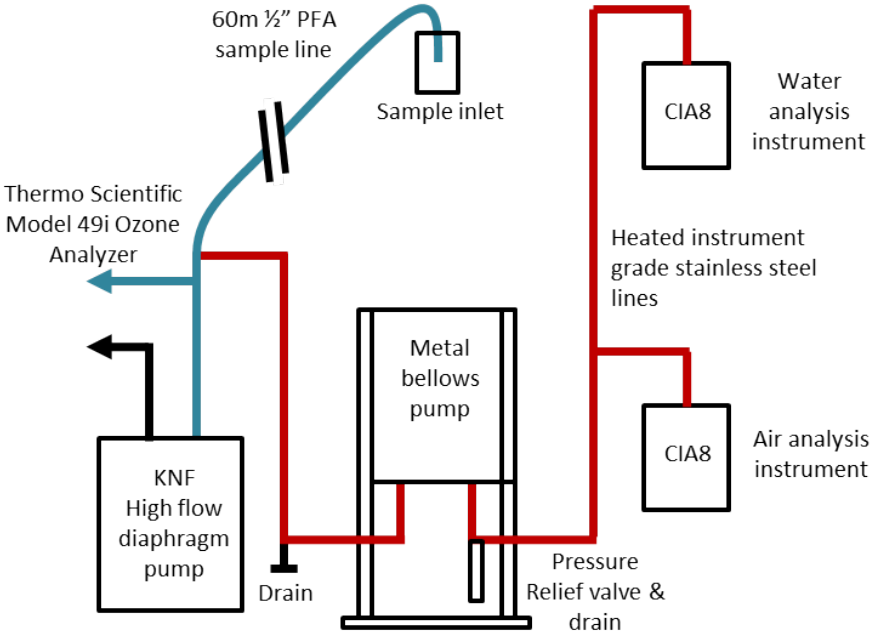

Figure 5.12 – Air sampling schematic showing air sample flow path. Blue lines, un-heated PFA; red lines, heated instrument grade stainless steel. The water instrument used air samples for sensitivity adjustment.

5.2.4.2 Water sampling

Niskin bottle samples from CTD casts

Water was taken from the Niskin bottles immediately after completion of the CTD profile. Water from each depth was sampled into amberised glass bottles which were rinsed with the sample water 4 times before being filled. Each sample was then filtered through a 0.45 μm Millipore filter using a glass gas syringe, the filter was changed for each sample. The syringe and filter were pre-rinsed with the sample water. The filtered water was then used to rinse a second amberised glass bottle reserved specifically for each depth. This

was performed before the bottle was filled with the filtered water to be analysed. The effectiveness of the sampling steps can be seen by comparing the 3 m CTD depth with the previous online surface water measurement and by the reproducibility of bottle samples (table 2.6.5.2, section 2.4). This validates the offline sampling and shows that there are negligible VSLH losses when the sample is stored in a Niskin bottle, filtered and stored in an amberised glass bottle before being analysed using the offline method. The CTD samples were introduced into the AutoP&T by switching the flow of the peristaltic pump to sample from the selected bottle sample (figure 5.13 (offline sample inlet)). The flow was switched 50 seconds prior to filling the purge tube with the final 20 seconds before filling with the flow path through the PTFE filter. The dead volume before the purge tube is approximately 5 mL and a 40 mL min^{-1} flow rate was used to purge before filling which ensures that the water analysed is the water from the sample bottle.

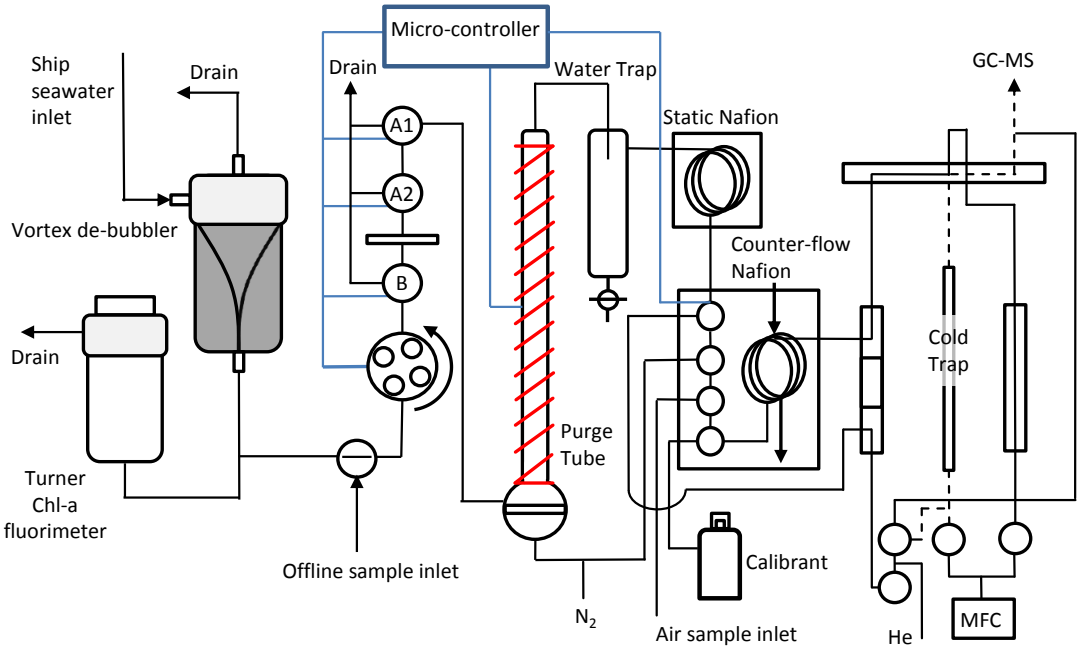

Figure 5.13 – Schematic of water instrument setup showing the connection of the Auto-P&T to the ship surface seawater inlet.

Online sampling from bow water inlet

Water was pumped from an inlet approx. 2–4 meters (depending on sea-state) below the water-line at the bow of the ship (figure 5.5) and through a vortex de-bubbler (Seabird)

to remove any air bubbles (figure 5.13). The flow was maintained at around 10 L min^{-1} through 1/2" PFA tubing and into a Turner C6 fluorimeter. Before entering the Turner C6 a peristaltic pump was used to divert a portion of the water to the AutoP&T system. The flow rate inside the AutoP&T (40 mL min^{-1}) was sufficiently high and the dead-volume sufficiently low (<10 mL) to ensure that the sample was representative of the water at the high flow rate side of the system. Similarly, the high flow rate of water before being diverted to the AutoP&T ensures the water reaching the instrument is representative of the water body in which the ship resides at that time.

GPS, Chl-a and meteorological data was then available on the same temporal frequency as the AutoP&T sample collection. The flow of water through the system was maintained at all times throughout the voyage.

5.2.4.3 Instrument stability

Mass spectrometers suffer from sensitivity changes during normal operation (section 3.2.3.3). Measurements of air and water from on-board ships are in far from normal conditions. The platform is moving and subject to vibration and forces from breaking waves. Due to the nature of the sampling environment, air sampled has a high water content and purging seawater to remove volatiles produces extremely humid samples. Despite extensive steps to remove water before analysis, the humidity of samples still negatively impacts the mass spectrometer performance.

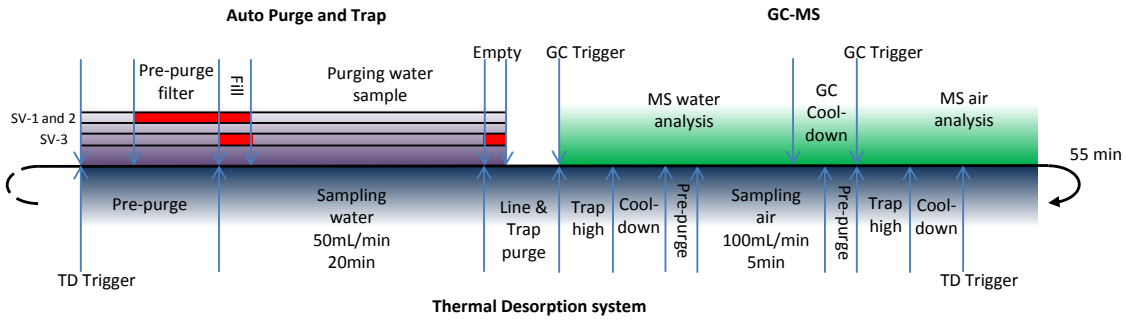

Figure 5.14 – Timing diagram for Auto-P&T operation. Red bars represent actuation of valves. The blue, purple and green shaded areas relate to Thermal Desorption, AutoP&T and GC-MS operations, respectively.

In order to account for short-term sensitivity changes between calibrations the analytes

were ratioed to CCl_4 (section 3.2.3.2). This is very effective for air samples where the concentration of CCl_4 in the atmosphere is stable. However, the ocean is a net sink of CCl_4 and dissolved concentrations can vary. In order to monitor sensitivity drift on the water instrument during TORERO, 500 mL of air was sampled and analysed between each water sample. By measuring CCl_4 in the air the sensitivity changes of the instrument could be tracked. Running this air sample between each water sample also acted as a blank to prevent carryover between water analysis. As CCl_4 was quantitatively retained on the adsorbent trap at +20°C, this temperature was used to provide a relatively dry sample between each water sample to allow the system to recover.

The concentrations of all VSLH were quantified in these air samples, but should be treated with caution as the air sample line between the pumps and the water instrument was unheated and there may have been carryover from the prior water sample. The concentration of CCl_4 in water is very low and there was no carryover into the air sample, allowing it to be used for the sensitivity adjustment.

5.2.5 Back Trajectory Analysis

The date/time and GPS co-ordinates were recorded with each air sample taken, however due to the dynamic nature of the boundary layer it is important to also understand the air mass history.

The position and altitude of the air arriving at the sampling position was modelled along its backward-trajectory for 315 hours using NOAAs Hybrid Single Particle Lagrangian Integrated Trajectory Model (HYSPLIT). This model uses archive meteorological data to calculate the trajectory of an air parcel as its moves through the atmosphere. This provides useful information on the history of the air that was sampled, such as its proximity to a potential source region, influence from certain terrain or contamination from anthropogenic emissions. Back-trajectory analysis was run at 12 hour intervals along the cruise track and is shown in figures 5.15 and 5.16.

For the first 3 days of the cruise the trajectories had not touched land, looping around and originating from the western Pacific. For section A of the cruise track no air parcel had been over land for at least 4 days.

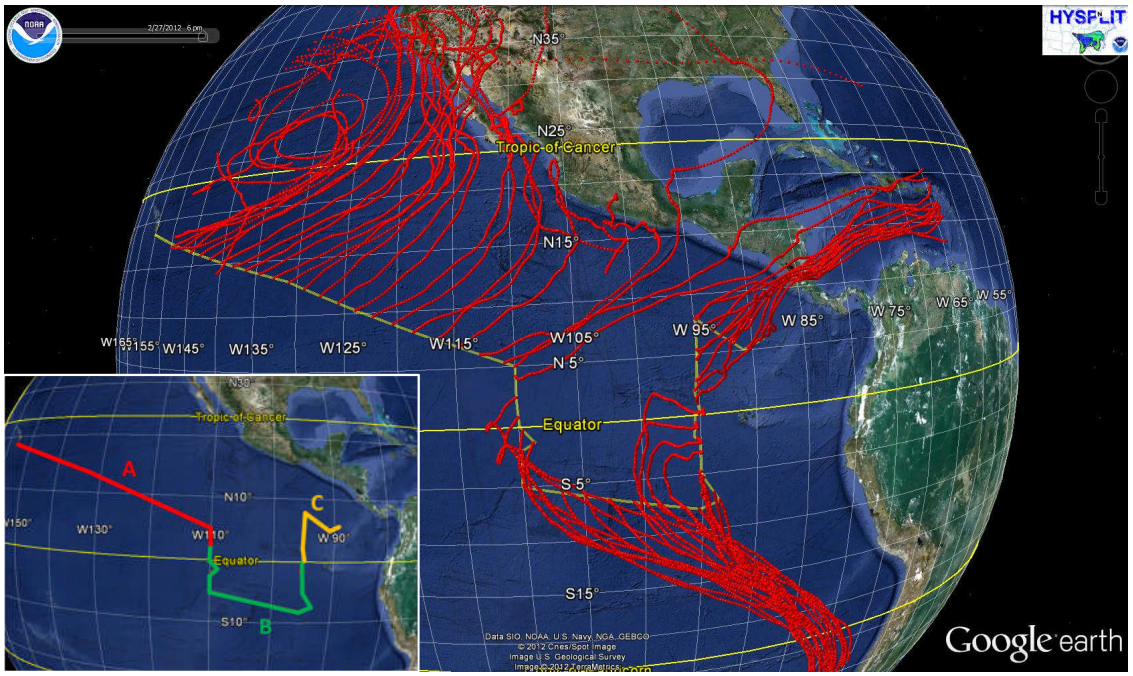

Figure 5.15 – NOAA HYSPLIT 315 hour backward trajectory models ran at 12 hour intervals for the duration of the cruise.

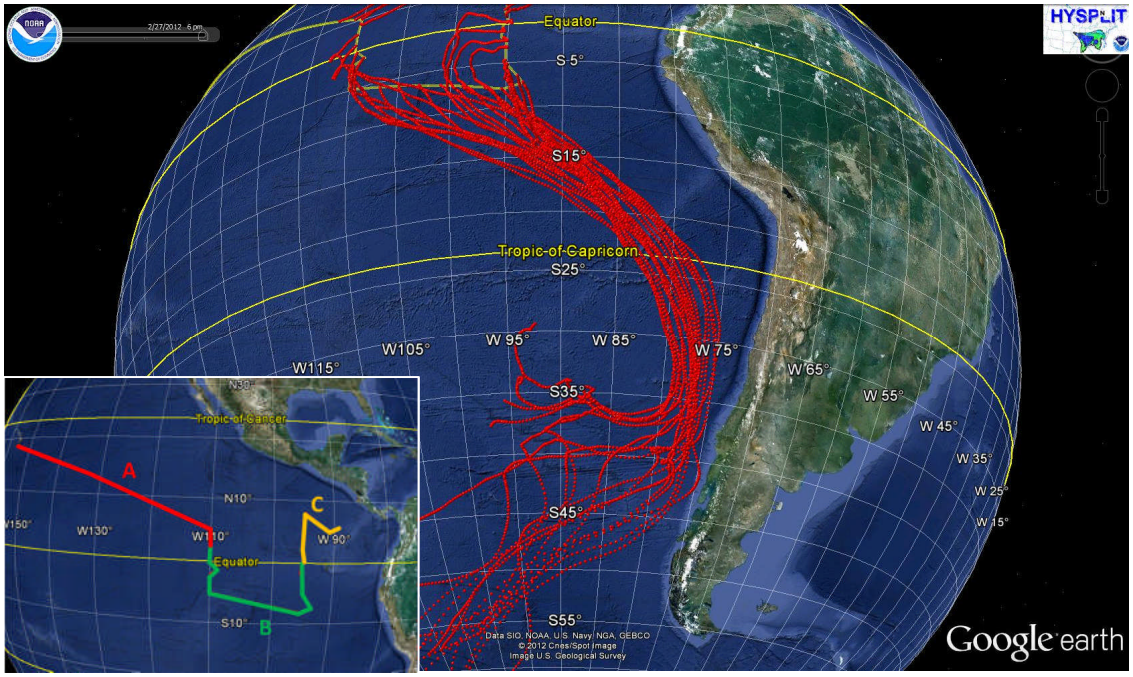

Figure 5.16 – Southern hemisphere NOAA HYSPLIT 315 hour backward trajectory models ran at 12 hour intervals for the duration of the cruise.

During section B the ship crossed beneath the ITCZ (3°N) and trajectories shifted accordingly to originate from the southern hemisphere. These trajectories never reached land, originating from the south Pacific and Antarctic. Some of the trajectories did pass within 200 miles of the Chilean coast which is a biologically active region of coastline. However, this was at least 9 days prior to arriving at the sampling position. As the ship headed north along the 95°W buoy line it passed within 200 miles of the Galapagos Islands. Due to upwelling around islands, this region is biologically productive (Feldman 1986) and is likely to be a source of VSLH similar to that of a productive coastal region. However, whilst passing through this region, trajectories originated from the south and approached from the west, completely by-passing any enhanced emissions.

Trajectories in cruise section C originated from the Caribbean and previously the North Atlantic Ocean, passing over Costa Rica 30-40 hours before sampling. The majority of air mass sampled could be defined as open ocean and devoid of any enhanced emission sources. This provided a useful measure of background air concentrations for longer lived species and the potential for identification of open-ocean sources of short-lived species. Air masses with terrestrial origin/influence did not have any major interaction with biomass burning regions but may have had coastal influence 4 days prior to arrival at the sampling position.

5.3 Results and Analysis

5.3.1 Thermohaline distribution

The physical conditions of the ocean and atmosphere must be understood in order to fully interpret the data. Salinity and temperature play a pivotal role in driving deep ocean currents and surface upwelling. Cold, nutrient rich, upwelled water prompts rapid biological growth.

5.3.1.1 Salinity

Salinity displayed a reduction between 0-10°N as the ship entered the north equatorial counter-current and eastern pacific warm pool. This reduction in salinity and presence of

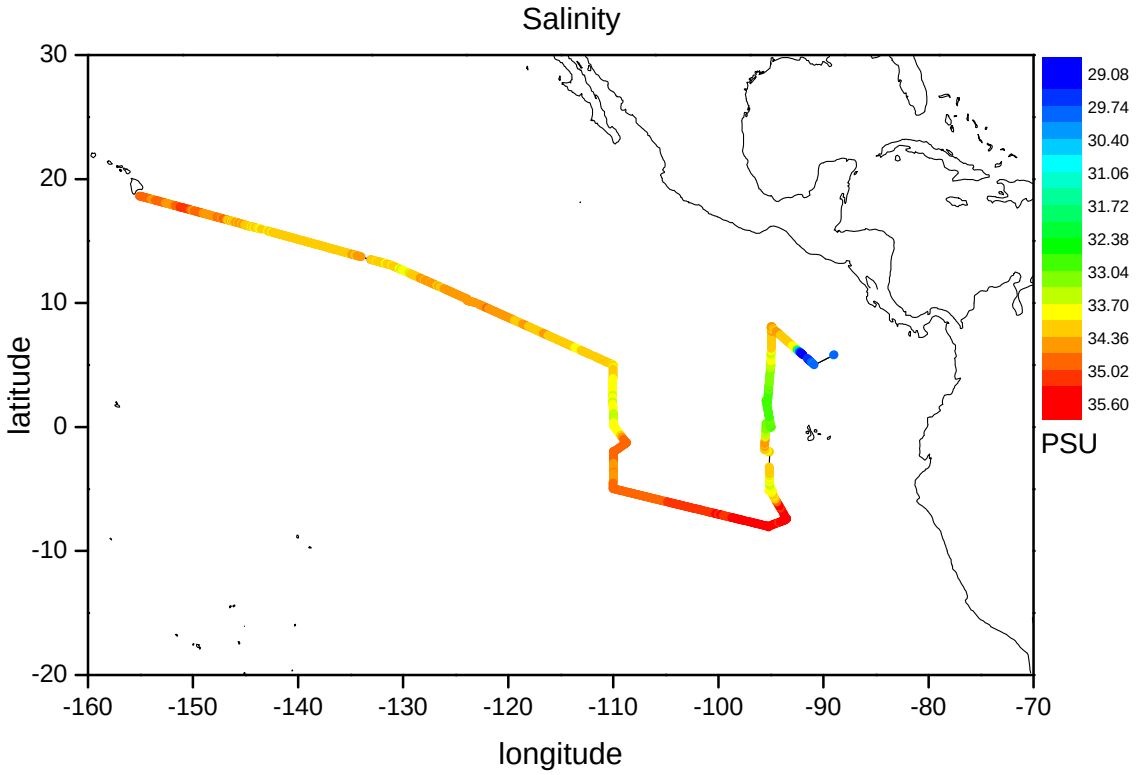

Figure 5.17 – Surface salinity measurements throughout the cruise in practical salinity units (PSU) averaged to air sampling frequency (20 min).

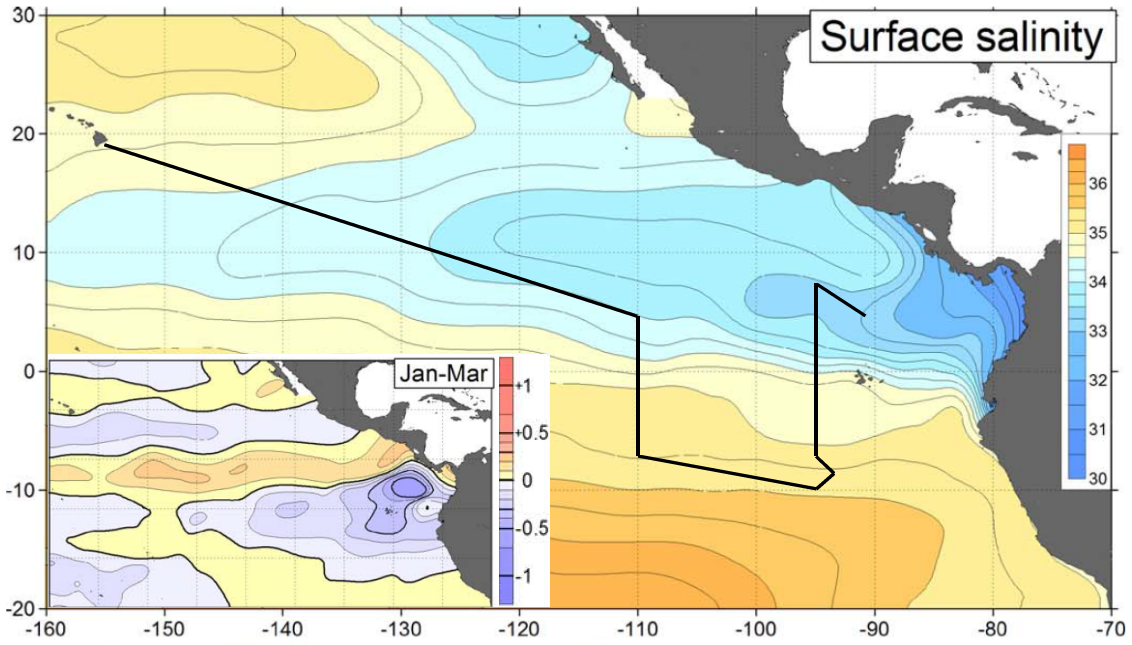

Figure 5.18 – Mean annual ETP surface salinity from bottle, surface and CTD data in PSU. Inset: deviation from the mean during January-March period (Adapted from Fielder et al. 2006).

the ITCZ at this latitude indicates precipitation dominating over evaporation in this area. There was a marked salinity increase in the southern hemisphere corresponding to a lack of precipitation and notably warm air temperatures resulting in net evaporation. As the ship approached Costa Rica toward the end of the cruise, salinity dropped to < 30 PSU which is likely due to the influence of rivers entering the coastal waters.

5.3.1.2 Temperature

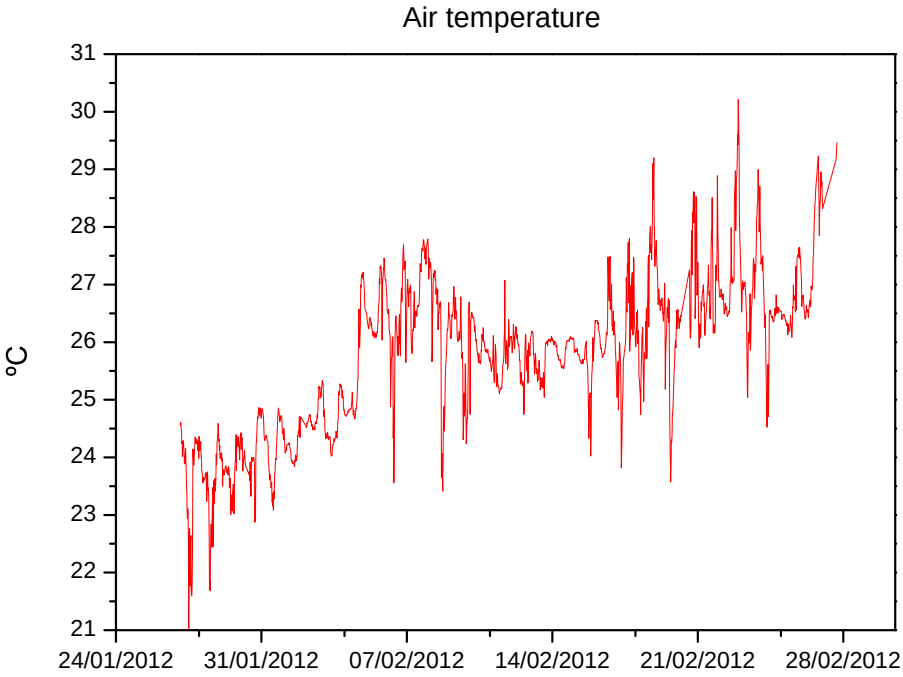

Figure 5.19 – Air temperature measurements throughout the cruise in °C averaged to air sampling frequency (20 min).

The air temperature increased as the ship sailed south east toward the equator. The largest diurnal cycle was measured in the southern hemisphere ($> \Delta 5$°C) with the daily range far exceeding the mean temperature range of an entire year (1–2°C) (Amador 2006).

SST measurements from the ship (figure 5.20) agree well with yearly means for this area (figure 5.21) except for a reduction in the intensity of the cold tongue which is often reduced in January/February. SST did decrease at around 2°N, 110°W but showed an increase at the same latitude 95°W where wind trajectories looped around and approached from the west (figure 5.15). This area west of the Galapagos Islands is usually a cold-spot due to island enhanced upwelling. These unusual trajectories may have reduced the upwelling

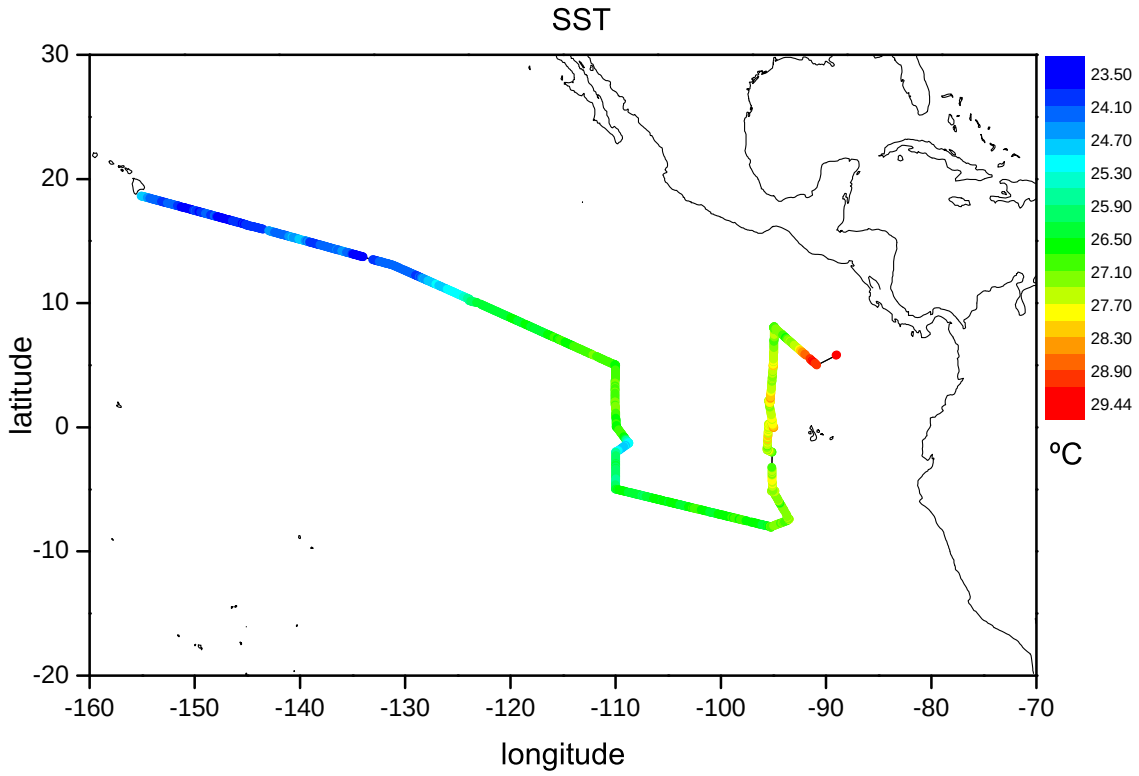

Figure 5.20 – Sea surface temperature (SST) measurements throughout the cruise in °C averaged to air sampling frequency (20 min).

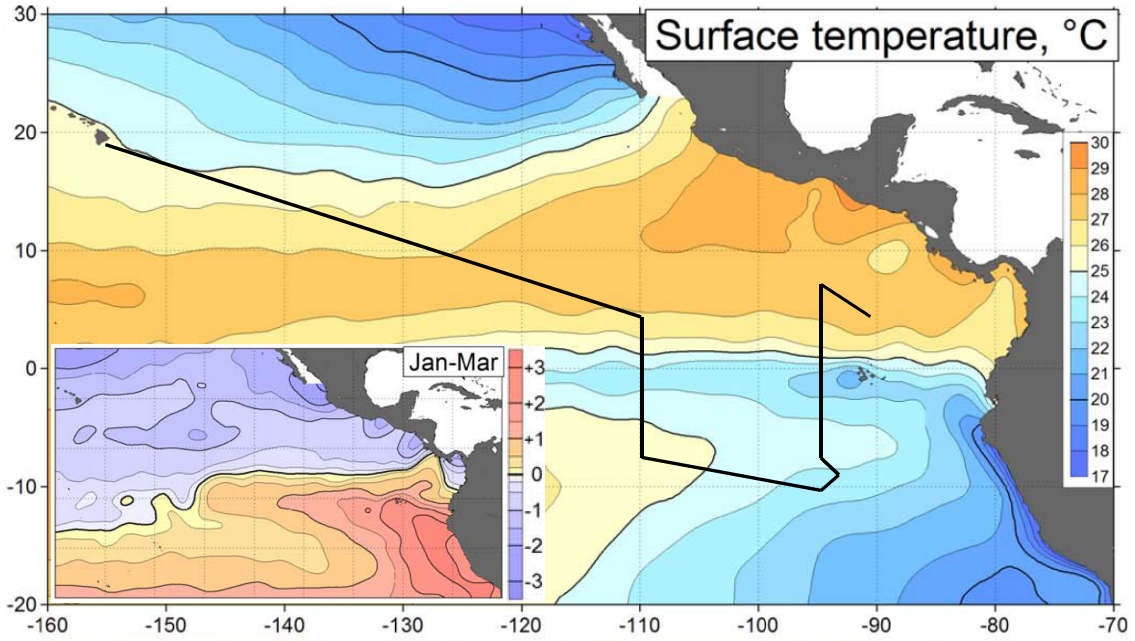

Figure 5.21 – Mean annual ETP surface seawater temperature (SST) from bottle, surface, buoy and CTD data in °C. Inset: deviation from the mean during January-March period (Adapted from Fielder et al. 2006).

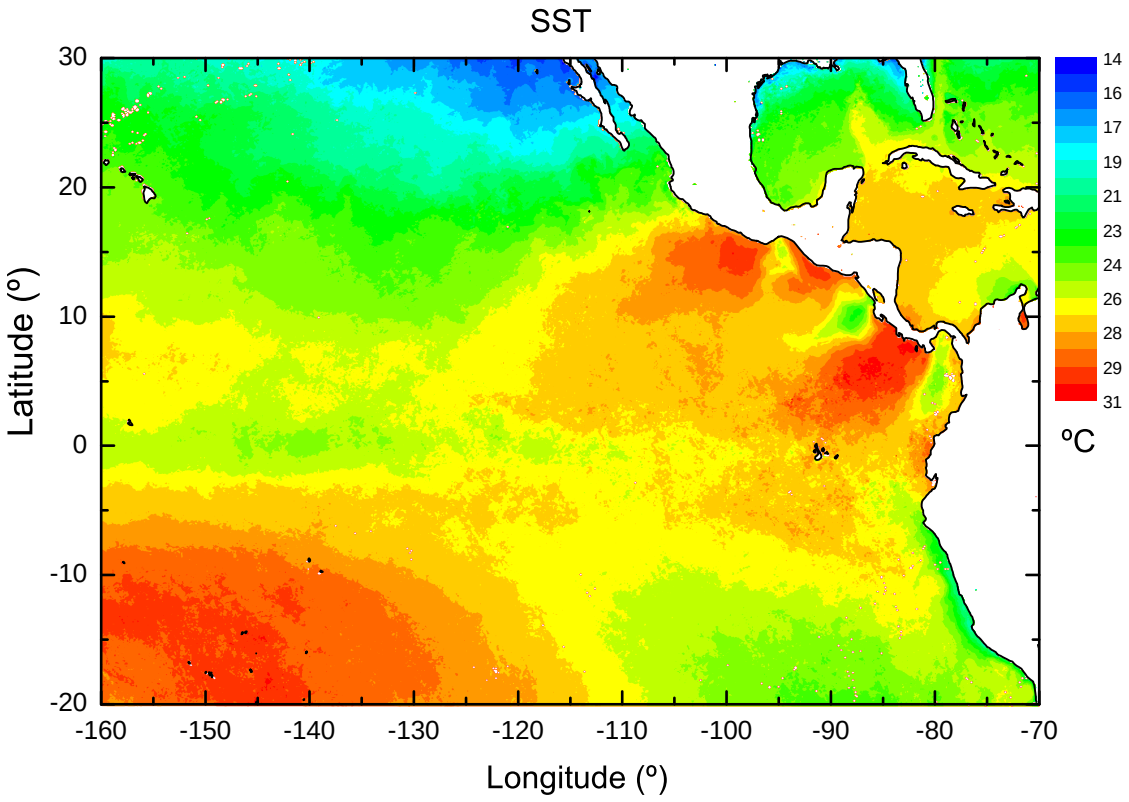

Figure 5.22 – 4 km resolution sea surface temperature (SST) retrieval from NASA MODIS Aqua satellite average for the month of February.

on the westward side which requires trajectories perpendicular to the west coast (section 5.2.5) and also could have reduced the influence of the Peru Current bringing cold water up from the south. This is confirmed by satellite retrieval from Modis Aqua averaged over February (figure 5.22) which shows very little evidence of a cold tongue or any upwelling at the Galapagos. The area around the Galapagos is usually 2–3°C higher than average from January to March (Fiedler and Talley, 2006) but here we observe in excess of 28°C, much warmer than usual and characteristic of very weak upwelling influence. As the ship approached Costa Rica the SST increased to the maximum of its range.

5.3.2 Ozone

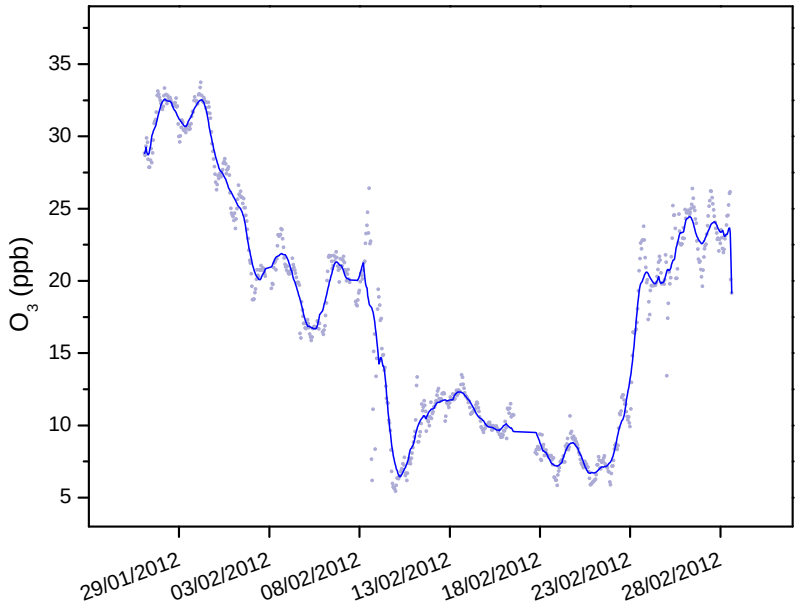

Figure 5.23 – Ozone concentration (ppb) measured by a Thermo Scientific Model 49i O_3 analyser (grey circles) with a 10 point average (blue line) temporally along the TORERO cruise track.

Ozone concentration at the beginning of the cruise was around 30–35 ppb, consistent with observations on Hawaii (Lin et al., 2014; Oltmans et al., 1998). This soon decreased as the ship sails away from, and up wind of the island to concentrations in-line with the open-ocean (∼20 ppb). There was a notable decrease when transistioning across the ITCZ into the southern hemisphere and remained very low (∼10 ppb) until the ship re-entered the Northern Hemisphere. The reason for the low ozone was likely due to very low NO resulting in net photochemical destruction, sea surface deposition and low net entrainment

as reported during flights within the west tropical Pacific boundary layer (Singh et al., 1996).

5.3.3 Wind speed and direction

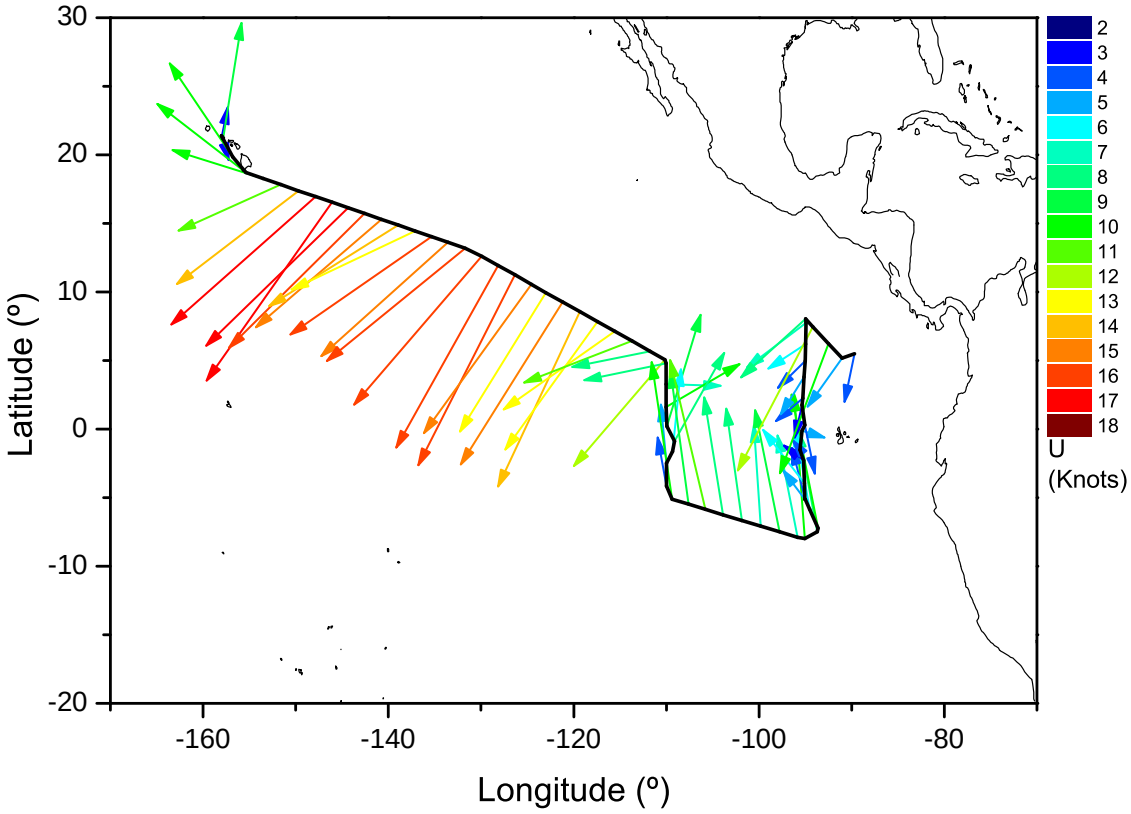

Figure 5.24 – 12 hour average true wind vectors coloured and scaled to true wind speed (U, Knots).

The most prominent winds during TORERO were the westerlies during section A of the cruise track (figure 5.24). The wind stress curl exerted on the ocean surface produces mesoscale eddies which drive mixed layer circulation, bringing nutrients, biology and dissolved gases to the surface where the latter can flux into the gas phase. Toward the end of section A the ship encountered low-level jets from the intra-Americas before beginning the transect down the 110°W buoy line. The Southern Hemisphere trade winds were lower velocity than the Northern Hemisphere trade winds and the warm pool region (see section 5.1) displayed relatively low velocity winds typical of this area (Wang and Fielder 2006).

5.3.3.1 Mixed layer depth variability

As the concentrations of the very-short lived species in air are strongly linked to their concentration in the ocean, physical factors affecting surface ocean concentrations will directly influence the spatial distribution in the gas phase. One of these important physical factors is oceanic mixed layer depth.

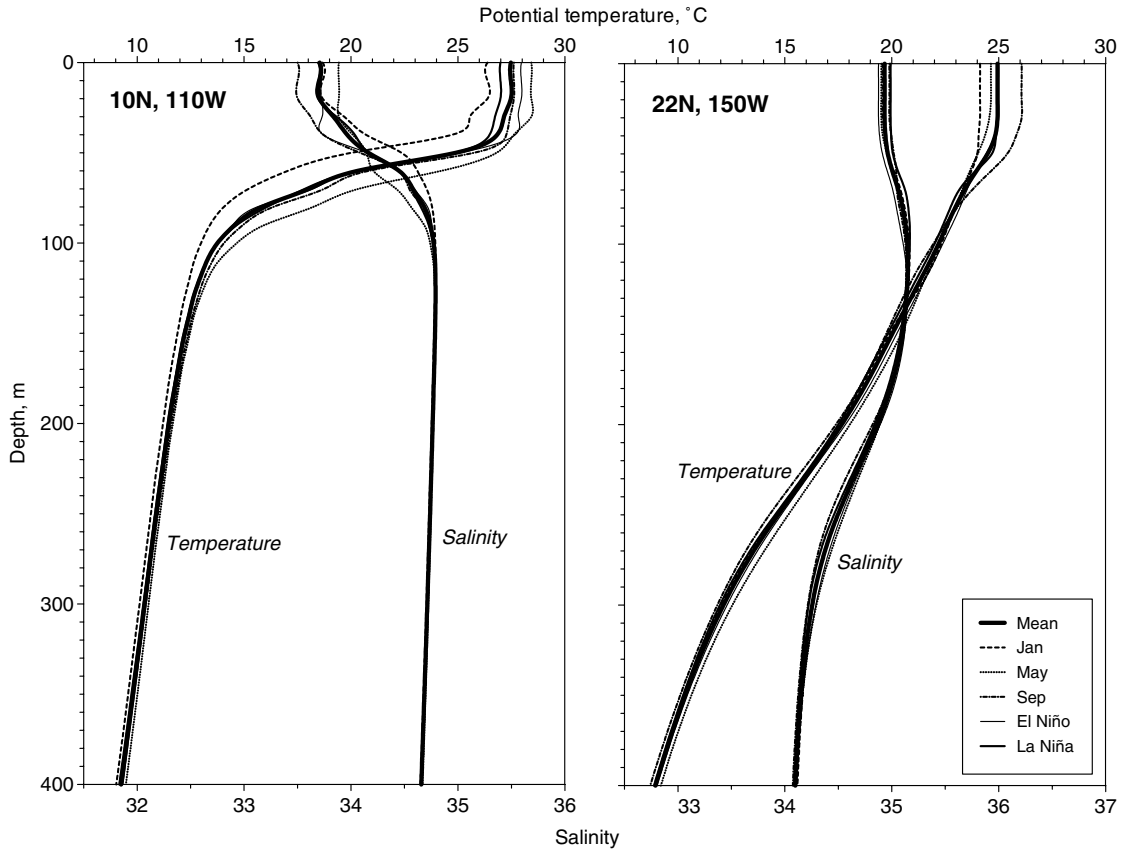

Figure 5.25 – Difference in mixed layer depths between 22°N, 150°W (The start of the cruise) and 10°N, 110°W (Top of TAO buoy line) reproduced from Fielder et al. 2006.

Mixed layer depth along the 110°W buoy line during TORERO was shallow and averaged around 60 m (section 5.4.1) which is comparable to literature data in the same region (figure 5.25). No CTDs were cast at the beginning of the cruise but literature data from 22°N, 150°W from the same source shows a deeper mixed layer depth which is due to lower sea-surface temperature, a shallower thermal gradient and a much less stratified halocline. A shallow mixed layer depth is usually associated with a supply of macronutrients (nitrate and phosphate) from cooler water beneath the thermocline (Pennington et al., 2006).

5.3.4 Nutrients

Within the TORERO study region, nutrient supply to the euphotic zone is controlled by the equatorial and the Peruvian upwellings. As discussed in section 1.3.3, upwelling supplies cold, nutrient rich water to the surface. Within the euphotic zone these nutrients can be utilised by phytoplankton to grow. The equatorial and upwelling regions of the ETP are enhanced in nutrients compared to the oligotrophic gyres to the north and south and the level of primary production is limited by the supply of the micronutrient, iron (Fiedler et al., 1991).

The ETP is notably deficient in iron (Chavez et al., 1996, and references therein) and leads to its classification as high nitrate-low chlorophyll (HNLC) waters. Addition of iron to this system results in increased primary production at a rapid rate and can be seen in the chl-a images of coastal regions (figure 5.29). The limited upwelling strength and low equatorial wind speeds encountered during TORERO likely result in both reduced upwelling of nutrients and less atmospheric transport of iron to the region.

5.3.5 Chlorophyll-a

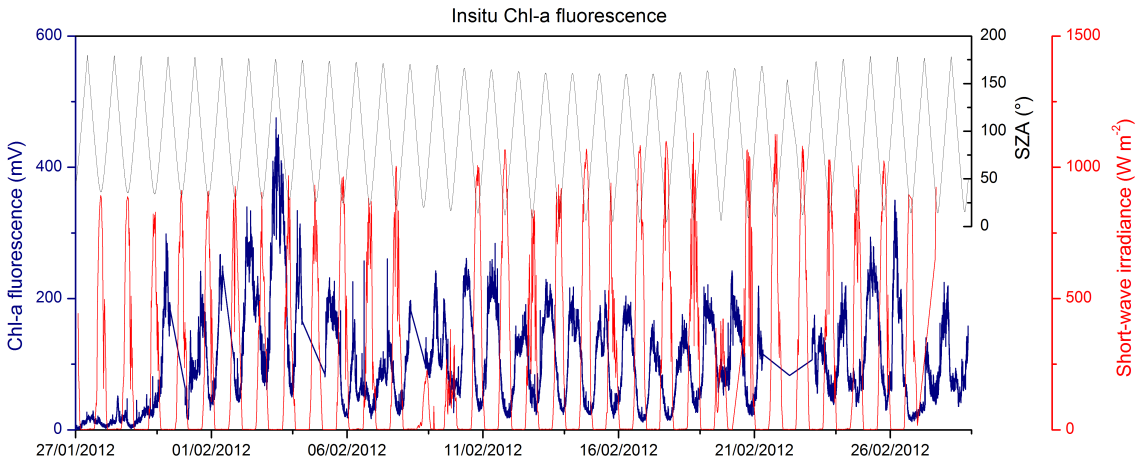

Figure 5.26 – Hourly averaged chlorophyll-a fluorescence measured using Turner C6 (blue line). Solar irradiance shown as red line, grey line denotes solar zenith angle.

Chlorophyll-a fluorescence displayed a negative correlation to solar irradiance with concentrations peaking at night and rapidly decreasing during the day. At first analysis this

could be attributed to the greater mixing of cold, nutrient rich water at night as surface water cools allowing phytoplankton to bloom. On closer inspection, the rate of concentration change is too fast for this cycle to be driven by production. It is more likely due to a physical factor such as the fluorescence by which the phytoplankton is being measured. Diurnal variations of *in vivo* fluorescence are well documented (Prézelin and Ley, 1980; Kiefer et al., 1989; Babin et al., 1996; Demmig-Adams et al., 1996; Maxwell and Johnson, 2000).

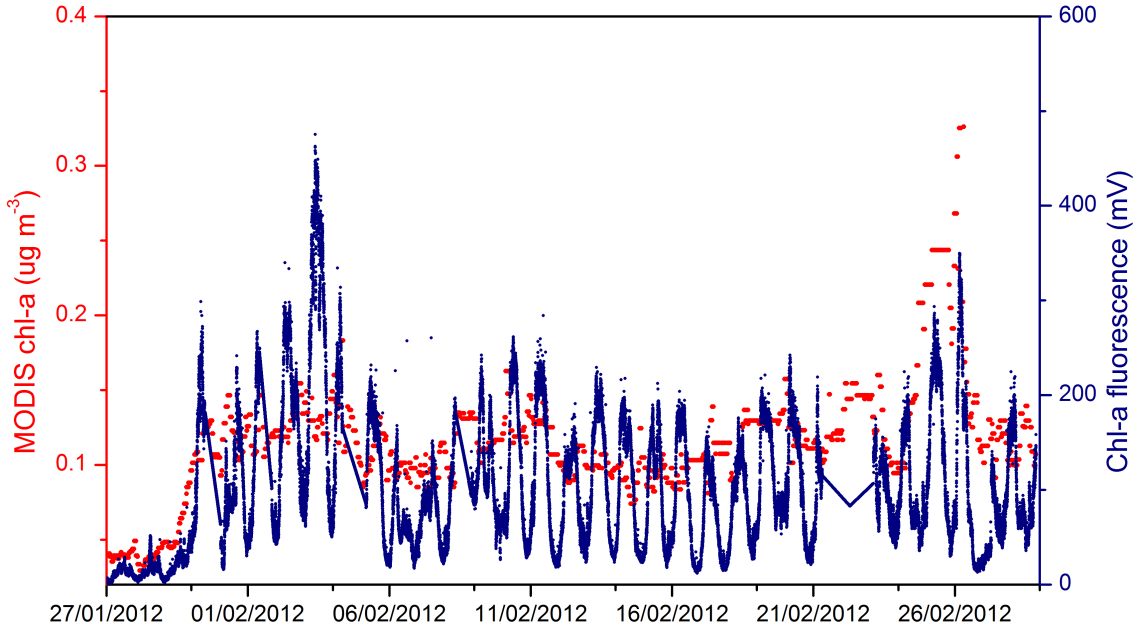

Figure 5.27 – Chlorophyll-a measured remotely from MODIS (red) and 1 min average in-situ using a Turner C6 fluorimeter (blue).

The cycle observed in TORERO can be explained by non-photochemical quenching. There are two processes which lead to reduced in-situ fluorescence; photochemical and non-photochemical quenching. Photochemical quenching is a rapid response to high solar irradiance where fluorescence is utilised by a cell to expel excess energy not required for photosynthesis. Non-photochemical quenching involves longer term (cells take hours to recover) photo-damage to reaction centres used for photosynthesis during exposure to high solar irradiance. Reaction centres become in-operant for photosynthetic and fluorescence processes causing a decrease in the fluorescence relative to solar irradiance (Dandonneau and Neveux, 1997).

The in-situ data compared well to satellite data from MODIS (figure 5.27). General trends

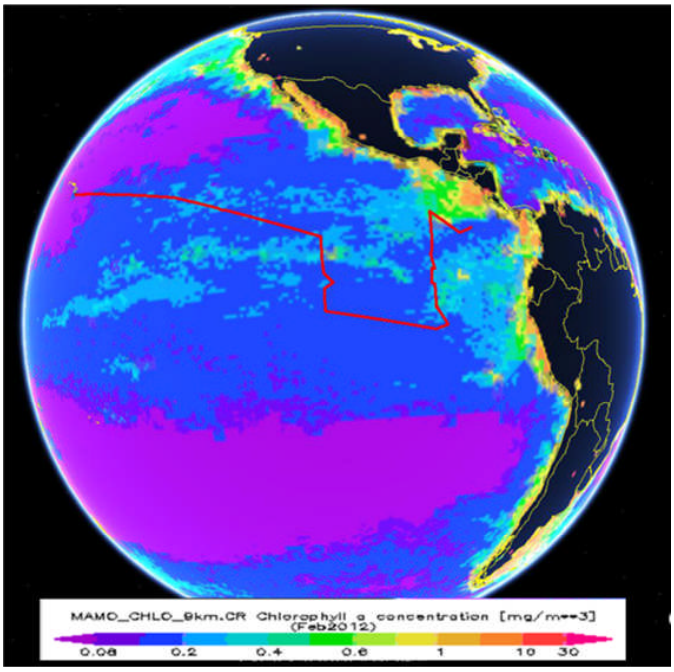

Figure 5.28 – Chlorophyll-a retrieval from NASA MODIS Aqua satellite average for the month of February 2012 overlaid onto Google Earth globe projection.

were captured by both techniques and the satellite data displayed some of the diurnal, negative sunlight correlation cycle seen in the in-situ measurements. A comparison of chl-a measurements between ship collected samples and satellite retrievals by Pennington et al. showed very good agreement in non-coastal regions (Pennington et al., 2006). Unfortunately, Chl-a primary standards were not available for calibration of the in-situ data during TORERO. However, the satellite data appeared to be an accurate representation of chl-a variability throughout the cruise, hence it was used as the primary indicator of bulk phytoplankton activity during data comparisons.

Chl-a satellite retrievals display an image of low productivity in the east tropical pacific during the month of February 2012. Global maps (figure 5.28) show some Chl-a enhancement along the Gulf of California and up around the western North American coast plus moderate concentration levels down the Peruvian and Chilean coast.

Higher resolution images (figure 5.29) highlight the Gulf of California, river outflows from Central America and Caribbean wind-jet driven coastal upwelling in regions such as the Gulf of Panama. The Peruvian and equatorial upwelling is very weak, displaying low

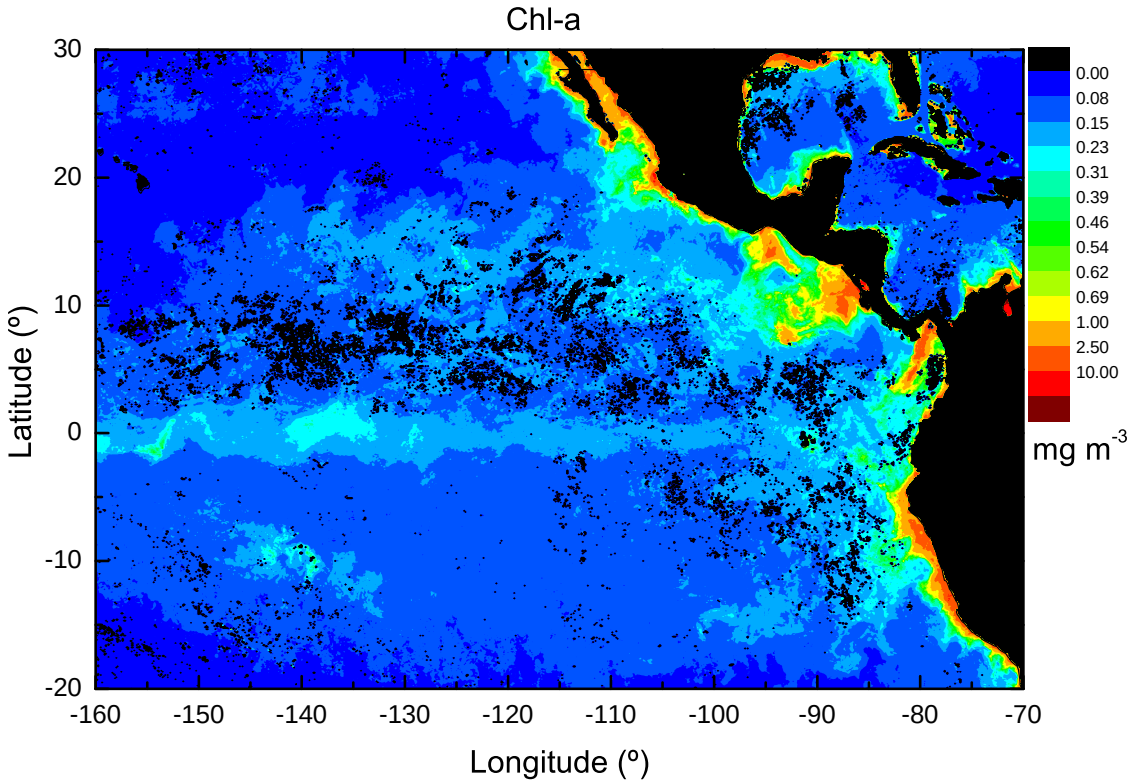

Figure 5.29 – 4 km resolution chlorophyll-a retrieval from NASA MODIS Aqua satellite average for the month of February 2012.

concetrations of chl-a, in-line with the observations of low wind speeds (figure 5.24), a weak cold tongue and warm surface ocean temperatures (figure 5.22).

5.3.6 VSLH in surface seawater and air

During the first few days of the campaign, concentrations of most VSLH were relatively high, especially the longer lived species such as CH_2Br_2 and $CHCl_3$ (∼1.1 and 11 pptv, respectively) which may indicate some coastal, island influence from Hawaii. $CHBr_3$ was relatively low (∼1 pptv), in-line with low Chl-a fluorescence.

$CHCl_3$, CH_2BrCl, CH_2Br_2, $CHBr_3$, CH_3I, CH_2ICl and CH_2I_2 all displayed significant temporal and spatial variation throughout the campaign. CH_2BrCl and $CHBrCl_2$ remained fairly constant, although the latter had a positive diurnal cycle (section 6.5.3). For the majority of gases, the measured surface seawater concentrations were positively correlated with air concentrations which is expected for localised oceanic emissions of VSLH (figure 5.30).

The only literature data available for the ETP is from the Blast I cruise in 1994 (Lobert and Elkins, 1996; Butler et al., 2007). Concentrations of $CHBr_3$ during TORERO were slightly higher, around 1–3 pptv compared to 0.5–2 pptv and showed a greater equatorial enhancement than during Blast I. CH_2Br_2 measurements during Blast I were consistent with TORERO and displayed a very similar NH/SH gradient with the Blast I measurements which extended further south to 50°S. Measurements of CH_3I again were in very good agreement between datasets with concentrations ranges for both cruises between 0.5 and 2 pptv. Neither cruise saw any equatorial or latitudinal gradient and the Blast I data showed concentration peaks above 20°N and below 20°S, which could indicate a correlation with SST or solar irradiance due to less cloud cover.

Air concentrations during TORERO were at the high end of measurement means, averaged globally of ∼1.1, 1.1 and 0.8 pptv for $CHBr_3$, CH_2Br_2 and CH_3I, respectively (Ziska et al., 2013). Water concentrations also fit into the range of previous measurements for $CHBr_3$ but were around 1 pmol dm^{-3} less for CH_2Br_2 (1–2 vs. ∼3) and up to 2 pmol dm^{-3} less for CH_3I (1–2 vs. ∼4).

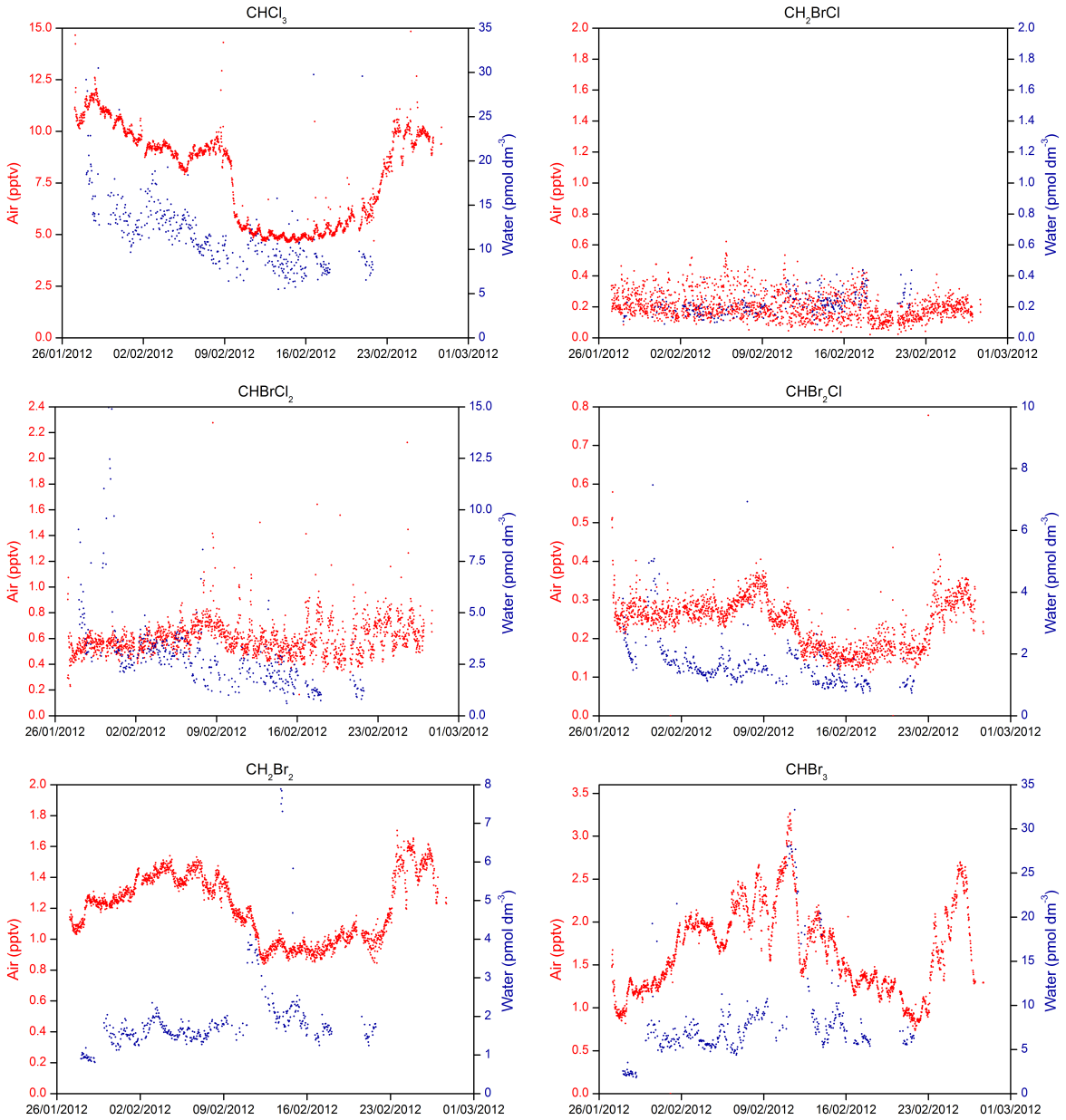

Figure 5.30 – Continued over...

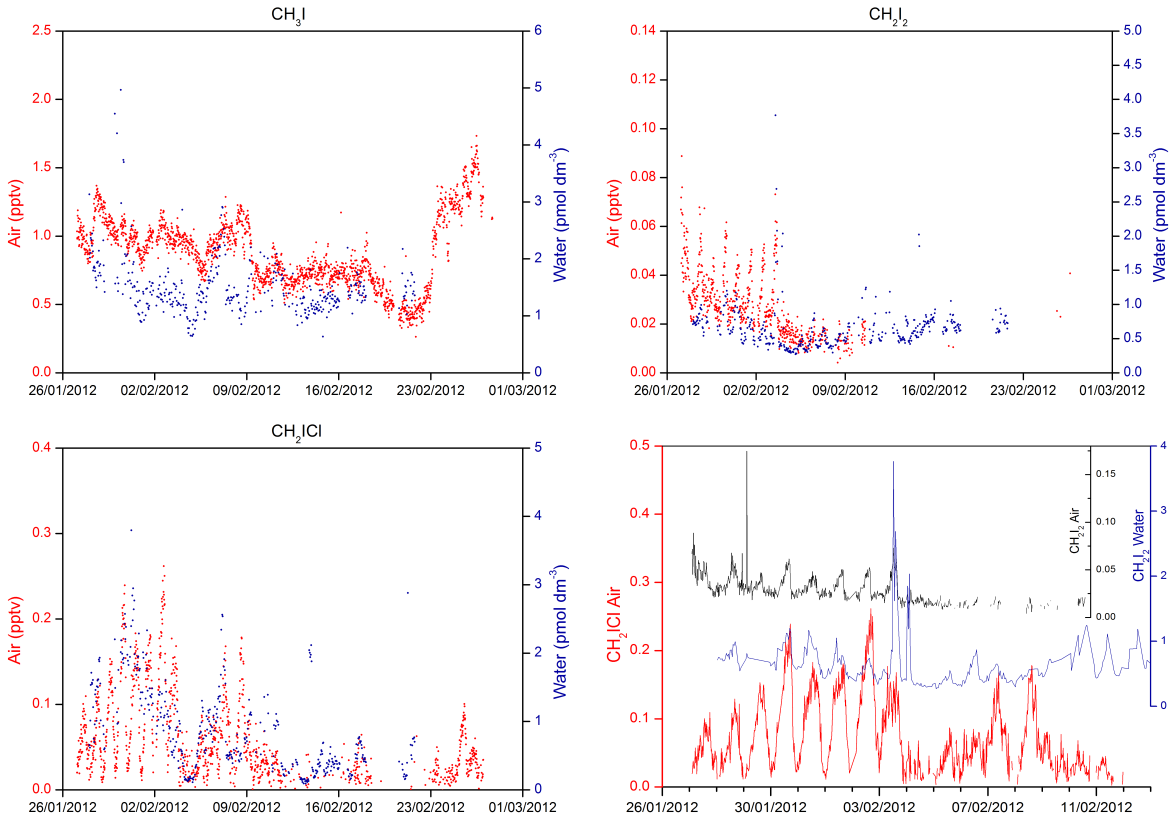

Figure 5.30 – Concentrations of VSLH in the air (blue) and surface seawater (red) during TORERO. Bottom right shows CH_2ICl in air (red), CH_2I_2 in air (black) and CH_2I_2 in water (blue) during section A of the cruise.

5.3.6.1 Iodocarbons

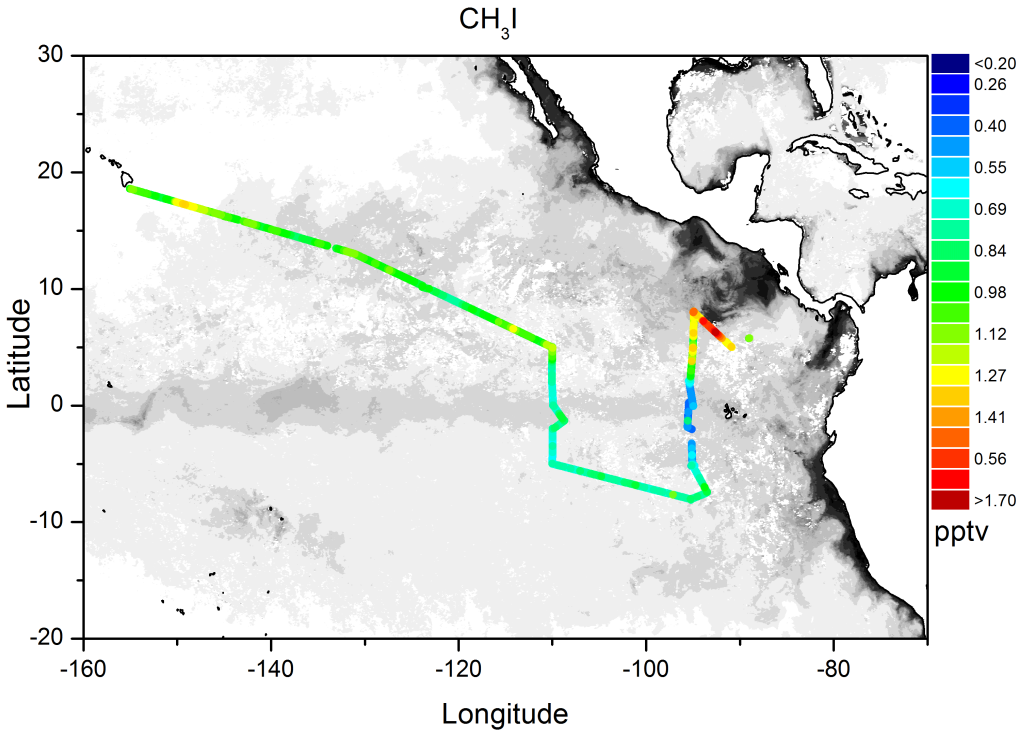

Figure 5.31 – CH_3I mixing ratios in air overlaid on grey scaled MODIS Chl-a.

CH_3I can be formed in the surface ocean (see section 1.5.3.1) and has been positively correlated with sea surface temperature (Yokouchi et al., 2001). CH_3I was detected almost ubiquitously in the ETP during TORERO (figure 5.31) although it did not show a strong correlation with SST. The first leg of the cruise displayed the lowest SST and a moderately high CH_3I concentration which dropped around 120°W despite an increase in SST. Cooler temperatures west of the Galapogos islands did result in a drop in CH_3I and concentration increased to its highest close to the warm pool but this could have been influenced by coastal upwelling, river outflow or the Costa Rica dome which result in the enhanced Chl-a that can be seen in the grey scaled MODIS satellite data in figure 5.31.

Back trajectories show that air sampled during the cruise has only passed over open ocean regions and has not had any coastal or terrestrial influence for at least 30 hours for section C which was the sampling region closest to land. As CH_2I_2 and CH_2ICl have lifetimes of <5 minutes and 2.5 hours, respectively (Montzka et al., 2011), these species are likely to have been emitted from the ocean. CH_2ICl showed evidence of an open ocean source, possibly from phytoplankton (figure 5.32). CH_2ICl was observed at elevated concentrations

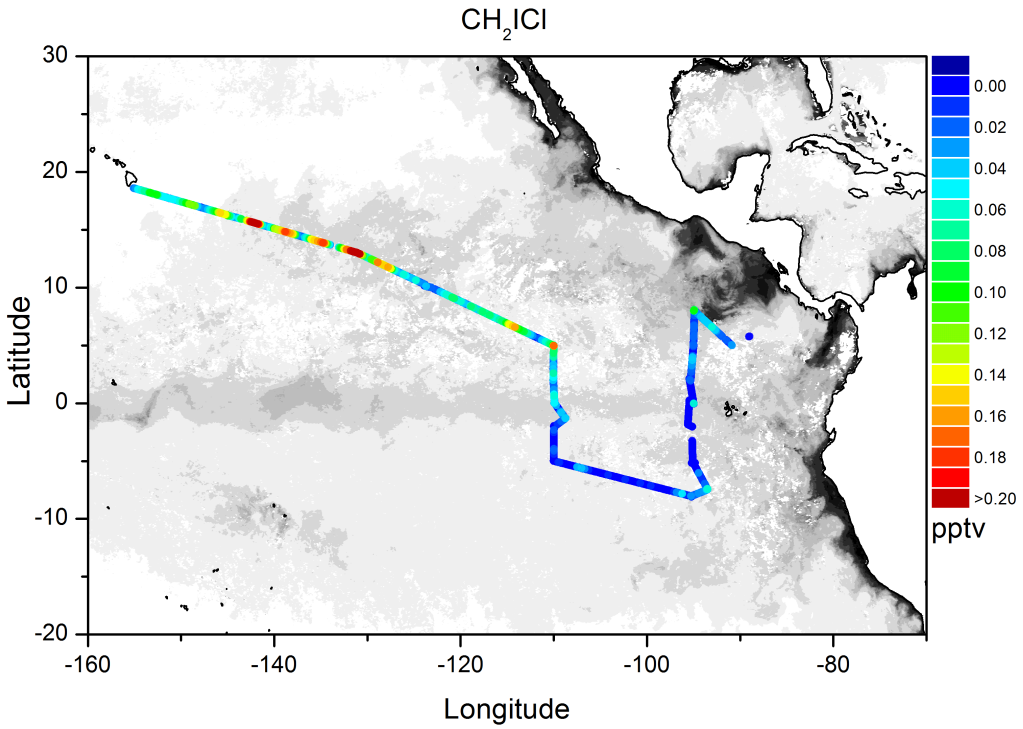

Figure 5.32 – CH_2ICl mixing ratios in air overlaid on grey scaled MODIS Chl-a.

in the open ocean in a previous research cruise (Moore and Tokarczyk 1993) and during the TROMPEX flights (Andrews et al. 2013, see chapter 4). Wind speed appeared to be driving the air and water concentrations with high wind speed resulting in greater flux and more mixing of the surface ocean resulting in higher CH_2ICl and CH_2I_2 concentrations (figure 5.30, bottom right). Open ocean air concentrations of CH_2ICl and CH_2I_2 were very low peaking at 0.25 pptv and 0.08 pptv, respectively with minima below the limit of detection. Due to the improving sensitivity of instrumentation, previous measurements may not have observed these low levels, with measurable concentrations encountered only at coastal or upwelling regions. Although the concentrations are small they could represent a widespread release over a very large area of ocean which could be significant to the MBL globally.

A modelling study of iodocarbons by Ordóñez et al. (2012) estimated a 2.5 fold greater flux from coastal to open ocean which was found to underestimate CH_2IBr. Increasing the flux by 5 fold, brought modelled values into line with observations but led to an over-estimation of CH_2ICl. This could be due to unaccounted for CH_2ICl flux in the open ocean as observed in this study. CH_2IBr was not detected in the open ocean measurements of

TORERO despite the instrument having a theoretical LOD of 0.04 pptv for this compound (see section 2.5.2.1, table 2.1).

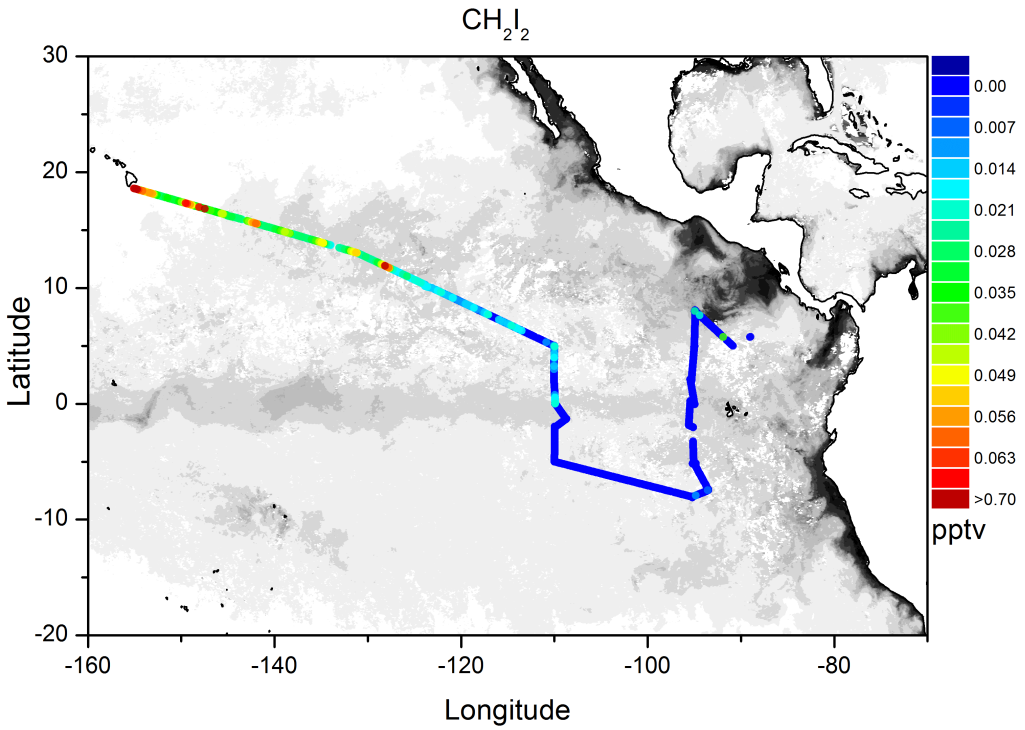

Figure 5.33 – CH_2I_2 mixing ratios in air overlaid on grey scaled MODIS Chl-a.

There is increasing evidence that disconnect exists between the iodocarbons and bromocarbons in the open ocean compared to coastal regions. One possibility is a difference in phytoplankton species present in open ocean regions that are a source of iodocarbons. There is evidence that in the ETP eutrophic coastal areas, large phytoplankton cells dominate and in the open ocean small cells are dominant (Pennington et al., 2006). Further study of iodocarbons should be accompanied by a much more comprehensive analysis of ocean biology and nutrient supply.

5.3.6.2 Chloro/Bromocarbons

Chloroform concentrations were highest at the start of the cruise close to Hawaii and were greater in magnitude in the Northern Hemisphere, displaying a distinct shift as the ship crossed the ITCZ. As chloroform has a lifetime of approximately 149 days (Montzka et al., 2011) the high concentrations at higher latitude could be an anthropogenic influence from

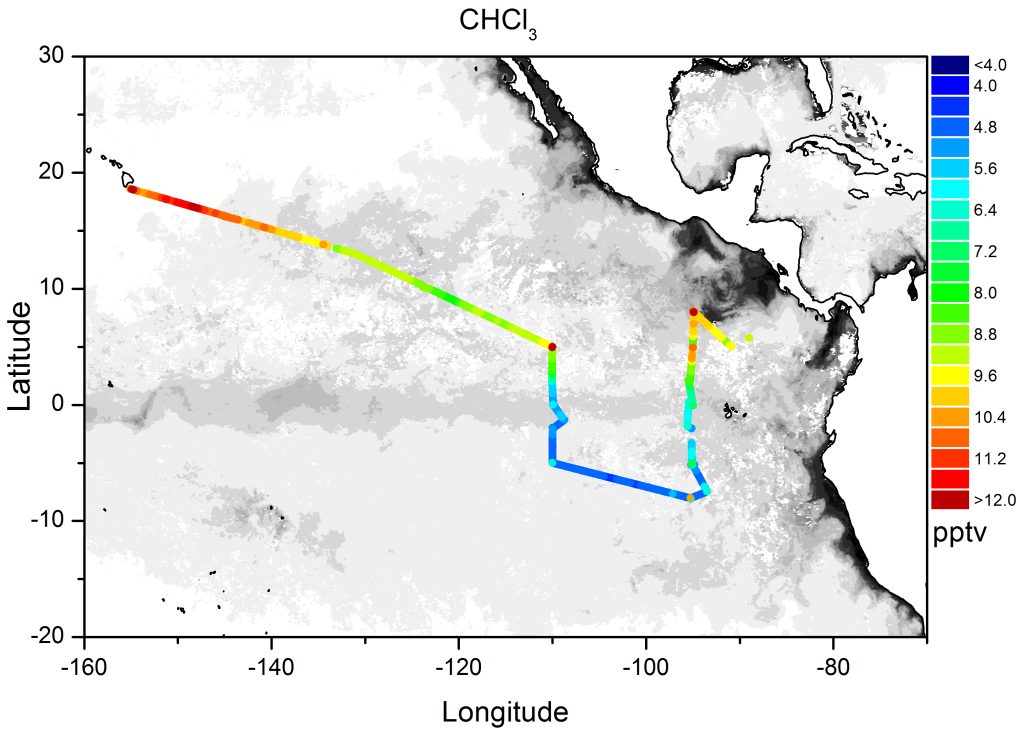

Figure 5.34 – $CHCl_3$ mixing ratios in air overlaid on grey scaled MODIS Chl-a.

North America. Wind speeds were highest between 140 and 120°W which would transport fresh terrestrial or coastal emissions from Mexico, however concentrations do not reflect this and perhaps the high concentrations at the beginning of the cruise were more heavily influenced by oceanic emissions, although Chl-a does not provide a link between emissions and ocean biology.

The bromochlorocarbons displayed less variation than the other VSLH with CH_2BrCl concentrations in water and air hardly changing throughout the cruise (figure 5.35). $CHBrCl_2$ displayed a diurnal cycle small in magnitude with average concentration remaining relatively constant; this is discussed further in section 6.5.3. $CHBr_2Cl$ had a larger range with higher concentrations observed from air trajectories originating from Mexico and Central America. It also showed a Northern- Southern Hemisphere concentration gradient similar to CH_2Br_2.

CH_2Br_2 and $CHBr_3$ are the largest contributors to MBL bromine of all the VLSH. CH_2Br_2 is relatively long lived (123 days, Montzka et al. (2011)) and shows influence from coastal upwelling and areas or high Chl-a upwind of the sampling site. These are most noticeable

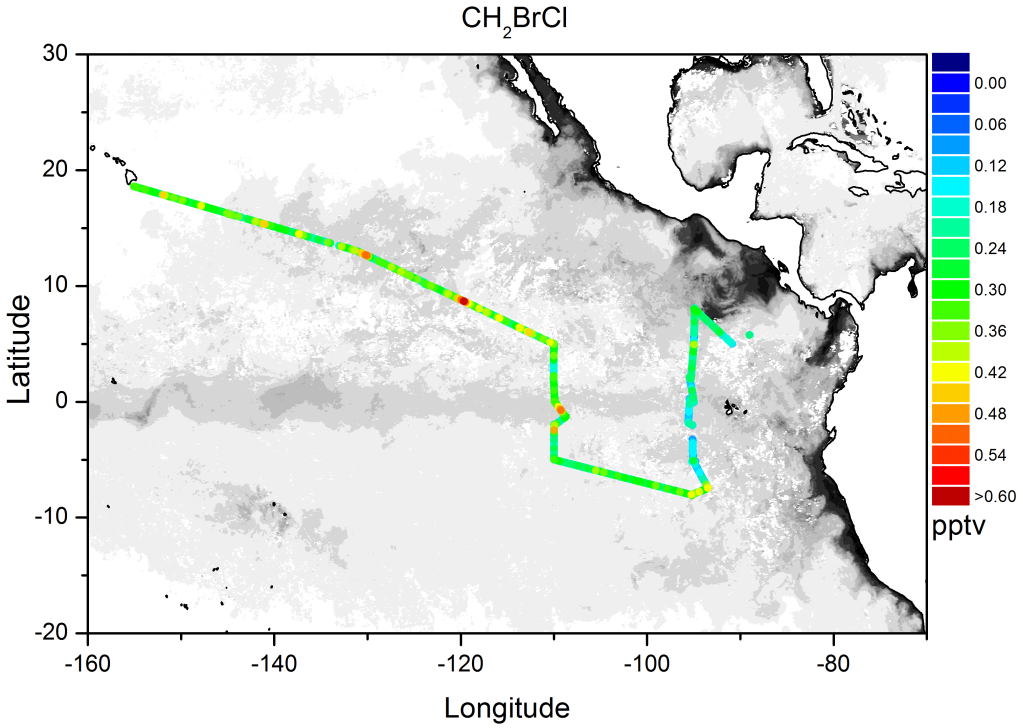

Figure 5.35 – CH_2BrCl mixing ratios in air overlaid on grey scaled MODIS Chl-a.

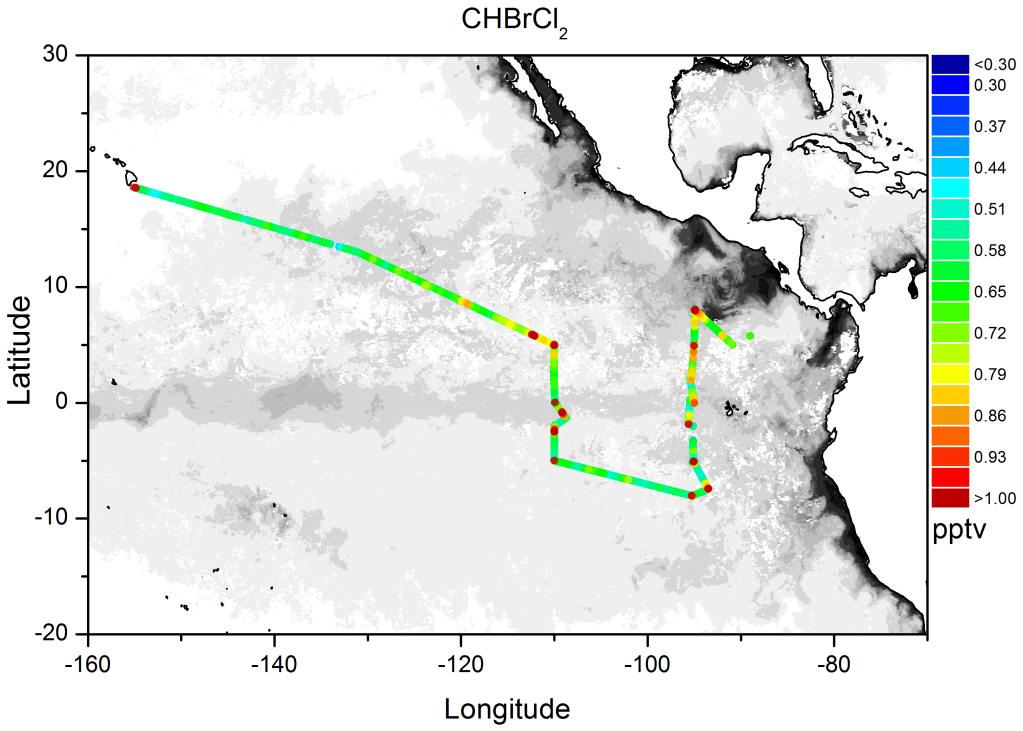

Figure 5.36 – $CHBrCl_2$ mixing ratios in air overlaid on grey scaled MODIS Chl-a.

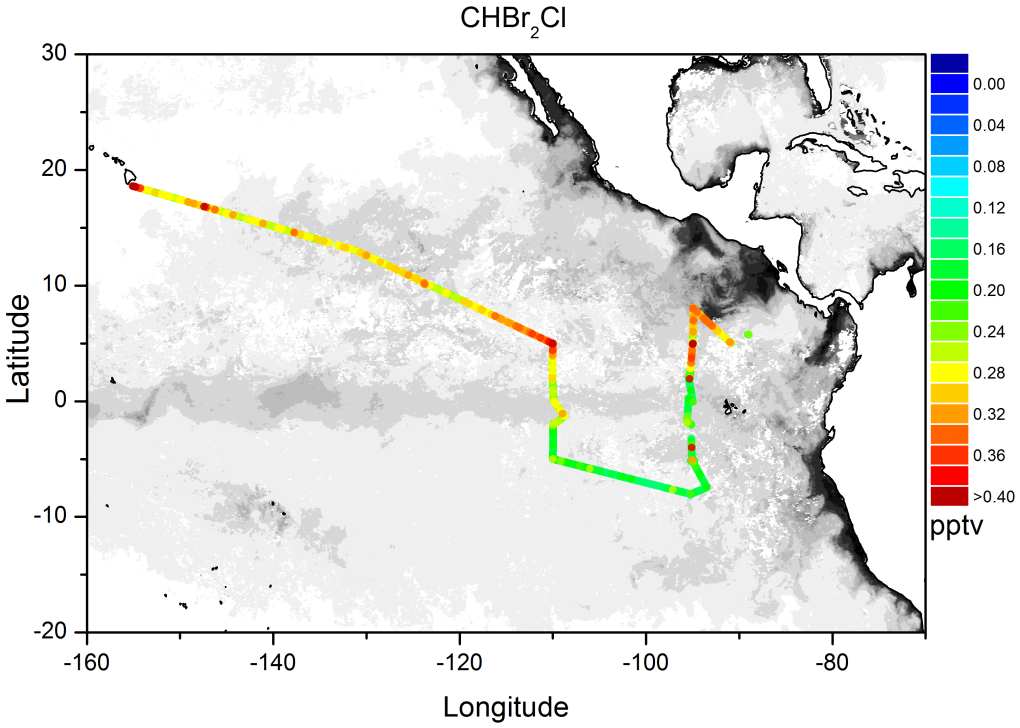

Figure 5.37 – $CHBr_2Cl$ mixing ratios in air overlaid on grey scaled MODIS Chl-a.

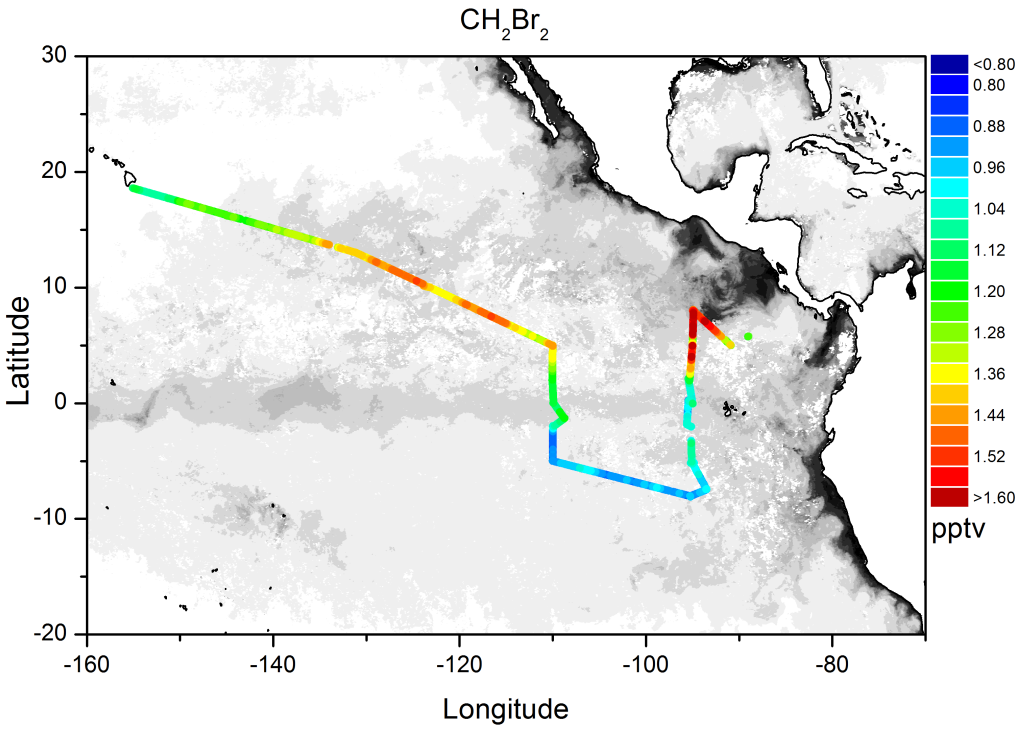

Figure 5.38 – CH_2Br_2 mixing ratios in air overlaid on grey scaled MODIS Chl-a.

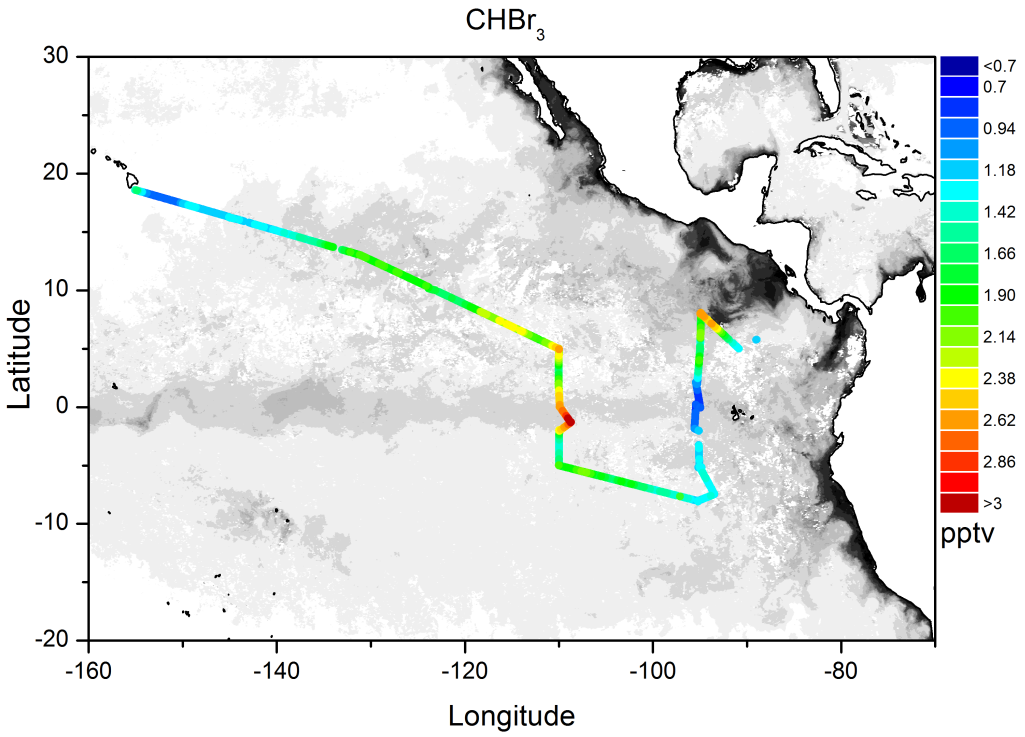

Figure 5.39 – $CHBr_3$ mixing ratios in air overlaid on grey scaled MODIS Chl-a.

during periods of high wind or closer to the Costa Rican coast when transport times are faster. As the CH_2Br_2 sink is mainly OH (photolysis lifetime >5000 days, Montzka et al. (2011)), emissions are able to travel long distances. Due to lack of NO_x and near constant convection at the ITCZ resulting in less entrainment of O_3 from the stratosphere, O_3 and thus OH concentrations are low in the TORERO study region. This would increase the local lifetime of CH_2Br_2.

CH_2Br_2 shows a distinct Northern-Southern Hemisphere concentration gradient at the ITCZ which is discussed in detail in section 6.5.2. Being shorter lived than CH_2Br_2, $CHBr_3$ displays less coastal influence and is likely more representative of the immediate ocean as back trajectories show that air parcels arriving at the cruise track were at least 4 days from land. Concentrations were greatest over the equator, which is consistent with previous datasets (Butler et al. 2007) but unusually the concentration drops off the west coast of the Galapagos Islands although this does correspond to the lowest wind speed regime encountered.

Figures 5.31–5.39 overlay VLSH onto Chl-a maps. In previous studies, MBL concentra-

tions have been directly compared with Chl-a in the ocean beneath the sampling site (O'Dowd et al., 2008; Carpenter et al., 2009). This approach often results in a good correlation for coastal or shelf regions of high productivity, however the boundary layer is very dynamic and air masses may not be representative of the position at which they were sampled. This is especially true of open-ocean measurements where background levels are low enough that influence from distant sources is significant. Arnold et al. 2010 used a Lagrangian transport model to determine the air mass history and calculate an age weighted Chl-a exposure value corresponding to each sampling position. This then takes into account the exposure each sampled air parcel has had to Chl-a along its back-trajectory, with a decreasing influence further back in time due to diffusion and atmospheric decay of the emitted species. This significantly increased the correlation of CH_3I, $CHCl_3$, CH_2Br_2 and $CHBr_3$ data from the OOMPH (Organics over the Ocean Modifying Particles in both Hemispheres) research cruise to a satellite Chl-a retrieval (SEA-WiFS). This study highlights the importance of understanding the air mass history when interpreting measurements of biogenic emitted VSLH.

5.3.7 GV vertical profiles

During section C of the TORERO cruise the GV aircraft (section 5.2.1) overpassed the KA on five occasions. For RF13 (Research Flight 13) the GV flew past the ship at low altitude and then started a vertical ascent. The intercalibrated instruments on board each platform allowed for comparison of surface air concentrations and atmospheric profiles for CH_2Br_2, $CHBr_3$, CH_3I and $CHCl_3$ (figure 5.40). Although inter-comparison of $CHBr_3$ between the two instruments was quite good (section 3.4.2), the variation seen in figure 5.40 is similar to the differences between the calibration techniques.

CH_3I and $CHBr_3$ display a typical vertical profile for short-lived gases showing exponential decay with altitude. Methyl iodide displays a distinct vertical profile in line with surface emission with subsequent dilution and photolytic degradation validating its use as a tracer for marine convection (Bell et al., 2002a). The $CHBr_3$ vertical profile is in agreement with data from TROMPEX in the tropical Atlantic (see chapter 4). CH_2Br_2 and $CHCl_3$ display a more unusual pattern with an enhancement above 5000 ft. This could be due to transport from coastal or terrestrial regions and is compounded by the longer lifetimes of these species which allows them to accumulate.

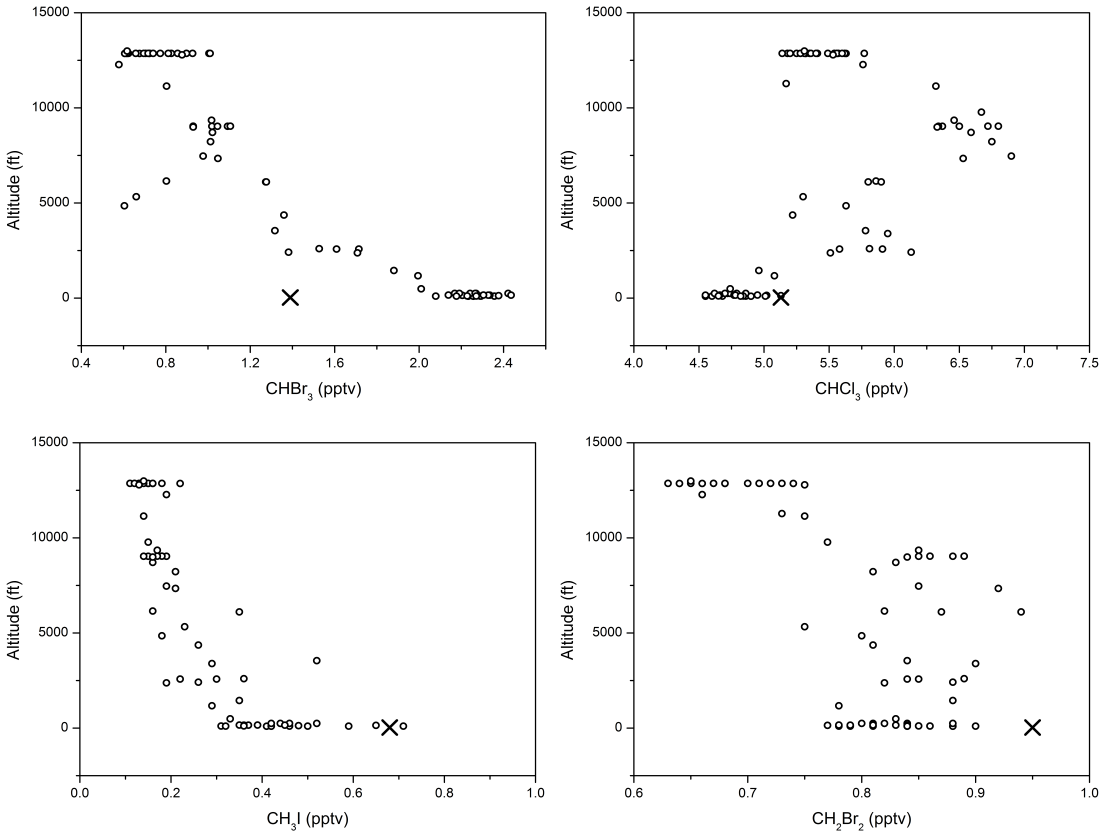

Figure 5.40 – Vertical profiles from the GV TOGA instrument after an overpass of the KA during RF13. Open circles denote GV data and crosses denote KA air sample

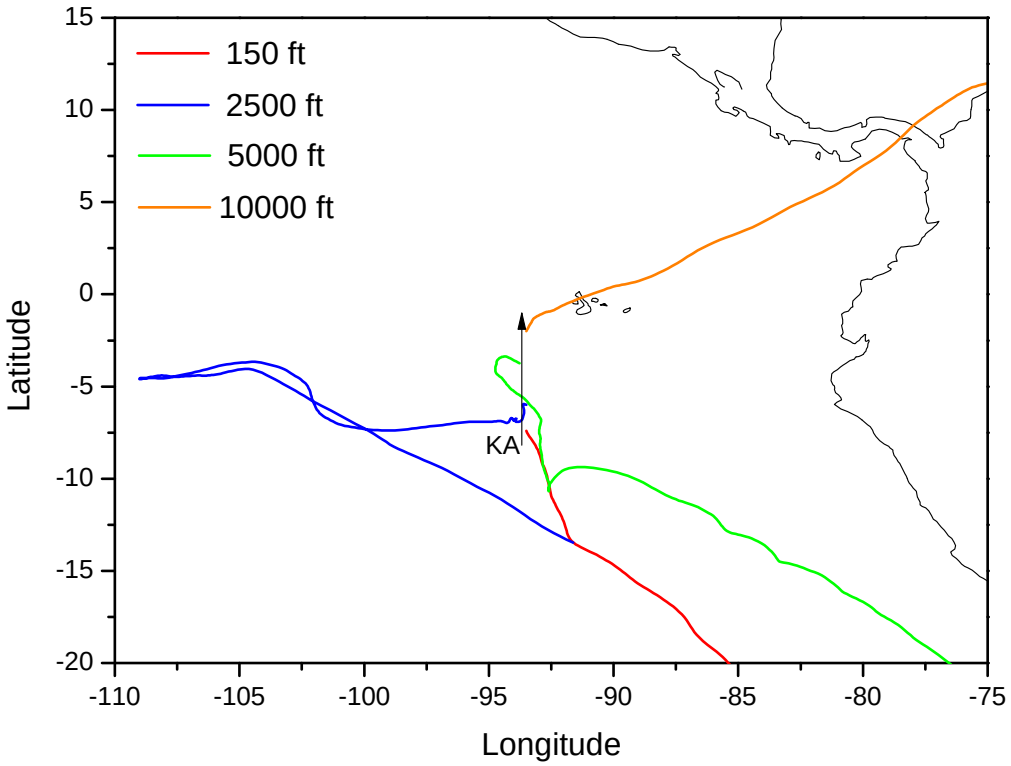

Figure 5.41 – 315 hr backwards trajectory modelled using NOAA HYSPLIT, corresponding to the vertical profiles (figure 5.40). Red line has a 150 ft AMSL start point, blue line is 2500 ft, green line is 5000 ft and orange line is 10000 ft. The position of the ship during the overpass is marked as 'KA' and the direction of GV flight indicated by the arrow

Figure 5.41 shows that the ITCZ moves further south with altitude and that a vertical profile starting at 100 m and ascending to over 10,000 m as tracked by the GV would result in sampling of multiple air mass origins throughout the climb. This could explain the enhancement above 5000 ft as air masses at higher altitudes have more Northern Hemisphere (NH) influence and have resided above the equatorial region for longer. This change in air mass origin from the Southern Hemisphere (SH) to the NH highlights the enhanced NH concentrations of CH_2Br_2 and $CHCl_3$. The reason for such NH/SH gradient is unknown and discussed in detail in chapter 6.

5.3.8 Diurnal cycles

CH_2ICl displayed the most notable diurnal cycle in the air data with concentrations steadily increasing during the night and rapidly decreasing at sunrise due to photolysis. This diurnal was even present in the surface water samples, consistent with the fact that that CH_2ICl is photochemically destroyed in seawater (Jones and Carpenter, 2005) (figure 5.42).

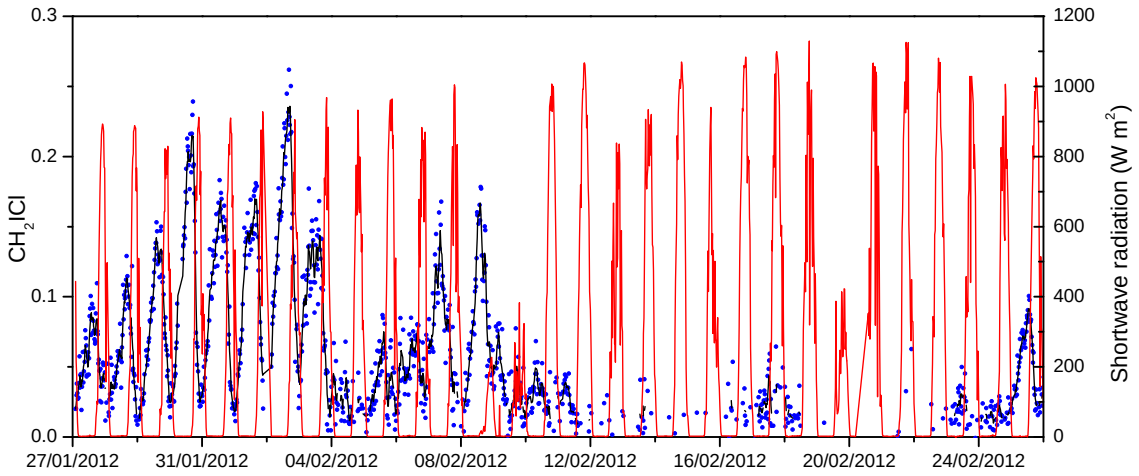

Figure 5.42 – Time series of CH_2ICl mixing ratios in air (blue circles, black line is 5 point adjacent average) and short-wave irradiance (red line).

During TORERO, from the 27^{th} January until 5^{th} February, wind speeds were high (>10 m s^{-1}) and peak concentrations of CH_2I_2 and CH_2ICl during the night reached their maximum measured during the campaign of 0.17 and 0.26 pptv, respectively. CH_2I_2 has an even shorter atmospheric lifetime than CH_2ICl and concentrations in the air were extremely low, dropping to below the LOD in the second half of the cruise. CH_2I_2 concentrations in

water displayed a diurnal cycle more prominent than for CH_2ICl with an extremely rapid decay at sunrise likely attributed to the photochemical reaction in seawater with Cl^- to form CH_2ICl and I^-.

Diurnal cycles were plotted for the entire TORERO dataset so that every data point taken within one specific hour of the day was averaged and plotted alongside measured solar irradiance (figure 5.43). This showed the rapid photolysis of CH_2ICl and CH_2I_2 occurring at sunrise and also a positive correlation of $CHBrCl_2$ and $CHCl_3$ with solar irradiance. The latter, positive correlations are studied in more detail in section 6.5.3. The drawback with plotting the diurnal cycles in this manner is that the ship was a moving measurement platform and as it sailed east it passed through multiple time zones. Instead of plotting against time of day, solar zenith angle (SZA) was used. In order to distinguish between AM and PM, a 360° SZA was calculated along the cruise track with 0° representing the sun being directly overhead. Averaging VLSH concentrations into 10° bins gives a better representation of diurnal cycles throughout the cruise. As the previous method was hindered by changes in longitude, this method has the problem that the SZA changes with latitude. To address this, the data was separated into Northern and Southern Hemisphere (figures 5.44 and 5.45, respectively).

Figure 5.46 shows that the diurnal cycle for CH_2ICl and CH_2I_2 is observed in water samples in addition to in air. This is the first time that a diurnal cycle for CH_2I_2 has been detected in surface seawater and as such has important implications for our understanding of iodocarbon and reactive iodine emissions into the MBL. The observation of such distinct diurnal cycles was made possible by the combination of the high sample throughput of the new automated purge and trap system and the homogeneous ocean region where the measurements were taken. The high sample throughput provided enough temporal resolution to capture the rapid photolysis at sunrise and the measurements in the oligotrophic ocean meant that multiple days of measurements were representative of physical processes rather than moving through areas of varying emissions as is often the case for coastal measurements.

A recent study by Ordóñez et al. (2012) assumed CH_2IX emissions followed a solar diurnal profile with peak emission in early afternoon and no emission at night, due to photosynthesis induced increased biological activity during the day. The modelled concentrations

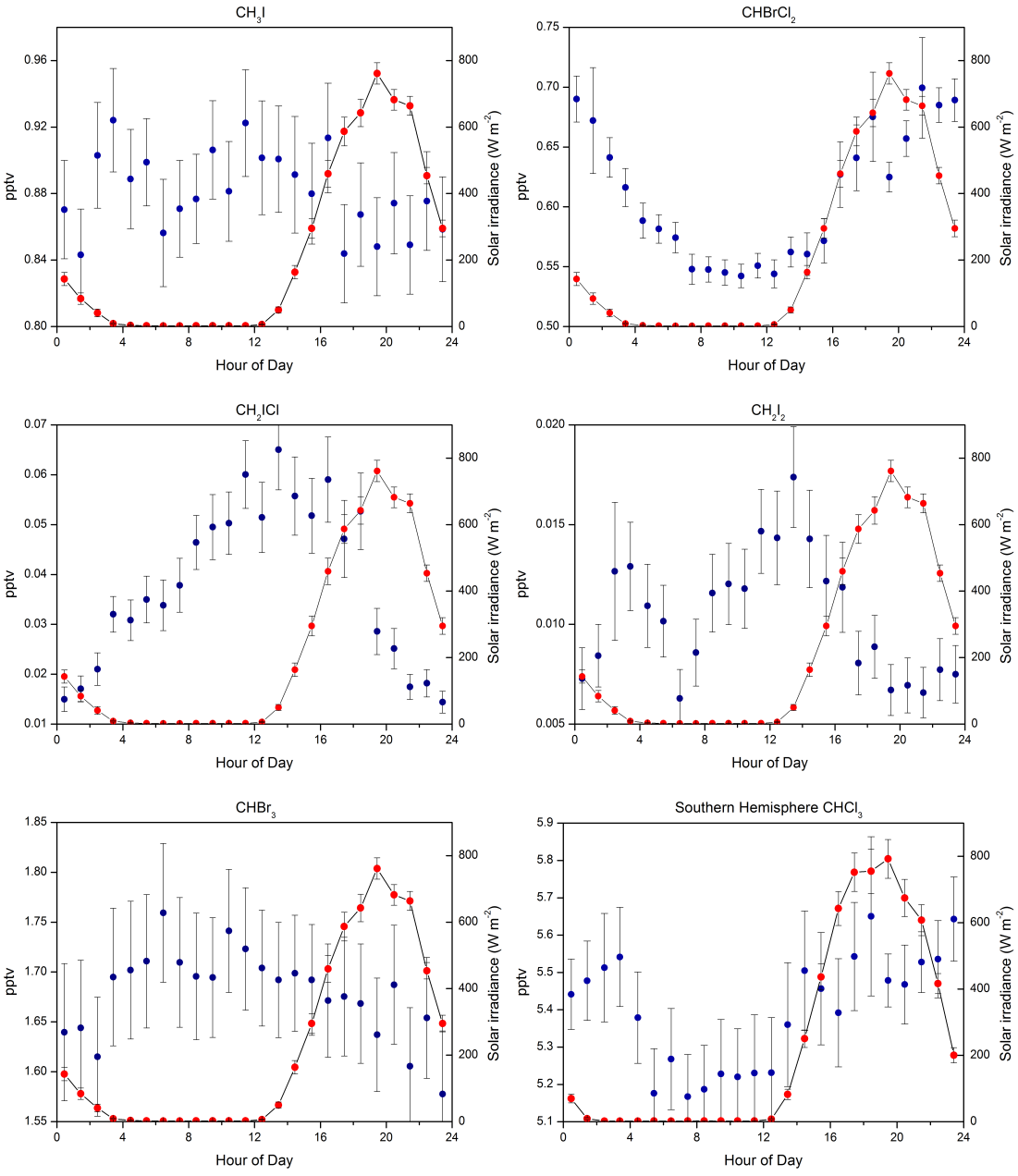

Figure 5.43 – VSLH concentrations averaged per hour of a day (GMT) as blue circles with short-wave solar irradiance overlaid as red circles. Error bars represent plus/minus one standard error.

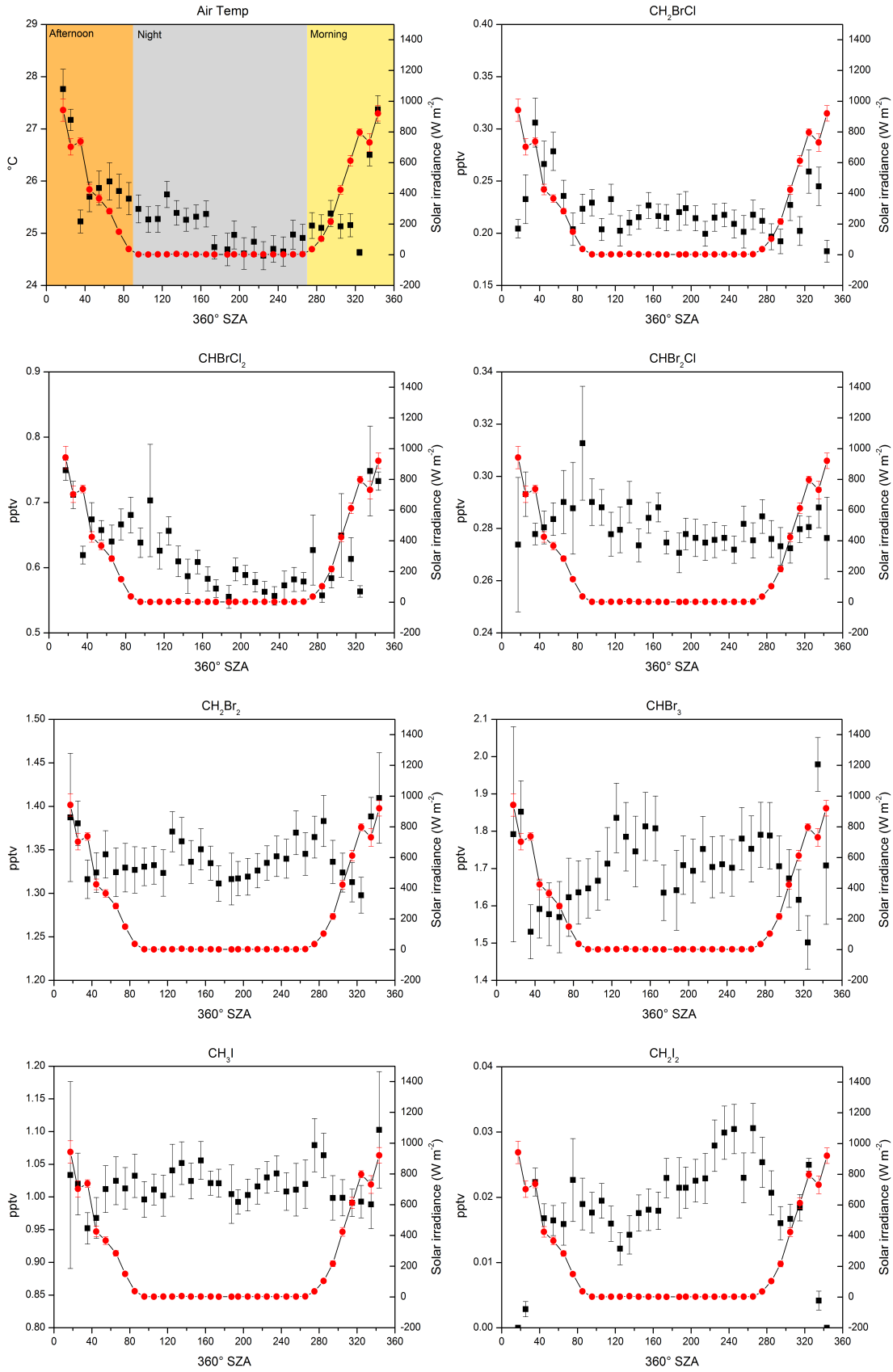

Figure 5.44 – Continued over...

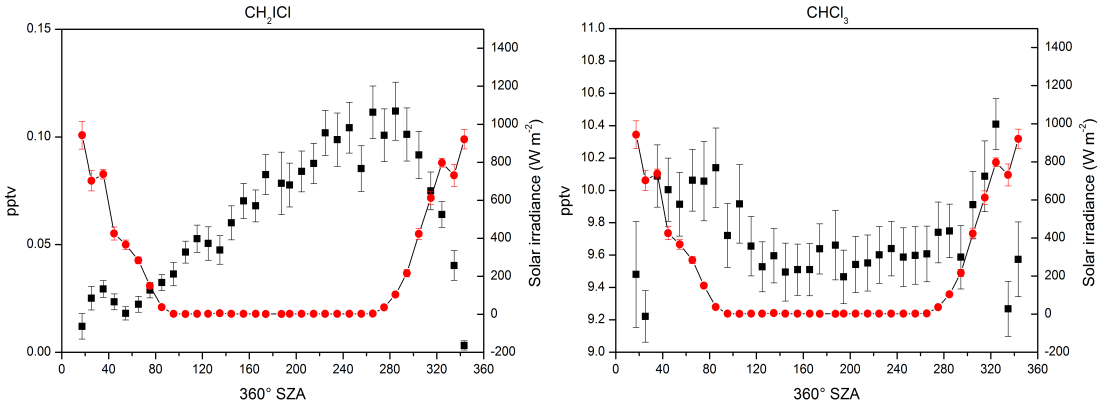

Figure 5.44 – VSLH concentrations in the NH averaged per 10° of 360° Solar Zenith Angle (SZA) as black circles with short-wave solar irradiance overlaid as red circles. Error bars represent plus/minus one standard error.

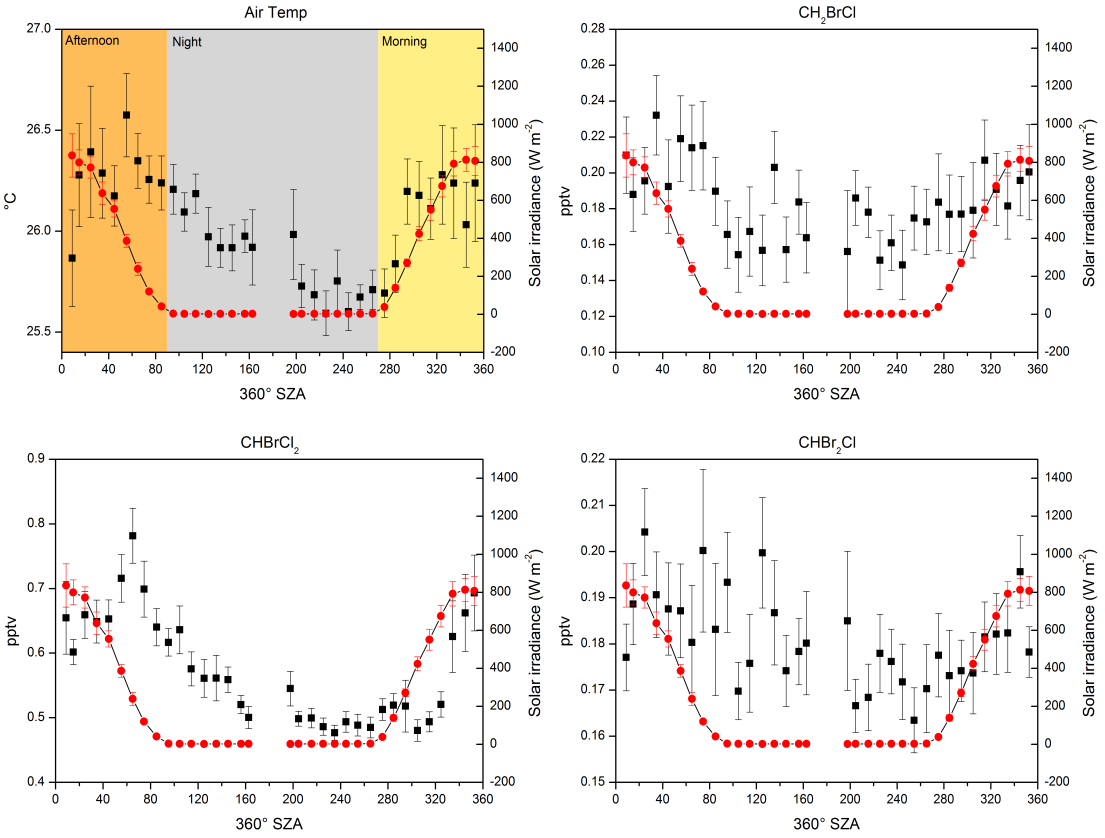

Figure 5.45 – Continued over...

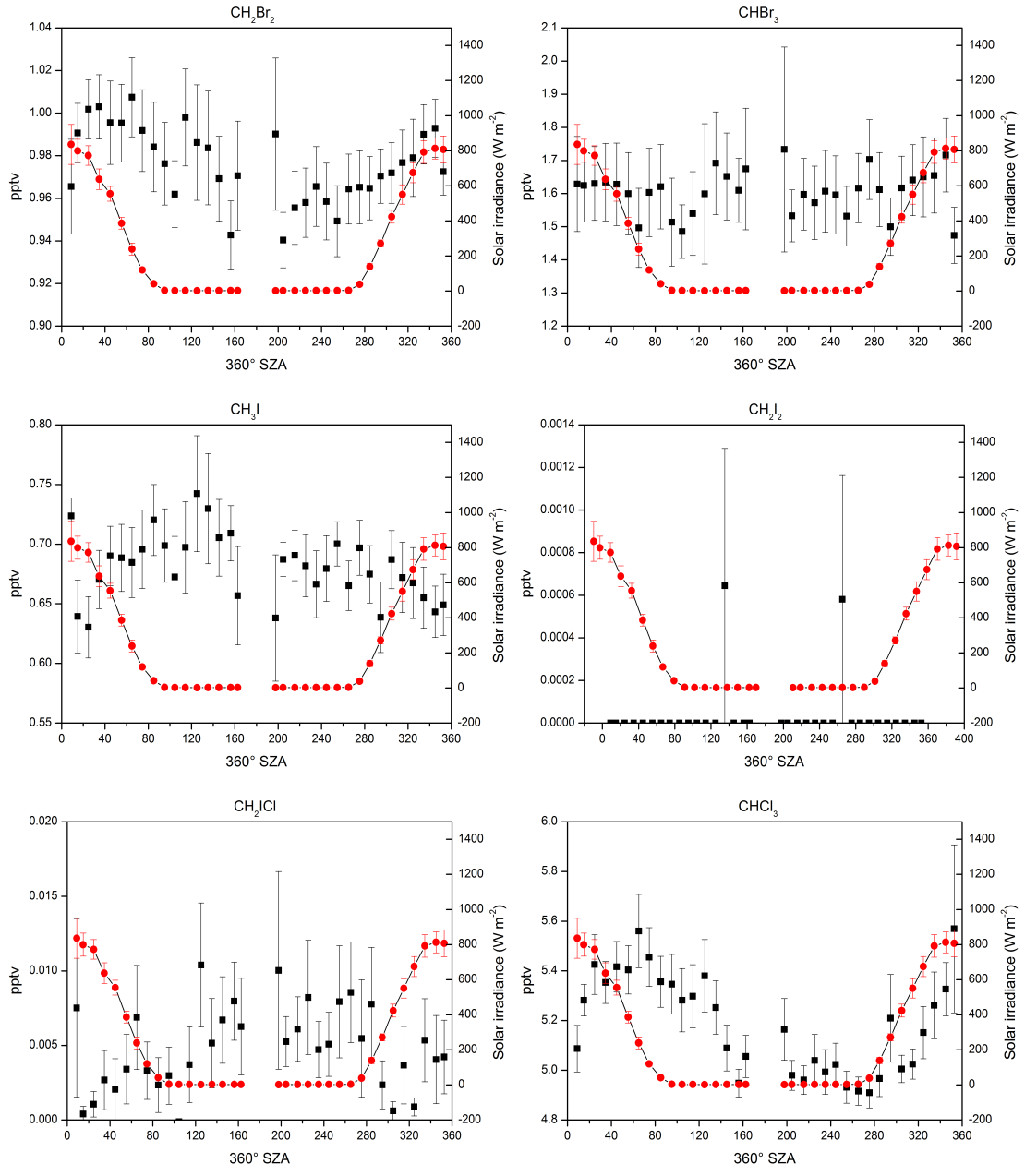

Figure 5.45 – VSLH concentrations in the SH averaged per 10° of 360° Solar Zenith Angle (SZA) as black circles with short-wave solar irradiance overlaid as red circles. Error bars represent plus/minus one standard error.

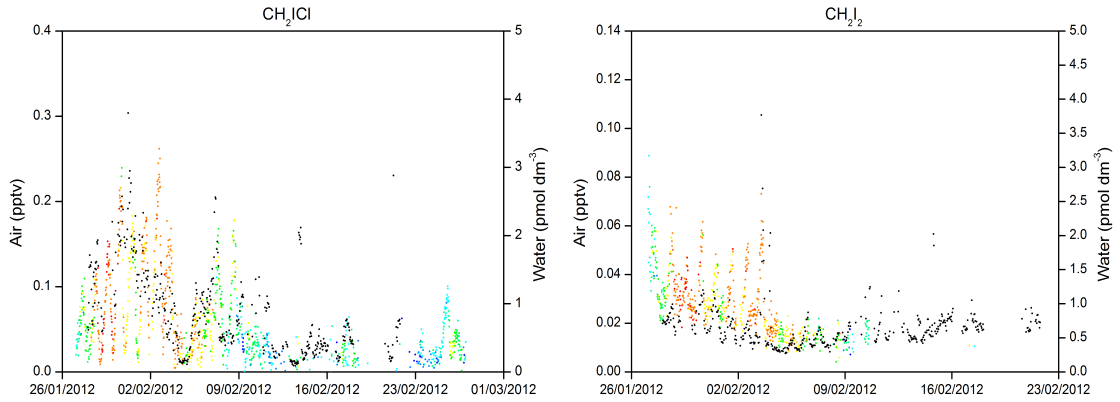

Figure 5.46 – Concentrations of iodocarbons in air (coloured by wind speed: blue is low, red is high) and water (black circles) for CH_2ICl (left) and CH_2I_2 (right).

of CH_2I_2 in air were largely underestimated compared to observations. The authors consequently increased the night-time emission to half that of the day which brought monthly average concentrations closer to observations. From the TORERO observations, the flux of CH_2I_2 during the night (see section 6.3.1) is far greater than that of the day. This is because the CH_2I_2 is rapidly photolysed within the surface seawater before it can transfer into the air resulting in very small emissions during the day. If measurements were taken closer to the coast or a strong source region then it is likely that daytime emission would occur. The photolysis of CH_2I_2 in the surface water still has implications for MBL iodine as it forms the product CH_2ICl. However, CH_2ICl is also photolytically degraded within the surface seawater though to a lesser extent than CH_2I_2. The TORERO dataset goes someway to understanding the shape of the diurnal emission profile which Ordóñez et al. (2012) emphasise is necessary in order to estimate the source strength of the shortest lived iodocarbons.

5.4 VSLH in the ocean

Surface ocean measurements were taken at 50 minute intervals along section A of the cruise. Along the 110 and 95°W TOA buoy lines (section B), on-line water samples were interrupted by the sampling of depth profiles from CTD casts. Normal on-line water sampling was resumed in section C. Due to problems with chromatography and instrument sensitivity during section C, this data has been omitted. The likely cause of these problems is the insufficient removal of water from the gas phase of the sample by the Nafion driers and subsequent build-up within the thermal desorption unit. Normally, cutting a short length off the front of the GC column or baking out the MS at elevated temperatures helps alleviate problems with water. In this case this did not solve the issue as the water was trapped inside the TD rather than the GC-MS, thus a preventative solution such as better water removal is required. This led to the development of the FPSC 'coldfinger' water trap (section 2.4.4.1).

5.4.0.1 CTD cross-sections

CTD profiles were taken at each degree of latitude along the 110°W buoy line. For each profile, water was sampled at 3, 20, 40, 60 80 and 100 m depth and analysed for VSLH. Temperature, salinity and fluorescence were measured at high vertical resolution in-situ with instruments mounted to the CTD cage. By compiling all the depth profiles at each degree latitude along the 110°W buoy line a cross section of the ocean across the equator can be visualised (figure 5.47). For the high resolution CTD data, such as temperature, the cross sections are interpolated between each degree latitudinally. The VSLH data is also interpolated through the vertical depth profile.

The extent of mixing in the surface ocean is dependent upon the mixed layer depth (isothermal layer). The thermocline remained very well defined and stratified down the 110°W line with warm surface temperatures creating a stable and shallow mixed layer (Figure 5.47). The mixed layer depth deepened above the equator whilst below the equator the halocline becomes less stratified and the mixed layer depth shallower. The increased salinity at equatorial and sub-equatorial latitudes is characteristic of cooler, denser water being upwelled in this region. According to Pennington et al. (2006) the yearly average for this

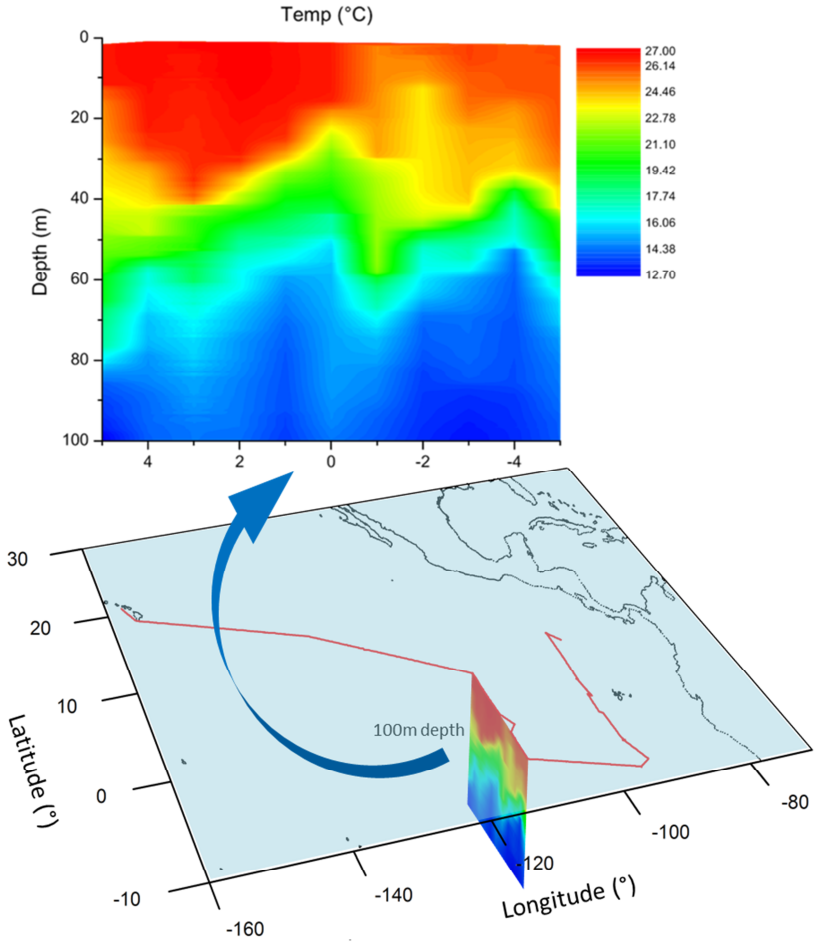

Figure 5.47 – Temperature cross section of the ocean between 5 and -5°N, 110°W with the location of the cross section portrayed in map format.

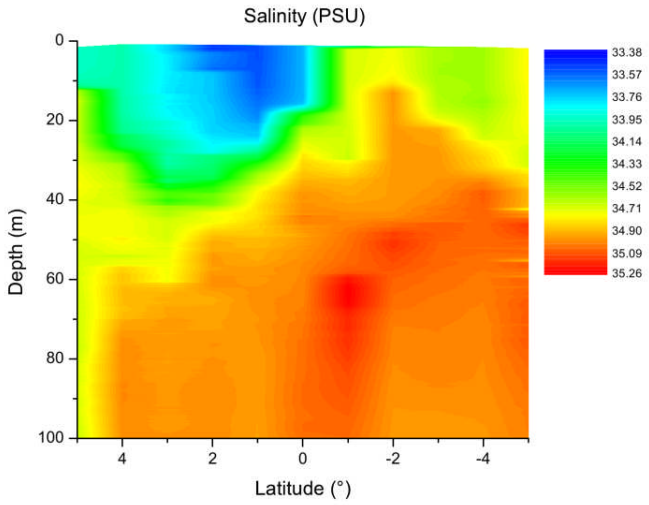

Figure 5.48 – Salinity cross section of the ocean between 5 and -5°N, 110°W

region above the equator (0–10°N) is a wind induced down-welling of ≈ 2 m day^{-}1. Below the equator there is net wind induced upwelling and average salinity is greater throughout the water column.

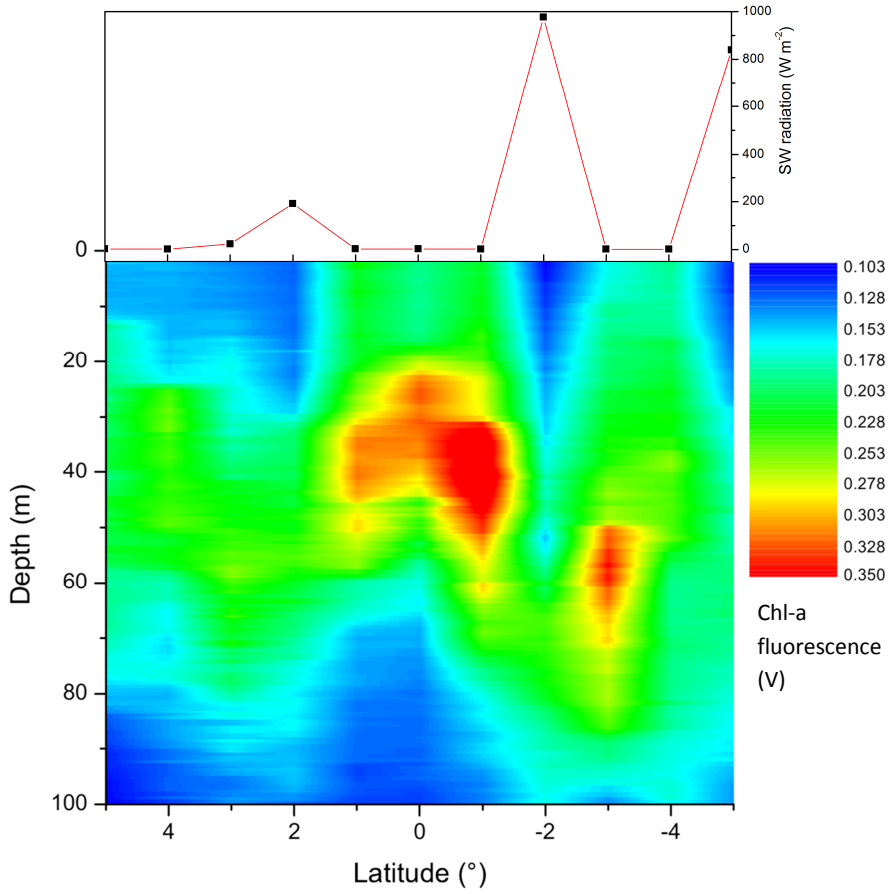

Figure 5.49 – Chl-a fluorescence cross section of the ocean between 5 and -5°N with solar irradiance (red line) depicting daylight and night-time casts.

Generally, the Chl-a maximum was between 30 and 60 m with the greatest concentration at the equator around 40 m depth. This is likely due to phytoplankton growth in nutrient rich water being upwelled with the greatest abundance of phytoplankton residing at a depth where solar penetration is sufficient for efficient photosynthesis yet temperatures are not so great as to inhibit growth. The increased Chl-a concentration at shallow depths at the equator and around 3°S compared to 2–5°N can be attributed to greater mixing and by the fluorescence behavior of Chl-a under different light conditions (discussed in section 5.3.5). This is evidenced by the anti-correlation of surface Chl-a fluorescence with shortwave irradiation shown at the top of figure 5.49.

5.4.1 Depth profiles

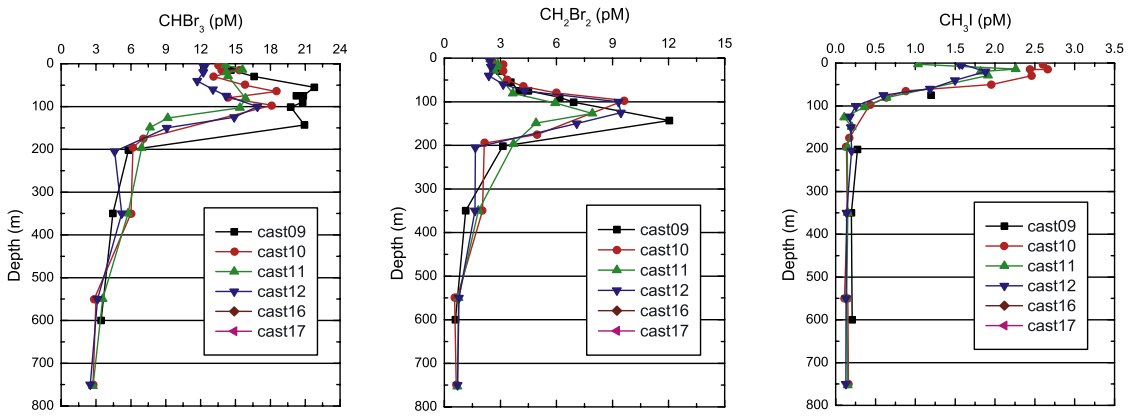

Figure 5.50 – Reproduced from Butler et al. (2007). Literature CTD casts collected during the PHASE 1 cruise at the equator, around 150°W showing $CHBr_3$, CH_2Br_2 and CH_3I

CTD casts were comparable to literature data (figure 5.50) with respect to CH_2Br_2 and $CHBr_3$ although the mixed layer depth was higher with concentrations of Chl-a and VSLH peaking around 40–60 m. CH_3I also agreed with literature data, displaying a surface influence (figures 5.51 and 5.52). A one dimensional profile plot, such as in figure 5.52, is often used to represent CTD profiles and by displaying data in this way it is easy to correlate VSLH concentrations with physical or biological parameters. For example $CHBr_3$, CH_2Br_2 and even CH_2ICl show strong correlation to Chl-a fluorescence while CH_3I is strongly correlated to temperature. This is only true in the depth dimension shown and by adding in a second dimension, latitude; it becomes clear that these correlations are not quite clear-cut (figures 5.53, 5.54 and 5.55).

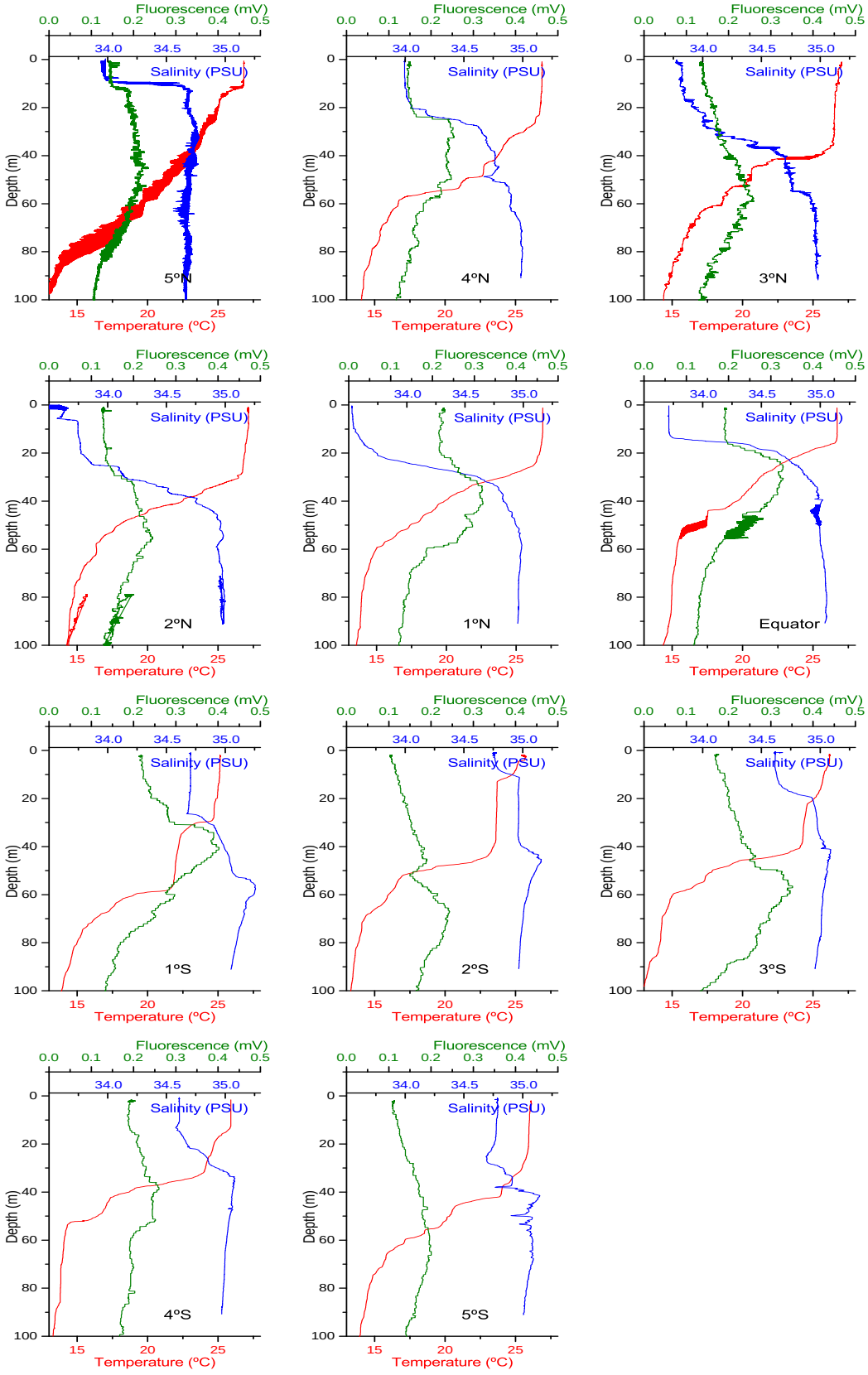

Figure 5.51 – Conductivity, temperature, depth (CTD) and fluorescence profiles for each degree between 5°N and 5°S along the 110°W TAO buoy line.

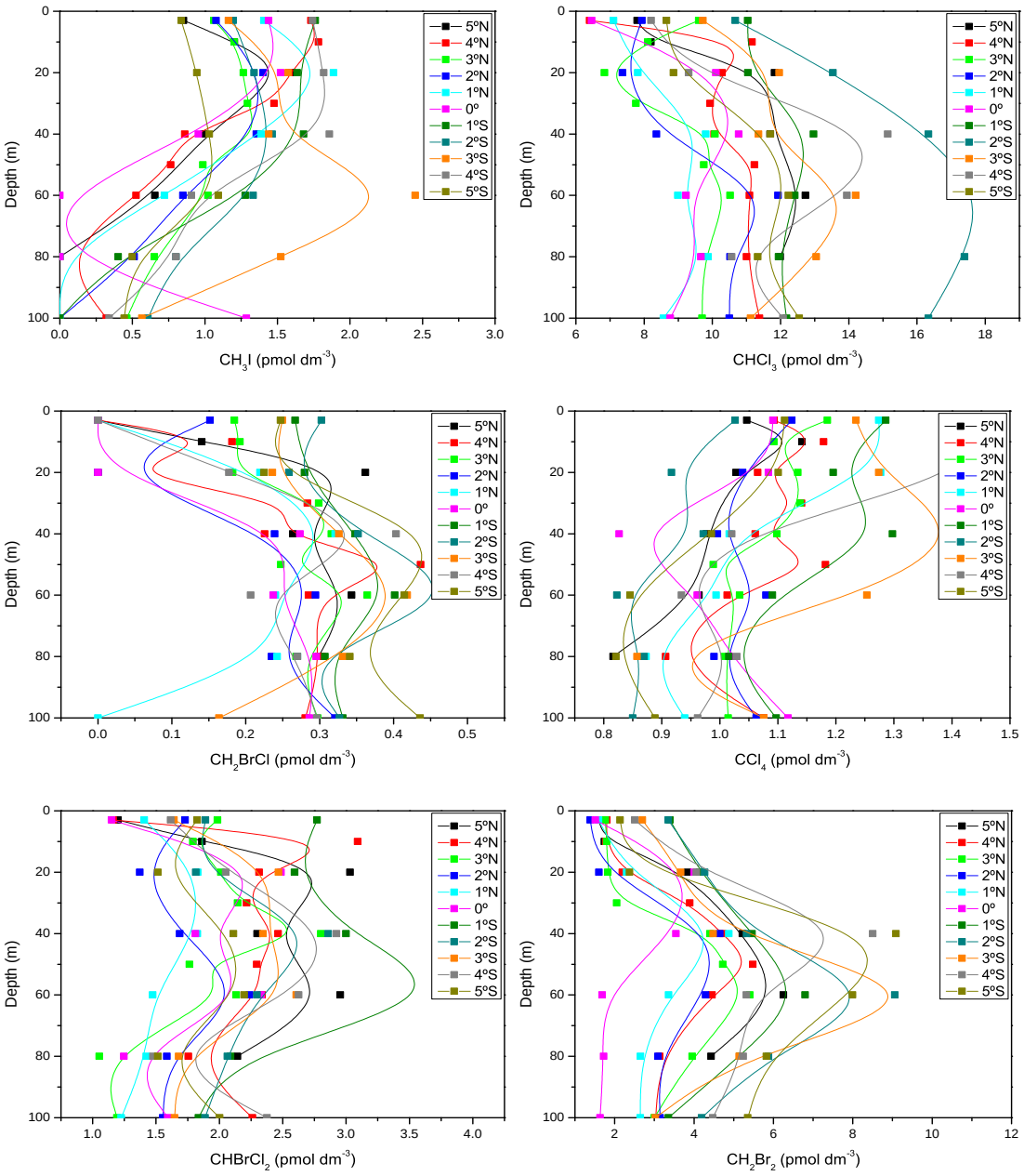

Figure 5.52 – Continued over...

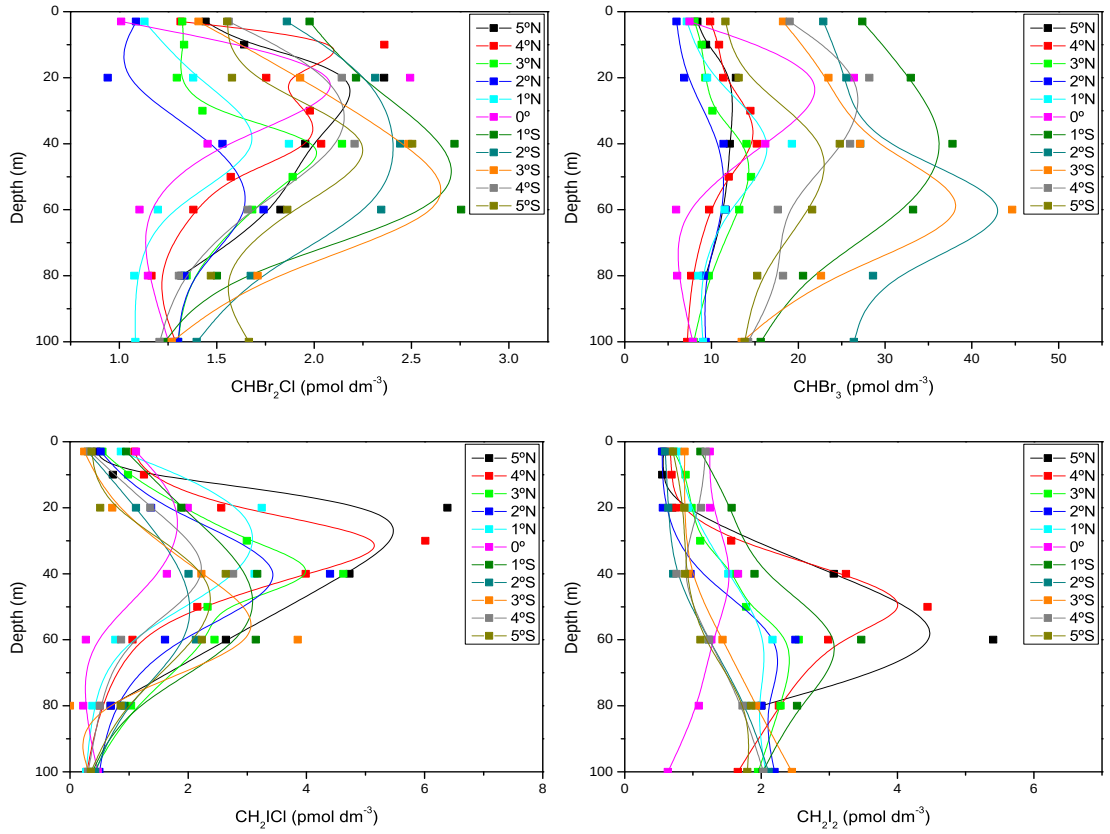

Figure 5.52 – VSLH measurements from CTD profiles taken at each degree between 5°N and 5°S along 110°W. Coloured lines are moving averages.

5.4.1.1 Iodocarbon depth profiles

The iodocarbon cross sections show that CH_2I_2 (figure 5.53) is concentrated at a lower depth (60–80 m) than CH_2ICl, which displayed a maximum typically at around 40 m depth, rising to around 20 m at the equator. Both show a similar latitudinal distribution which suggests a similar source or production of CH_2ICl as a photochemical product of CH_2I_2, which encounters higher solar radiation as it is mixed upward. This is inkeeping with literature observations of the direct photolysis of CH_2ICl to CH_2I_2 (Moore and Tokarczyk, 1992; Tokarczyk and Moore, 1994) in addition to iodine substitution by chlorine (Jones and Carpenter, 2005). CH_2I_2 concentrations, even at depth, are considerably lower than the concentrations of CH_2ICl in the overlying water. This could suggest either a biological contribution of CH_2ICl and/or the chlorination of CH_2I_2 still occurs at depths where solar radiation is strongly attenuated.

Varner et al. (2008) speculate that CH_2I_2 is the major source of CH_2ICl in surface water but a direct source of CH_2ICl from plankton or bacteria (Klick and Abrahamsson, 1992; Tokarczyk and Moore, 1994; Moore et al., 1996; Yamamoto et al., 2001; Amachi et al., 2005a,b) could also make a significant contribution. Surface waters were depleted in CH_2I_2 relative to 60 m depth highlighting its short photolytic lifetime. CH_2ICl has a longer photolytic lifetime and could be mixed to the surface although it too showed depletion in the top few meters of ocean. This in-situ photodissociation corroborates observations by Yamamoto et al. (2001) and Martino et al. (2005).

The CH_2I_2 maxima appeared to be deeper than the Chl-a maxima which could indicate that the biological species which produce CH_2I_2 are distributed differently to Chl-a or that CH_2I_2 is produced in the senescence (dying) phase of sinking phytoplankton (which are no longer fluorescing). Interestingly, the maximum CH_2I_2 and CH_2ICl concentrations were measured at 5°N where the Chl-a maxima was at its lowest concentration, unlike the bromocarbons, chlorocarbons and even CH_3I which displayed a maxima at 3°S. Yamamoto et al. (2001) observed CH_2I_2 and CH_2ICl which correlated well with Chl-a in depth profiles collected from the Bay of Bengal, although these were more coastal measurements compared to the open ocean measurements during TORERO.

Mahajan et al. (2012) reported a positive correlation between CH_3I and SST in the Eastern Pacific which suggested a non-biological mechanism for its production and noted a negative correlation with Chl-a. During TORERO, CH_3I displayed a much different distribution to the other iodocarbons with the highest concentrations generally being at the surface. This supports the theory of surface photochemical production from radical recombination (see section 1.5.3.1). CH_3I also displayed a maxima at 60 m depth at 3°S which correlates with a maxima for the bromocarbons and is a point of enhanced Chl-a. This could be due to biological production or to accumulation at the MLD without the large loss term from flux to the atmosphere that controls the surface concentrations.

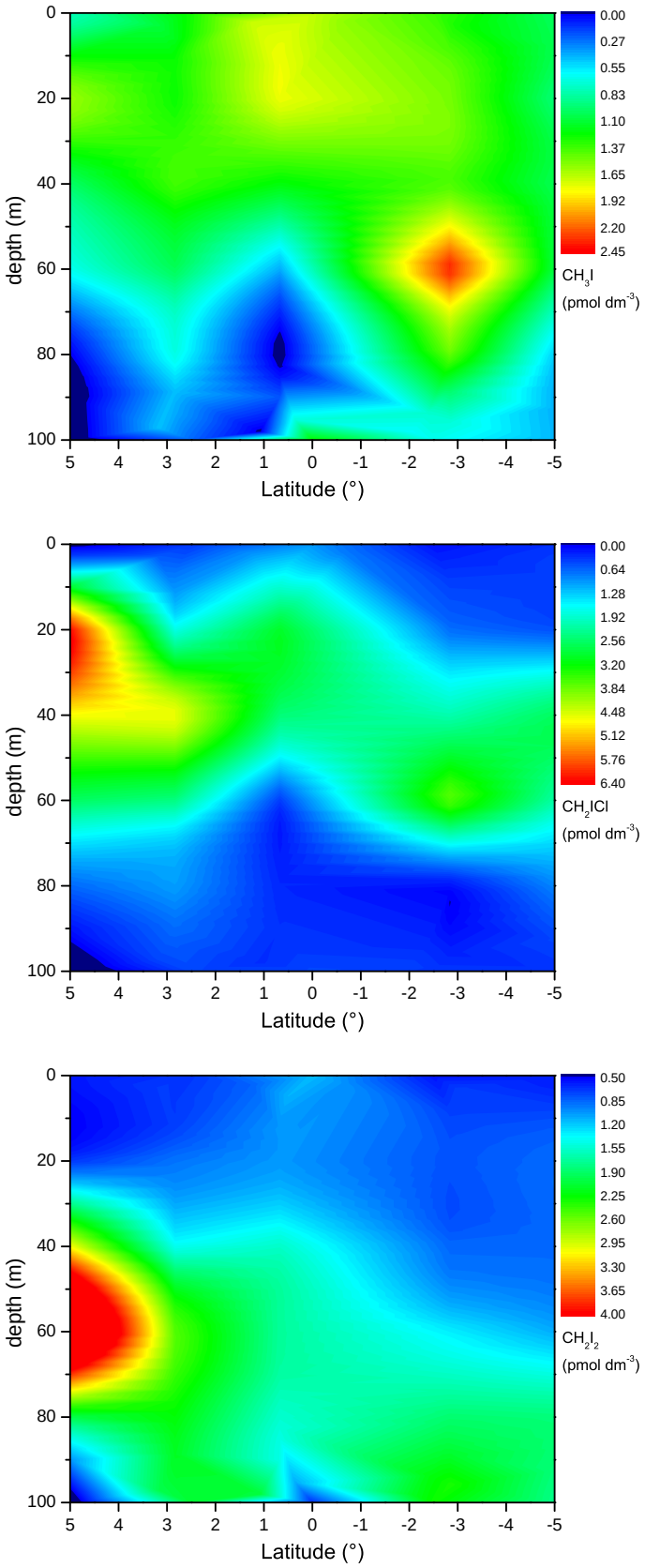

Figure 5.53 – Iodocarbon cross sections of the ocean between 5 and -5°N

5.4.1.2 Chloro/bromocarbon depth profiles

Despite their correlation in air and surface water (section 5.3.6), CH_2Br_2 and $CHBr_3$ showed noticeably different distributions in their depth profiles. This could be due to differences in their lifetimes or to a different distribution of their production sources. $CHBr_3$ and CH_2Br_2 are believed to have similar sources due to their linear correlation ratio which is often consistent in magnitude between regions (Butler et al., 2007). Hughes et al. (2013) showed that CH_2Br_2 can be formed from $CHBr_3$ in diatom cultures and that CH_2Br_2 was susceptible to bacterial breakdown. $CHBr_3$ was not broken down but bacteria did inhibit its production. The marine diatoms studied produced both CH_2Br_2 and $CHBr_3$ but the latter was restricted to the growth phase. This study suggests that differences in CH_2Br_2 and $CHBr_3$ distribution could be encountered, coinciding with different stages in the diatom life-cycle and/or bacterial influence. Ignoring minor differences, the chloro/bromocarbons, with the exception of $CHBrCl_2$, all show a similar pattern with a maxima at around 60 m at 3°S and although generally showing a similar trend to Chl-a, they all lack its large equatorial enhancement.

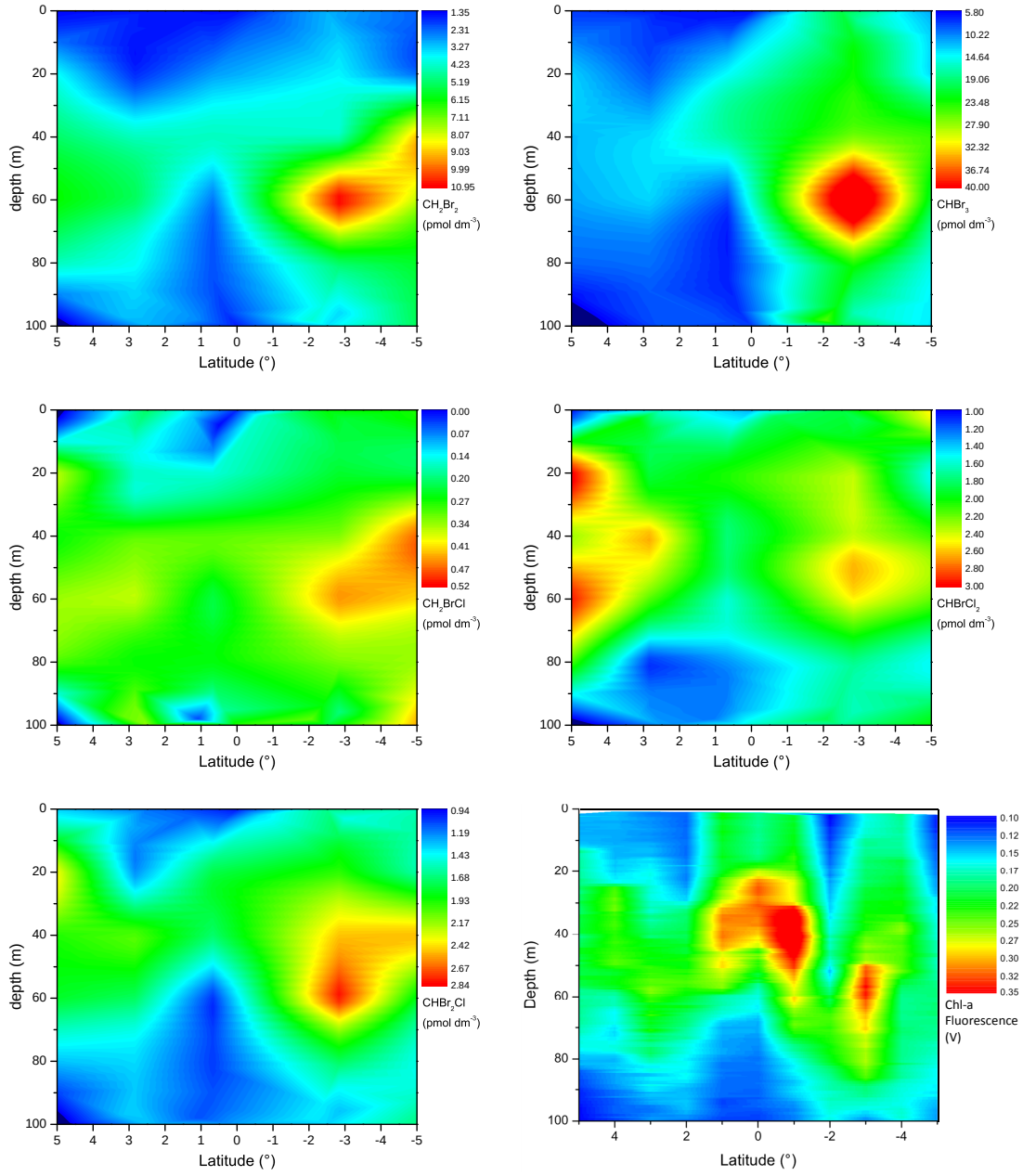

Figure 5.54 – Chloro/bromocarbon cross sections of the ocean between 5 and -5°N

5.4.1.3 Chlorocarbon biological production

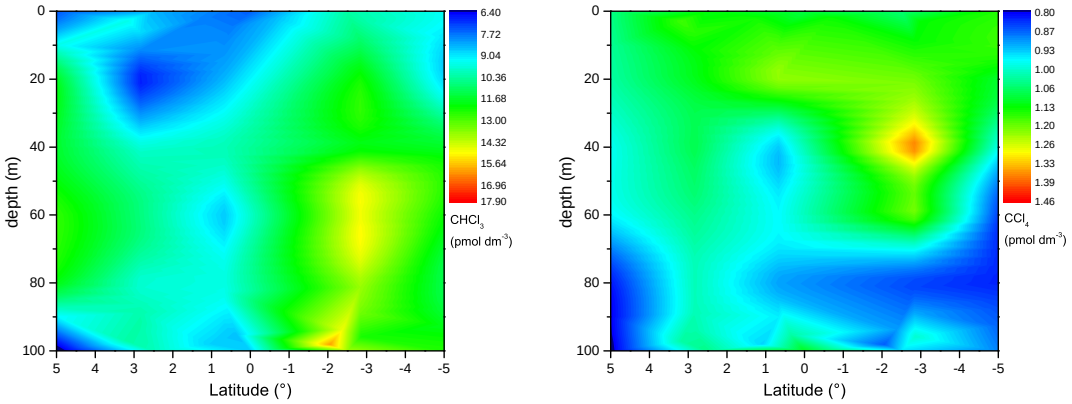

Figure 5.55 – Chlorocarbon cross sections of the ocean between 5 and -5°N; left, $CHCl_3$; right, CCl_4.

$CHCl_3$ (figure 5.55, left) displayed a similar distribution to the chloro/bromocarbons (figure, 5.54) indicating a biological source in the ocean. CCl_4 had a distribution in agreement with the ocean being a sink but also shows an enhancement slightly shallower than the bromocarbons at 40 m depth at 3°S and at 20 m depth at 1°N (figure 5.55, right). This could indicate a small biological source or possibly a physical factor which causes the enhancements. For instance, less mixing at this co-ordinate could result in the accumulation of dissolved gases at this particular depth. Certainly salinity is higher at this point compared to the same depths north of the equator (figure 5.48). This would also apply to the chloro/bromocarbon species which have longer residence times in seawater than the iodocarbons (Yamamoto et al., 2001) and therefore their distributions could be attributed to ocean dynamics in addition to source distributions. Also, the older the water, the greater the CCl_4 concentration since the atmospheric mixing ratio would have been higher when it entered the ocean. Thus enhancements, such as at 100 m, could indicate upwelling of old water masses.

5.5 Summary

A comprehensive range of VSLH have been observed in air and seawater of the East Tropical Pacific, an area with very few previous measurements of these species. The fast temporal resolution of the data revealed rapid changes in concentrations both diurnally and over a relatively small geographical area.

Atmospheric mixing ratios were fairly comparable to BLAST I (Lobert and Elkins, 1996; Butler et al., 2007) the only previous cruise in the ETP region with a north–south transect rather than west–east as per TORERO. The data was at the high end of the range of global mean measurements (Ziska et al., 2013). Atmospheric concentrations of CH_2Br_2, $CHBr_3$ and $CHCl_3$ showed notable NH/SH gradients, and $CHBr_3$ showed a strong equatorial enhancement in air but not water concentrations. $CHBr_3$, CH_2Br_2 and CH_3I showed some coastal influence as the ship neared Costa Rica. These features and possible explanations for them are discussed further in Chapter 6. The atmospheric concentrations at the surface were compared to aircraft measurements aboard the NSF/NCAR GV and were fairly comparable for most species at the lowest altitudes. Vertical profiles displayed greater concentrations for CH_2Br_2 and $CHCl_3$ at altitude in comparison to the surface. This was likely due to sampling different air masses at higher altitudes. The TORERO dataset provides no evidence for enhancements of CH_3I or other organic iodine compounds in the East Tropical Pacific compared to other oceanic regions (Jones et al., 2010; Chuck et al., 2005). Thus, the tentative suggestion of enhanced IO concentrations extending out across this region (Schönhardt et al., 2008) (figure 5.3) remains unexplained by currently understood atmospheric chemistry.

Surface seawater concentrations were in the range of previous measurements for $CHBr_3$ but CH_2Br_2 and CH_3I were slightly lower than global means published from the HalOcAt database (Ziska et al., 2013). Open ocean measurements of the shortest-lived species such as CH_2ICl and CH_2I_2 are very rare and their emissions and distributions are not well understood. During TORERO, we observed diurnal cycles in both surface seawater and air of these species for the first time, with concentrations in both cases peaking at night. These measurements provide a better understanding of the diurnal emission profile required in order to constrain iodocarbon source strengths. The observations are at odds with Ordóñez et al. (2012) who implemented a diurnal emission profile of iodocarbons

peaking at solar noon and with no night-time emissions into the global CAM-Chem model. Ordóñez et al. (2012) found that CH_2I_2 mixing ratios were underestimated due to rapid daytime photolysis, but were brought reasonably into line with measurements if night-time emissions were increased to half that of the day. In the TORERO data the night-time flux of CH_2I_2 was found to be 3–4 x the daytime flux (chapter 6, section 6.3.1). The TORERO data implies that emissions of CH_2I_2 may currently be underestimated and that if working from a top down approach, night-time atmospheric data should be used to calculate global emission estimates.

VSLH depth profiles from CTD casts were comparable to previous studies (Yamamoto et al., 2001; Butler et al., 2007; Quack et al., 2004) with concentration maxima for most species generally occurring within the euphotic zone at around 60 m and coinciding with the deep Chl-a maximum. CH_3I showed evidence of a surface source with concentrations decreasing with depth, validating the photochemical production mechanism proposed by (Moore and Zafiriou, 1994). Latitudinal cross-sections across the equator highlighted distinct differences between the iodocarbons and bromocarbons. These also revealed that although many VSLH appeared to share a similar depth profile to Chl-a in individual CTD casts, there were distinct differences in latitudinal distribution when the entire cross section was considered.

Chapter 6

Factors controlling the emission of VSLH

In this chapter the GeosChem model has been used as a tool to help interpret measurements from the TORERO and TROMPEX campaigns. GeosChem model data extractions and simulations were ran by Dene Bowdalo and Mat Evans at the University of York.

In order to model and predict atmospheric concentrations of VSLH and subsequent processes it is necassary to understand their production in the ocean, how ocean chemistry and dynamics influence their distribution in the water column, and their transition from sea to air. As discussed previously, the majority of VSLH emissions are ocean derived but the climatically important processes occur in the gas phase. In chapter 5, the production of VSLH in the east tropical Pacific ocean was discussed alongside measurements of atmospheric mixing ratios. In this chapter, VSLH distribution in the ocean mixed layer and subsequent flux from ocean to atmosphere are studied. The GeosChem model is utilised to better understand the processes occurring once VSLH enter the atmosphere and how these observations fit our understanding of the global VSLH budget.

6.1 Controls on VSLH oceanic production

VSLH is known to be produced in the ocean but the exact sources and their magnitude are still relatively undefined. Marine biota are a known source with the enzyme bromoperoxidase thought responsible for the production of bromocarbons (Hill and Manley, 2009; Lin and Manley, 2012; Manley and Barbero, 2001; Moore et al., 1996; Wever et al., 1991). Biological influence can usually be seen in the analysis of CTD profiles, with dissolved VSLH concentrations peaking at or near to the Chl-a maximum (figures 5.51 & 5.52). However, many studies have not found a direct link between biological parameters and VSLH concentration, with little or weak correlations between surface water or air concentrations and surface Chl-a (Abrahamsson et al., 2004; Quack et al., 2007b). Kurihara et al. (2012) found no significant correlation between Chl-a and $CHBrCl_2$, $CHBr_2Cl$ or $CHBr_3$ despite observing a positive correlation for Chl-a with isoprene ($r^2 = 0.5$). Palmer and Reason (2009) modelled $CHBr_3$ paramaterised by Chl-a, SST, salinity and wind with the resulting model calculations showing only weak correlations with measurements ($r^2 = 0.02$–0.41), highlighting our lack of understanding of the complex processes involved. However, Kurihara et al. (2010) observed that Chlorophyll-b and prasinoxanthin (a pigment found in phytoplankton) had a positive correlation with CH_2I_2 ($r^2 = 0.69$ and $r^2 = 0.71$, respectively) and CH_2ICl ($r^2 = 0.87$ and $r^2 = 0.77$, respectively).

Table 6.1 – Bulk correlations for all TORERO CTD casts along 110°W from 5°N to 5°S. $VSLH_{max}$ and Chl-a_{max} defined as the concentration maxima during the depth profile, generally between 40–60 m (figure 5.51). Correlations mentioned in the text are shown in bold font.

		CH_3I	CH_2Br_2	$CHBr_2Cl$	$CHBr_3$	CH_2ICl	CH_2I_2
$VSLH_{max}$ vs.	r^2	**0.385008**	0.00197	0.173888	0.168725	0.063109	0.006052
Chl-a_{max}	slope	3.653133	-1.64136	2.304532	90.06042	-6.11769	-1.50968
$VSLH_{surf}$ vs.	r^2	**0.289168**	0.125756	0.012863	0.180881	0.186934	**0.393095**
Chl-a_{max}	slope	3.04036	4.250944	0.569951	51.54385	2.334293	2.614453
$VSLH_{surf}$ vs.	r^2	**0.426971**	0.000675	0.012913	0.020801	**0.260542**	**0.511763**
Chl-a_{surf}	slope	5.35859	0.451697	-0.82829	25.35274	3.997165	4.326809
$VSLH_{max}$ vs.	r^2	0.181644	**0.483138**	**0.305061**	**0.695532**	0.005078	0.136609
$VSLH_{surf}$	slope	0.443805	2.14439	0.607404	1.508768	0.32141	-1.72003

By collecting profiles along one line of longitude (110°W) during the TORERO campaign, it becomes apparent that variability in Chl-a fluorescence does not explain the variability in water concentrations for most VSLH. A multitude of parameters were plotted against each other in an attempt to identify links between VSLH and Chl-a and is summerised in table 6.1, to which the following discussion refers. Plotting the maximum VSLH concentration ([VSLH$_{(max)}$]) against the maximum Chl-a concentration ([Chl-a$_{(max)}$]) for each degree latitude along the 110°W line suggests very little bulk correlation between these two parameters when not confined to one individual depth profile. This suggests that any biological production is either not well represented by Chl-a abundance, or that other processes exert strong controls over the steady state VSLH$_{(aq)}$ concentration. Either way, it seems that VSLH sea-air emissions cannot be parameterised as a simple function of Chl-a. As for Chl-a in isolation, [Chl-a$_{(max)}$] vs. [Chl-a$_{(surface)}$] gives an r^2 of 0.6. This may be expected to be stronger and highlights that even [Chl-a$_{(surface)}$] is not always representative of its concentration in the deep productive region. This is not due to photochemical quenching of the fluorescence response (section 5.3.5) as CTDs were mainly cast during the night (figure 5.49) and removing the daylight CTDs actually reduced the correlation ($r^2 = 0.46$).

CH_3I displays the best correlation between its concentration at deep maximum and [Chl-a$_{(max)}$] ($r^2 = 0.39$) which may be due to biological production but could also be explained by physical processes combined with photochemical production at the surface (section 6.2). Generally, increasing [Chl-a$_{(max)}$] does not correlate with an increase in [VSLH$_{(max)}$].

Interestingly, plotting VSLH concentration in the surface water (3 m, [VSLH$_{(surface)}$]) against [Chl-a$_{(max)}$] displays some correlation with increasing [Chl-a] resulting in increased CH_2I_2 at the surface ($r^2 = 0.39$). This is interesting as CH_2I_2, at its maximum in the depth profile, is not correlated with CH_2I_2 at the surface ($r^2 = 0.14$), likely due to photolytic degradation. CH_2I_2 and CH_3I at the surface display an improved correlation with [Chl-a$_{(surface)}$] ($r^2 = 0.51$ and 0.43, respectively), again with a positive slope. This relationship could be explained for CH_2I_2 via an indirect link with Chl-a. A higher Chl-a concentration is indicative of greater biomass in the water column and thus greater turbidity. This leads to greater light attenuation and would result in the shortest-lived species having comparatively longer lifetimes in that particular water mass. This would allow them to be mixed to the surface before being photolysed. For CH_3I, increased [Chl-a$_{(surface)}$] could

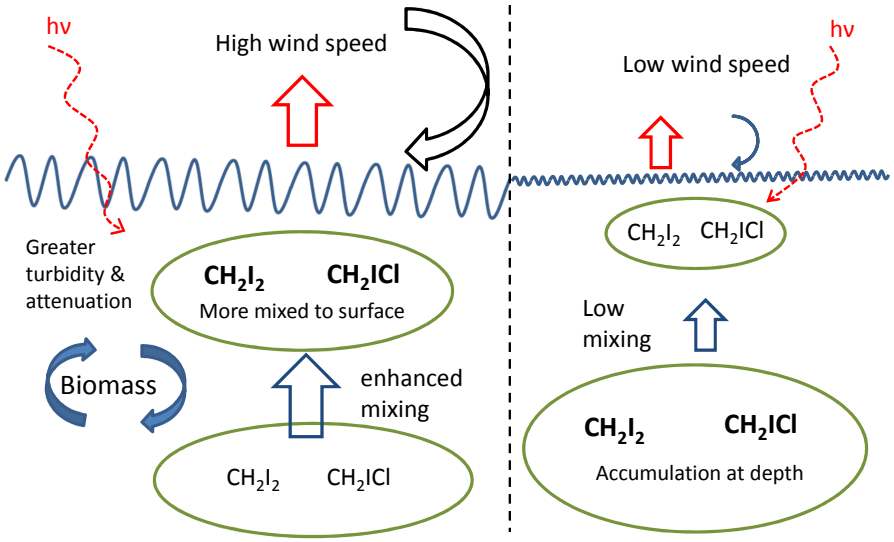

Figure 6.1 – Simplified schematic demonstrating how surace wind shear could create a negative slope in the correlation between the concentration of short-lived species at the surface and at depth.

be a link to the increased availability of DOM in the surface water for photochemically driven radical recombination from methyl radicals and iodine atoms.

Bromocarbon concentrations at the surface are positively correlated with those at the $VSLH_{(max)}$ due to their relatively long lifetimes in the water column (Quack and Wallace, 2003), thus production at the $VSLH_{(max)}$ results in greater surface concentrations (figure 6.2).

The shorter-lived iodocarbon's surface concentrations would not be expected to correlate well with their concentrations at the $VSLH_{(max)}$ due to their rapid photolysis in the water column, and are in fact negatively correlated (figure 6.3). When there are higher concentrations at the $VSLH_{(max)}$, there are generally lower concentrations at the surface. This highlights the importance of ocean boundary layer mixing on the distribution throughout the water column. High surface concentrations would be expected under conditions of vigorous mixing if the main production occurred sub-surface, but this would reduce the average $VSLH_{(max)}$ concentrations as they would be diluted with water from throughout the MLD (figure 6.1). Conversely, lower mixing allows accumulation at depths where photolytic degradation is slower and would result in a lower rate of transport of VSLH to the surface. This would increase the influence of surface VSLH photo-degradation and therefore this argument is in favour of a sub-surface production mechanism.

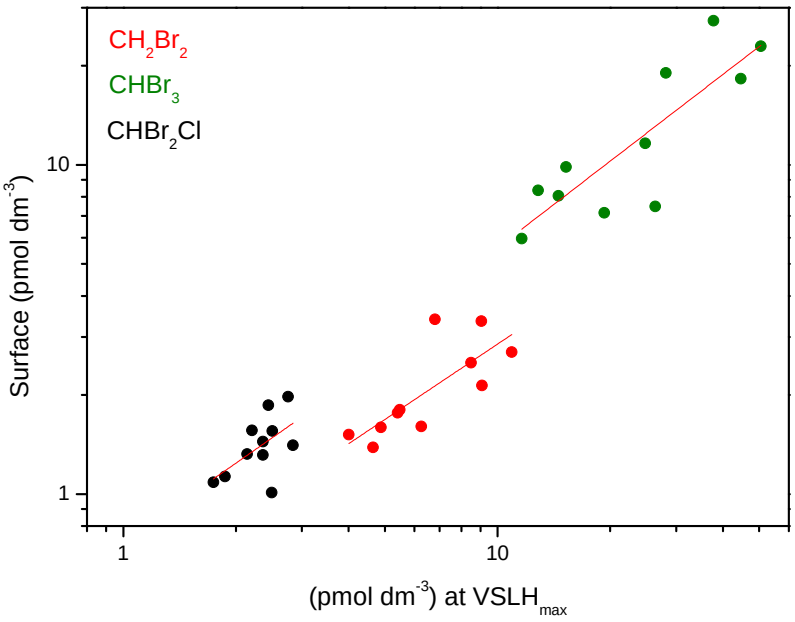

Figure 6.2 – CH_2Br_2, $CHBr_3$ and $CHBr_2Cl$ concentrations at the ocean surface (pmol dm^{-3}) against their maximum concentration (pmol $dm^{-}3$) during the depth profile for each CTD.

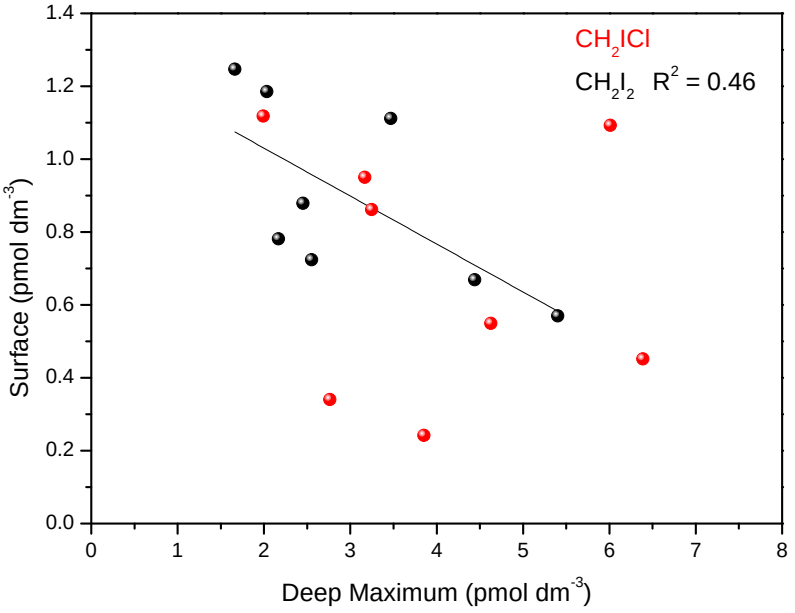

Figure 6.3 – CH_2ICl and CH_2I_2 surface ocean concentrations (pmol dm^{-3}) correlation with concentrations at their respective deep maxima.

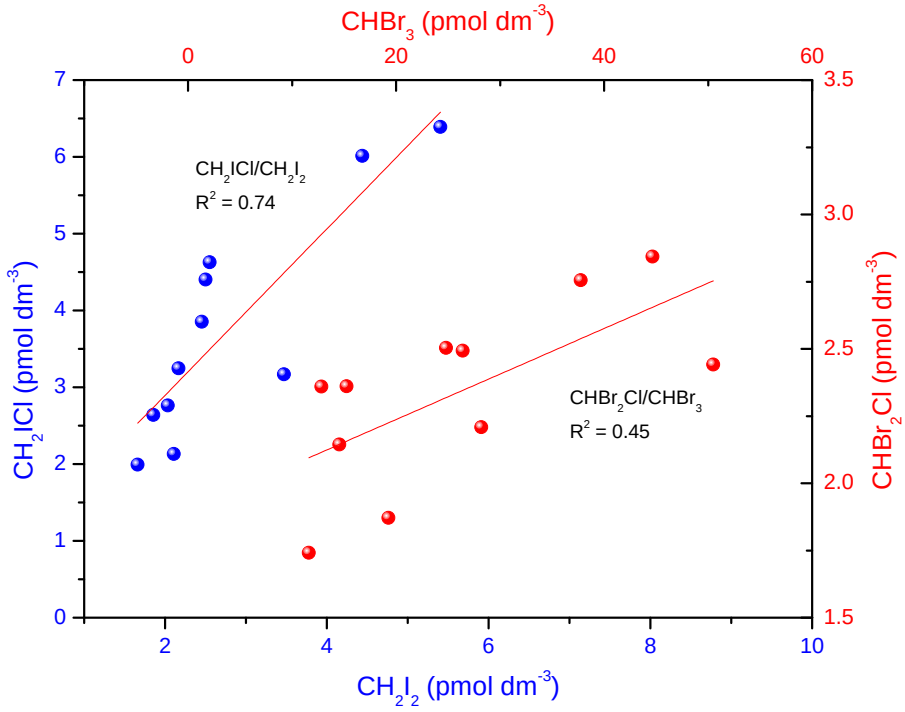

Figure 6.4 – CH_2ICl vs. CH_2I_2 and $CHBr_3$ vs. $CHBr_2Cl$ concentrations at their respective deep maxima (pmol dm^{-3}).

At the $VSLH_{(max)}$, CH_2I_2 concentration correlates well with CH_2ICl and $CHBr_2Cl$ similarly with $CHBr_3$ (figure 6.4). This could be indicative of substitution reactions with chloride ions as documented by Class and Ballschmiter (1988), or by related biological production mechanisms. In the case of CH_2I_2 and CH_2ICl, it is likely that the correlation is due to production as they no longer correlate when they reach the surface ($r^2 = 0.1$), likely due to their different surface water lifetimes.

The production of $CHBr_2Cl$ from $CHBr_3$ is a possibility. Chloride substitution of $CHBr_3$ is temperature dependent and half-lives can range between 5 years at 25°C and 74 years at 2°C (Hense and Quack, 2009). Hydrolysis is 10–100 times slower still (Geen, 1992; Vogel et al., 1987). Thus, if these reaction rates are correct, chlorine substitution of $CHBr_3$ is unlikely to explain the correlation as it is much too slow.

In addition, Hughes et al. (2013) demonstrated that CH_2Br_2 can be formed from $CHBr_3$ in diatom cultures. The TORERO CTD data showed that CH_2Br_2 and $CHBr_3$ were moderately correlated at their deep maximium ($r^2 = 0.5$) but showed much stronger correlation at the surface ($r^2 = 0.97$). If they are produced at depth then there must be a surface mechanism driving the improved correlation, a change in this mechanism could

then control CH_2Br_2:$CHBr_3$ emission ratios. Hughes et al. (2013) also demostrated that CH_2Br_2 was broken down by bacteria while $CHBr_3$ was not. In the ETP, the vertical distribution of bacteria in the water column places the highest abundance in the top 30 m (Ma et al., 2009). This could explain the decreased ratio of CH_2Br_2 to $CHBr_3$ at the surface compared to depths <30 m (figure 6.5). Similarly to CH_2Br_2, the correlation between $CHBr_3$ and $CHBr_2Cl$ increased when comparing $VSLH_{(max)}$ to $VSLH_{(surface)}$ (r^2 = 0.45 $\longrightarrow$ 0.8). $CHBr_2Cl$ was not measured in the experiments by Hughes et al. (2013) and may also have a source linked biologically to $CHBr_3$ (for $CHBr_2Cl$:$CHBr_3$ vs. depth see appendix, figure A.4).

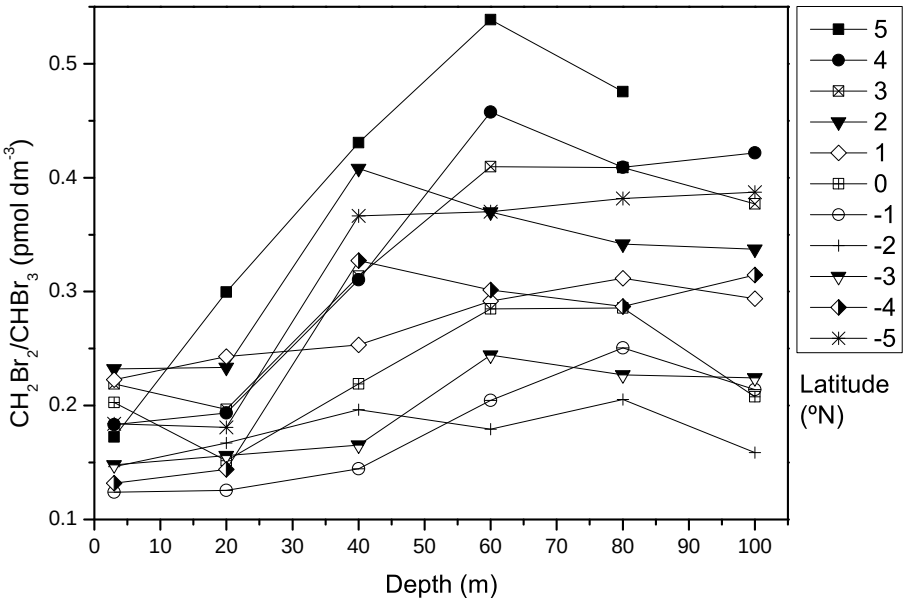

Figure 6.5 – $CH_2Br_2/CHBr_3$ in depth profiles along 110°W during TORERO.

6.2 Factors controlling VSLH distribution in the water column

Understanding what controls the VSLH distribution in the vertical water column is key to predicting surface water concentrations and thus flux into the atmosphere, when working from a bottom-up scenario. For VSLH it is clear that concentrations at the surface derive from a multitude of parameters, biological and physical.

CTD depth profiles from the TORERO campaign were fairly inter-comparable, with shallow mixed layer depths (MLDs) and strong density gradients. Profiles from 4° and 5°,

110°W displayed similar temperature and salinity inversions characterising the MLD and had Chl-a maxima at the MLD and below (figure 5.51). Species such as $CHBr_3$ and to a lesser extent CH_2ICl, appear to be higher in concentration at depths corresponding to enhanced Chl-a (figure 5.52). At each CTD station (figure 5.52) the CH_2ClI and $CHBr_3$ maximum lies just below the corresponding MLD. Interestingly, CH_2I_2 appears to reach its maxima significantly below the MLD. CH_3I has maxima just below each MLD but concentrations are much higher at the surface, especially at 4°N. This fits with the theory of surface production (Happell and Wallace, 1996; Richter and Wallace, 2004), with an additional contribution from biological production.

A recent numerical model study of CH_3I in the East Tropical Atlantic by Stemmler et al. (2013) provides a new perspective on interpreting the distribution of CH_3I in a water column. Using the GOTM (General Ocean Turbulence Model) they model the production, destruction and the resultant concentration of CH_3I followed by the subsequent flux. Destruction is via photolysis, hydrolysis and chloride substitution reactions. Production is separated between biological production from phytoplankton and photochemical production from radical recombination between DOC and iodine atoms (Richter and Wallace, 2004). They run the model under biology-only and photochemical-only conditions and visualise the data as a seasonal time-series depth profile (figure 6.6).

In the first column of figure 6.6, only the biological source of CH_3I is switched on. This results in production below the MLD and at the surface during winter. Degradation occurs in a similar distribution but production is dominant. Production at the surface is balanced by loss from the water via flux into the air but production below the MLD results in concentrations increasing at this depth. Therefore sea-air emissions are controlled by mixed layer depth and net production.

In the second column of figure 6.6, only the photochemical source of CH_3I is switched on. Here production occurs at the surface where solar irradiance is greatest, however degradation also occurs at the surface where concentrations are controlled by this balance. Enhanced concentrations in the surface water are mixed down beneath the MLD, especially when the MLD is very shallow in summer. This forms a sub-MLD enhancement not dissimilar to the depth profile for the biological-only production regime. It is therefore very difficult to de-convolute the biological from the photochemical source strengths as photochemical production can also produce sub-MLD profiles that correlate with the Chl-a

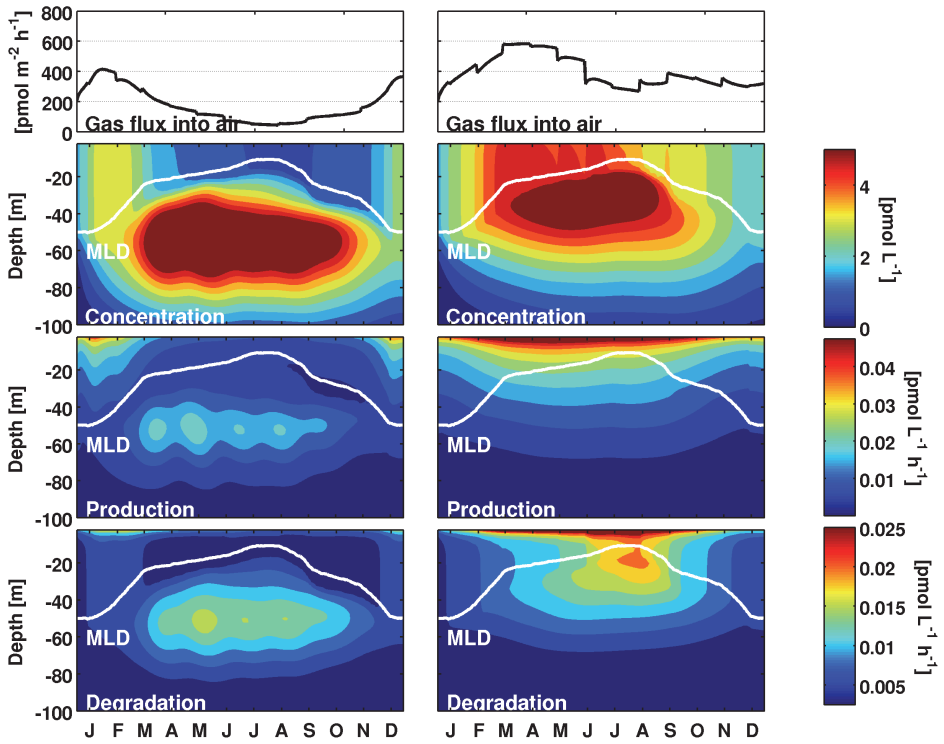

Figure 6.6 – CH_3I seasonal ocean depth profile adapted from model data from Stemmler et al. (2013). Left column models biological production only and the right column models photochemical production only. Model configured for the Cape Verde region (16°N, 24°W).

vertical distribution.

The TORERO CCl_4 data supports this model. CCl_4 is likely to be purely anthropogenic and has been used as a tracer for dating water masses (Krysell et al., 1994). It partitions into the ocean from the atmosphere (section 6.3.1, table 6.6) and its distribution through the water column can be attributed to mixing and age of the water mass. The model of Stemmler et al. (2013) suggests that a sub-surface maxima can occur via the mixing down of gases from the surface. Figure 6.7 shows sub-surface enhancements which are likely due to the in-flux of atmospheric CCl_4 and its accumulation around the MLD boundary as the destruction term in surface water is removed due to the stability of CCl_4 in seawater (∼90 years, Montzka et al. (2011)).

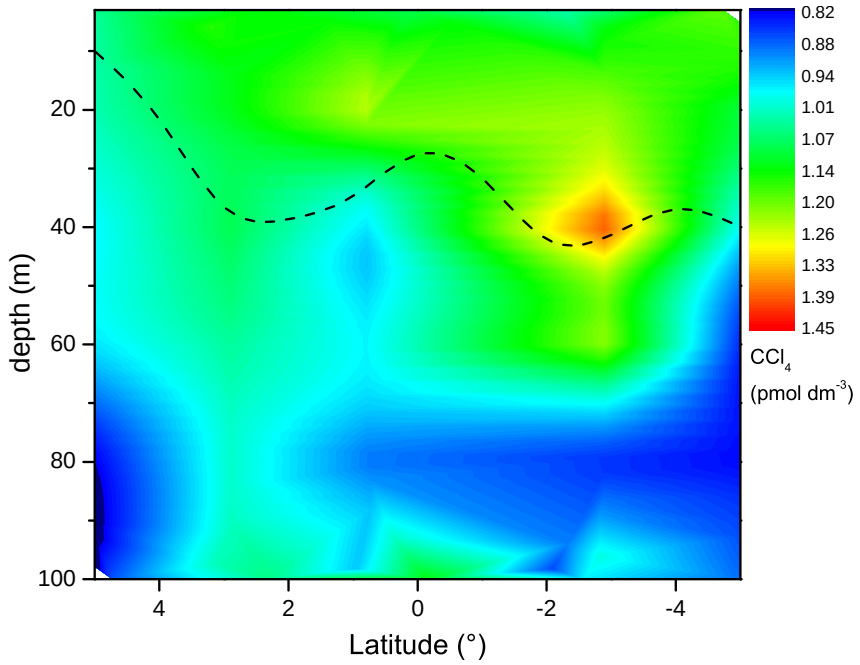

Figure 6.7 – CCl_4 cross section of the ocean between 5 and -5°N. Dotted line represents approximate MLD.

6.2.1 Another route to iodocarbon production?

A similar scenario could be hypothesised for other iodocarbons too. From the TORERO CTD profiles (figure 6.3), CH_2I_2 and CH_2ICl indicate that rapid photolysis is occurring in the surface water, as shown in laboratory studies of Jones and Carpenter (2005) and Martino et al. (2005). This is their major destruction mechanism and this would be exponentially greater at the surface than at depth. Biological production from plankton is predicted (Klick and Abrahamsson, 1992; Tokarczyk and Moore, 1994; Moore et al., 1996; Yamamoto et al., 2001) but there is a disconnect between iodocarbon concentrations, bromocarbons and Chl-a (chapter 5, section 5.4.1.1). A surface production mechanism could occur, as suggested by Martino et al., (2009), or at least, production disconnected from Chl-a. The deep maxima could then occur, like with CH_3I, just below the MLD due to accumulation from a lack of mixing and greater light attenuation at this depth. CH_2I_2 displays a notably deeper maximum compared to any other species measured (figure 5.52) and is the most photo-labile. The increasing CH_2I_2 concentration at depth could be due to a longer lifetime at depth rather than linked with deep production and the actual source could be located at any or all depths of the water column. This discussion diverts attention away from attempts to explain all VSLH production via linkages with Chl-a and highlights

the requirement to identify a more direct measure or at least define a suitable proxy. It is becoming increasing apparent that physical factors play an important role and it is likely that concentrations of the very short-lived species can be better constrained by assuming an average production rate and accurately modeling the physical parameters that lead to its subsequent sea-air flux.

6.3 Surface ocean- MBL exchange of VSLH

Once at the surface, VSLH can cross the sea-air interface and flux into the atmosphere. Many factors, such as wind-driven mixing, influence the rate at which a species moves across this interface and these factors can themselves impart a control upon surface VSLH concentrations.

Published iodocarbon flux data sets where the water and air concentrations have been measured simultaneously are very sparse (Moore and Groszko, 1999; Butler et al., 2007; Law and Sturges, 2007; Chuck et al., 2005; Jones et al., 2010). Often the air concentrations are assumed, extrapolated or interpolated. For the TORERO data the fluxes were always calculated from simultaneous air and water measurements and as the air sampling frequency was nearly three times greater than the water sampling frequency the air data was averaged so that the water data was always bracketed by two air samples.

The influx or out flux of VSLH from the ocean can be calculated as the departure of the observed VSLH concentrations in the surface ocean from equilibrium with air using equation 6.1 (Chuck et al., 2005) and is known as the percentage saturation anomaly.

$$Saturation\ anomaly(\%) = 100\left(\frac{[water] - [air]/H_c}{[air]/H_c}\right) \tag{6.1}$$

Where H_c is the temperature dependent Henry's law constant for the species of interest (Sander, 1999).

The saturation anomaly uses the temperature dependant gas over liquid form of the Henry's law constant and as such is sensitive to SST due to decreased gas solubility at warmer water temperatres. CH_3I, CH_2ICl and CH_2I_2 are all super-saturated in the ocean

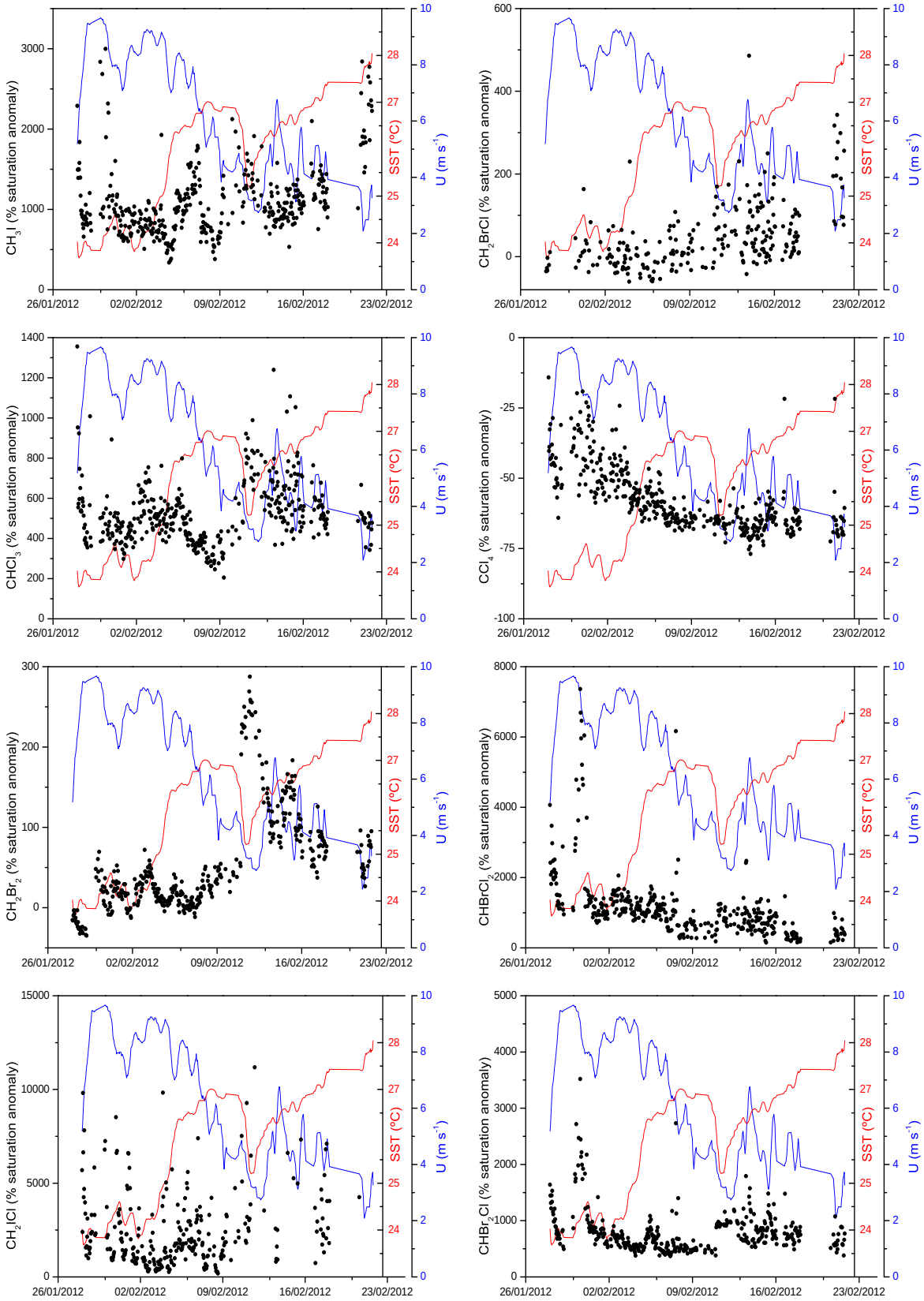

Figure 6.8 – Continued over...

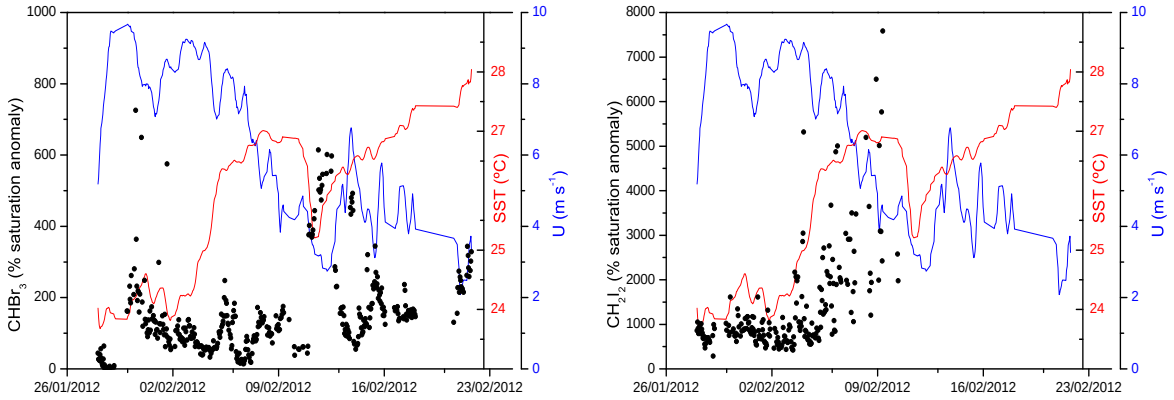

Figure 6.8 – % saturation anomaly during TORERO- black circles. Blue line shows wind speed (U, m s^{-1}) and red line shows sea surface temperature (SST, °C)

relative to the air. This is due to their short atmospheric lifetimes compared to water and is consistent with the ocean being a strong source.

CH_2Br_2 and $CHBr_3$ are saturated in the ocean but to a lesser extent as their atmospheric lifetimes are comparatively much longer. In highly oligotrophic oceans with very low oceanic VSLH production and low oxidant concentration, the ocean can act as a sink for longer lived species such as CH_2Br_2 and CH_3BrCl. These two species in particular have very long photolytic lifetimes of 5000 and 15000 days, respectively. The ocean is clearly a strong source of $CHCl_3$ and an important sink of anthropogenically produced CCl_4.

6.3.1 Fluxes

The ocean-atmospheric flux was calculated as a two layer film model (Liss and Slater, 1974) using methods described by Johnson (2010) and explained in detail in section 1.8. Eight different measurements are required to calculate flux empirically (table 6.2), the other parameters can be calculated or are experimentally derived constants (section 1.8.3, table 1.5).

The major drivers of flux are wind speed, SST and the aqueous concentration. These affect the liquid phase transfer velocity (K_w), the speed at which a gas can move in or out of a liquid, which is rate determining as the gas phase transfer velocity term (K_a) is two orders of magnitude faster. This can be described as a water-side limiting scenario. Often

Table 6.2 – Measurements required for the calculation of ocean-atmospheric flux

Symbol	Description	Unit
P	Atmospheric pressure	atm
C_a	Air-side concentration	mol cm^{-3}
C_w	Water-side concentration	mol cm^{-3}
T	Air temperature	Kelvin
T (SST)	Sea-surface temperature	°C
U	Wind speed (preferably at 10 AMSL)	m s^{-1}
S	Salinity	PSU
%RH	Percentage relative humidity	%

K_a is omitted from flux calculations but here it was calculated and found to reduce the calculated flux by around 1-17% depending on species (table 6.3).

Figure 6.9 highlights the importance of wind speed to fluxes with K_w being the major flux-controlling factor with a logarithmic relationship to wind speed. Yokouchi et al. (2001) and Jones et al. (2010) calculate the total transfer velocity (K_t) following Wanninkhof (1992) and Khalil et al. (1999) (equations 6.2 and 6.3).

$$K = 0.31u^2 f(t) \tag{6.2}$$

$$f(T) = \left(\frac{335.6 M^{\frac{1}{2}} (1 - 0.065T + 0.002043T^2 - 2.6 \times 10^{-5} T^3}{660} \right)^{\frac{1}{2}} \tag{6.3}$$

Where u is windspeed (m s^{-1}), M is molecular mass of the species and T is SST (°C). The method proposed by Johnson (2010), and used in this chapter, is more detailed and takes salinity into account when calculating K_w (Chp1. figX). Both methods were tested using the TORERO dataset and it was found that by not factoring salinity into the calculation, fluxes are overestimated by between 1-18% (section 1.8).

The flux of the shortest-lived species CH_2I_2 and CH_2ClI was very much wind speed de-

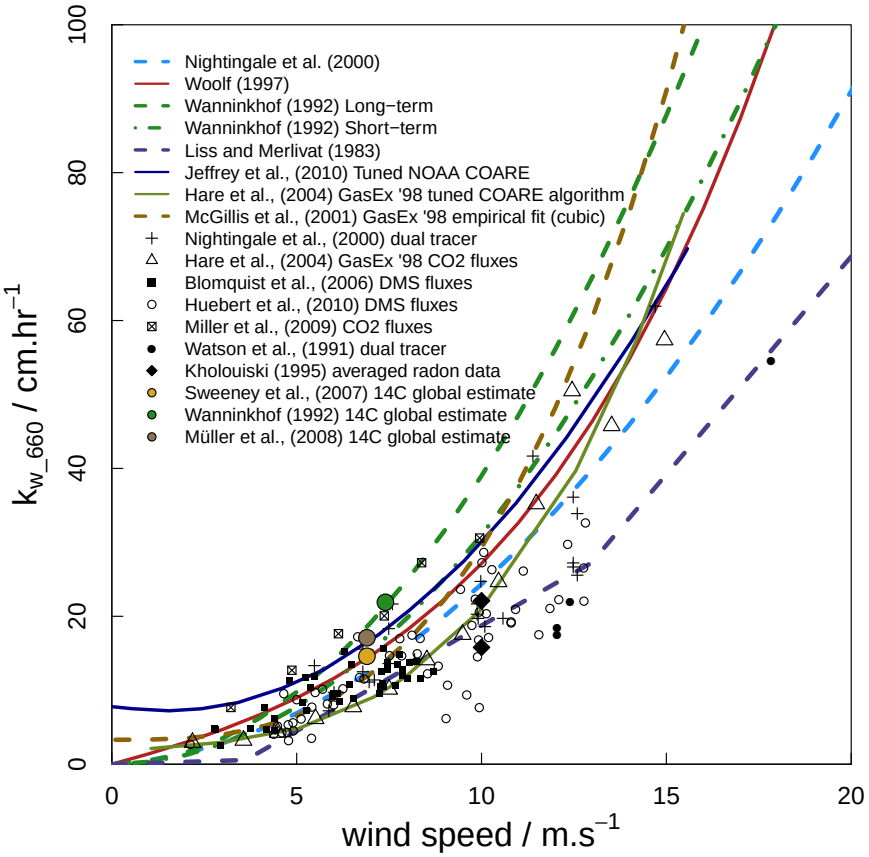

Figure 6.9 – Comparison of various observations, parameterizations and model predictions of the relationship between wind speed and liquid phase transfer velocity (K_w) scaled to a Schmidt number of 660. Adapted from Johnson (2010)

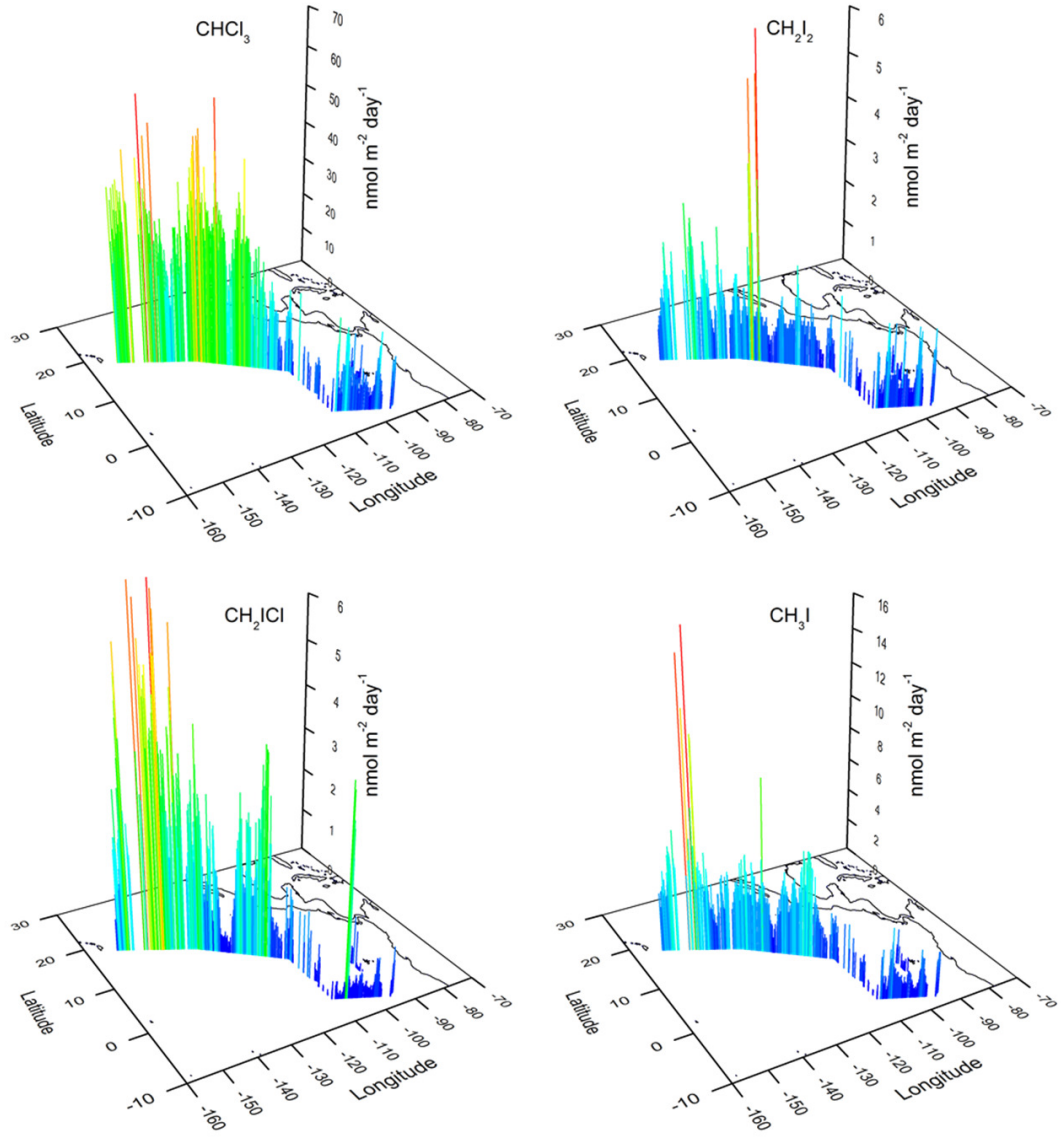

Figure 6.10 – Calculated sea-air fluxes for the TORERO campaign plotted along the cruise track and coloured by flux intensity.

Table 6.3 – Comparison of different flux calculation techniques. A&WSL: calculation includes air and water side limiting terms, WSL: Water side limiting term only.

Species	Flux (Yokouchi et al. (2001)) A&WSL	Flux (Johnson (2010)) WSL	Flux (Johnson (2010)) A&WSL	%reduction (Johnson (2010)WSL Vs A&WSL)	%reduction (Yokouchi et al. (2001) vs. Johnson (2010))
CH_3I	3.18	2.74	2.70	1	15
$CHCl_3$	25.97	21.63	21.13	2	18
CCl_4	-3.43	-2.98	-2.97	0	13
$CHBrCl_2$	7.45	6.84	6.56	3	11
CH_2Br_2	1.26	1.24	1.14	7	10
CH_2ICl	1.90	1.87	1.72	7	9
$CHBr_2Cl$	3.35	3.37	3.13	6	6
$CHBr_3$	7.11	8.14	7.01	13	1
CH_2I_2	1.11	1.36	1.11	17	0

pendent as wind speed not only controls the transfer velocity, it also imparts a control on the surface concentration of these species. Surface wind shear drives surface ocean mixing and defines the speed at which transport to the surface can occur.

Apart from a number of spikes the flux of bromocarbons along the cruise track remained relatively constant and did not change dramatically as the ship transitioned between areas of high or low oceanic productivity. At the beginning of the cruise, CH_2Br_2 was undersaturated in the surface ocean (figure 6.11). At times, such as around the equator, fluxes alone could not fully explain the changes in observed air-side concentration and this is discussed in section 6.5.1.

Salinity dependent Henry's law constants were calculated using the numerical scheme by Johnson (2010) (section 1.8.3.1). This tended to shift the equilibrium more toward the air-side and had the greatest effect on gas flux into the ocean where it served to virtually eliminate any in-flux, from atmosphere to ocean, by CH_2Br_2 or $CHBr_3$ and reduce the in-flux of CCl_4.

Extrapolated globally, fluxes during TORERO (table 6.6) were much lower than literature estimates (table 6.5) with the exception of $CHCl_3$. Fluxes during TORERO represent open ocean fluxes and medians compare well with median (range) tropical ocean fluxes calculated by Butler et al. (2007) for $CHBr_3$ (6.1 (-1.4–51) nmol m^{-2} day^{-1} TORERO vs.

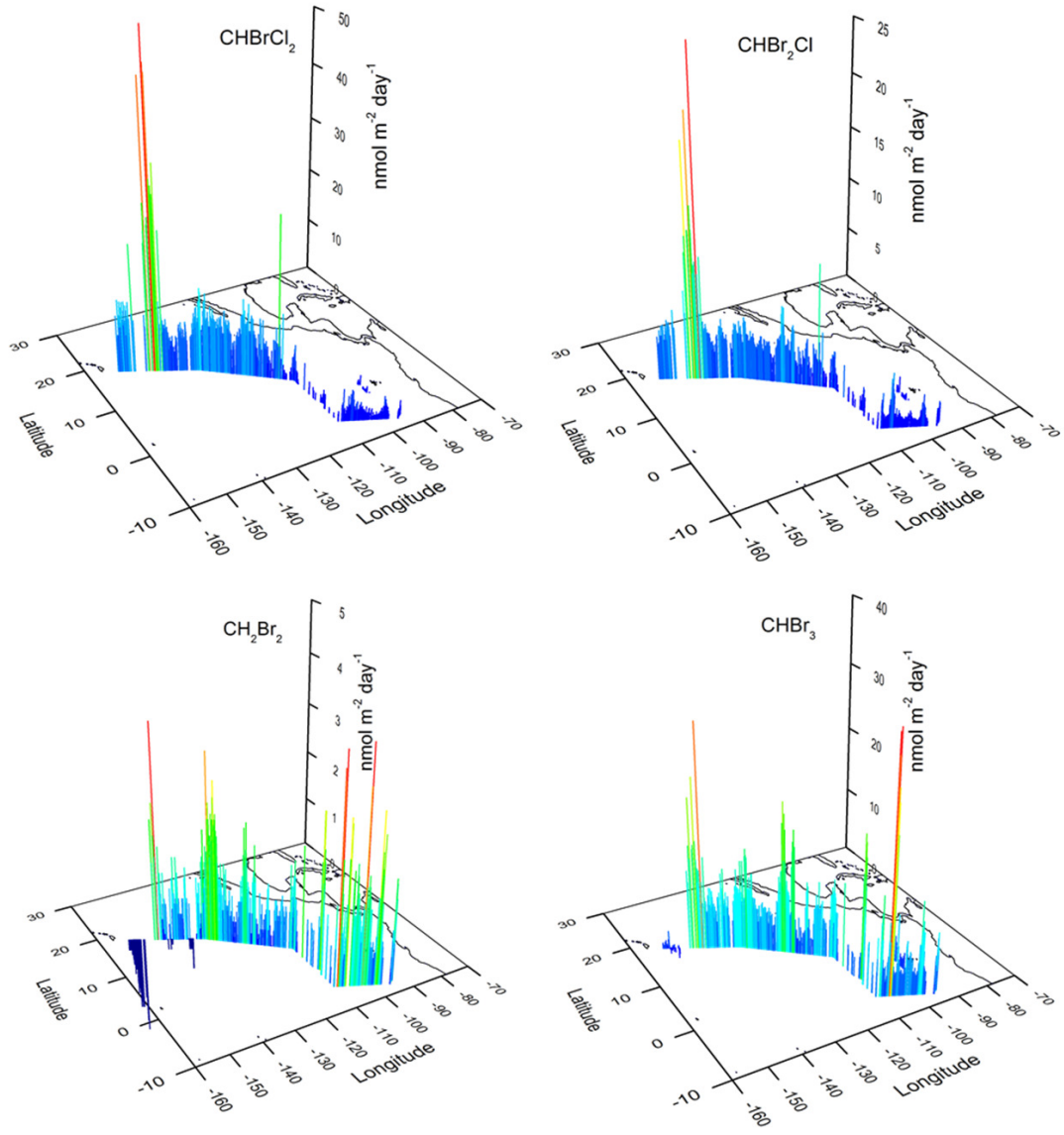

Figure 6.11 – Calculated sea-air fluxes for the TORERO campaign plotted along the cruise track and coloured by flux intensity

Table 6.4 – Average (range) VSLH flux using a Henry's law constant calculated for pure water compared to the salinity dependent Henry's law constant calculated using the scheme by Johnson (2010).

Species	Mean flux (pure water) nmol m^{-2} day^{-1}	Mean flux (salinity dependent) nmol m^{-2} day^{-1}	Mean Δ flux nmol m^{-2} day^{-1}
CH_3I	2.7 (0.1–17.4)	2.8 (0.1–17.5)	0.05 (0.001–0.14)
CH_2BrCl	-0.1 (-0.9–0.9)	-0.1 (-0.7–1.0)	0.1 (0.0–0.2)
$CHCl_3$	21.3 (0.63–90.2)	22.1 (0.68–92.0)	0.8 (0.02–2.45)
CCl_4	-3.6 (-8.2–0.1)	-2.1 (-5.3–1.1)	1.5 (0.1–3.7)
$CHBrCl_2$	6.6 (0.1–107.8)	6.7 (0.1–108.0)	0.1 (0.0–0.2)
CH_2Br_2	1.5 (-1.1–18.4)	1.9 (-0.3–18.7)	0.4 (0.0–0.9)
CH_2ICl	1.7 (0.0–8.1)	1.7 (0.0–8.2)	0.0 (0.0–0.1)
$CHBr_2Cl$	3.1 (0.1–59.8)	3.2 (0.1–59.9)	0.1 (0.0–0.2)
$CHBr_3$	7.1 (-1.4–50.9)	8.0 (-0.1–52.1)	0.9 (0.3–2.0)
CH_2I_2	1.1 (0.1–11.1)	1.1 (0.1–11.1)	0.0 (0.0–0.1)

5.7 (0.2–27) nmol m^{-2} day^{-1}) and CH_2Br_2 (1.2 (-1.1–18.4) nmol m^{-2} day^{-1} TORERO vs. 1.9 (0.4–6.9) nmol m^{-2} day^{-1}) but are much lower for CH_3I (2.4 (0.1–17.4) nmol m^{-2} day^{-1} TORERO vs. 10 (1.6–33) nmol m^{-2} day^{-1}) and compare better with southern ocean fluxes (2 (0.4–9.8) nmol m^{-2} day^{-1}).

The flux of $CHCl_3$ during TORERO was more than double the estimated mean global oceanic flux calculated by Worton et al. (2006) (table 6.5). It is likely that the tropical waters of the East Pacific make a significant contribution to the $CHCl_3$ global budget and possible that the ocean flux calculation by Worton et al. (2006) underestimates the $CHCl_3$ ocean source or that there is a large unaccounted for anthropogenic source.

Table 6.5 – Literature estimates of VSLH fluxes.

Species	Region	Flux rate (Gg yr^{-1})	Reference
CH_3I	Oceans	130–360	Moore and Groszko (1999)
		210	Bell et al. (2002a)
		610	Butler et al. (2007)
		303	Ordóñez et al. (2012)
	Terrestrial	90–123	Bell et al. (2002a); Sive et al. (2007)
CH_2ClI	Oceans	132	Law and Sturges (2007); Chuck et al. (2005)
		130	Jones et al. (2010)
		280	Jones et al. (2010)
		234	Ordóñez et al. (2012)
CH_2I_2	Oceans	235	Jones et al. (2010)
		116	Ordóñez et al. (2012)
$CHCl_3$	Oceans	180	Worton et al. (2006)
	Soils	100	
	Anthropogenic	90	
$CHBr_3$	Oceans	822	Quack and Wallace (2003)
	Oceans	400–600	Warwick et al. (2006)
	Oceans	840	Butler et al. (2007)
	Oceans	450	Liang et al. (2010)
CH_2Br_2	Oceans	108	Warwick et al. (2006)
		300	Butler et al. (2007)
		61	Liang et al. (2010)

Table 6.6 – Summary of VSLH fluxes during TORERO. Average flux is representative of a mostly background, open-ocean source. Fluxes extrapolated assuming total ocean area is 3.6×10^{14} m^2 (Liss and Slater, 1974), area of Pacific as 46% of the Earth's oceans and the east tropical Pacific (ETP) 17%.

	Flux (nmol m^{-2} day^{-1})			Flux (Gg $year^{-1}$)		
Species	Mean	NH	SH	Total Ocean	Pacific	ETP
CH_3I	2.7	3.7	1.2	52	24	4
$CHCl_3$	21.1	30.0	7.5	341	186	31
CCl_4	-3.0	-3.8	-1.7	-62	-26	-4
$CHBrCl_2$	3.1	9.8	1.5	69	28	28
CH_2Br_2	1.1	0.7	1.8	27	10	10
CH_2ICl	1.7	2.5	0.5	41	15	15
$CHBr_2Cl$	3.1	4.5	1.1	88	28	28
$CHBr_3$	7.0	7.6	6.2	239	62	62
CH_2I_2	1.1	1.4	0.7	40	10	10

Table 6.7 – Contribution of bromine and iodine to the MBL from open-ocean fluxes calculated during TORERO and extrapolated globally.

Bromocarbons	nmol m^{-2} day^{-1}					Bromine Gg $year^{-1}$		
	$CHBrCl_2$	CH_2Br_2	$CHBr_2Cl$	$CHBr_3$	Bromine	Total ocean	Pacific	East tropical Pacific
All	3.13	2.29	6.27	21.02	32.72	778	357	60
NH	9.84	1.48	8.96	22.65	42.93	1019	468	79
SH	1.53	3.53	2.14	18.52	25.71	598	274	47
Iodocarbons	nmol m^{-2} day^{-1}					Iodine Gg $year^{-1}$		
	CH_3I	CH_2ICl	CH_2I_2		Iodine			
All	2.70	1.72	2.22		6.64	173	79	13
NH	3.67	2.52	2.81		9.00	232	106	18
SH	1.20	0.48	1.31		2.98	82	37	6

6.4 Wind speed dependence

Wind speed appears to be the dominant control on CH_2ICl and CH_2I_2 air concentrations, controlling their flux in addition to mixing them to the ocean surface (figures 6.12 and 6.15).

6.4.1 Surface water VSLH vs wind speed (U)

As discussed, windspeed is an important control on VSLH emission. Combined with thermohaline mixing, wind speed controls mixing in the water column which was discussed in section 6.2 and used to investigate the distribution of VSLH in depth profiles. Transport of VSLH in the water column determines water concentrations and therefore, especially for gases which have short lifetimes in seawater such as the dihalomethanes, wind speed may enhance surface concentrations. For other gases where volatilisation from the ocean mixed layer is the major sink, increased wind speed could deplete surface water concentrations (figure 6.12).

During TORERO, increased horizontal winds were generally associated with increased surface seawater concentrations of CH_3I, CH_2I_2 and CH_2ICl (figure 6.12), but relationships with other gases were less clear. Tegtmeier et al. (2013a) use the FLEXPART model (Stohl et al., 2005) to highlight how the simultaneous occurrence of large CH_3I emissions and strong vertical uplift can result in a greater contribution of CH_3I to the TTL with maximum modelled mixing ratios of 0.6 ppt (in the upper TTL, based on peak emissions during the SHIVA-Sonne campaign in the coastal West Pacific). In the TORERO dataset it is evident that the conditions required for rapid vertical transport to the UTLS, such as high wind speed, SST and convection, not only exert a control on ocean-atmosphere exchange but also on surface water concentrations of CH_2ICl, despite the flux to atmosphere being a major loss process for gases in the surface ocean.

CH_2ICl concentrations in surface water are likely due to fresh entrainment from depth to the surface during periods of high wind speed on a timescale shorter than its photolytic and removal lifetimes in the surface water. At low wind speed, the loss rate > mixing rate and at high wind speeds, the loss rate < mixing rate. At wind speeds greater than 8 m s^{-1} surface water concentrations appear to drop. This could be due to greater sea-air flux at

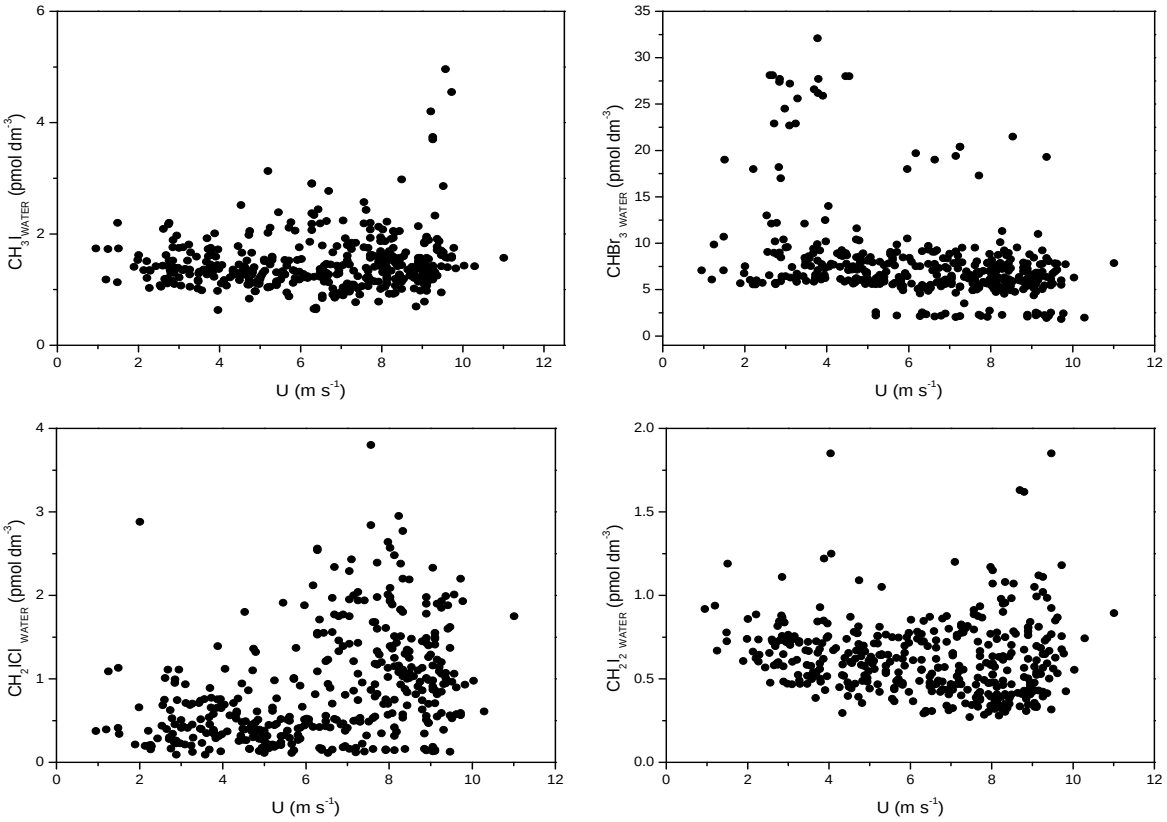

Figure 6.12 – Correlations between wind speed (U, m s^{-1}) and selected VSLH surface water concentrations (pmol dm^{-3})

higher wind speed where loss rate dominates once more whilst the supply of CH_2ICl to the surface remains the same either by a negligible increase in mixing with wind speed or by VSLH concentrations throughout the mixed layer depth becoming constant.

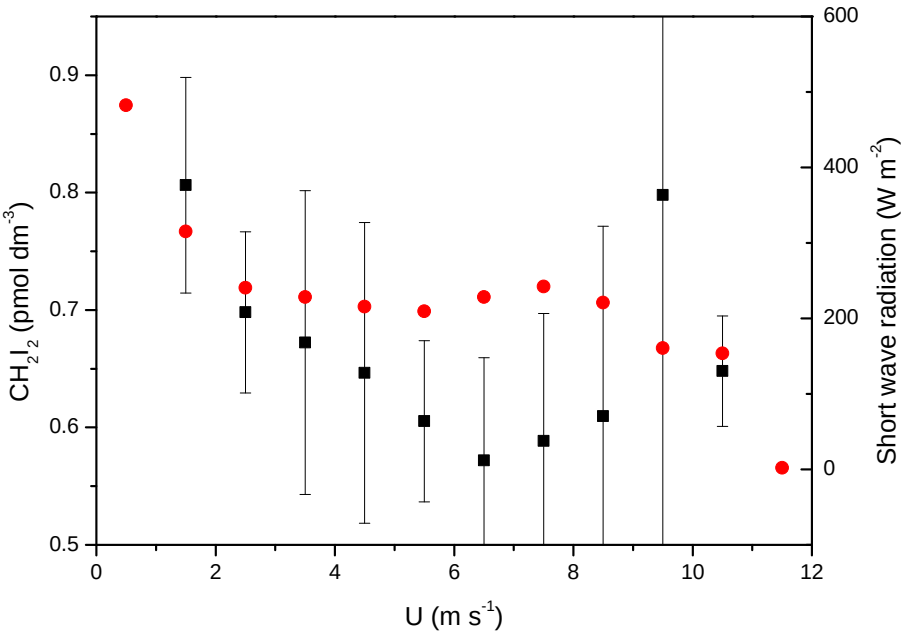

Figure 6.13 – CH_2I_2 surface water concentrations (red circles, pmol dm^{-3}) and incoming short wave radiation (black squares, W m^{-2}) sorted into 1 m s^{-1} bins then averaged. Y-error bars represent the spread of the data within each bin.

CH_2I_2 surface water concentrations could be expected to increase with wind speed but the data shows a relatively flat relationship and possibly a slight enhancement at low wind speed (figure 6.12). This could be caused by noisy data due to concentrations at the surface being very low as CH_2I_2 is rapidly photolysed. Low wind speeds also coincided with high solar irradiance (figure 6.13) and may tentatively suggest a surface photochemical production mechanism.

Surface production of CH_2I_2 and CH_2ICl was discussed in section 6.2.1 with reference to Martino et al. (2009) who report production of these species from the reaction of DOM with HOI and I_2, formed at the sea surface from the reaction of O_3 with dissolved iodide. Low wind speed regimes during TORERO were encountered predominately between the equator and 5°S (figure 5.24). This area of the Pacific is known as the doldrums and

gives this ocean its name due to the calm waters, low wind and high solar irradiance which historically would hinder sailing ships crossing the equator. During TORERO this was also a region of very low O_3 (section 5.3.2 figure 5.23). Due to these very low ozone concentrations it is unlikely that surface production here would follow this mechanism.

CH_3I and CH_2I_2 in surface water show a slight increase with wind speed but are not as dependent as CH_2ICl. CH_3I oceanic lifetime is longer than that of CH_2ICl and mixing throughout the water column can occur over a longer timescale without as much photochemical destruction at the surface. It is also produced at the surface photochemically thus it would be expected to show an increase in surface concentration at low windspeeds– less mixing, and greater solar irradiance, which it doesn't. This demonstrates that care must be taken in the interpretation of these datasets as many factors are working together that are difficult to deconvolute. CH_3I is highly super-saturated in the surface ocean (500-2000%) with respect to air (figure 6.8) and the resulting flux may not significantly influence water concentrations.

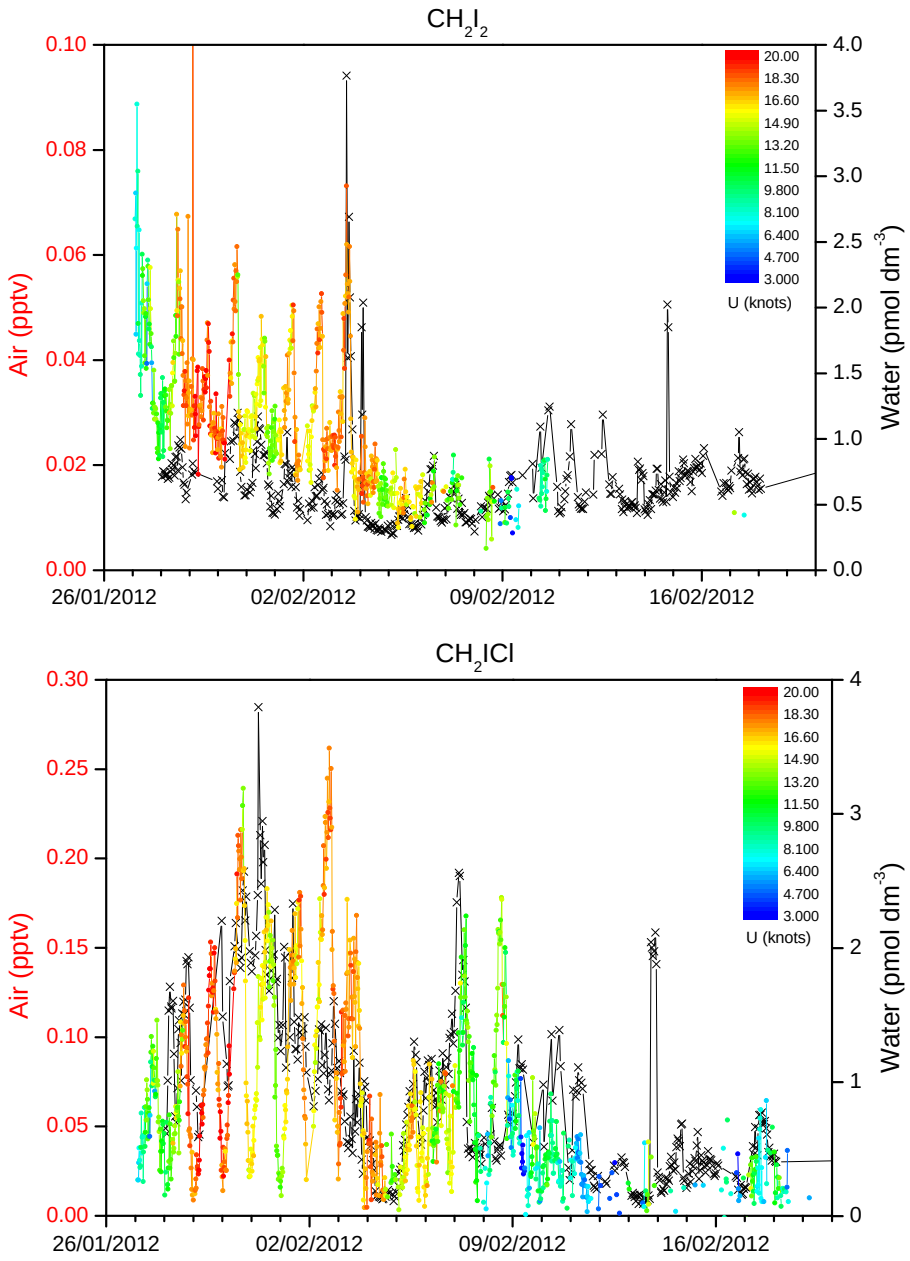

Figure 6.14 – Concentrations of CH_2ICl (top) and CH_2I_2 (bottom) in air (coloured by wind speed. Blue is low, red is high) and water (black circles).

6.4.2 Air VSLH vs wind speed (U)

VSLH in the surface water is emitted into the air which is driven by wind speed, among other factors including the concentration gradient. Where air concentrations are driven by local sea-air flux, such as for open ocean regions or for very short-lived species, the wind speed exerts a strong control on the flux (figure 6.15). Longer lived species such as the

bromocarbons show less of this relationship and include data points where the flux appears to be anomalously high. This is due to the air concentration not being representative of the local surface water concentrations probably due to atmospheric transport or contribution from another source.

The combination of enhanced surface water concentrations, flux and vertical transport during periods of high wind speed, could result in the underestimate of the quantities of VSLH lofted to the UTLS if not accounted for by models.

VSLH air concentrations are a balance between emissions and sinks. As photolytic destruction is much faster in the atmosphere than in water, the air data displays much more scatter depending upon time of day and solar irradiance. The contributions of photolysis, dilution and flux would require a model to deconvolute. In order to visulize the air data trends more easily it was averaged into wind speed bins for every 1 m s^{-1} from 0-12 m s^{-1} (figure 6.16). For CH_2ICl the air concentrations are wind speed dependent because at lower wind speeds, photolytic destruction dominates and at higher windspeed, emissions dominate.

CH_3I displays more wind speed dependence in air than it does in water. This could be because it has a shorter lifetime in air and wind-driven flux controls its atmospheric concentration. Wind has less of an effect on its water concentration as it has a surface photochemical source and does not depend upon mixing from depth like CH_2ICl.
CH_2Br_2 and $CHBr_3$ tend to increase with wind speed as the air concentrations are controlled by flux but are ultimately limited by dilution, causing the relationship to breakdown at higher wind speeds. Dilution of emissions is evident for $CHBrCl_2$, $CHBr_2Cl$, CH_2Br_2 and $CHCl_3$, where higher wind speeds result in lower air-side concentrations, probably due to mixing of the emissions throughout a thicker MBL.
$CHCl_3$ displays an interesting relationship with wind speed because the bulk data shows a positive relationship whereas including only SH data, a negative relationship is evident. This could be linked to the low wind speed and high solar irradiance regime in the SH cruise leg and the observation of a slight positive diurnal cycle in the SH data (section 6.5.3).

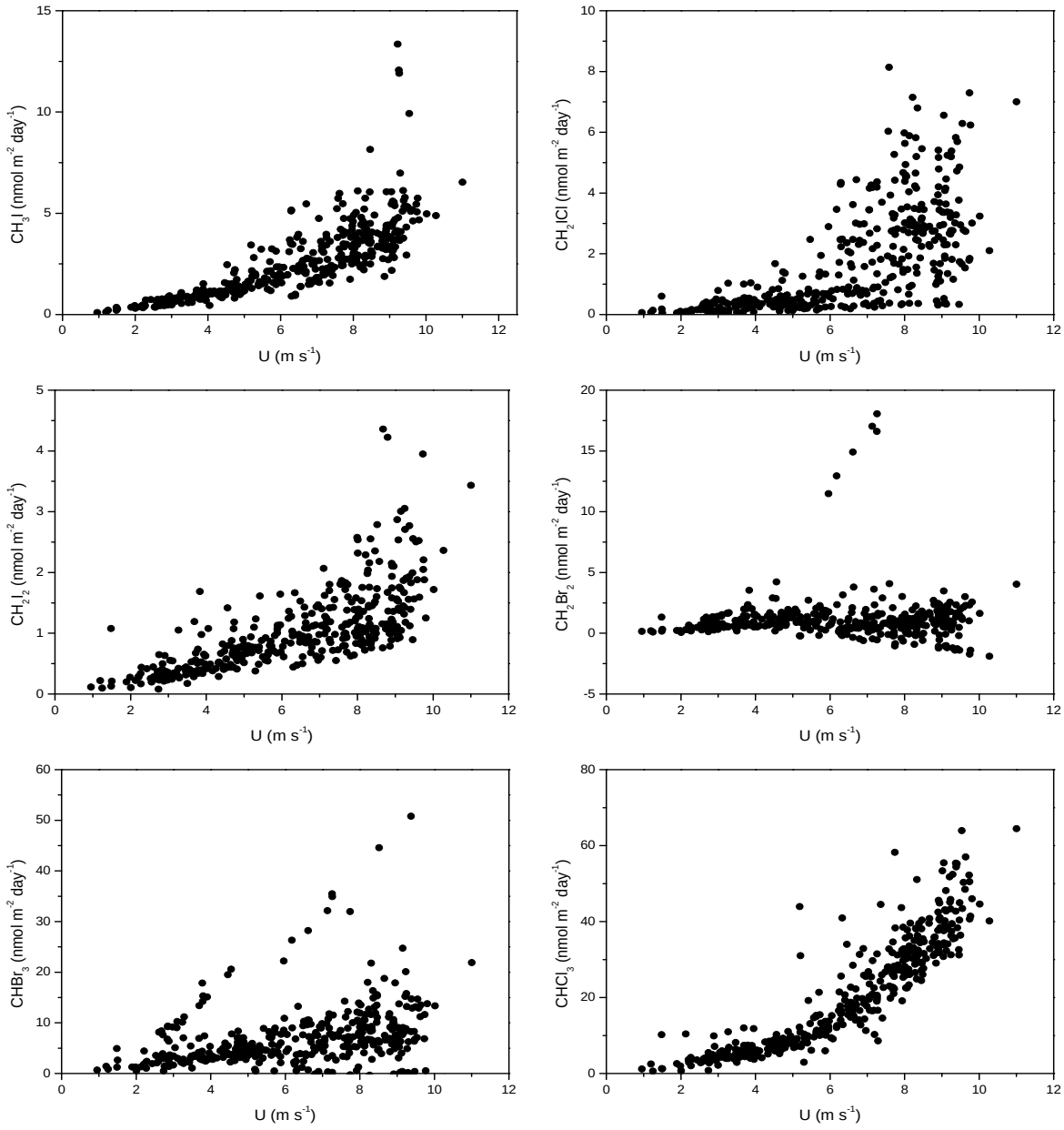

Figure 6.15 – VSLH flux (nmol m^{-2} day^{-1} correlation with wind speed (U, m s^{-1}.

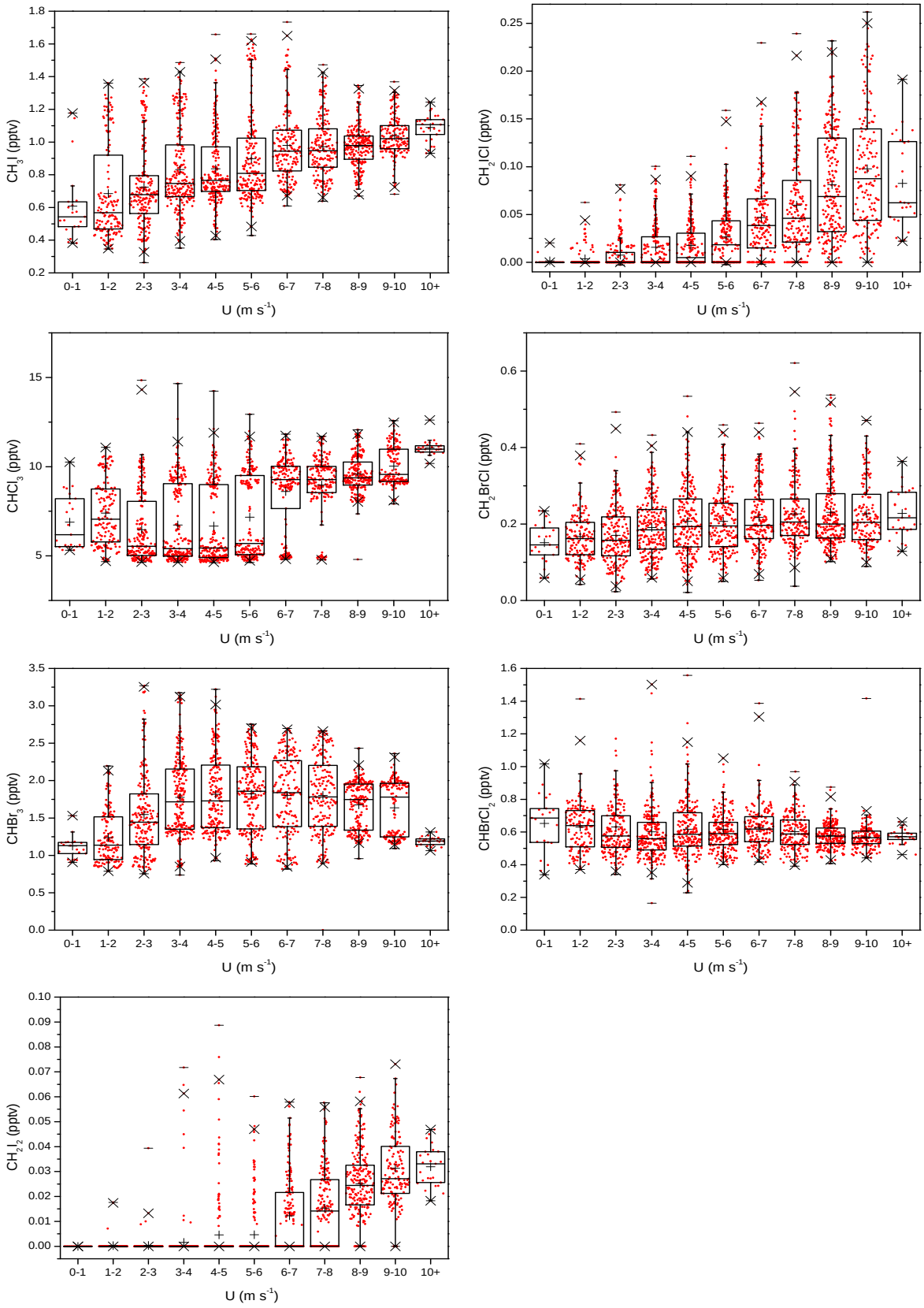

Figure 6.16 – Continued over...

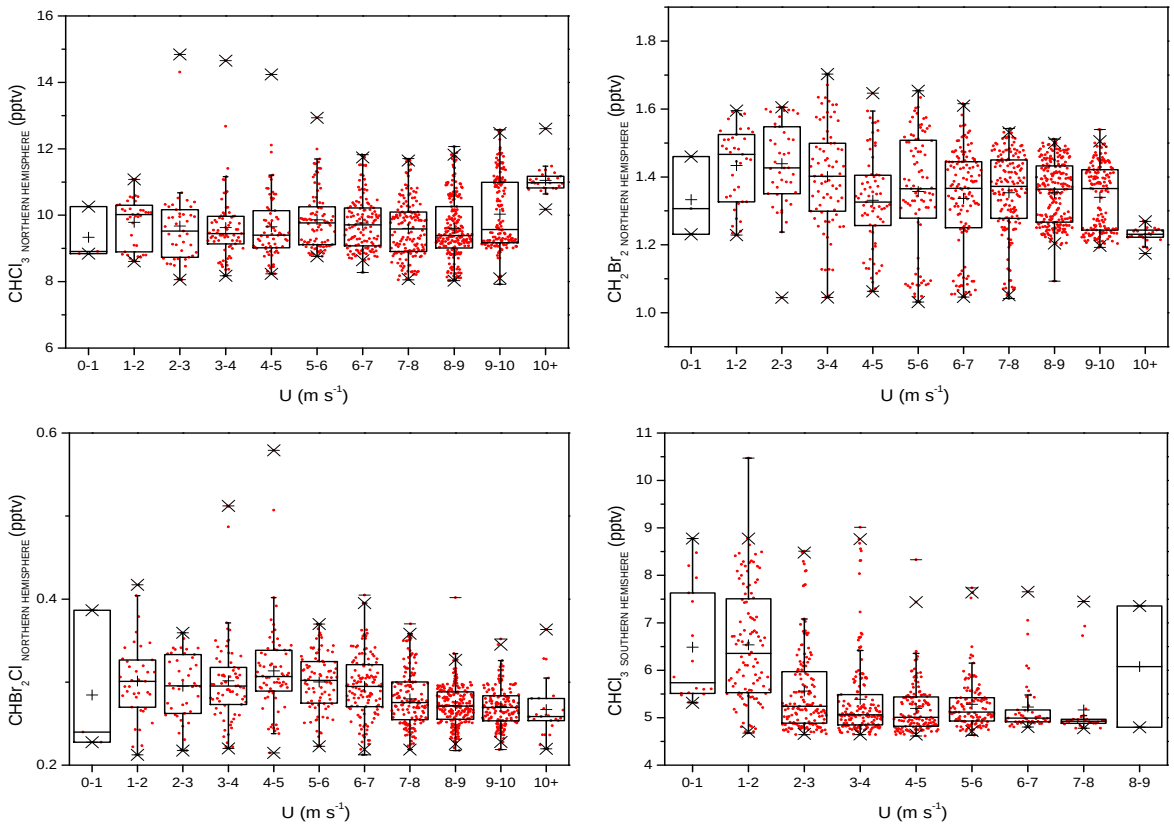

Figure 6.16 – VSLH air concentrations (ppt) during TORERO vs. wind speed (m s^{-1}). Data was binned by wind speed into 1 m s^{-1} groups. The box represents the interquartile range, and the line, plus and cross represent the median, mean and range respectively.

6.4.2.1 CH_2ICl wind speed relationship

An exponential relationship between wind speed up to 9 m s^{-1} and CH_2ICl atmospheric concentration has previously been observed at Appledore Island in the North Atlantic (Varner et al., 2008), however measurements from Hawaii by the same authors, a more relevant site for comparison with this dataset, did not show a wind speed relationship.

The observation by Varner et al. (2008) is consistent with the binned CH_2ICl data from TORERO with the exception of concentrations during the latter being much lower due to this being an open ocean dataset rather than coastal, as is the case at Appledore Island (figure 6.17, figure 6.18).

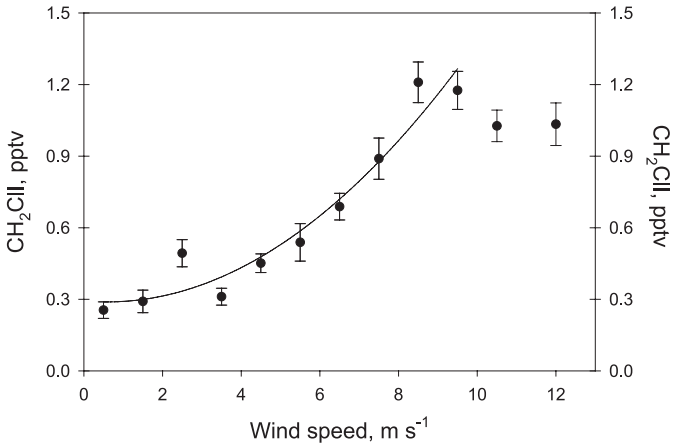

Figure 6.17 – Wind speed (m s^{-1}) versus CH_2ICl mixing ratios (pptv) at Appledore Island, Japan. CH_2ICl was binned into equally weighted groups of 1 m s^{-1} intervals and then averaged. Error bars indicate standard error of the binned grouping. Reproduced from (Varner et al., 2008).

Varner et al. (2008) attribute the drop in concentrations at wind speeds >9 m s^{-1} to their high wind speed regime sampling coinciding with daytime measurements where solar radiation was high and photolysis rates fast. This is not the case for the TORERO data where high wind speeds generally coincided with lower solar irradiance (figure 6.19). The drop in concentrations at wind speeds >9 m s^{-1} could be due to more dilution and a deeper boundary layer depth or could be an artifact of the statistical approach (figure 6.19).

Figure 6.19 shows the number of data points per wind speed bin (blue line), which follows

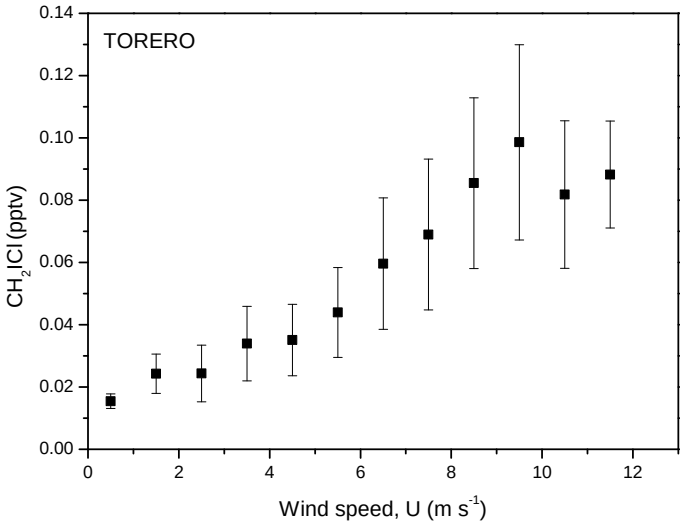

Figure 6.18 – Wind speed (m s^{-1}) versus CH_2ClI mixing ratios (pptv) during TORERO. CH_2ClI was binned into equally weighted groups of 1 m s^{-1} intervals and then averaged. Error bars indicate standard error of the binned grouping.

the expected normal distribution. The distribution of CH_2ICl data points is strongly weighted towards night time and is not distributed normally as concentrations were always very near to the limit of detection (figure 6.20). Averaged values at the extremes of the binned wind speed dataset have significantly less data and the weighting toward zero concentration results in a negative bias toward the averaged concentration.

The relationships between VSLH and wind speed shown here confirms that a multitude of factors control VSLH and that wind speed is just one of them. However, it does impart a significant influence and evidently, wind speed controls on iodocarbon fluxes must be constrained in order to accurately model global budgets.

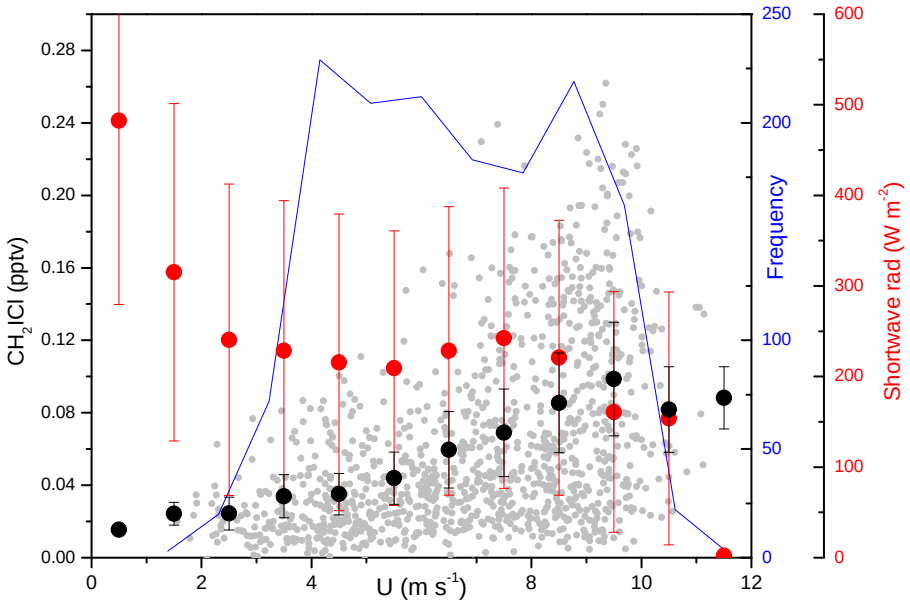

Figure 6.19 – CH_2ICl mixing ratios (grey circles) and shortwave radiation binned into equally weighted groups of 1 m s^{-1} intervals and then averaged (black and red circles, respectively). The blue line represents the distribution of the binned data.

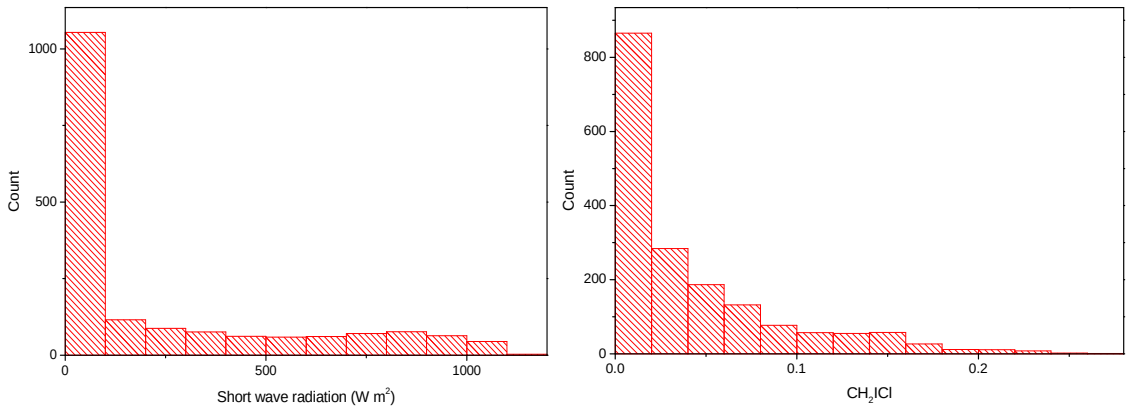

Figure 6.20 – Left: Binned solar radiation averages corresponding to individual CH_2ICl air measurements. Right: Binned CH_2ICl concentrations.

6.5 Factors controlling the atmospheric distribution of VSLH

6.5.1 Equatorial enhancements

There have been many measurements made of VSLH enhancements in equatorial regions which have been attributed to enhanced emissions from biologically productive waters associated with upwelling of cold water and nutrients (Quack and Wallace, 2003; Quack et al., 2004, 2007a; Class and Ballschmiter, 1988; Atlas et al., 1993). These measurements have a strong influence on global emission estimates as they span such large areas of ocean. Most global models such as GeosChem, which lacks the fine details of local emissions, includes an equatorial enhancement between 20°N and 20°S in its emission inventory (Hossaini et al., 2013). The question is whether the measurements that led to this assumption, which were often atmospheric mixing ratios, are actually representative of enhanced emissions and can be extrapolated across the entire equatorial region.

An enhancement of $CHBr_3$ in air was observed during TORERO across the Pacific equatorial upwelling where the northern and southern hemisphere water masses diverge. Water concentrations in this area show a small enhancement, however the calculated fluxes do not (figure 6.22). According to the observations, water concentrations are not sufficient to maintain the enhanced air concentrations relative to other sections of the cruise track.

Fluxes during TORERO were calculated using simultaneous measurements of both sides of the sea-air interface and allow us to separate flux-driven air concentration relationships from other factors. This allows us to determine whether oceanic production and emissions explain air concentrations or if other, physical relationships play a role.

The enhancement observed in air concentrations measured at the equator is not driven by flux because the flux does not change. This indicates a disconnect between the correlating sea and air concentrations, likely due to low wind speed at this point decreasing the transfer velocity from sea-air, despite the higher water concentrations. If the air concentrations cannot be explained by oceanic emissions then their levels must be explained by another factor.

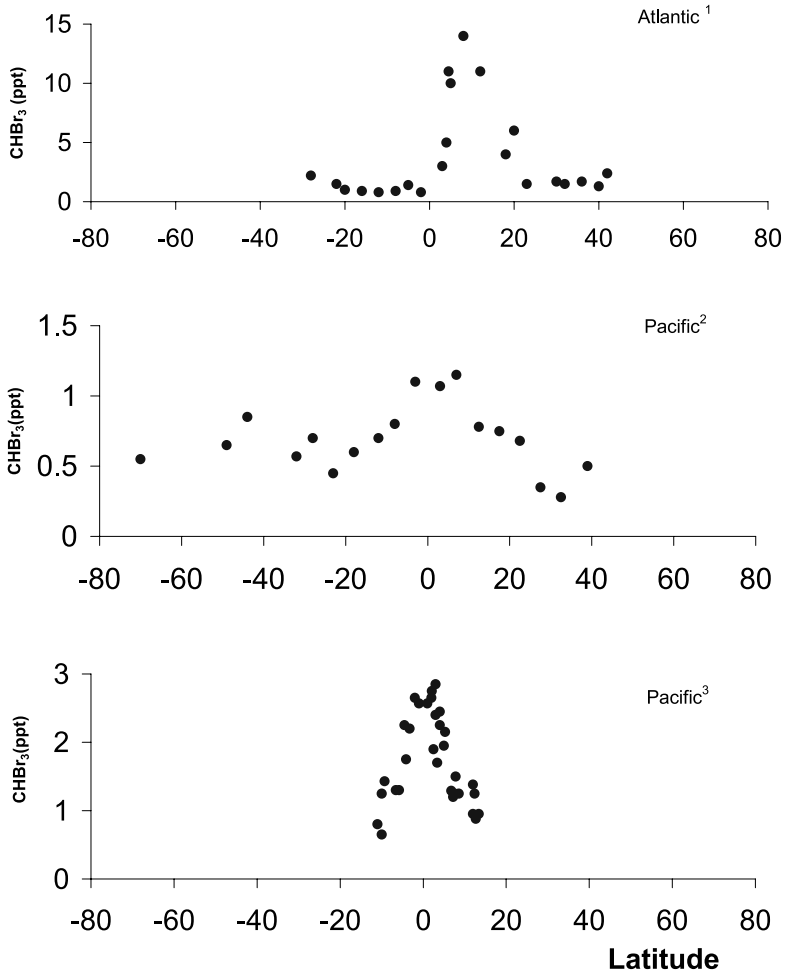

Figure 6.21 – Measurements of equatorial enhancements of MBL bromoform taken from Quack and Wallace (2003), over the Atlantic (1, 20°–10°W [Class and Ballschmiter (1988)]) and Pacific (2, 80°–160°W [Schauffler et al. (1999)]; 3, 145°–165°W [Atlas et al. (1993)]).

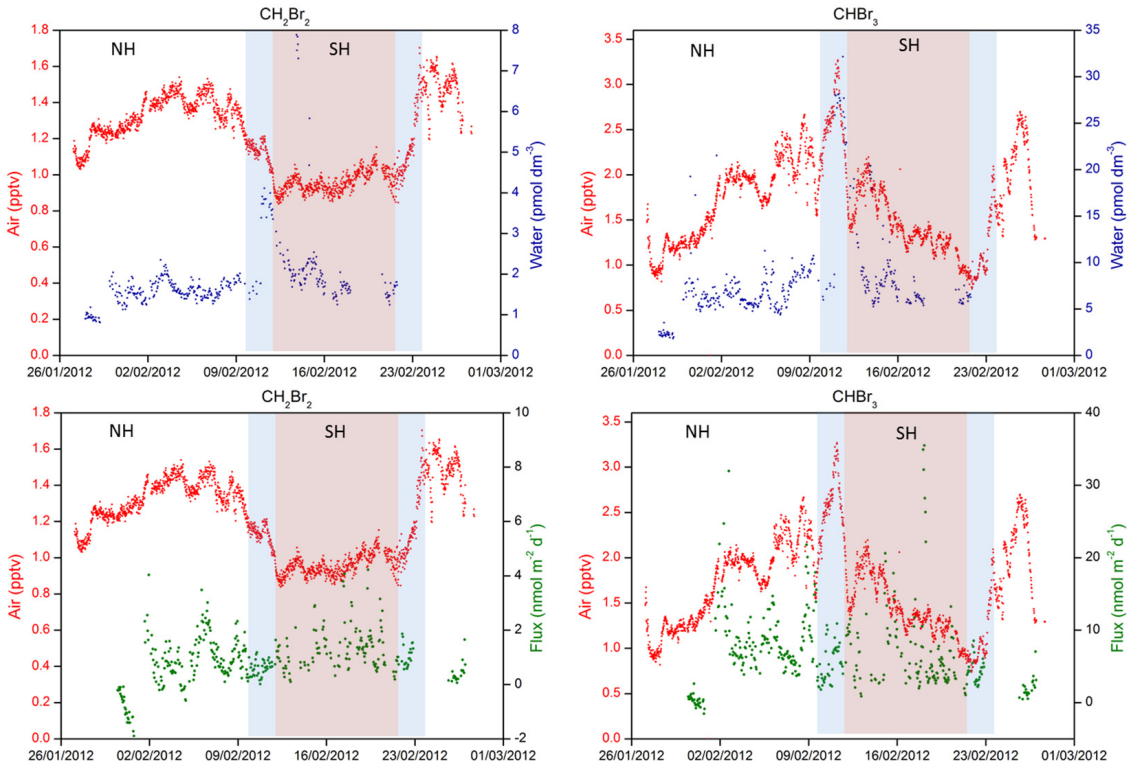

Figure 6.22 – $CHBr_3$ and CH_2Br_2 concentrations in air (red), water (blue) and the subsequent calculated flux from water to air (green) temporally along the cruise track. Blue sections indicate equatorial regions and red defines the southern hemisphere leg.

6.5.1.1 MBL

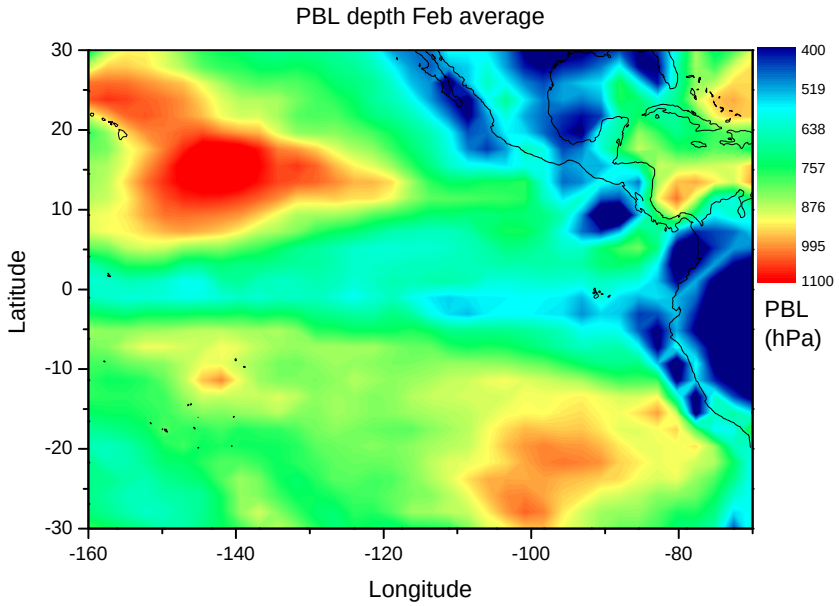

Figure 6.23 – Modeled planetary boundary layer depth (MBL) averaged for February during the TORERO cruise. Colour scale represents PBL depth, pressure at surface minus pressure at the top of the boundary layer.

Low boundary layer mixing in the equatorial region offers an explanation for the enhancement in air. Cold water upwelled at the equator produces increased biological production but the resulting bromocarbon flux is not enhanced therefore cannot explain air-side concentrations. The cold waters also cause the MBL to sink as it cools and it becomes very stable (figure 6.23). This serves to accumulate ocean derived trace gases close to the ocean surface and as they are not being mixed away and diluted, enhanced levels can be observed. Therefore, equatorial enhancements can often be attributed to meteorology rather than biology.

A good example of this can be seen in figure 6.24 where the highest $CHBr_3$ concentration is seen just below the equator 110°W over the equatorial upwelling corresponding to a drop in sea surface temperature. This is contrast with the lowest $CHBr_3$ concentration measured at around the same latitude 95°W off the coast of the Galopagos islands (figure 6.25). This region has a higher ocean chlorophyll concentration and is usually an area of coastal island upwelling but at this time the Peruvian cold tongue was weak, SSTs were high and there was little upwelling in this area. The high SST could thicken the MBL and the increased mixing result in bromocarbon depletion comparative to the 110°W region

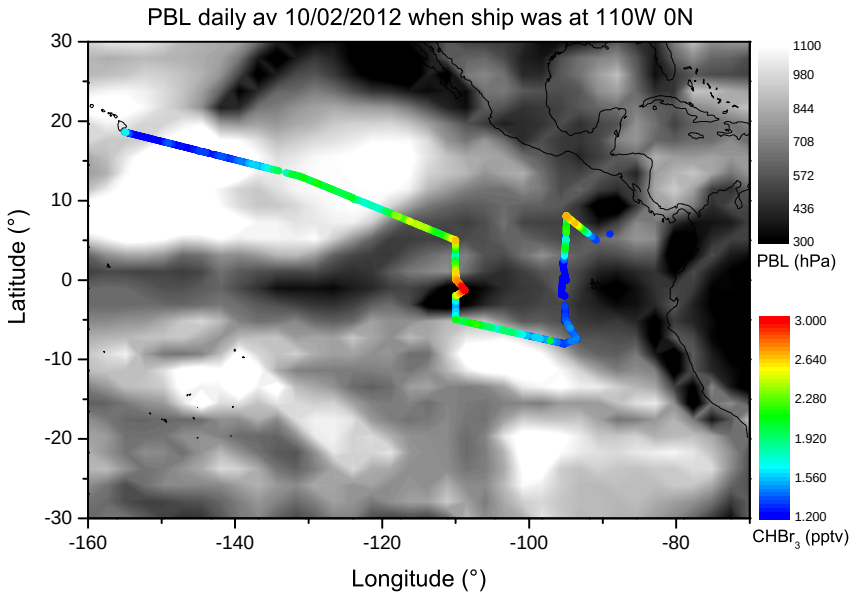

Figure 6.24 – GeosChem modeled planetary boundary layer depth (MBL) averaged for 10/02/2012 when the ship was at position 110°W, 0°N. Grey scale represents PBL depth, pressure at surface minus pressure at the top of the boundary layer.

despite the increased ocean productivity.

At latitudes below the equatorial upwelling, air ascends displaced by the sinking air over the cold region. This causes a decrease in the observed air-side concentrations as they are mixed and diluted. This is especially evident in the $CHCl_3$, CH_2Br_2 and $CHBr_3$ data, which show a rapid drop in concentration at lower latitudes. $CHBr_3$ is a little less affected due to the relatively high fresh source emissions replenishing atmospheric concentrations whereas CH_2Br_2 and $CHCl_3$ are longer lived and their MBL concentrations are more representative of well mixed, more background in magnitude, levels.

Figure 6.26 shows the modeled Planetary Boundary Layer (PBL, analogous to MBL) time series with $CHBr_3$ and CH_2Br_2 air concentration measurements. $CHBr_3$ concentration is negatively correlated with PBL thickness especially in the first half of the cruise where wind speed in the model was well constrained and correlated well with TORERO measurements. In the latter half the model meteorology did not correlate as well with measurements (figure 6.27). Model wind speed was underestimated in the southern hemisphere cruise leg and thus dilution would be greater. Water concentrations did not decrease during this period and fluxes remained fairly constant.

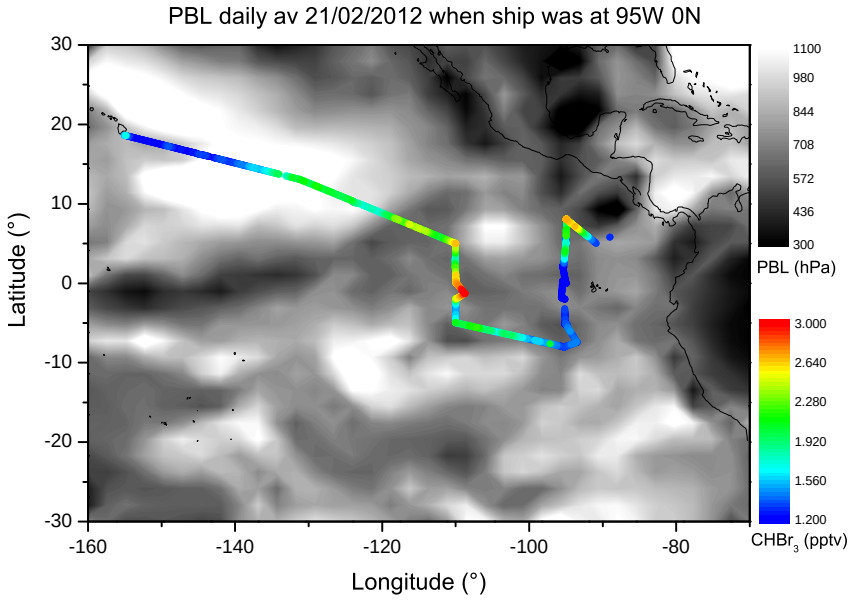

Figure 6.25 – GeosChem modeled planetary boundary layer depth (MBL) averaged for 22/02/2012 when the ship was at position 95°W, 0°N. Grey scale represents PBL depth, pressure at surface minus pressure at the top of the boundary layer.

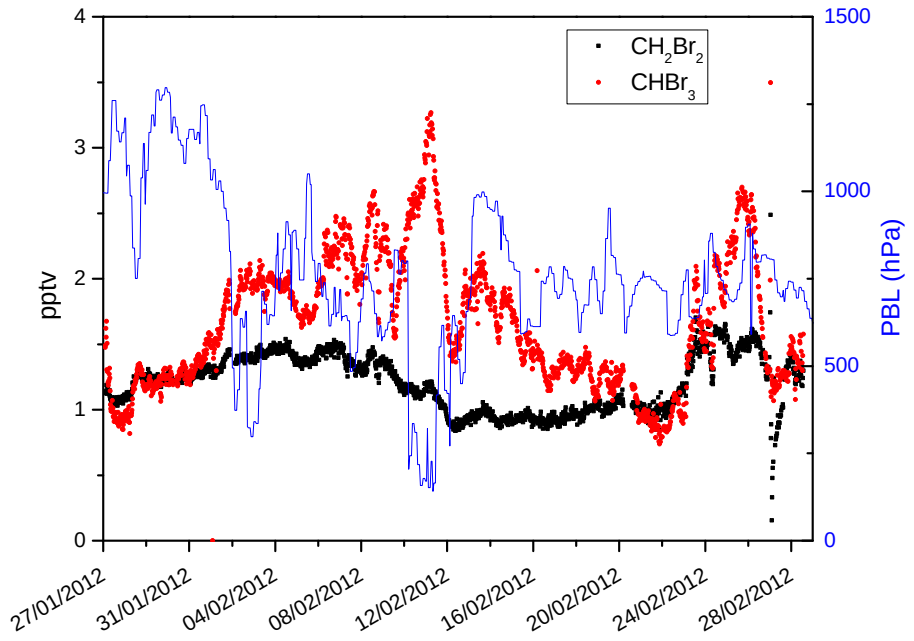

Figure 6.26 – Modeled planetary boundary layer depth (MBL) along the TORERO cruise track (blue line) with corresponding $CHBr_3$ and CH_2Br_2 atmospheric mixing ratios as red and black circles, respectively.

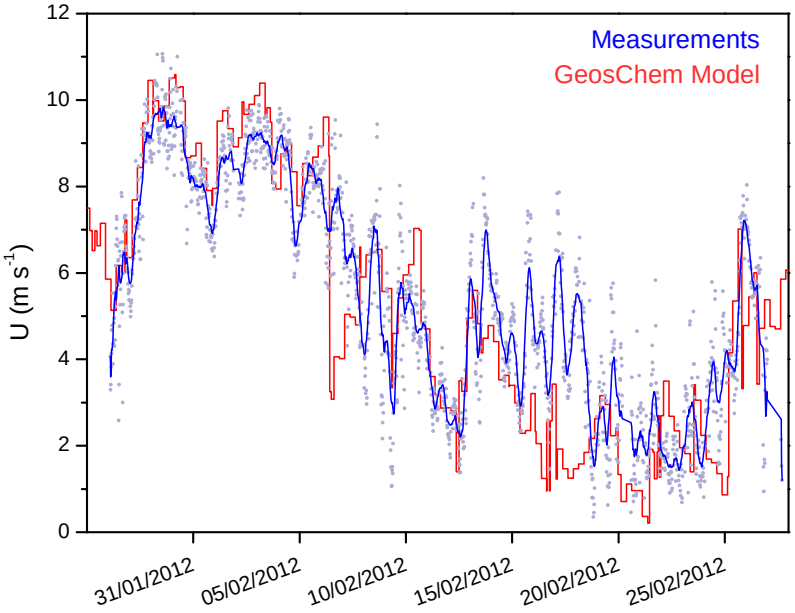

Figure 6.27 – Modeled wind vs. measurements along the TORERO cruise track. Measurements shown as grey circles with a 10 point average (blue line), GeosChem model output shown as red line.

This ocean driven MBL stability scheme can also be applied to the equatorial Atlantic Ocean. Enhanced bromocarbon air concentrations have been measured around the Mauritanian upwelling region (Quack et al., 2007a; Carpenter et al., 2009; Andrews et al., 2013) where cold water upwelled at the coast could result in a stable boundary layer and enhanced atmospheric concentrations. The theory of a sinking MBL over cold water causing adjacent vertical atmospheric transport and boundary layer thickening could explain the open ocean measurements of CH_2ICl made during the TROMPEX campaign (section 4.3.2). The theory of an open ocean source of CH_2ICl still holds but with vertical mixing transporting it to the altitudes at which it was measured on timescales shorter than its local lifetime of 0.1 days (Montzka et al., 2011). This could be why it was observed to increase in concentration further from the upwelling. At the upwelling it was likely produced in the biologically rich waters and fluxed into the air but not mixed to high enough altitude to be measured by the aircraft before being photolysed.

6.5.2 Hemispheric differences crossing the ITCZ

Positive correlations between VSLH, notably bromocarbons, are well documented (Carpenter and Liss, 2000; Quack and Wallace, 2003; Quack et al., 2004; Butler et al., 2007; Quack et al., 2007a,b; Carpenter et al., 2007, 2009; Raimund et al., 2011). These species often increase proportionally, which is likely due to similar sources in the environment. This can be direct biogenic production from micro/macro algae and phytoplankton or from subsequent substitution reactions with chlorine in seawater. Once emitted into the atmosphere from the source, bromocarbons will be subject to dilution and processing primarily from reaction with OH and breakdown by photolysis. Different bromocarbons have different local lifetimes based upon the combination of OH and photolytic degradation, listed in table 6.8.

Table 6.8 – Atmospheric lifetimes of various VLSH species. Values from Law and Sturges (2007).

	Lifetime (days)		
Species	OH	Photolytic	Local
$CHCl_3$	149	>15000	150
$CHBrCl_2$	121	222	78
CH_2BrCl	137	15000	137
CH_2Br_2	123	5000	123
$CHBr_2Cl$	94	161	59
$CHBr_3$	76	36	24

6.5.2.1 Chloroform distribution

Although its use as a common laboratory solvent is widespread and well known, the main source of chloroform ($CHCl_3$) in the environment is actually from biogenic sources (table 6.9). A clear inter-hemispherical difference in the mixing ratio is well documented with $CHCl_3$ concentrations being much greater in the northern hemisphere (Laturnus et al., 2002). The reasons for this are unclear as the ocean is the major source of $CHCl_3$ into the atmosphere (44%, table 6.9) yet the northern hemisphere only contains around 40%

of the global oceans. The influence of biogenic terrestrial sources is also significant despite land only covering 29% of the earths surface.

Table 6.9 – Sources and sinks of atmospheric chloroform, adapted from Laturnus et al. (2002).

	Average emission ($Gg\ yr^{-1}$)	Reference
Biogenic sources		
Total Ocean	364	Nightingale et al. (1995); Scarratt and Moore (1999); Khalil et al. (1999)
Total terrestrial	333	Haselmann et al. (2000); Khalil et al. (1999); Dimmer et al. (2001)
Anthropogenic sources		
Paper manufacture	34	Aucott et al. (1999)
Water treatment	22	Aucott et al. (1999)
Other	17	Aucott et al. (1999); Khalil et al. (1990); Aucott et al. (1999)
Sinks		
OH radicals	560	Keene et al. (1999)
Transport to stratosphere	2	Keene et al. (1999)

$CHCl_3$ air measurements at the beginning of the campaign were the highest recorded during TORERO, despite being furthest from land and the lowest surface Chl-a concentrations. However, during the cruise, this was the most northerly point and air masses originate from the west coast of America.

The contribution of anthropogenic emissions to the atmospheric concentration of $CHCl_3$ in the northern hemisphere is much greater than in the southern hemisphere and usage statistics have been recorded that highlight this inter-hemispheric gradient (figure 6.29).

Although anthropogenic emission is much greater in the NH, the global contribution of these emissions is relatively small, if the data from Worton et al. (2006) is correct. The ocean is the dominant source and the SH contains the largest oceanic area therefore, combining terrestrial, oceanic and anthropogenic emissions and comparing between the hemispheres should not result in a 50% decrease in concentrations when transitioning across the ITCZ as seen during TORERO.

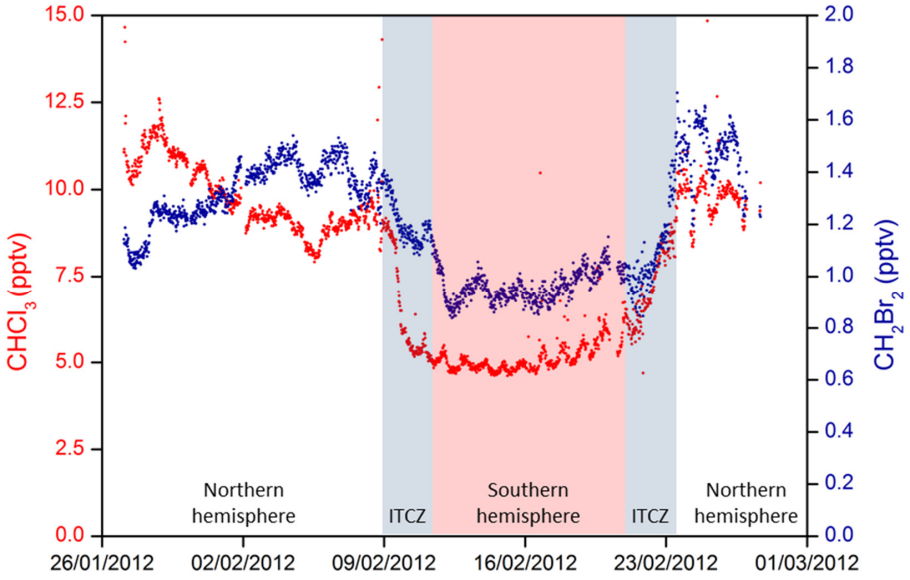

Figure 6.28 – $CHCl_3$ (red circles) and CH_2Br_2 (blue circles) mixing ratios throughout the TORERO campaign. Blue sections indicate when the ship was crossing the ITCZ and the red section represents measurements of air which had originated from the southern hemisphere.

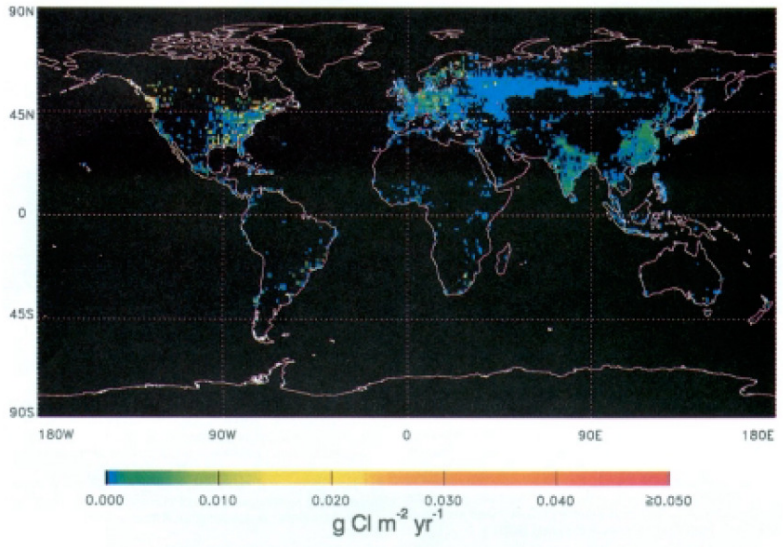

Figure 6.29 – $CHCl_3$ emissions from anthropogenic sources, reproduced from Aucott et al. (1999).

Because $CHBr_3$ is shorter-lived than $CHCl_3$, by plotting $\ln(CHCl_3/CHBr_3)$ against $\ln(CHBr_3)$ (figure 6.30, top), the ratio should increase with decreasing $CHBr_3$ concentration if atmospheric decay is taking place. This yields two distinct linear relationships with a clear latitudinal dependence. The negative gradient shows decay away from the source and the offset, parallel slopes show that the emission ratios are different in the northern and southern hemispheres but the rate of change is the same. That is the corresponding $CHCl_3$ concentration when $CHBr_3$ is emitted into the atmosphere is lower in the southern hemisphere but processed at the same rate as in the northern hemisphere. This is consistent with an additional anthropogenic component in the northern hemisphere in addition to a biogenic source; likely the same source or linked to the source of $CHBr_3$. Replacing $CHCl_3$ with CH_2Br_2 produces a similar distribution (figure 6.30, bottom). This would also suggest a NH anthropogenic CH_2Br_2 source. However, there is no evidence that any CH_2Br_2 is produced anthropogenically and as discussed, the anthropogenic component of $CHCl_3$ is not that strong.

The influence of coastal, Californian upwelling air could account for the greater CH_2Br_2 and $CHCl_3$ in the northern hemisphere data. Back trajectories (section 5.2.5, figure 5.15) show air masses travelling along the Californian coastline before taking a very direct route to the point of analysis. As CH_2Br_2 and $CHCl_3$ have reasonably long lifetimes it is likely that open ocean measurements would be influenced by coastal emissions whereas for $CHBr_3$, measured concentrations are more representative of local sources. As the ship entered the SH leg the air masses originate from the southern Pacific and have not touched land for at least 8 days where just a few of the trajectories touch the coastal waters of Chile.

An interesting observation is the high salinity measured during the SH leg. This is likely due to being south of the ITCZ with a lack of rain and high solar irradiance causing evaporation of surface water. Bromocarbon ratios show a similar shift with salinity as they do with latitude (appendix, figure A.3), which highlights that multiple factors can be linked to VSLH distribution and they may be directly linked to VSLH or indirectly though one another. Factors may correlate with VSLH when actually they are a result of another factor linked to VSLH and do not actually impact VSLH at all. In order to understand VSLH distribution, factors must be designated as driving or driven.

Although the log ratio of $CHBr_3$ to $CHBr_2$ is expected to be fairly constant, Lin and

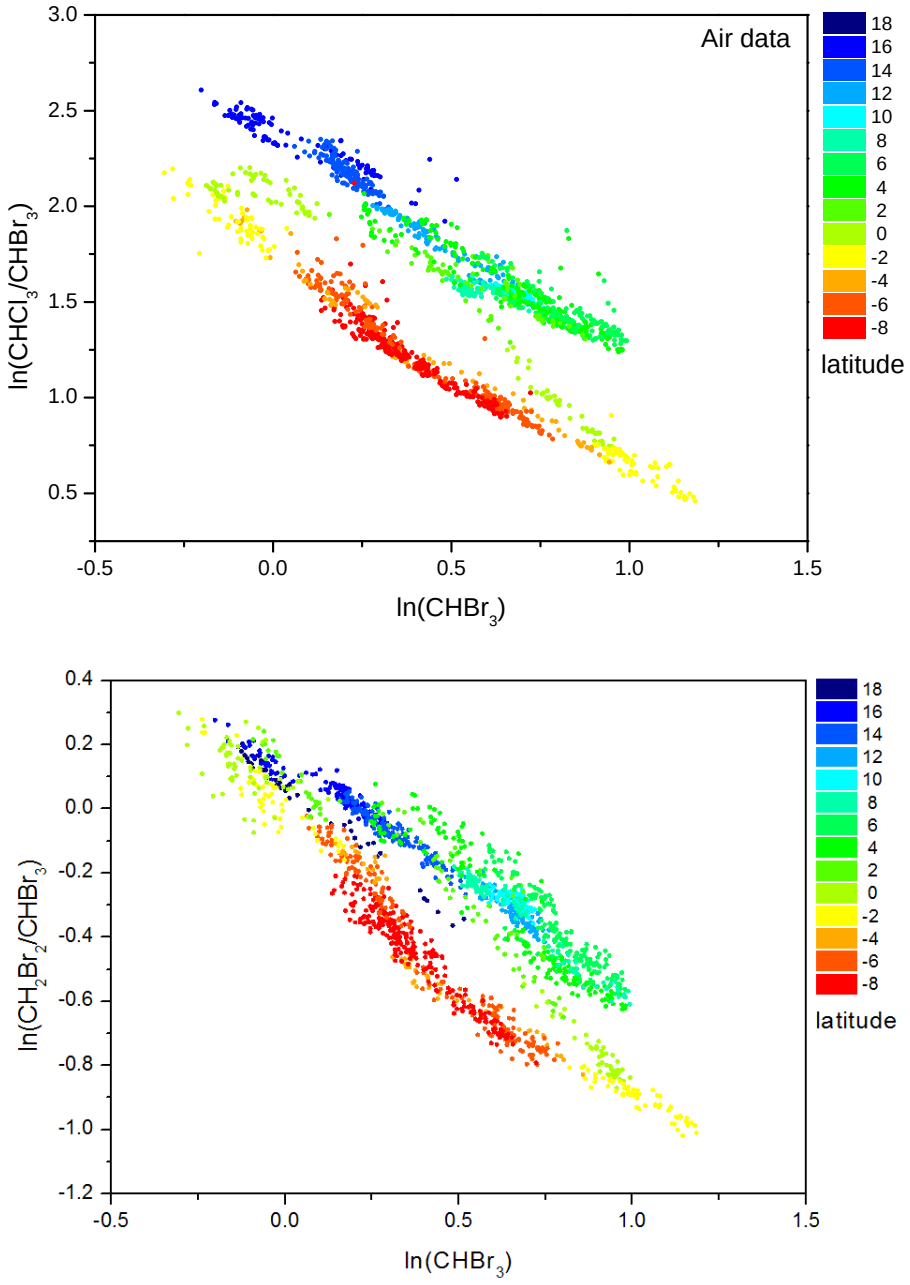

Figure 6.30 – Ratios of $CHCl_3$ (top) and CH_2Br_2 (bottom) to $CHBr_3$. Decreasing ratio shows processing of the air mass, y-axis offset shows different emission ratios, slope = ratio of the lifetimes. Data coloured by latitude.

Manley (2012) see seasonal differences in $CH_2Br_2/CHBr_3$ ratios produced from seawater treated with bromoperoxidase and Liu et al. (2013a) find that heterotrophic bacterial abundance was significantly correlated with CH_2Br_2 but not with $CHBr_3$. As each hemisphere is in its respective winter or summer the $CH_2Br_2/CHBr_3$ release ratio could change with latitude.

Utilising the GeosChem model, CH_2Br_2 and $CHBr_3$ can be modelled across the course of a year (2012) along the 110°W line, where the TORERO samples were taken, at different latitudes between 30°S and 30°N and averaged monthly (figure 6.31).

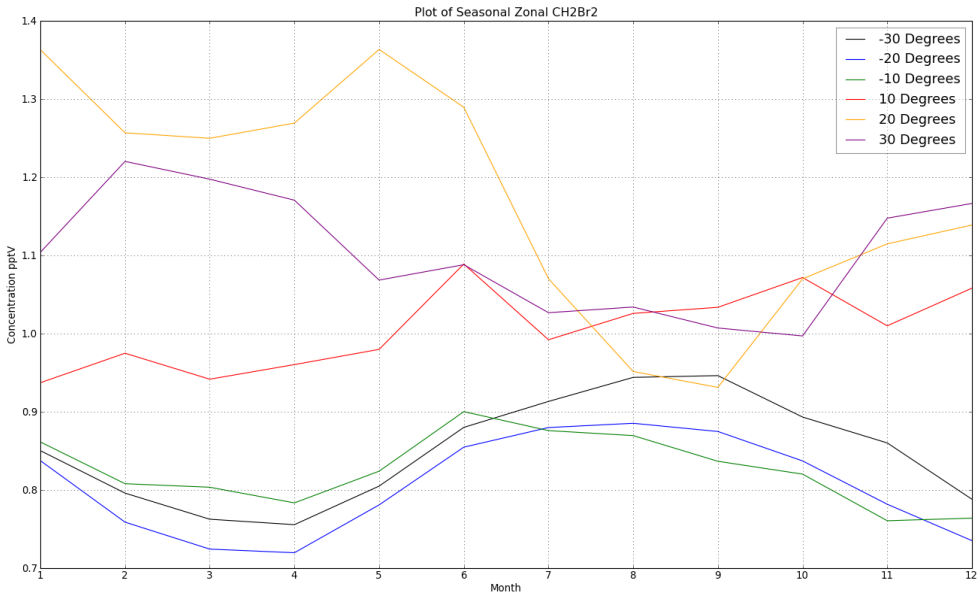

Figure 6.31 – CH_2Br_2 modelled using GeosChem across the course of 2012 at 10° increments between 30°S and 30°N along 110°W.

The model shows a clear seasonality and displays out of phase cycles between each hemisphere. The seasonal cycle does not appear as strongly in the northern hemisphere, which could be due to the coastal source influence discussed previously.

Plotting $CHBr_3$ in the same way predicts that a very similar pattern would exist as for CH_2Br_2 (figure 6.32). The emission ratio of CH_2Br_2 and $CHBr_3$ is fixed within the model, so differences in seasonality must be due to differences in oxidant concentrations.

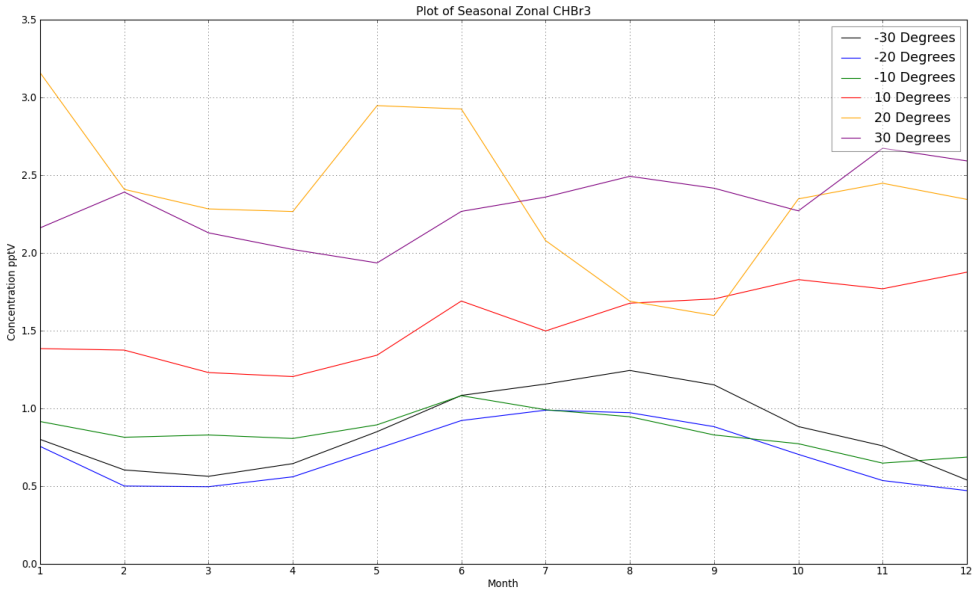

Figure 6.32 – $CHBr_3$ modelled using GeosChem across the course of 2012 at 10° increments between 30°S and 30°N along 110°W.

6.5.3 VSLH in air positively correlated to solar radiation

A few of the VSLH species showed diurnal cycles in air which were positively correlated to solar irradiance. Most notable were $CHBrCl_2$ and $CHCl_3$ which increased with increasing solar irradiance, although with a temporal offset. The cycles were most prominent in the Southern Hemisphere for $CHCl_3$, this may be due to a decrease in the background air concentration rendering the diurnal more visible. There was no noticeable diurnal cycle in the surface water data for either species but this could be obscured by sampling reproducibility noise and/or temporal resolution of the water sampling when compared to the air data. For $CHBrCl_2$ the air concentrations were similar between hemispheres with surface water concentrations actually decreasing (figure 6.33) and air concentrations increasing slightly. Flux calculations (section 6.3.1) show that the flux decreases in the Southern Hemisphere due to the drop in wind speed. Therefore the extra $CHBrCl_2$ is likely not coming from the ocean and the rapid diurnal cycling suggests that it is likely not transported a large distance and thus this is not due to a contribution from a remote source.

Two theories can be presented to attempt to explain these results. First is photochemical production of these species in the surface water. Production in the surface water is unlikely

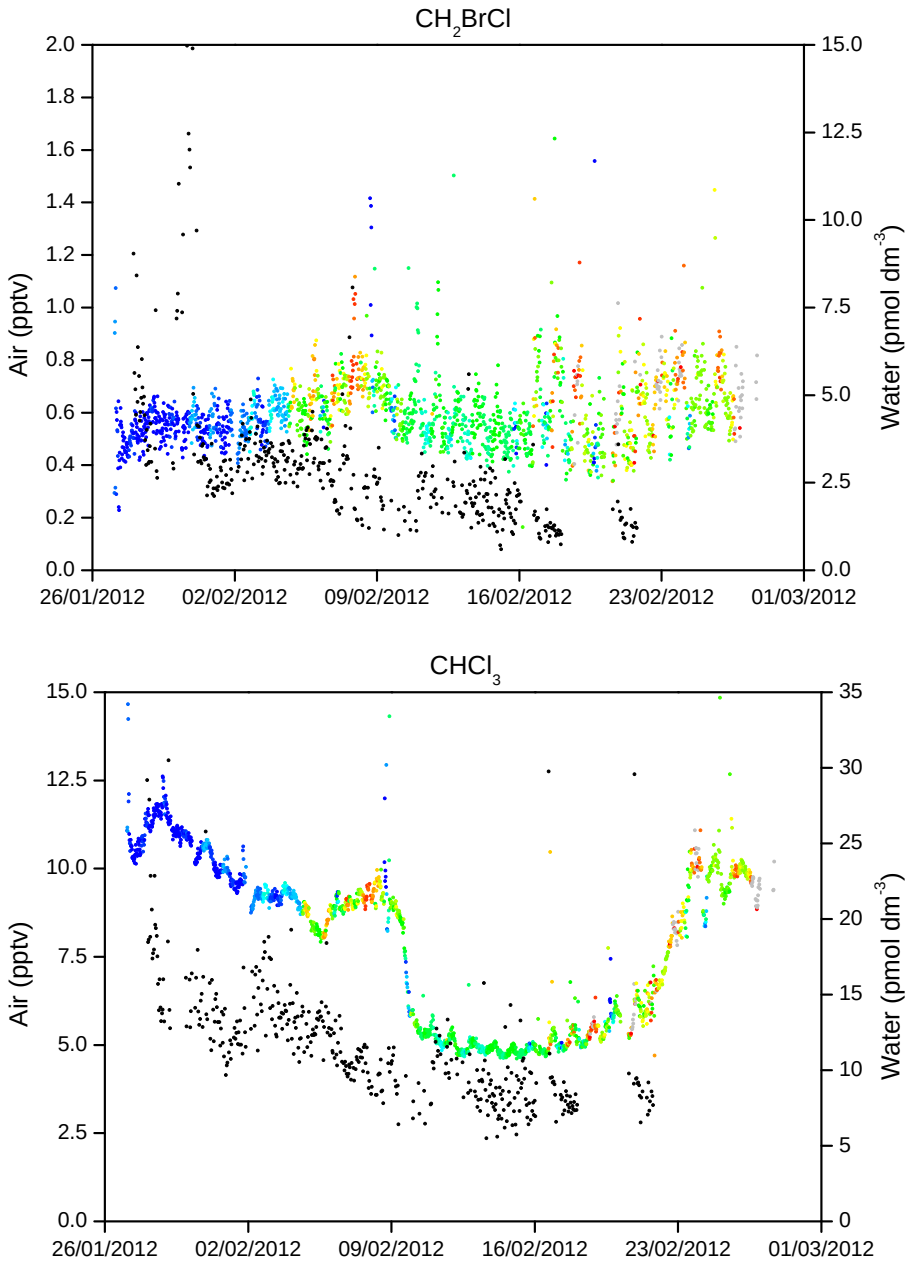

Figure 6.33 – $CHCl_3$ (top) and $CHBrCl_2$ (bottom) showing evidence of positive diurnal cycles. Air data coloured by air temperature, water measurements in black

as the diurnals were not observed in the water data and in the case of $CHBrCl_2$, the water concentration decreased whilst the air concentration increased around the 8^{th} February. A possibility is production in the ocean layer at the very surface. Surface water measurements were taken from approximately 3 m depth and may not have been representative of the very top of the ocean surface. Wind speed was very low during the Southern Hemisphere leg of the cruise and as such the sea surface was very flat. Sea surface temperature was high and displayed a greater diurnal variation during the second half of the cruise, similar to the $CHBrCl_2$ concentrations.

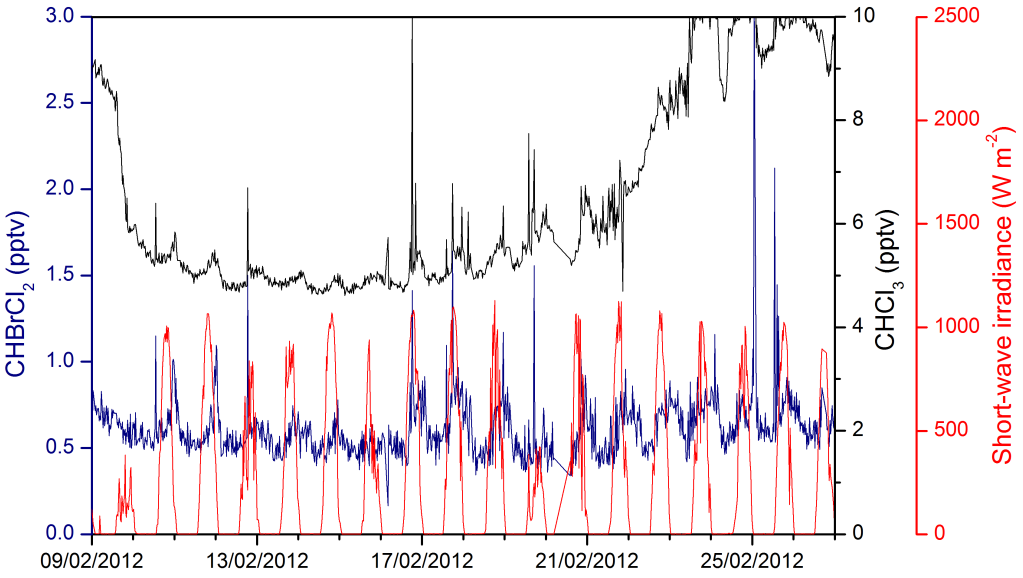

Figure 6.34 – $CHBrCl_2$ (blue line) and $CHCl_3$ (black line) showing evidence of a positive diurnal cycle. Short-wave irradiance shown in red

A second theory is that there exists a positive interference with the air sampling technique. One such possibility is the retention of analytes on the 1/2" PFA sampling line which are desorbed as the line is heated by the sun. $CHBrCl_2$ concentrations were only weakly correlated with air temperature (figure 6.35) but this may not be directly linked. An argument against sample artifacts is that $CHCl_3$ and $CHBrCl_2$ are volatile and the positive diurnal cycle was not seen in other, less volatile species. Some other compounds, namely CH_2Br_2, CH_2BrCl and $CHBr_2Cl$, showed possible evidence of a positive diurnal when averaged across the entire Southern Hemisphere section of the cruise as can be seen in figure 5.45. However, $CHBr_3$ and CH_2I_2 showed no clear positive diurnal despite being the least volatile compounds analysed and most susceptible to sticking on sampling lines. Recent sample line tests have found high $CHBrCl_2$ when drawing air through the sample

line, with concentrations reducing over time. This supports the theory of desorption of analytes from the sample line walls during solar heating.

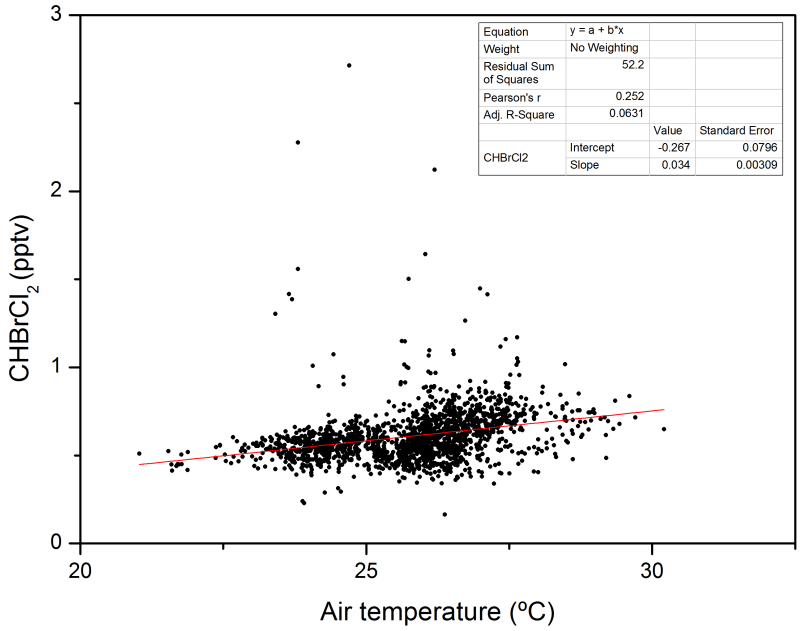

Figure 6.35 – Weak positive correlation between $CHBrCl_2$ and air temperature. linear regression line shown in red

6.6 Summary

Whilst individual CTD depth profiles showed that VSLH generally peaked at or near the Chl-a maximum, analyses showed very little bulk correlation between Chl-a and VSLH concentrations when comparing all CTD profiles collected during TORERO. Generally it seems that VSLH sea-air emissions cannot be parameterised as a simple function of Chl-a. The very short-lived VSLH CH_2I_2 and CH_2ICl actually displayed a negative relationship with Chl-a, as well as between surface and deep maximum concentrations. These relationships could be attributed to physical and mixing processes. Higher surface concentrations of Chl-a are associated with greater turbidity and attenuation of solar irradiation which is likely to result in decreased surface water depletion of CH_2I_2 and CH_2ICl during daylight hours. High surface Chl-a may also be associated with enhanced mixing, leading to higher entrainment of VSLS from the Chl-a maximum. This analysis highlights the importance of physical processes on the distribution of CH_2I_2 and CH_2ICl throughout the water column.

Conversely, $CHBr_3$, CH_2Br_2 and $CHBr_2Cl$ showed a good correlation between surface and deep maximum concentrations, indicating their relatively long lifetimes in seawater. This suggests that if a suitable proxy for production of these compounds can be found, then there is potential to parameterise their surface seawater concentrations without the necessity of using a water column model to compute the complex interactions between physical, biological and chemical processes. However, currently there is a lack of understanding regarding production of these gases within the water column. The TORERO data revealed an increased correlation of $CHBr_3$ with $CHBr_2Cl$ and CH_2Br_2 at the ocean surface compared to their deep maxima, although reasons for this are currently unknown. The ratio of $CH_2Br_2/CHBr_3$decreases toward the surface which could be linked to preferential bacterial break-down of CH_2Br_2 in surface waters.

By comparing the TORERO depth profile of CCl_4 to the ocean mixing model by Stemmler et al. (2013), it is evident that sub-surface enhancements can be formed by mixing down of dissolved gases from the surface. This makes it difficult to define the depth at which production is occurring and link sub-surface maxima to biological production of VSLH.

Simultaneous air and water sampling during TORERO allowed for the calculation of saturation anomalies and fluxes. Significant differences in flux estimates can be obtained by

using different calculation methods, resulting in uncertainties greater than analytical or calibration uncertainties between datasets. The ocean was super-saturated for the majority of VSLH with the exception of CH_2BrCl, which was near equilibrium, and CCl_4, which was under-saturated. In general VSLS sea-air fluxes during TORERO were representative of previous open ocean data, except for $CHCl_3$ which was double the previous global estimate of Worton et al. (2006). This high $CHCl_3$ flux could be indicative of greater than previously estimated oceanic emissions, or an overestimate of the anthropogenic contribution to $CHCl_3$ emissions (approximately 50%).

The TORERO data showed that emissions of VSLH were driven by wind speed with an exponential relationship for CH_3I, CH_2ICl, CH_2I_2 and $CHCl_3$. This has implications for global models which generally assume constant emissions, although meteorological models are well constrained by measurements therefore incorporating this relationship into a chemical model should be possible. The combination of enhanced flux and rapid vertical transport during periods of high wind speed could result in enhanced quantities of VSLH being transported to the UTLS. The wind speed relationship to VSLH emissions could prove important if the future climate was to become warmer and more strongly convective as suggested by Salawitch (2006) with respect to wind-driven upwellings.

Equatorial enhancements of atmospheric $CHBr_3$, and to a lesser extent CH_2Br_2, were not associated with higher sea-air emissions of these compounds in the tropics. Instead most of the variability in atmospheric bromocarbon concentrations during TORERO can be attributed to changes in MBL thickness and atmospheric mixing caused by the cold tongue of the East Pacific ocean upwelling. MBL concentrations of VSLH are sensitive to atmospheric dynamics and care should be exercised when interpreting air concentrations and linking them to oceanic emissions. The common assumption in global models of much higher sea-air emissions of bromocarbons in the equatorial regions compared to higher latitudes may need to be revisited.

Chapter 7

Concluding remarks

Very short-lived halocarbons (VSLH) are produced at depth and at the surface of the ocean (chapter 5). The production mechanisms are not comprehensively understood but include biological and photochemical production (section 6.1). The spatial distribution of VSLH is dependent on chemical species. Coastal regions provide high concentration, localised sources (chapter 4) whereas open-ocean fluxes are much lower yet widespread and for some VSLH, even ubiquitous over huge expanses of ocean with significant global contribution (section 6.3).

Iodocarbons often show spatial distributions disconnected from bromocarbons (section 4.4) in both the ocean (section 5.4.1) and the atmosphere (section 5.3.6). Methyl iodide has a surface ocean photochemical source (section 5.4.1.1), chloroiodomethane and diiodomethane show evidence of open-ocean, possibly phytoplankton derived sources (sections 4.3.2 and 5.3.6.1). More detailed investigations into VSLH production mechanisms are required to allow for the progression of accurate estimates of VSLH emission and distribution.

Advances in analytical instrumentation permit the detection of VSLH with ever increasing sensitivity and temporal resolution (chapter 2). However, accurate calibration of VSLH remains the most important factor in producing useful and comparable datasets (chapter 3). Stable gas standards are now available at atmospheric concentrations which should allow for more comparability of future datasets. Instrument and calibration gas standard inter-comparison between multiple research institutions is required in order to produce

global datasets for short-lived, reactive species with such varied spatial and temporal distributions.

Even with accurate calibration, care must be taken in the interpretation of VSLH measurements as physical parameters such as tropospheric boundary layer depth and ocean mixing can strongly influence their distributions in the atmosphere and ocean, respectively (sections 4.4, 6.5.1 and 6.5.1.1).

Due to the formation of reactive halogen species, VSLH play an important role in the troposphere and in conjunction with rapid vertical transport in the tropics, contribute to stratospheric ozone depletion. Meterological factors driving this rapid transport in the atmosphere also influence oceanic transport and sea-air flux of VSLH. For example, at high wind speeds, VSLH produced within the ocean mixed layer are transported to the surface via ocean mixing (section 6.2). The sea-air flux is strongly wind speed dependant thus more VSLH enters the atmosphere.

Positive net radiative flux in the tropics drives inter-tropical air mass convergence, sea surface temperature, evaporation and convection in this region. It also influences thermohaline circulation, equatorial upwelling and even photochemical production at the sea-surface. This link between ocean and atmosphere is often missing in global models which assume fixed oceanic emissions (Liang et al., 2010; Ordóñez et al., 2012; Santos and Rast, 2013). Atmospheric chemistry models are often detached from their oceanic counterparts although work is ongoing for dimethyl sulphide, a species with large global dataset coverage, in combining climate and global ocean models such as NEMO (Nucleus for European Modelling of the Ocean, Le Clainche et al. (2010))

Future predictions of climate suggest that the atmosphere will become warmer and more convective (Salawitch, 2006), with implications on nutrient, temperature and upwelling sensitive, biological production of VSLH (Carpenter and Liss, 2000; Quack et al., 2004). On the other hand, melting polar ice caps providing freshwater input are predicted to weaken thermohaline circulation (Stouffer et al., 2006). Predicted ocean changes are numerous and include ecosystem (Rost et al., 2008), de-nitrification (Canfield et al., 2010) and ocean acidification from the increase of anthropogenic CO_2 (Doney et al., 2009) to name a few. The complex relationship between climate, oceanic and atmospheric circulation, oceanic production and ocean-atmospheric exchange requires a model to interpret.

Whilst the recent past climate change gradient may permit ocean-atmosphere disconnect in models, rapid climate shifts, such as the current polar ice retreat (Stammerjohn et al., 2012), could strongly influence ocean-atmosphere gas exchanges. With such sparse datasets for VSLH, measurements can span a decade in order to obtain reasonable global coverage (e.g. $CHBr_3$ –Quack and Wallace (2003)-present day 2013). In this same decade atmospheric CO_2 concentration has increased by 10 ppm (2.5%, at Mauna Loa observatory, NOAA). With such rapidly changing climate and chemistry, modelling of VSLH is paramount and should aim to model not only their atmospheric fate, but also their oceanic production otherwise the effect of future climate, or other rapidly changing variable, on the emission of these gases can never be predicted.

A logical extension to this body of work would be an attempt to link ocean and atmospheric models with respect to VSLH using meteorological inputs to drive an ocean model which would, in-turn, feed back into existing atmospheric chemistry models. The atmosphere driving the ocean and subsequent flux of trace gases from ocean to atmosphere modelled in this way would allow the model to better react to future and even current changes not accounted for with the data available to date.

Appendix A

Supplementary Figures and Information

A.1 Appendix figures

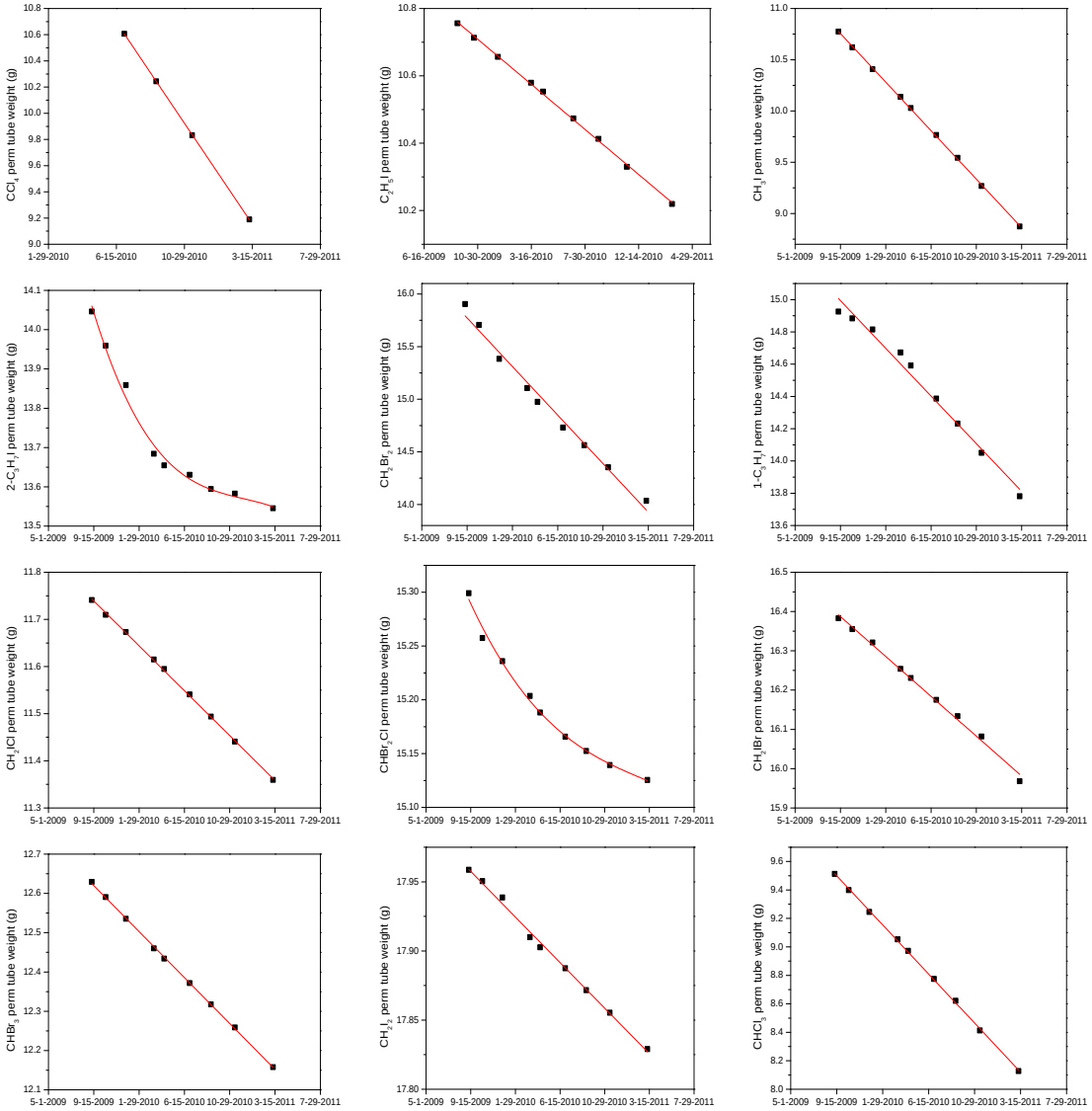

Figure A.1 – Mass loss graphs used for calculation of the permeation oven output.

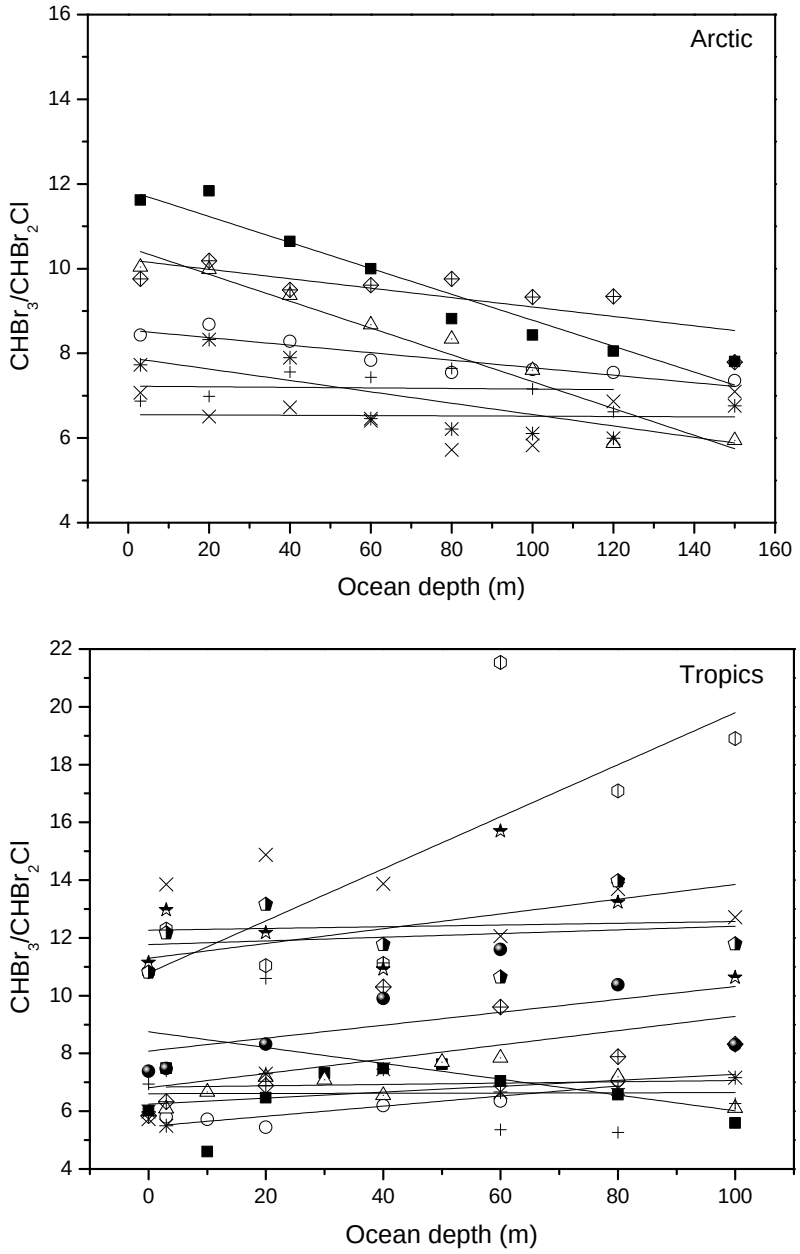

Figure A.2 – Comparison of $CHBr_3/CHBr_2Cl$ ratio with depth in the Arctic (~ 0°C SST) and the ETP (~ 27°C SST).

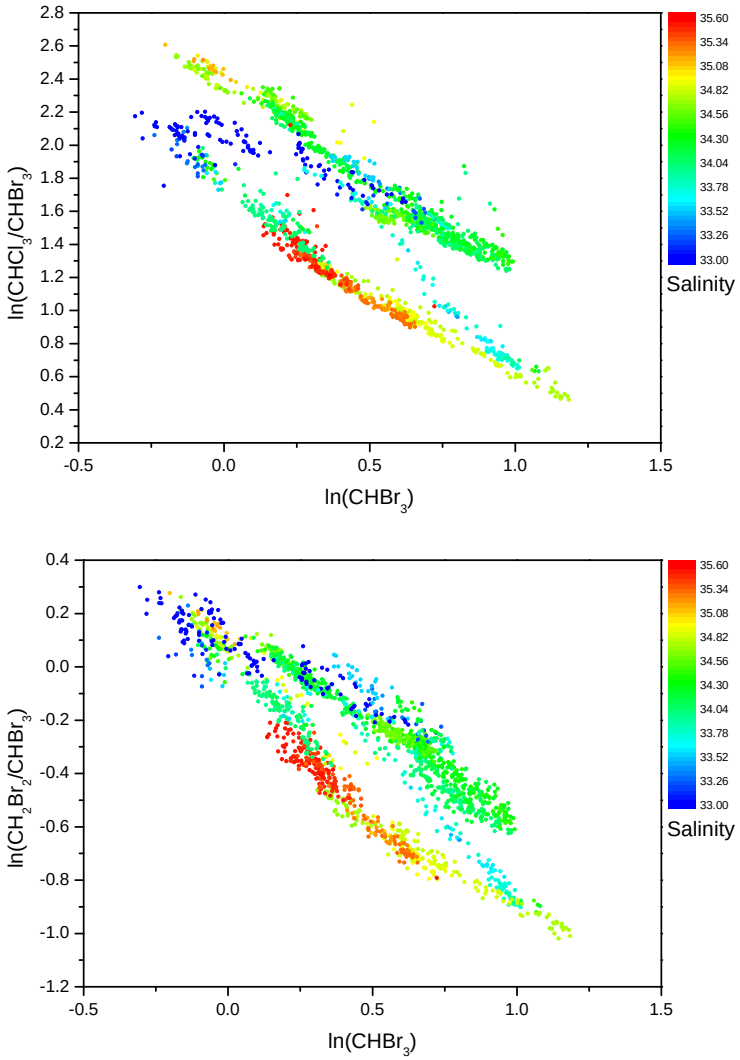

Figure A.3 – Ratios of $CHCl_3$ (top) and CH_2Br_2 (bottom) to $CHBr_3$. Decreasing ratio shows processing of the air mass, y-axis offset shows different emission ratios, slope = ratio of the lifetimes. Data coloured by salinity.

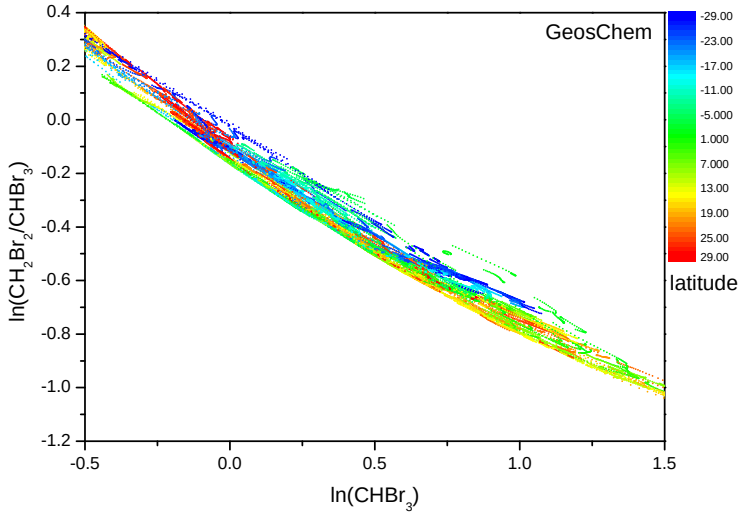

Figure A.4 – GeosChem output ratio of CH_2Br_2 to $CHBr_3$. Decreasing ratio shows processing of the air mass, y-axis offset shows different emission ratios, slope = ratio of the lifetimes. Data coloured by latitude.

A.2 Auto Purge and Trap code

```
//Arduino code for auto purge and trap system. This code reads a relay trigger from the Unity2 and controls
//two valves which fill and empty the purge tube. Outputs to an LCD screen.
//it also runs isothermal heating control of the purge tube in the background.
//author Stephen J. Andrews

const int TDrelaypin = 7; // Pin attatched to TD sample valve relay
const int SolenoidApin = 13; // Pin attached to solenoid via a transistor and relay
const int SolenoidBpin = 8; //same as above
const int LM35Pin = A3; //analog in with LM35 temp senor attached
const int heaterPin = 10; //PWM output to SSR to control heating tape
const int tempsetpoint = 50; //what temp do you want the tube to be?
const int manualtriggerpin = 6;
const int omegaSSRout = 9;
const int peristaltic = 0;
const int floatswitch = A5;
const int omegatempvalue = 2;

float tempC;
float tempdiff;
int extrapower = 1;
boolean Running = false;
boolean linespurged = false;
boolean tubefilled = false;
boolean tubepurged = false;
```

```
boolean tubeflushed = false;
long countdownitem = 0;
long countdown = 0;
long count = 0;
long triggertime = 0;
long currenttime = 0;
long previoustemptime = 0;
int dataupdatespeed = 1000;
long filterpurgeinterval = 280000; //105000
long linepurgeinterval = 305000; //125000
long fillinterval = 351500; //156500 adjust this to set the time in ms for the tube to fill for. 46.5sec =30mL
long flushinterval = 2146500; //1325000 time(ms) from triggertime until the water is emptied to waste
long flushtime = 2166500; //1345000 time(ms) that it empties the water for (from triggertime)
int LM35value = 0; //value read from temp sensor
int heatervalue = 0; //PWM value to trim heater by
long POS = 0; //percentage of setpoint
int mappedLM35 = 0;

LiquidCrystal lcd(12, 11, 5, 4, 3, 2);

void setup() {
// set up the LCD's number of columns and rows:
lcd.begin(20, 4);
// initialize serial communications at 9600 bps:
analogReference(INTERNAL); //analog scale to 1.1V for better resolution!
pinMode(TDrelaypin, INPUT); //specify the pin modes
pinMode(SolenoidApin, OUTPUT);
pinMode(SolenoidBpin, OUTPUT);
pinMode(omegaSSRout, OUTPUT);
pinMode(peristaltic, OUTPUT);
pinMode(floatswitch, INPUT);
pinMode(manualtriggerpin, INPUT);
digitalWrite(SolenoidApin, LOW);
digitalWrite(SolenoidBpin, LOW);
digitalWrite(peristaltic, HIGH);
}
void loop() {
int floatswitchstate = digitalRead(floatswitch);
if (floatswitchstate == LOW) {digitalWrite(peristaltic, LOW);
lcd.setCursor(0,0);
lcd.print(" LEAK DETECTED!!!!! ");
}
if (floatswitchstate == HIGH) {
lcd.setCursor(0,0);
if (tempC < (tempsetpoint-1)){
lcd.print("Tube is below temp!!");}
else lcd.print("Automated Purge&Trap");}
```

```
LM35value = analogRead(LM35Pin); //read the value from the temp sensor
tempC = LM35value / 9.31;
tempdiff = tempsetpoint - tempC;
float temppercent = tempdiff * 2.5 * extrapower;
//mappedLM35 = map(LM35value, 0, 1023, 0, 255); //scale 1024 analoge bits to 256 digital
//POS = mappedLM35 / tempsetpoint *100;
// if (POS < 80) {
if (tempC >= tempsetpoint) {
heatervalue = 0;
}
if (tempC < tempsetpoint) {
heatervalue = temppercent * 2.55;
}// }
// if (POS > 80) {
// heatervalue = (255/100)*(100 - POS);
// }
analogWrite(omegaSSRout, heatervalue); //write the PWM value to the heater pin
analogWrite(heaterPin, omegatempvalue);

int TDtrigger = digitalRead(TDrelaypin);
int manualtrigger = digitalRead(manualtriggerpin);
if ((manualtrigger == LOW) && (Running == false)) {TDtrigger = HIGH;}
if (TDtrigger == HIGH) {
count = count + 1;

if ((count == 1) && (Running == false)){
triggertime = millis();
lcd.setCursor(0,1);
lcd.print("Purging sample lines");
countdownitem = linepurgeinterval;
linespurged = false;
tubefilled = false;
tubepurged = false;
tubeflushed = false;
Running = true;
}}
else {count = 0 ;}

currenttime = millis();
if (Running == true){

if ((currenttime - triggertime > filterpurgeinterval) && (linespurged == false)) {
digitalWrite(SolenoidApin, HIGH);
lcd.setCursor(0,1);
lcd.print("Purging lines&filter");}

if ((currenttime - triggertime > linepurgeinterval) && (linespurged == false)) {
```

```
digitalWrite(SolenoidApin, HIGH);
digitalWrite(SolenoidBpin, HIGH);
//extrapower = 4;
lcd.setCursor(0,1);
lcd.print(" Filling purge tube ");
countdownitem = fillinterval;
linespurged = true;
}
// if ((currenttime - triggertime > linepurgeinterval) && (linespurged == false)) { // }
if ((currenttime - triggertime > fillinterval) && (tubefilled == false)) {
digitalWrite(SolenoidApin, LOW);
digitalWrite(SolenoidBpin, LOW);
lcd.setCursor(0,1);
lcd.print(" Purging tube ");
countdownitem = flushinterval;
tubefilled = true;
//extrapower = 4;
}
// if ((currenttime - triggertime > linepurgeinterval) && (linespurged == false)) {
// }
if ((currenttime - triggertime ¿ flushinterval) && (tubepurged == false)) {
digitalWrite(SolenoidApin, LOW);
digitalWrite(SolenoidBpin, HIGH);
lcd.setCursor(0,1);
lcd.print(" Evacuating tube ");
countdownitem = flushtime;
tubepurged = true;
}
// if ((currenttime - triggertime > linepurgeinterval) && (linespurged == false)) {
// }
if ((currenttime - triggertime > flushtime) && (tubeflushed == false)){
digitalWrite(SolenoidApin, LOW);
digitalWrite(SolenoidBpin, LOW);
Running = false;
lcd.setCursor(0,1);
lcd.print(" Waiting for sample ");
tubeflushed = true;
} }
if (currenttime - previoustemptime > dataupdatespeed) {
previoustemptime = currenttime;
lcd.setCursor(0, 3);
lcd.print("Tube = ");
lcd.print(tempC,1);
lcd.print((char)223);
lcd.print("C ");
lcd.setCursor(14,3);
lcd.print(" P=");
```

```
lcd.print(temppercent,0);
lcd.print("% ");

if (Running == true) {
countdown = countdownitem - (currenttime - triggertime);
lcd.setCursor(8,2);
lcd.print(countdown/1000);
lcd.print("sec ");
// lcd.setCursor(15,3);
// lcd.print("TRUE ");
}
else {lcd.setCursor(8,2);
lcd.print(" ");
// lcd.setCursor(15,3);
// lcd.print("FALSE");
}}}
```

Abbreviations

VSLH	Very Short-Lived Halocarbons
NOAA	National Oceanic and Atmospheric Administration
TROMPEX	TRade wind Ozone Photochemistry EXperiment
ETP	East Tropical Pacific
ITCZ	Inter Tropical Convergence Zone
Chl-a	Chlorophyll-a
CFC	Chlorofluorocarbon
ODP	Ozone Depletion Potential
HCFC	Hydrochlorofluorocarbon
NASA-NEO	North American Space Agency-Near Earth Observation
UV	Ultra Violet
PSC	Polar Stratospheric Clouds
MBL	Marine Boundary Layer
IOP	Iodine Oxidation Particles
CCN	Cloud Condensation Nuclei
RHS	Reactive Halogen Species
HFC	Hydrofluorocarbons
DOAS	Differential Optical Absorbtion Spectroscopy
HNLC	High Nutrient Low Chlorophyll

DMS	Dimethyl sulphide
DMSO	Dimethyl sulphoxide
TTL	Tropical Tropopause Layer
DOM	Dissolved Organic Matter
LP-DOAS	Long Path Differential Optical Absorption
HalOcAt	Halocarbons in the Oceans and Atmosphere
TD-GC-MS	Thermal Desorption- Gas Chromatography- Mass Spectrometry
TOF	Time Of Flight
QMS	Quadrupole Mass Spectrometer
LC-MS	Liquid Chromatography- Mass Spectrometry
SIM	Single Ion Monitoring
S/N	Signal to Noise ratio
NIST	National Institute of Standards and Technology
EI	Electron Ionisation
PCI	Positive Chemical Ionisation
NCI	Negative Chemical ionisation
ECD	Electron Capture Detector
RF	Research Flight
DC	Direct Current
LN_2	Liquid Nitrogen
WAS	Whole Air Samples
I.D.	Internal Diameter

FPSC	Free Piston Stirling Cooler
PTFE	Polytrifluoroethylene
PLOT	Porous Layer Open Tubular
EPC	Electronic Pressure Control
LOD	Limit of Detection
LOQ	Limit of Quantification
THM	Trihalomethane
VOC	Volatile Organic Compound
PFA	Polyfluoroacetate
CTD	Conductivity Temperature Depth
TAO	Tropical Atmosphere Ocean project
KA	NOAA ship Ka'imimoana
LDR	Linear Dynamic Range
PA	peak Area
SD	Standard Deviation
IS	internal Standard
MRR	Molar Response Ratio
PEEK	Polyether ether ketone
NOAA-ESRL	National Oceanic and Atmospheric Administration- Earth System Research Laboratory
IHALACE	International HALocarbons in Air Comparison Experiment
NCAR	National Center for Atmospheric Research
GV	Gulf stream 5

NEODAAS	NERC Earth Observation Data Acquisition and Analysis Service
FAAM	Facility for Airborne Atmospheric Measurement
SST	Sea Surface temperature
BAE	British Aerospace Engineering
MODIS	Moderate Resolution Imaging Spectroradiometer
HYSPLIT	HYbrid Single Particle Lagrangian Integrated Trajectory model
R/V	Research Vessel
NSF	National Science Foundation
TORERO	Tropical Ocean tRoposphere Exchange of Reactive halogen species and Oxygenated VOC
STSW	Sub Tropical Surface Water
TSW	Tropical Surface Water
ESW	Equatorial Surface Water
ENSO	El Nino/Southern Oscillation
SCIAMACHY	SCanning Imaging Absorption spectroMeter for Atmospheric CHartographY
NCAR	Trace Organic Gas Analyser
PVC	Poly(vinyl chloride)
GPS	Global Positioning System
PSU	Practical Salinity Units
HNLC	High Nutrient Low Chlorophyll
OOMPH	Organics over the Ocean Modifying Particles in both Hemispheres
SEA-WiFS	Sea-viewing Wide Field-of-view Sensor

SZA	Solar Zenith Angle
NH	Northern Hemisphere
SH	Southern Hemisphere
MLD	Mixed Layer Depth
SIO	cripps Institution of Oceanography
EqPOS	Equatorial Pacific Ocean and stratospheric/tropospheric atmosphere Study

References

Abbatt, J. P. D. and Waschewsky, G. C. G.: Heterogeneous Interactions of HOBr, HNO3, O3, and NO2 with Deliquescent NaCl Aerosols at Room Temperature, The Journal of Physical Chemistry A, 102, 3719–3725, doi:10.1021/jp980932d, URL http://pubs.acs.org/doi/abs/10.1021/jp980932d, 1998.

Abrahamsson, K., Bertilsson, S., Chierici, M., Fransson, A., Froneman, P., Loren, A., and Pakhomov, E.: Variations of biochemical parameters along a transect in the Southern Ocean, with special emphasis on volatile halogenated organic compounds, Deep Sea Research Part II: Topical Studies in Oceanography, 51, 2745–2756, 2004.

Aguzzi, A. and Rossi, M. J.: The kinetics of the heterogeneous reaction of $BrONO_2$ with solid alkali halides at ambient temperature. A comparison with the interaction of $ClONO_2$ on NaCl and KBr, Physical Chemistry Chemical Physics, 1, 4337–4346, 1999.

Alicke, B., Hebestreit, K., Stutz, J., and Platt, U.: Iodine oxide in the marine boundary layer, Nature, 397, 572–573, 1999.

Allan, B. J., McFiggans, G., Plane, J. M. C., and Coe, H.: Observations of iodine monoxide in the remote marine boundary layer, Journal of Geophysical Research: Atmospheres, 105, 14 363–14 369, 2000.

Amachi, S., Kamagata, Y., Kanagawa, T., and Muramatsu, Y.: Bacteria mediate methylation of iodine in marine and terrestrial environments, Applied and Environmental microbiology, 67, 2718–2722, 2001.

Amachi, S., Mishima, Y., Shinoyama, H., Muramatsu, Y., and Fujii, T.: Active transport and accumulation of iodide by newly isolated marine bacteria, Applied and environmental microbiology, 71, 741–745, 2005a.

Amachi, S., Muramatsu, Y., Akiyama, Y., Miyazaki, K., Yoshiki, S., Hanada, S., Kamagata, Y., Ban-nai, T., Shinoyama, H., and Fujii, T.: Isolation of iodide-oxidizing bacteria from iodide-rich natural gas brines and seawaters, Microbial ecology, 49, 547–557, 2005b.

Andrews, S. J., Jones, C. E., and Carpenter, L. J.: Aircraft measurements of very short-lived halocarbons over the tropical Atlantic Ocean, Geophysical Research Letters, 40, 1005–1010, 2013.

Apel, E., Hills, A., Lueb, R., Zindel, S., Eisele, S., and Riemer, D.: A fast-GC/MS system to measure C_2 to C_4 carbonyls and methanol aboard aircraft, Journal of Geophysical Research: Atmospheres (1984–2012), 108, 2003.

Asare, N. K., Turley, C. M., Nightingale, P. D., and Nimmo, M.: Microbially-Mediated Methyl Iodide Production in Water Samples from an Estuarine System, Journal of Environment, 1, 75–83, 2012.

Ashfold, M., Harris, N., Manning, A., Robinson, A., Warwick, N., and Pyle, J.: Estimates of tropical bromoform emissions using an inversion method, Atmospheric Chemistry and Physics Discussions, 13, 20 463–20 502, 2013.

Atlas, E., Pollock, W., Greenberg, J., Heidt, L., and Thompson, A. M.: Alkyl nitrates, nonmethane hydrocarbons, and halocarbon gases over the equatorial Pacific Ocean during SAGA 3, Journal of Geophysical Research: Atmospheres, 98, 16 933–16 947, 1993.

Aucott, M., McCulloch, A., Graedel, T., Kleiman, G., Midgley, P., and Li, Y.: Anthropogenic emissions of trichloromethane(chloroform, $CHCl_3$) and chlorodifluoromethane(HCFC-22)- Reactive Chlorine Emissions Inventory, Journal of geophysical research, 104, 8405–8415, 1999.

Babin, M., Morel, A., and Gentili, B.: Remote sensing of sea surface sun-induced chlorophyll fluorescence: consequences of natural variations in the optical characteristics of phytoplankton and the quantum yield of chlorophyll-a fluorescence, International Journal of Remote Sensing, 17, 2417–2448, 1996.

Baker, A., Thompson, D., Campos, M., Parry, S., and Jickells, T.: Iodine concentration and availability in atmospheric aerosol, Atmospheric Environment, 34, 4331–4336, 2000.

Baker, A. R.: Marine Aerosol Iodine Chemistry: The Importance of Soluble Organic Iodine, Environmental Chemistry, 2, 295–298, 2005.

Baker, J., Sturges, W., Sugier, J., Sunnenberg, G., Lovett, A., Reeves, C., Nightingale, P., and Penkett, S.: Emissions of CH_3Br, organochlorines, and organoiodines from temperate macroalgae, Chemosphere-Global Change Science, 3, 93–106, 2001.

Bassford, M. R., Nickless, G., Simmonds, P. G., Lewis, A. C., Pilling, M. J., and Evans, M. J.: The concurrent observation of methyl iodide and dimethyl sulphide in marine air; implications for sources of atmospheric methyl iodide, Atmospheric environment, 33, 2373–2383, 1999.

Bell, N., Hsu, L., Jacob, D., Schultz, M., Blake, D., Butler, J., King, D., Lobert, J., and Maier-Reimer, E.: Methyl iodide: Atmospheric budget and use as a tracer of marine convection in global models, Journal of geophysical research, 107, 4340, 2002a.

Bell, N., Hsu, L., Jacob, D., Schultz, M., Blake, D., Butler, J., and Maier-Reimer, E.: Global budgets of oceanic and atmospheric methyl iodide: Development of methyl iodide as a tracer for marine convection in atmospheric models, J. Geophys. Res, 10, 2002b.

Blake, N., Blake, D., Wingenter, O., Sive, B., Kang, C., Thornton, D., Bandy, A., Atlas, E., Flocke, F., Harris, J., et al.: Aircraft measurements of the latitudinal, vertical, and seasonal variations of NMHCs, methyl nitrate, methyl halides, and DMS during the First Aerosol Characterization Experiment (ACE 1), Journal of geophysical research, 104, 21 803–21, 1999.

Blake, N. J., Blake, D. R., Chen, T.-Y., Collins Jr, J. E., Sachse, G. W., Anderson, B. E., and Rowland, F. S.: Distribution and seasonality of selected hydrocarbons and halocarbons over the western Pacific basin during PEM-West A and PEM-West B, Journal of geophysical research, 102, 28 315–28, 1997.

Boucher, O., Moulin, C., Belviso, S., Aumont, O., Bopp, L., Cosme, E., Von Kuhlmann, R., Lawrence, M., Pham, M., Reddy, M., et al.: DMS atmospheric concentrations and sulphate aerosol indirect radiative forcing: a sensitivity study to the DMS source representation and oxidation, Atmospheric Chemistry and Physics, 3, 2003.

Bridgeman, C., Pyle, J., and Shallcross, D.: A three-dimensional model calculation of

the ozone depletion potential of 1-bromopropane (1- C_3H_7Br), Journal of geophysical research, 105, 26 493–26, 2000.

Brioude, J., Portmann, R., Daniel, J., Cooper, O., Frost, G., Rosenlof, K., Granier, C., Ravishankara, A., Montzka, S., Stohl, A., et al.: Variations in ozone depletion potentials of very short-lived substances with season and emission region, Geophys. Res. Lett, 37, L19 804, 2010.

Bruland, K. W., Rue, E. L., and Smith, G. J.: Iron and macronutrients in California coastal upwelling regimes: Implications for diatom blooms, Limnology and Oceanography, 46, 1661–1674, 2001.

Burkholder, J. B., Curtius, J., Ravishankara, A. R., and Lovejoy, E. R.: Laboratory studies of the homogeneous nucleation of iodine oxides, Atmospheric Chemistry and Physics, 4, 19–34, 2004.

Buser, H. R.: Selective detection of brominated aromatic compounds using gas chromatography/negative chemical ionization mass spectrometry, Analytical Chemistry, 58, 2913–2919, 1986.

Butler, J., Bell, T., Hall, B., Quack, B., Carpenter, L., and Williams, J.: Technical Note: Ensuring consistent, global measurements of very short-lived halocarbon gases in the ocean and atmosphere, Atmos. Chem. Phys, 10, 327–330, 2010.

Butler, J. H., King, D. B., Lobert, J. M., Montzka, S. A., Yvon-Lewis, S. A., Hall, B. D., Warwick, N. J., Mondeel, D. J., Aydin, M., and Elkins, J. W.: Oceanic distributions and emissions of short-lived halocarbons, Global Biogeochemical Cycles, 21, 2007.

Butz, A., Bösch, H., Camy-Peyret, C., Chipperfield, M., Dorf, M., Kreycy, S., Kritten, L., Prados-Román, C., Schwärzle, J., and Pfeilsticker, K.: Constraints on inorganic gaseous iodine in the tropical upper troposphere and stratosphere inferred from balloon-borne solar occultation observations, Atmos. Chem. Phys, 9, 7229–7242, 2009.

Canfield, D. E., Glazer, A. N., and Falkowski, P. G.: The evolution and future of Earths nitrogen cycle, Science, 330, 192–196, 2010.

Carpenter, D., Beets, R., and Crout, R.: National Data Buoy Center transition of the Tropical Atmosphere Ocean (TAO) program, in: OCEANS 2011, pp. 1–8, 2011.

Carpenter, L., Sturges, W., Penkett, S., Liss, P., Alicke, B., Hebestreit, K., and Platt, U.: Short-lived alkyl iodides and bromides at Mace Head, Ireland: Links to biogenic sources and halogen oxide production, Journal of geophysical research, 104, 1679–1689, doi:doi:10.1029/98JD02746, 1999.

Carpenter, L., Malin, G., Liss, P., and Kupper, F.: Novel biogenic iodine-containing trihalomethanes and other short-lived halocarbons in the coastal East Atlantic, Global biogeochemical cycles, 14, 1191–1204, 2000.

Carpenter, L., Hebestreit, K., Platt, U., Liss, P., et al.: Coastal zone production of IO precursors: a 2-dimensional study, Atmos. Chem. Phys, 1, 9–18, 2001.

Carpenter, L., Liss, P., and Penkett, S.: Marine organohalogens in the atmosphere over the Atlantic and Southern Oceans, Journal of geophysical research, 108, 4256, 2003.

Carpenter, L., Wevill, D., Palmer, C., and Michels, J.: Depth profiles of volatile iodine and bromine-containing halocarbons in coastal Antarctic waters, Marine chemistry, 103, 227–236, 2007.

Carpenter, L., Jones, C., Dunk, R., Hornsby, K., and Woeltjen, J.: Air-sea fluxes of biogenic bromine from the tropical and North Atlantic Ocean, Atmos. Chem. Phys, 9, 1805–1816, 2009.

Carpenter, L., Fleming, Z., Read, K., Lee, J., Moller, S., Hopkins, J., Purvis, R., Lewis, A., Mller, K., Heinold, B., Herrmann, H., Fomba, K., Pinxteren, D., Mller, C., Tegen, I., Wiedensohler, A., Mller, T., Niedermeier, N., Achterberg, E., Patey, M., Kozlova, E., Heimann, M., Heard, D., Plane, J., Mahajan, A., Oetjen, H., Ingham, T., Stone, D., Whalley, L., Evans, M., Pilling, M., Leigh, R., Monks, P., Karunaharan, A., Vaughan, S., Arnold, S., Tschritter, J., Phler, D., Frie, U., Holla, R., Mendes, L., Lopez, H., Faria, B., Manning, A., and Wallace, D.: Seasonal characteristics of tropical marine boundary layer air measured at the Cape Verde Atmospheric Observatory, Journal of Atmospheric Chemistry, 67, 87–140, 2010.

Carpenter, L., MacDonald, S., Shaw, M., Kumar, R., Saunders, R., Parthipan, R., Wilson, J., and Plane, J.: Atmospheric iodine levels influenced by sea surface emissions of inorganic iodine, Nature Geoscience, 6, 108–111, 2013.

Carpenter, L. J. and Liss, P. S.: On temperate sources of bromoform and other reactive organic bromine gases, Journal of Geophysical Research: Atmospheres, 105, 20 539–20 547, 2000.

Carpenter, L. J., Hopkins, J. R., Jones, C. E., Lewis, A. C., Parthipan, R., Wevill, D. J., Poissant, L., Pilote, M., and Constant, P.: Abiotic Source of Reactive Organic Halogens in the Sub-Arctic Atmosphere?, Environmental Science & Technology, 39, 8812–8816, 2005.

Chameides, W. L., Stedman, D. H., Dickerson, R. R., Rusch, D. W., and Cicerone, R. J.: NOx Production in Lightning, J. Atmos. Sci., 34, 143–149, doi:10.1175/1520-0469(1977)034¡0143:NPIL¿2.0.CO;2, URL http://dx.doi.org/10.1175/1520-0469(1977)034<0143:NPIL>2.0.CO;2, 1977.

Chance, R., Baker, A. R., Kpper, F. C., Hughes, C., Kloareg, B., and Malin, G.: Release and transformations of inorganic iodine by marine macroalgae, Estuarine, Coastal and Shelf Science, 82, 406 – 414, 2009.

Chavez, F. P., Buck, K. R., Service, S. K., Newton, J., and Barber, R. T.: Phytoplankton variability in the central and eastern tropical Pacific, Deep Sea Research Part II: Topical Studies in Oceanography, 43, 835 – 870, 1996.

Chuck, A., Turner, S., and Liss, P.: Oceanic distributions and air-sea fluxes of biogenic halocarbons in the open ocean, Journal of geophysical research, 110, C10 022, 2005.

Class, T. and Ballschmiter, K.: Chemistry of organic traces in air IX: Evidence of natural marine sources for chloroform in regions of high primary production, Fresenius' Journal of Analytical Chemistry, 327, 40–41, 1987.

Class, T. and Ballschmiter, K.: Chemistry of organic traces in air, Journal of atmospheric chemistry, 6, 35–46, 1988.

Dandonneau, Y. and Neveux, J.: Diel variations of *in vivo* fluorescence in the eastern equatorial Pacific: an unvarying pattern, Deep Sea Research Part II: Topical Studies in Oceanography, 44, 1869–1880, 1997.

Davis, D., Chen, G., Kasibhatla, P., Jefferson, A., Tanner, D., Eisele, F., Lenschow, D., Neff, W., and Berresheim, H.: DMS oxidation in the Antarctic marine boundary layer: Comparison of model simulations and held observations of DMS, DMSO, $DMSO_2$,

$H_2SO_{4(}$g), $MSA_{(}$g), and $MSA_{(}$p), Journal of Geophysical Research: Atmospheres (1984–2012), 103, 1657–1678, 1998.

de Blas, M., Navazo, M., Alonso, L., Durana, N., and Iza, J.: Trichloroethylene, tetrachloroethylene and carbon tetrachloride in an urban atmosphere: mixing ratios and temporal patterns, International Journal of Environmental Analytical Chemistry, 93, 228–244, doi:10.1080/03067319.2011.629346, URL http://www.tandfonline.com/doi/abs/10.1080/03067319.2011.629346, 2013.

Deiber, G., George, C., Le Calvé, S., Schweitzer, F., and Mirabel, P.: Uptake study of $ClONO_2$ and $BrONO_2$ by Halide containing droplets, Atmospheric Chemistry and Physics, 4, 1291–1299, doi:10.5194/acp-4-1291-2004, URL http://www.atmos-chem-phys.net/4/1291/2004/, 2004.

Demmig-Adams, B., Adams III, W. W., Barker, D. H., Logan, B. A., Bowling, D. R., and Verhoeven, A. S.: Using chlorophyll fluorescence to assess the fraction of absorbed light allocated to thermal dissipation of excess excitation, Physiologia Plantarum, 98, 253–264, 1996.

Dimmer, C. H., Simmonds, P. G., Nickless, G., and Bassford, M. R.: Biogenic fluxes of halomethanes from Irish peatland ecosystems, Atmospheric Environment, 35, 321–330, 2001.

Dix, B., Baidar, S., Bresch, J. F., Hall, S. R., Schmidt, K. S., Wang, S., and Volkamer, R.: Detection of iodine monoxide in the tropical free troposphere, Proceedings of the National Academy of Sciences, 110, 2035–2040, 2013.

Doney, S. C., Fabry, V. J., Feely, R. A., and Kleypas, J. A.: Ocean acidification: the other CO2 problem, Marine Science, 1, 2009.

Dorf, M., Butz, A., Camy-Peyret, C., Chipperfield, M., Kritten, L., and Pfeilsticker, K.: Bromine in the tropical troposphere and stratosphere as derived from balloon-borne BrO observations, Atmos. Chem. Phys, 8, 7265–7271, 2008.

Doskey, P. V.: The effect of treating air samples with magnesium perchlorate for water removal during analysis for non-methane hydrocarbons, Journal of High Resolution Chromatography, 14, 724–728, 1991.

Duce, R., Liss, P., Merrill, J., Atlas, E., Buat-Menard, P., Hicks, B., Miller, J., Prospero, J., Arimoto, R., Church, T., et al.: The atmospheric input of trace species to the world ocean, Global biogeochemical cycles, 5, 193–259, 1991.

Dvortsov, V., Geller, M., Solomon, S., Schauffler, S., Atlas, E., and Blake, D.: Rethinking reactive halogen budgets in the midlatitude lower stratosphere, Geophysical research letters, 26, 1699–1702, 1999.

E., H. R. and Barna, L.: The Atmospheric Chemistry of Iodine Monoxide, chap. 5, pp. 31–40, doi:10.1021/bk-1995-0611.ch004, URL http://pubs.acs.org/doi/abs/10.1021/bk-1995-0611.ch004, 1997.

Eckenrode, B.: Environmental and forensic applications of field-portable GC-MS: an overview, Journal of the American Society for Mass Spectrometry, 12, 683 – 693, 2001.

Ekdahl, A., Pedersén, M., and Abrahamsson, K.: A study of the diurnal variation of biogenic volatile halocarbons, Marine Chemistry, 63, 1–8, 1998.

Falkowski, P. and Kiefer, D. A.: Chlorophyll-a fluorescence in phytoplankton: relationship to photosynthesis and biomass, Journal of Plankton Research, 7, 715–731, 1985.

Fan, S.-M. and Jacob, D. J.: Surface ozone depletion in Arctic spring sustained by bromine reactions on aerosols, 1992.

Farman, J. C., Gardiner, B. G., and Shanklin, J. D.: Large losses of total ozone in Antarctica reveal seasonal ClOx/NOx interaction, Nature, 315, 207–210, URL http://dx.doi.org/10.1038/315207a0, 1985.

Fiedler, P. C. and Talley, L. D.: Hydrography of the eastern tropical Pacific: A review, Progress in Oceanography, 69, 143 – 180, a Review of Eastern Tropical Pacific Oceanography, 2006.

Fiedler, P. C., Philbrick, V., and Chavez, F. P.: Oceanic upwelling and productivity in the eastern tropical Pacific., Limnology and Oceanography, 36, 1834–1850, 1991.

Finlayson-Pitts, B. J. and Pitts Jr, J. N.: Atmospheric chemistry. Fundamentals and experimental techniques, 1986.

Frieß, U., Wagner, T., Pundt, I., Pfeilsticker, K., and Platt, U.: Spectroscopic measurements of tropospheric iodine oxide at Neumayer Station, Antarctica, Geophysical Research Letters, 28, 1941–1944, 2001.

Fuhlbrügge, S., Krüger, K., Quack, B., Atlas, E., Hepach, H., and Ziska, F.: Impact of the marine atmospheric boundary layer conditions on VSLS abundances in the eastern tropical and subtropical North Atlantic Ocean, Atmospheric Chemistry and Physics, 13, 6345–6357, 2013.

Fuller, E., Schettler, P., and Giddings, J.: New method for prediction of binary gas-phase diffusion coefficients, Industrial & Engineering Chemistry, 58, 18–27, 1966.

Geen, C. E.: Selected marine sources and sinks of bromoform and other low molecular weight organobromines, Ph.D. thesis, Dalhousie, Univ. Halifax, Nova Scotia, Canada, 1992.

Gettelman, A., Lauritzen, P., Park, M., and Kay, J.: Processes regulating short-lived species in the tropical tropopause layer, Journal of Geophysical Research: Atmospheres (1984–2012), 114, 2009.

Giese, B., Laturnus, F., Adams, F., and Wiencke, C.: Release of volatile iodinated C_1-C_4 hydrocarbons by marine macroalgae from various climate zones, Environmental science & technology, 33, 2432–2439, 1999.

Goodwin, K., North, W., and Lidstrom, M.: Production of bromoform and dibromomethane by giant kelp: factors affecting release and comparison to anthropogenic bromine sources, Limnology and oceanography, pp. 1725–1734, 1997.

Gross, J. H.: Mass Spectrometry, in: Mass Spectrometry, pp. 507–559, Springer, 2011.

Großmann, K., Frieß, U., Peters, E., Wittrock, F., Lampel, J., Yilmaz, S., Tschritter, J., Sommariva, R., von Glasow, R., Quack, B., et al.: Iodine monoxide in the Western Pacific marine boundary layer, Atmos. Chem. Phys, 13, 3363–3378, 2013.

Hall, B., Engel, A., Mühle, J., Elkins, J., Artuso, F., Atlas, E., Aydin, M., Blake, D., Brunke, E., Chiavarini, S., et al.: Results from the International Halocarbons in Air Comparison Experiment (IHALACE), ACPD, 6, 8021–8069, 2013.

Hanson, D. R. and Ravishankara, A.: The reaction probabilities of $ClONO_2$ and N_2O_5 on polar stratospheric cloud materials, Journal of Geophysical Research: Atmospheres (1984–2012), 96, 5081–5090, 1991.

Happell, J. and Wallace, D.: Methyl iodide in the Greenland/Norwegian Seas and the tropical Atlantic Ocean: Evidence for photochemical production, Geophysical research letters, 23, 2105–2108, 1996.

Haselmann, K. F., Ketola, R. A., Laturnus, F., Lauritsen, F. R., and Grøn, C.: Occurrence and formation of chloroform at Danish forest sites, Atmospheric Environment, 34, 187–193, 2000.

Hayduk, W. and Minhas, B.: Correlations for prediction of molecular diffusivities in liquids, The Canadian Journal of Chemical Engineering, 60, 295–299, 1982.

Heard, D., Read, K., Methven, J., Al-Haider, S., Bloss, W., Johnson, G., Pilling, M., Seakins, P., Smith, S., Sommariva, R., et al.: The North Atlantic marine boundary layer experiment (NAMBLEX). Overview of the campaign held at Mace Head, Ireland, in summer 2002, Atmospheric Chemistry and Physics, 6, 2241–2272, 2006.

Hense, I. and Quack, B.: Modelling the vertical distribution of bromoform in the upper water column of the tropical Atlantic Ocean, Biogeosciences (BG), 6, 535–544, 2009.

Heumann, K. G. et al.: Determinations of methyl iodide in the Antarctic atmosphere and the South Polar Sea, Atmospheric Environment. Part A. General Topics, 26, 2905–2912, 1992.

Hill, V. L. and Manley, S. L.: Release of reactive bromine and iodine from diatoms and its possible role in halogen transfer in polar and tropical oceans, Limnol. Oceanogr, 54, 812–822, 2009.

Holzer, M. and Polvani, L. M.: Lifetime dependent flux into the lowermost stratosphere for idealized trace gases of surface origin, Journal of Geophysical Research: Atmospheres, 2013.

Hönninger, G., Friedeburg, C. v., and Platt, U.: Multi axis differential optical absorption spectroscopy (MAX-DOAS), Atmospheric Chemistry and Physics, 4, 231–254, 2004.

Horowitz, L. W., Walters, S., Mauzerall, D. L., Emmons, L. K., Rasch, P. J., Granier, C., Tie, X., Lamarque, J.-F., Schultz, M. G., Tyndall, G. S., et al.: A global simulation of tropospheric ozone and related tracers: Description and evaluation of MOZART, version 2, Journal of Geophysical Research: Atmospheres (1984–2012), 108, 2003.

Hossaini, R., Chipperfield, M., Monge-Sanz, B., Richards, N., Atlas, E., and Blake, D.: Bromoform and dibromomethane in the tropics: a 3-D model study of chemistry and transport, Atmos. Chem. Phys, 10, 719–735, 2010.

Hossaini, R., Chipperfield, M., Dhomse, S., Ordóñez, C., Saiz-Lopez, A., Abraham, N., Archibald, A., Braesicke, P., Telford, P., Warwick, N., et al.: Modelling future changes to the stratospheric source gas injection of biogenic bromocarbons, Geophysical Research Letters, 39, L20 813, 2012a.

Hossaini, R., Chipperfield, M., Feng, W., Breider, T., Atlas, E., Montzka, S., Miller, B., Moore, F., and Elkins, J.: The contribution of natural and anthropogenic very short-lived species to stratospheric bromine, Atmospheric Chemistry and Physics, 12, 371–380, 2012b.

Hossaini, R., Mantle, H., Chipperfield, M., Montzka, S., Hamer, P., Ziska, F., Quack, B., Krüger, K., Tegtmeier, S., Atlas, E., et al.: Evaluating global emission inventories of biogenic bromocarbons, Atmospheric Chemistry and Physics Discussions, 13, 12 485–12 539, 2013.

Huff, A. K. and Abbatt, J. P. D.: Kinetics and Product Yields in the Heterogeneous Reactions of HOBr with Ice Surfaces Containing NaBr and NaCl, The Journal of Physical Chemistry A, 106, 5279–5287, doi:10.1021/jp014296m, URL `http://pubs.acs.org/doi/abs/10.1021/jp014296m`, 2002.

Hughes, C., Malin, G., Turley, C., Keely, B., Nightingale, P., and Liss, P.: The production of volatile iodocarbons by biogenic marine aggregates, Limnology and Oceanography, pp. 867–872, 2008.

Hughes, C., Johnson, M., Utting, R., Turner, S., Malin, G., Clarke, A., and Liss, P.: Microbial control of bromocarbon concentrations in coastal waters of the western Antarctic Peninsula, Marine Chemistry, 2013.

Itoh, N., Tsujita, M., Ando, T., Hisatomi, G., and Higashi, T.: Formation and emission of monohalomethanes from marine algae, Phytochemistry, 45, 67 – 73, 1997.

Jähne, B., Huber, W., Dutzi, A., Wais, T., and Ilmberger, J.: Wind/wave-tunnel experiment on the Schmidt number and wave field dependence of air/water gas exchange, Gas transfer at water surfaces, University of Heidelberg, Reidel publishing, pp. 303–309, 1984.

Jeffery, C., Woolf, D., Robinson, I., and Donlon, C.: One-dimensional modelling of convective CO_2 exchange in the Tropical Atlantic, Ocean Modelling, 19, 161–182, 2007.

Jickells, T. D., An, Z. S., Andersen, K. K., Baker, A. R., Bergametti, G., Brooks, N., Cao, J. J., Boyd, P. W., Duce, R. A., Hunter, K. A., Kawahata, H., Kubilay, N., laRoche, J., Liss, P. S., Mahowald, N., Prospero, J. M., Ridgwell, A. J., Tegen, I., and Torres, R.: Global Iron Connections Between Desert Dust, Ocean Biogeochemistry, and Climate, Science, 308, 67–71, doi:10.1126/science.1105959, URL `http://www.sciencemag.org/content/308/5718/67.abstract`, 2005.

Jimenez, J. L., Bahreini, R., Cocker, D. R., Zhuang, H., Varutbangkul, V., Flagan, R. C., Seinfeld, J. H., O'Dowd, C. D., and Hoffmann, T.: New particle formation from photooxidation of diiodomethane (CH2I2), Journal of Geophysical Research: Atmospheres, 108, n/a–n/a, doi:10.1029/2002JD002452, URL `http://dx.doi.org/10.1029/2002JD002452`, 2003.

Johnson, M. T.: A numerical scheme to calculate temperature and salinity dependent air-water transfer velocities for any gas, Ocean Science, 6, 913–932, 2010.

Jones, C. and Carpenter, L.: Solar photolysis of CH_2I_2, CH_2ICl, and CH_2IBr in water, saltwater, and seawater, Environmental science & technology, 39, 6130–6137, 2005.

Jones, C., Hornsby, K., Sommariva, R., Dunk, R., Von Glasow, R., McFiggans, G., and Carpenter, L.: Quantifying the contribution of marine organic gases to atmospheric iodine, Geophysical Research Letters, 37, L18 804, 2010.

Jones, C., Andrews, S., Carpenter, L., Hogan, C., Hopkins, F., Laube, J., Robinson, A., Spain, T., Archer, S., Harris, N., et al.: Results from the first national UK intercomparison laboratory calibration for very short-lived halocarbons, Atmospheric Measurement Techniques Discussions, 4, 765–787, 2011.

Jones, C. E., Hornsby, K. E., Dunk, R. M., Leigh, R. J., and Carpenter, L. J.: Coastal measurements of short-lived reactive iodocarbons and bromocarbons at Roscoff, Brittany during the RHaMBLe campaign, Atmospheric Chemistry and Physics, 9, 8757–8769, 2009.

Keene, W., Khalil, M., Erickson III, D., McCulloch, A., Graedel, T., Lobert, J., Aucott, M., Gong, S., Harper, D., Kleiman, G., et al.: Composite global emissions of reactive chlorine from anthropogenic and natural sources: Reactive Chlorine Emissions Inventory, Journal of Geophysical Research, 104, 8429–8440, 1999.

Keene, W. C., Sander, R., Pszenny, A. A., Vogt, R., Crutzen, P. J., and Galloway, J. N.: Aerosol pH in the marine boundary layer:: A review and model evaluation, Journal of Aerosol Science, 29, 339–356, 1998.

Kerkweg, A., Jöckel, P., Warwick, N., Gebhardt, S., Brenninkmeijer, C., Lelieveld, J., et al.: Consistent simulation of bromine chemistry from the marine boundary layer to the stratosphere? Part 2: Bromocarbons, Atmospheric Chemistry and Physics Discussions, 8, 9477–9530, 2008.

Khalil, M., Rasmussen, R., French, J., and Holt, J.: The influence of termites on atmospheric trace gases: CH4, CO2, CHCl3, N2O, CO, H2, and light hydrocarbons, Journal of Geophysical Research: Atmospheres (1984–2012), 95, 3619–3634, 1990.

Khalil, M., Moore, R., Harper, D., Lobert, J., Erickson, D., Koropalov, V., Sturges, W., and Keene, W.: Natural emissions of chlorine-containing gases: Reactive Chlorine Emissions Inventory, Journal of geophysical research, 104, 8333–8346, 1999.

Kiefer, D., Chamberlin, W., and Booth, C.: Natural fluorescence of chlorophyll a: Relationship to photosynthesis and chlorophyll concentration in the western South Pacific gyre, Limnology and Oceanography, pp. 868–881, 1989.

Klick, S.: The release of volatile halocarbons to seawater by untreated and heavy metal exposed samples of the brown seaweed *Fucus Vesiculosus*, Marine chemistry, 42, 211–221, 1993.

Klick, S. and Abrahamsson, K.: Biogenic volatile iodated hydrocarbons in the ocean, Journal of Geophysical Research, 97, 12 683–12, 1992.

Ko, M., Poulet, G., Blake, D., Boucher, O., Burkholder, J., Chin, M., Cox, R., George, C., Graf, H., Holton, J., et al.: Very short-lived halogen and sulfur substances, Scientific Assessment of Ozone Depletion: 2002, Global Ozone Res. Monit. Proj. Rep, 47, 2–1, 2003.

Kritz, M., Rosner, S., Kelly, K., Loewenstein, M., and Chan, K.: Radon measurements in the lower tropical stratosphere: Evidence for rapid vertical transport and dehydration of tropospheric air, Journal of geophysical research, 98, 8725–8736, 1993.

Kroger, P., Demou, P., and Riley, S.: Polyhalide photofragment spectra. I. Two-photon two-step photodissociation of methylene iodide, Journal of Chemical Physics, 65, 1823–1834, 1976.

Krummel, P., Fraser, P., Steele, P., Porter, L., Derek, N., Rickard, C., Dunse, B., Langenfelds, R., Miller, B., Baly, S., et al.: The AGAGE in situ program for non-CO_2 greenhouse gases at Cape Grim, 2005–2006; methane, nitrous oxide carbon monoxide, hydrogen, CFCs, HCFCs, HFCs, PFCs, halons, chlorocarbons, hydrocarbons and sulphur hexafluoride, Baseline Atmospheric Program Australia 2005–2006, pp. 65–77, 2007.

Krysell, M., Fogelqvist, E., and Tanhua, T.: Apparent removal of the transient tracer carbon tetrachloride from anoxic seawater, Geophysical research letters, 21, 2511–2514, 1994.

Küpper, F. C., Carpenter, L. J., McFiggans, G. B., Palmer, C. J., Waite, T. J., Boneberg, E.-M., Woitsch, S., Weiller, M., Abela, R., Grolimund, D., et al.: Iodide accumulation provides kelp with an inorganic antioxidant impacting atmospheric chemistry, Proceedings of the National Academy of Sciences, 105, 6954–6958, 2008.

Küpper, F. C., Carpenter, L. J., Leblanc, C., Toyama, C., Uchida, Y., Maskrey, B. H., Robinson, J., Verhaeghe, E. F., Malin, G., Luther, G. W., et al.: In vivo speciation studies and antioxidant properties of bromine in Laminaria digitata reinforce the significance of iodine accumulation for kelps, Journal of experimental botany, 2013.

Kurihara, M., Kimura, M., Iwamoto, Y., Narita, Y., Ooki, A., Eum, Y., Tsuda, A., Suzuki, K., Tani, Y., Yokouchi, Y., et al.: Distributions of short-lived iodocarbons and biogenic trace gases in the open ocean and atmosphere in the western North Pacific, Marine Chemistry, 118, 156–170, 2010.

Kurihara, M., Iseda, M., Ioriya, T., Horimoto, N., Kanda, J., Ishimaru, T., Yamaguchi, Y., and Hashimoto, S.: Brominated methane compounds and isoprene in surface seawater of Sagami Bay: Concentrations, fluxes, and relationships with phytoplankton assemblages, Marine Chemistry, 134-135, 71 – 79, 2012.

Laliberté, M.: Model for calculating the viscosity of aqueous solutions, Journal of Chemical & Engineering Data, 52, 321–335, 2007.

Laturnus, F.: Volatile halocarbons released from Arctic macroalgae, Marine Chemistry, 55, 359–366, 1996.

Laturnus, F., Adams, F., and Wiencke, C.: Methyl halides from Antarctic macroalgae, Geophysical research letters, 25, 773–776, 1998.

Laturnus, F., Haselmann, K., Borch, T., and Grøn, C.: Terrestrial natural sources of trichloromethane (chloroform, CHCl 3)–An overview, Biogeochemistry, 60, 121–139, 2002.

Law, K. S. and Sturges, W. T.: Halogenated very short-lived substances, Chapter 2 in Scientific Assessment of Ozone Depletion: 2006, Global Ozone and Research and Monitoring Project-Report, World Meteorological Organization, Geneva, Switzerland, No. 50, 2007.

Le Bouteiller, A., Blanchot, J., and Rodier, M.: Size distribution patterns of phytoplankton in the western Pacific: towards a generalization for the tropical open ocean, Deep Sea Research Part A. Oceanographic Research Papers, 39, 805–823, 1992.

Le Clainche, Y., Vzina, A., Levasseur, M., Cropp, R. A., Gunson, J. R., Vallina, S. M., Vogt, M., Lancelot, C., Allen, J. I., Archer, S. D., Bopp, L., Deal, C., Elliott, S., Jin, M., Malin, G., Schoemann, V., Sim, R., Six, K. D., and Stefels, J.: A first appraisal of prognostic ocean DMS models and prospects for their use in climate models, Global Biogeochemical Cycles, 24, n/a–n/a, doi:10.1029/2009GB003721, URL `http://dx.doi.org/10.1029/2009GB003721`, 2010.

Leedham, E. C., Hughes, C., Keng, F. S. L., Phang, S.-M., Malin, G., and Sturges, W. T.: Emission of atmospherically significant halocarbons by naturally occurring and farmed tropical macroalgae, Biogeosciences, 10, 3615–3633, 2013.

Leifer, I., Patro, R. K., and Bowyer, P.: A study on the temperature variation of rise velocity for large clean bubbles, Journal of Atmospheric and Oceanic Technology, 17, 1392–1402, 2000.

Leigh, R., Ball, S., Whitehead, J., Leblanc, C., Shillings, A., Mahajan, A., Oetjen, H., Lee, J., Jones, C., Dorsey, J., et al.: Measurements and modelling of molecular iodine emissions, transport and photodestruction in the coastal region around Roscoff, Atmospheric Chemistry and Physics, 10, 11 823–11 838, 2010.

Leshin, L. A., Mahaffy, P. R., Webster, C. R., Cabane, M., Coll, P., Conrad, P. G., Archer, P. D., Atreya, S. K., Brunner, A. E., Buch, A., Eigenbrode, J. L., Flesch, G. J., Franz, H. B., Freissinet, C., Glavin, D. P., McAdam, A. C., Miller, K. E., Ming, D. W., Morris, R. V., Navarro-Gonzlez, R., Niles, P. B., Owen, T., Pepin, R. O., Squyres, S., Steele, A., Stern, J. C., Summons, R. E., Sumner, D. Y., Sutter, B., Szopa, C., Teinturier, S., Trainer, M. G., Wray, J. J., Grotzinger, J. P., and Team, M. S.: Volatile, Isotope, and Organic Analysis of Martian Fines with the Mars Curiosity Rover, Science, 341, doi:10.1126/science.1238937, URL http://www.sciencemag.org/content/341/6153/1238937.abstract, 2013.

Li, H.-J., Yokouchi, Y., and Akimoto, H.: Measurement of methyl halides in the marine atmosphere, Atmospheric Environment, 33, 1881–1887, 1999.

Li, H.-J., Yokouchi, Y., Akimoto, H., and Narita, Y.: Distribution of methyl chloride, methyl bromide, and methyl iodide in the marine boundary air over the Western Pacific and Southeastern Indian Ocean, Geochemical Journal, 35, 137–144, 2001.

Liang, Q., Stolarski, R., Kawa, S., Nielsen, J., Douglass, A., Rodriguez, J., Blake, D., Atlas, E., and Ott, L.: Finding the missing stratospheric Bry: a global modeling study of CHBr3 and CH2Br2, Atmos. Chem. Phys, 10, 2269–2286, 2010.

Lin, C. Y. and Manley, S. L.: Bromoform production from seawater treated with bromoperoxidase, Limnology and Oceanography, 57, 1857, 2012.

Lin, M., Horowitz, L. W., Oltmans, S. J., Fiore, A. M., and Fan, S.: Tropospheric ozone trends at Mauna Loa Observatory tied to decadal climate variability, Nature Geosci, 7, 136–143, URL http://dx.doi.org/10.1038/ngeo2066, 2014.

Liss, P. and Slater, P.: Flux of gases across the air-sea interface, Nature, doi:10.1021/es00110a006, 181–184, 1974.

Liu, Y., Yvon-Lewis, S. A., Thornton, D. C., Butler, J. H., Bianchi, T. S., Campbell, L., Hu, L., and Smith, R. W.: Spatial and temporal distributions of bromoform and dibromomethane in the Atlantic Ocean and their relationship with photosynthetic biomass, Journal of Geophysical Research: Oceans, pp. n/a–n/a, 2013a.

Liu, Y., Yvon-Lewis, S. A., Thornton, D. C., Campbell, L., and Bianchi, T. S.: Spatial distribution of Brominated very short-lived substances in the Eastern Pacific, Journal of Geophysical Research: Oceans, pp. n/a–n/a, 2013b.

Lobert, J., J. B. S. Y. S. M. R. M. A. C. and Elkins, J.: Blast 94: Bromine Latitudinal Air/Sea Transect, 1994, Report on oceanic measurements of methyl bromide and other compounds, Tech. Memo. ERL CMDL-10, Tech. rep., Res. Lab., Natl. Oceanic and Atmos. Admin., Boulder, Colo., 1996.

Lovelock, J. E. and Lipsky, S. R.: Electron Affinity SpectroscopyA New Method for the Identification of Functional Groups in Chemical Compounds Separated by Gas Chromatography1, Journal of the American Chemical Society, 82, 431–433, doi: 10.1021/ja01487a045, URL `http://pubs.acs.org/doi/abs/10.1021/ja01487a045`, 1960.

Luo, L., Yates, S., and Ashworth, D.: Predicting Methyl Iodide Emission, Soil Concentration, and Pest Control in a Two–Dimensional Chamber System, Journal of Environmental Quality, 40, 109–117, 2011.

Ma, Y., Zeng, Y., Jiao, N., Shi, Y., and Hong, N.: Vertical distribution and phylogenetic composition of bacteria in the Eastern Tropical North Pacific Ocean, Microbiological Research, 164, 624–633, 2009.

Mackay, D. and Yeun, A.: Mass transfer coefficient correlations for volatilization of organic solutes from water, Environmental Science & Technology, 17, 211–217, 1983.

Mahajan, A., Oetjen, H., Saiz-Lopez, A., Lee, J., McFiggans, G., Plane, J., et al.: Reactive iodine species in a semi-polluted environment, Geophys. Res. Lett, 36, L16 803, 2009.

Mahajan, A., Plane, J., Oetjen, H., Mendes, L., Saunders, R., Saiz-Lopez, A., Jones, C., Carpenter, L., and McFiggans, G.: Measurement and modelling of tropospheric reactive

halogen species over the tropical Atlantic Ocean, Atmos. Chem. Phys, 10, 4611–4624, 2010.

Mahajan, A., Martın, J. G., Hay, T., Royer, S., Yvon-Lewis, S., Liu, Y., Hu, L., Prados-Roman, C., Ordóñez, C., Plane, J., et al.: Latitudinal distribution of reactive iodine in the Eastern Pacific and its link to open ocean sources, Atmos. Chem. Phys, 12, 11 609–11 617, 2012.

Manley, S. and de la Cuesta, J.: Methyl iodide production from marine phytoplankton cultures, Limnology and oceanography, pp. 142–147, 1997.

Manley, S. L. and Barbero, P. E.: Physiological constraints on bromoform $CHBr_3$ production by Ulva lactuca (Chlorophyta), Limnology and oceanography, 46, 1392–1399, 2001.

Manley, S. L. and Dastoor, M. N.: Methyl Halide (CH_3X) Production from the Giant Kelp, Macrocystis, and Estimates of Global CH_3X Production by Kelp, Limnology and Oceanography, 32, pp. 709–715, 1987.

Martino, M., Liss, P., and Plane, J.: The photolysis of dihalomethanes in surface seawater, Environmental science & technology, 39, 7097–7101, 2005.

Martino, M., Mills, G., Woeltjen, J., and Liss, P.: A new source of volatile organoiodine compounds in surface seawater, Geophys. Res. Lett, 36, L01 609, 2009.

Maxwell, K. and Johnson, G. N.: Chlorophyll fluorescencea practical guide, Journal of experimental botany, 51, 659–668, 2000.

McClenny, W. A., Pleil, J. D., Holdren, M. W., and Smith, R. N.: Automated cryogenic preconcentration and gas chromatographic determination of volatile organic compounds in air, Analytical Chemistry, 56, 2947–2951, 1984.

McConnell, J., Henderson, G., Barrie, L., Bottenheim, J., Niki, H., Langford, C., and Templeton, E.: Photochemical bromine production implicated in Arctic boundary-layer ozone depletion, 1992.

McFiggans, G., Coe, H., Burgess, R., Allan, J., Cubison, M., Alfarra, M. R., Saunders, R., Saiz-Lopez, A., Plane, J., Wevill, D., et al.: Direct evidence for coastal iodine particles from Laminaria macroalgae–linkage to emissions of molecular iodine, Atmos. Chem. Phys, 4, 701–713, 2004.

McFiggans, G., Bale, C. S. E., Ball, S. M., Beames, J. M., Bloss, W. J., Carpenter, L. J., Dorsey, J., Dunk, R., Flynn, M. J., Furneaux, K. L., Gallagher, M. W., Heard, D. E., Hollingsworth, A. M., Hornsby, K., Ingham, T., Jones, C. E., Jones, R. L., Kramer, L. J., Langridge, J. M., Leblanc, C., LeCrane, J.-P., Lee, J. D., Leigh, R. J., Longley, I., Mahajan, A. S., Monks, P. S., Oetjen, H., Orr-Ewing, A. J., Plane, J. M. C., Potin, P., Shillings, A. J. L., Thomas, F., von Glasow, R., Wada, R., Whalley, L. K., and Whitehead, J. D.: Iodine-mediated coastal particle formation: an overview of the Reactive Halogens in the Marine Boundary Layer (RHaMBLe) Roscoff coastal study, Atmospheric Chemistry and Physics, 10, 2975–2999, 2010.

Miller, B. R., Weiss, R. F., Salameh, P. K., Tanhua, T., Greally, B. R., Muhle, J., and Simmonds, P. G.: Medusa: A Sample Preconcentration and GC/MS Detector System for in Situ Measurements of Atmospheric Trace Halocarbons, Hydrocarbons, and Sulfur Compounds, Analytical Chemistry, 80, 1536–1545, pMID: 18232668, 2008.

Millero, F. and Poisson, A.: International one-atmosphere equation of state of seawater, Deep Sea Research Part A. Oceanographic Research Papers, 28, 625–629, 1981.

Mills, G., Hayes, F., Simpson, D., Emberson, L., Norris, D., Harmens, H., and Baoeker, P.: Evidence of widespread effects of ozone on crops and (semi-)natural vegetation in Europe (1990-2006) in relation to AOT40- and flux-based risk maps, Global Change Biology, 17, 592–613, doi:10.1111/j.1365-2486.2010.02217.x, URL http://dx.doi.org/10.1111/j.1365-2486.2010.02217.x, 2011.

Minschwaner, K., Hoffmann, L., Brown, A., Riese, M., Müller, R., and Bernath, P.: Stratospheric loss and atmospheric lifetimes of CFC-11 and CFC-12 derived from satellite observations, Atmospheric Chemistry and Physics Discussions, 12, 28 733–28 764, 2012.

Molina, M., Zhang, R., Wooldridge, P., McMahon, J., Kim, J., Chang, H., and Beyer, K.: Physical chemistry of the $H_2SO_4/HNO_3/H_2O$ system: Implications for polar stratospheric clouds, Science, 261, 1418–1423, 1993.

Molina, M. J. and Rowland, F. S.: Stratospheric sink for chlorofluoromethanes: chlorine atomc-atalysed destruction of ozone, Nature, 249, 810–812, URL http://dx.doi.org/10.1038/249810a0, 1974.

Montzka, S., Reimann, S., O'Doherty, S., Engel, A., Krüger, K., and Sturges, W.: Ozone-depleting substances (ODSs) and related chemicals, 2011.

Montzka, S. A., Myers, R. C., Butler, J. H., Elkins, J. W., and Cummings, S. O.: Global tropospheric distribution and calibration scale of HCFC-22, Geophysical Research Letters, 20, 703–706, 1993.

Montzka, S. A., Myers, R. C., Butler, J. H., Elkins, J. W., Lock, L. T., Clarke, A. D., and Goldstein, A. H.: Observations of HFC-134a in the remote troposphere, Geophysical Research Letters, 23, 169–172, 1996.

Montzka, S. A., Hall, B. D., and Elkins, J. W.: Accelerated increases observed for hydrochlorofluorocarbons since 2004 in the global atmosphere, Geophysical Research Letters, 36, n/a–n/a, doi:10.1029/2008GL036475, URL `http://dx.doi.org/10.1029/2008GL036475`, 2009.

Moore, R. and Tokarczyk, R.: Volatile biogenic halocarbons in the northwest Atlantic, Global biogeochemical cycles, 7, 195–210, 1993.

Moore, R. and Zafiriou, O.: Photochemical production of methyl iodide in seawater, Journal of geophysical research, 99, 16 415–16, 1994.

Moore, R. M. and Groszko, W.: Methyl iodide distribution in the ocean and fluxes to the atmosphere, Journal of Geophysical Research: Oceans, 104, 11 163–11 171, 1999.

Moore, R. M. and Tokarczyk, R.: Chloro-iodomethane in N. Atlantic waters: A potentially significant source of atmospheric iodine, Geophysical research letters, 19, 1779–1782, 1992.

Moore, R. M., Webb, M., Tokarczyk, R., and Wever, R.: Bromoperoxidase and iodoperoxidase enzymes and production of halogenated methanes in marine diatom cultures, Journal of Geophysical Research: Oceans, 101, 20 899–20 908, 1996.

Ni, N. and Yalkowsky, S. H.: Prediction of Setschenow constants, International journal of pharmaceutics, 254, 167–172, 2003.

Nightingale, P., Malin, G., and Liss, P.: Production of chloroform and other low-molecular-weight halocarbons by some species of macroalgae, Limnology and Oceanography, 40, 680–680, 1995.

Nightingale, P., Malin, G., Law, C., Watson, A., Liss, P., Liddicoat, M., Boutin, J., and Upstill-Goddard, R.: In situ evaluation of air-sea gas exchange parameterizations using novel conservative and volatile tracers, Global Biogeochem. Cycles, 14, 373–387, 2000.

O'Dowd, C. D., Jimenez, J. L., Bahreini, R., Flagan, R. C., Seinfeld, J. H., Hämeri, K., Pirjola, L., Kulmala, M., Jennings, S. G., and Hoffmann, T.: Marine aerosol formation from biogenic iodine emissions, Nature, 417, 632–636, 2002.

O'Dowd, C. D., Langmann, B., Varghese, S., Scannell, C., Ceburnis, D., and Facchini, M. C.: A combined organic-inorganic sea-spray source function, Geophysical Research Letters, 35, 2008.

Oehme, M.: Quantification of fg-pg amounts by electron capture negative ion mass spectrometry Parameter optimisation and practical advices, Fresenius' Journal of Analytical Chemistry, 350, 544–554, 1994.

Oltmans, S., Lefohn, A., Scheel, H., Harris, J., Levy, H., Galbally, I., Brunke, E.-G., Meyer, C., Lathrop, J., Johnson, B., et al.: Trends of ozone in the troposphere, Geophysical Research Letters, 25, 139–142, 1998.

Ordóñez, C., Lamarque, J., Tilmes, S., Kinnison, D., Atlas, E., Blake, D., Santos, G., Brasseur, G., and Saiz-Lopez, A.: Bromine and iodine chemistry in a global chemistry-climate model: description and evaluation of very short-lived oceanic sources, Atmospheric Chemistry and Physics, 12, 1423–1447, 2012.

Palmer, C. J. and Reason, C. J.: Relationships of surface bromoform concentrations with mixed layer depth and salinity in the tropical oceans, Global Biogeochemical Cycles, 23, 2009.

Pechtl, S., Lovejoy, E. R., Burkholder, J. B., and von Glasow, R.: Modeling the possible role of iodine oxides in atmospheric new particle formation, Atmospheric Chemistry and Physics, 6, 505–523, 2006.

Pedder, R. E.: Practical quadrupole theory: graphical theory, Excel Core Mass Spectrometers, Pittsburgh, PA, Extrel Application Note RA_2010 A, 2001.

Pelley, J.: Methyl iodide, a fumigant under fire, Environmental Science & Technology, 43, 6898–6898, 2009.

Pennington, J., Mahoney, K., Kuwahara, V., Kolber, D., Calienes, R., and Chavez, F.: Primary production in the eastern tropical Pacific: A review, Progress in Oceanography, 69, 285–317, 2006.

Peters, C., Pechtl, S., Stutz, J., Hebestreit, K., Hönninger, G., Heumann, K., Schwarz, A., Winterlik, J., Platt, U., et al.: Reactive and organic halogen species in three different European coastal environments, Atmos. Chem. Phys, 5, 3357–3375, 2005.

Platt, U. and Lehrer, E.: Arctic tropospheric ozone chemistry, ARCTOC, Final Report of the EU-Project EV5V-CT93-0318, Heidelberg, 1997.

Pratte, P. and Rossi, M. J.: The heterogeneous kinetics of HOBr and HOCl on acidified sea salt and model aerosol at 40-90temperature, Phys. Chem. Chem. Phys., 8, 3988–4001, doi:10.1039/B604321F, URL http://dx.doi.org/10.1039/B604321F, 2006.

Prézelin, B. and Ley, A. C.: Photosynthesis and chlorophyll a fluorescence rhythms of marine phytoplankton, Marine Biology, 55, 295–307, 1980.

Puentedura, O., Gil, M., Saiz-Lopez, A., Hay, T., Navarro-Comas, M., Gómez-Pelaez, A., Cuevas, E., Iglesias, J., and Gomez, L.: Iodine monoxide in the north subtropical free troposphere, Atmos. Chem. Phys, 12, 4909–4921, 2012.

Pyle, J., Ashfold, M., Harris, N., Robinson, A., Warwick, N., Carver, G., Gostlow, B., O'Brien, L., Manning, A., Phang, S., et al.: Bromoform in the tropical boundary layer of the Maritime Continent during OP3, Atmospheric Chemistry and Physics, 11, 529–542, 2011.

Quack, B. and Wallace, D.: Air-sea flux of bromoform: Controls, rates, and implications, Global Biogeochem. Cycles, 17, 1023, 2003.

Quack, B., Atlas, E., Petrick, G., Stroud, V., Schauffler, S., and Wallace, D.: Oceanic bromoform sources for the tropical atmosphere, Geophys. Res. Lett, 31, L23S05, 2004.

Quack, B., Atlas, E., Petrick, G., and Wallace, D.: Bromoform and dibromomethane above the Mauritanian upwelling: Atmospheric distributions and oceanic emissions, Journal of Geophysical Research-Atmospheres, 112, D09 312, 2007a.

Quack, B., Peeken, I., Petrick, G., and Nachtigall, K.: Oceanic distribution and sources of bromoform and dibromomethane in the Mauritanian upwelling, Journal of Geophysical Research: Oceans (1978–2012), 112, 2007b.

Raimund, S., Quack, B., Bozec, Y., Vernet, M., Rossi, V., Garçon, V., Morel, Y., and Morin, P.: Sources of short-lived bromocarbons in the Iberian upwelling system, Biogeosciences (BG), 8, 1551–1464, 2011.

Rasmussen, R., Khalil, M., Gunawardena, R., and Hoyt, S.: Atmospheric methyl iodide (CH3I), Journal of Geophysical Research: Oceans (1978–2012), 87, 3086–3090, 1982.

Rattigan, O., Shallcross, D., and Cox, R.: UV absorption cross-sections and atmospheric photolysis rates of CF_3I, CH_3I, C_2H_5I and CH_2ICl, J. Chem. Soc., Faraday Trans., 93, 2839–2846, 1997.

Read, K., Mahajan, A., Carpenter, L., Evans, M., Faria, B., Heard, D., Hopkins, J., Lee, J., Moller, S., Lewis, A., et al.: Extensive halogen-mediated ozone destruction over the tropical Atlantic Ocean, Nature, 453, 1232–1235, 2008.

Redeker, K., Wang, N., Low, J., McMillan, A., Tyler, S., and Cicerone, R.: Emissions of methyl halides and methane from rice paddies, Science, 290, 966–969, 2000.

Richter, U. and Wallace, D.: Production of methyl iodide in the tropical Atlantic Ocean, Geophys. Res. Lett, 31, L23S03, 2004.

Robinson, A., McIntyre, J., Harris, N., Pyle, J., Simmonds, P., and Danis, F.: A lightweight balloon-borne gas chromatograph for in situ measurements of atmospheric halocarbons, Review of Scientific Instruments, 71, 4553–4560, 2000.

Rost, B., Zondervan, I., and Wolf-Gladrow, D.: Sensitivity of phytoplankton to future changes in ocean carbonate chemistry: current knowledge, contradictions and research directions, Marine ecology progress series, 373237., 227, 227–237, 2008.

Ryther, J. H.: Photosynthesis and fish production in the sea, Science, 166, 72–76, 1969.

Saiz-Lopez, A. and Plane, J.: Novel iodine chemistry in the marine boundary layer, Geophysical research letters, 31, L04 112, 2004.

Saiz-Lopez, A. and von Glasow, R.: Reactive halogen chemistry in the troposphere, Chem. Soc. Rev., 41, 6448–6472, 2012.

Saiz-Lopez, A., Chance, K., Liu, X., Kurosu, T., and Sander, S.: First observations of iodine oxide from space, Geophysical research letters, 34, L12 812, 2007a.

Saiz-Lopez, A., Mahajan, A. S., Salmon, R. A., Bauguitte, S. J.-B., Jones, A. E., Roscoe, H. K., and Plane, J. M. C.: Boundary Layer Halogens in Coastal Antarctica, Science, 317, 348–351, 2007b.

Saiz-Lopez, A., Lamarque, J., Kinnison, D., Tilmes, S., Ordónez, C., Orlando, J., Conley, A., Plane, J., Mahajan, A., Sousa Santos, G., et al.: Estimating the climate significance of halogen-driven ozone loss in the tropical marine troposphere, Atmos. Chem. Phys, 12, 3939–3949, 2012.

Salawitch, R., Weisenstein, D., Kovalenko, L., Sioris, C., Wennberg, P., Chance, K., Ko, M., and McLinden, C.: Sensitivity of ozone to bromine in the lower stratosphere, Geophysical research letters, 32, L05 811, 2005.

Salawitch, R. J.: Atmospheric chemistry: Biogenic bromine, Nature, 439, 275–277, 2006.

Sander, R.: Compilation of Henry's law constants for inorganic and organic species of potential importance in environmental chemistry, 1999.

Sander, R., Keene, W., Pszenny, A., Arimoto, R., Ayers, G., Baboukas, E., Cainey, J., Crutzen, P., Duce, R., Hönninger, G., et al.: Inorganic bromine in the marine boundary layer: a critical review, Atmospheric Chemistry and Physics Discussions, 3, 2963–3050, 2003.

Santos, G. S. and Rast, S.: A global model study of natural bromine sources and the effects on tropospheric chemistry using MOZART4, Journal of Atmospheric Chemistry, pp. 1–21, 2013.

Saunders, R., Kumar, R., Gomez Martin, J., Mahajan, A., Murray, B., and Plane, J.: Studies of the formation and growth of aerosol from molecular iodine precursor, Zeitschrift für Physikalische Chemie, 224, 1095–1117, 2010.

Saunders, R. W. and Plane, J. M.: Formation pathways and composition of iodine oxide ultra-fine particles, Environmental Chemistry, 2, 299–303, 2006.

Scarratt, M. and Moore, R.: Production of chlorinated hydrocarbons and methyl iodide by the red microalga Porphyridium purpureum, Limnology and oceanography, 44, 703–707, 1999.

Schall, C. and Heumann, K.: GC determination of volatile organoiodine and organobromine compounds in Arctic seawater and air samples, Fresenius' Journal of Analytical Chemistry, 346, 717–722, 1993.

Schall, C., Laturnus, F., and Heumann, K.: Biogenic volatile organoiodine and organobromine compounds released from polar macroalgae, Chemosphere, 28, 1315–1324, 1994.

Schauffler, S., Atlas, E., Blake, D., Flocke, F., Lueb, R., Lee-Taylor, J., Stroud, V., and Travnicek, W.: Distributions of brominated organic compounds in the troposphere and lower stratosphere, Journal of geophysical research, 104, 21 513–21, 1999.

Schofield, R., Fueglistaler, S., Wohltmann, I., and Rex, M.: Sensitivity of stratospheric Bry to uncertainties in very short lived substance emissions and atmospheric transport, Atmospheric Chemistry and Physics. 11, pp. 1379–1392, 2011.

Schönhardt, A., Richter, A., Wittrock, F., Kirk, H., Oetjen, H., Roscoe, H., Burrows, J., et al.: Observations of iodine monoxide columns from satellite, Atmospheric Chemistry and Physics, 8, 637–653, 2008.

Selin, N. E.: Global Biogeochemical Cycling of Mercury: A Review, Annual Review of Environment and Resources, 34, 43–63, doi:10.1146/annurev.environ.051308.084314, URL `http://www.annualreviews.org/doi/abs/10.1146/annurev.environ.051308.084314`, 2009.

Setschenow, J. Z.: Über die Konstitution der Salzlösungen auf Grund ihres Verhaltens zu 20 Kohlensäure, Z. Physik. Chem., 4, 117125, 1889.

Singh, H., Gregory, G., Anderson, B., Browell, E., and Sachse, G.: Low ozone in the marine boundary layer of the tropical Pacific Ocean: Photochemical loss, chlorine atoms, Journal of geophysical research, 101, 1907–1917, 1996.

Sive, B., Varner, R., Mao, H., Blake, D., Wingenter, O., and Talbot, R.: A large terrestrial source of methyl iodide, Geophysical Research Letters, 34, L17 808, 2007.

Smith, S.: Wind stress and heat flux over the ocean in gale force winds, Journal of Physical Oceanography, 10, 709–726, 1980.

Solomon, S., Garcia, R. R., and Ravishankara, A. R.: On the role of iodine in ozone depletion, Journal of Geophysical Research: Atmospheres, 99, 20 491–20 499, 1994.

Stammerjohn, S., Massom, R., Rind, D., and Martinson, D.: Regions of rapid sea ice change: An inter-hemispheric seasonal comparison, Geophysical Research Letters, 39, 2012.

Stemmler, I., Rothe, M., and Hense, I.: Numerical modelling of methyl iodide in the Eastern Tropical Atlantic, Biogeosciences Discussions, 10, 1111–1145, 2013.

Stohl, A., Forster, C., Frank, A., Seibert, P., and Wotawa, G.: Technical note: The Lagrangian particle dispersion model FLEXPART version 6.2, Atmospheric Chemistry and Physics, 5, 2461–2474, 2005.

Stouffer, R. J., Yin, J., Gregory, J., Dixon, K., Spelman, M., Hurlin, W., Weaver, A., Eby, M., Flato, G., Hasumi, H., et al.: Investigating the causes of the response of the thermohaline circulation to past and future climate changes., Journal of Climate, 19, 2006.

Studnikov, E.: The viscosity of moist air, Journal of Engineering Physics and Thermophysics, 19, 1036–1037, 1970.

Sturges, W. and Barrie, L.: Chlorine, bromine and iodine in Arctic aerosols, Atmospheric Environment (1967), 22, 1179–1194, 1988.

Sturges, W., Sullivan, C., Schnell, R., Heidt, L., and Pollock, W.: Bromoalkane production by Antarctic ice algae, Tellus B, 45, 120–126, 1993.

Tang, T. and McConnell, J.: Autocatalytic release of bromine from Arctic snow pack during polar sunrise, Geophysical Research Letters, 23, 2633–2636, 1996.

Tegtmeier, S., Krüger, K., Quack, B., Atlas, E., Blake, D. R., Boenisch, H., Engel, A., Hepach, H., Hossaini, R., Navarro, M. A., Raimund, S., Sala, S., Shi, Q., and Ziska, F.: The contribution of oceanic methyl iodide to stratospheric iodine, Atmospheric Chemistry and Physics Discussions, 13, 11 427–11 471, 2013a.

Tegtmeier, S., Krüger, K., Quack, B., Atlas, E., Blake, D. R., Boenisch, H., Engel, A., Hepach, H., Hossaini, R., Navarro, M. A., Raimund, S., Sala, S., Shi, Q., and Ziska, F.: The contribution of oceanic methyl iodide to stratospheric iodine, Atmospheric Chemistry and Physics, 13, 11 869–11 886, doi:10.5194/acp-13-11869-2013, URL http://www.atmos-chem-phys.net/13/11869/2013/, 2013b.

Tokarczyk, R. and Moore, R.: Production of volatile organohalogens by phytoplankton cultures, Geophysical research letters, 21, 285–288, 1994.

van Deemter, J., Zuiderweg, F., and Klinkenberg, A.: Longitudinal diffusion and resistance to mass transfer as causes of nonideality in chromatography, Chemical Engineering Science, 5, 271 – 289, doi:http://dx.doi.org/10.1016/0009-2509(56)80003-1, URL http://www.sciencedirect.com/science/article/pii/0009250956800031, 1956.

Varner, R., Zhou, Y., Russo, R., Wingenter, O., Atlas, E., Stroud, C., Mao, H., Talbot, R., and Sive, B.: Controls on atmospheric chloroiodomethane (CH_2ClI) in marine environments, J. Geophys. Res, 113, D10 303, 2008.

Vogel, T. M., Criddle, C. S., and McCarty, P. L.: ES&T critical reviews: transformations of halogenated aliphatic compounds, Environmental Science & Technology, 21, 722–736, 1987.

von Glasow, R. and Crutzen, P. J.: Tropospheric halogen chemistry, Treatise on Geochemistry, 4, 1–67, 2007.

von Glasow, R., Von Kuhlmann, R., Lawrence, M., Platt, U., Crutzen, P., et al.: Impact of reactive bromine chemistry in the troposphere, Atmospheric Chemistry and Physics, 4, 2481–2497, 2004.

Wang, C. and Enfield, D. B.: The tropical Western Hemisphere warm pool, Geophysical Research Letters, 28, 1635–1638, 2001.

Wang, L., Moore, R. M., and Cullen, J. J.: Methyl iodide in the NW Atlantic: Spatial and seasonal variation, Journal of Geophysical Research: Oceans (1978–2012), 114, 2009.

Wanninkhof, R.: Relationship between wind speed and gas exchange, J. Geophys. Res, 97, 7373–7382, 1992.

Warwick, N., Pyle, J., and Shallcross, D.: Global modelling of the atmospheric methyl bromide budget, Journal of atmospheric chemistry, 54, 133–159, 2006.

Wayne, R. P.: Chemistry of atmospheres, 1993.

Wennberg, P.: Atmospheric chemistry: Bromine explosion, Nature, 397, 299–301, 1999.

Wever, R., Tromp, M. G., Krenn, B. E., Marjani, A., and Van Tol, M.: Brominating activity of the seaweed Ascophyllum nodosum: impact on the biosphere, Environmental science & technology, 25, 446–449, 1991.

Wevill, D. and Carpenter, L.: Automated measurement and calibration of reactive volatile halogenated organic compounds in the atmosphere, Analyst, 129, 634–638, 2004.

Wilke, C. and Chang, P.: Correlation of diffusion coefficients in dilute solutions, AIChE Journal, 1, 264–270, 1955.

Williams, J., Gros, V., Atlas, E., Maciejczyk, K., Batsaikhan, A., Schöler, H., Forster, C., Quack, B., Yassaa, N., Sander, R., et al.: Possible evidence for a connection between methyl iodide emissions and Saharan dust, Journal of geophysical research, 112, D07 302, 2007.

Worton, D., Sturges, W., Schwander, J., Mulvaney, R., Barnola, J.-M., and Chappellaz, J.: 20th century trends and budget implications of chloroform and related tri-and dihalomethanes inferred from firn air, Atmospheric Chemistry and Physics, 6, 2847–2863, 2006.

Worton, D. R., Mills, G. P., Oram, D. E., and Sturges, W. T.: Gas chromatography negative ion chemical ionization mass spectrometry: Application to the detection of alkyl nitrates and halocarbons in the atmosphere, Journal of Chromatography A, 1201, 112 – 119, doi:http://dx.doi.org/10.1016/j.chroma.2008.06.019, URL http://www.sciencedirect.com/science/article/pii/S0021967308010480, 2008.

Xie, W., Shiu, W., and Mackay, D.: A review of the effect of salts on the solubility of organic compounds in seawater, Marine Environmental Research, 44, 429–444, 1997.

Yamamoto, H., Yokouchi, Y., Otsuki, A., and Itoh, H.: Depth profiles of volatile halogenated hydrocarbons in seawater in the Bay of Bengal, Chemosphere, 45, 371–377, 2001.

Yang, X., Cox, R., Warwick, N., Pyle, J., Carver, G., O'Connor, F., and Savage, N.: Tropospheric bromine chemistry and its impacts on ozone: A model study, Journal of geophysical research, 110, D23 311, 2005.

Yokouchi, Y., Mukai, H., Yamamoto, H., Otsuki, A., Saitoh, C., and Nojiri, Y.: Distribution of methyl iodide, ethyl iodide, bromoform, and dibromomethane over the ocean

(east and southeast Asian seas and the western Pacific), Journal of geophysical research, 102, 8805–8809, 1997.

Yokouchi, Y., Nojiri, Y., Barrie, L. A., Toom-Sauntry, D., and Fujinuma, Y.: Atmospheric methyl iodide: High correlation with surface seawater temperature and its implications on the sea-to-air flux, Journal of Geophysical Research: Atmospheres, 106, 12 661–12 668, 2001.

Yokouchi, Y., Hasebe, F., Fujiwara, M., Takashima, H., Shiotani, M., Nishi, N., Kanaya, Y., Hashimoto, S., Fraser, P., Toom-Sauntry, D., et al.: Correlations and emission ratios among bromoform, dibromochloromethane, and dibromomethane in the atmosphere, Journal of geophysical research, 110, D23 309, 2005.

Yokouchi, Y., Osada, K., Wada, M., Hasebe, F., Agama, M., Murakami, R., Mukai, H., Nojiri, Y., Inuzuka, Y., Toom-Sauntry, D., et al.: Global distribution and seasonal concentration change of methyl iodide in the atmosphere, J. Geophys. Res, 113, D18 311, 2008.

Yokouchi, Y., Saito, T., Ooki, A., and Mukai, H.: Diurnal and seasonal variations of iodocarbons (CH_2ClI, CH_2I_2, CH_3I, and C_2H_5I) in the marine atmosphere, Journal of Geophysical Research, 116, D06 301, 2011.

Zhou, Y., Varner, R. K., Russo, R. S., Wingenter, O. W., Haase, K. B., Talbot, R., and Sive, B. C.: Coastal water source of short-lived halocarbons in New England, Journal of Geophysical Research: Atmospheres (1984–2012), 110, 2005.

Ziska, F., Quack, B., Abrahamsson, K., Archer, S. D., Atlas, E., Bell, T., Butler, J. H., Carpenter, L. J., Jones, C. E., Harris, N. R. P., Hepach, H., Heumann, K. G., Hughes, C., Kuss, J., Krüger, K., Liss, P., Moore, R. M., Orlikowska, A., Raimund, S., Reeves, C. E., Reifenhäuser, W., Robinson, A. D., Schall, C., Tanhua, T., Tegtmeier, S., Turner, S., Wang, L., Wallace, D., Williams, J., Yamamoto, H., Yvon-Lewis, S., and Yokouchi, Y.: Global sea-to-air flux climatology for bromoform, dibromomethane and methyl iodide, Atmospheric Chemistry and Physics Discussions, 13, 5601–5648, 2013.